CHEMICAL MECHANISMS GOVERNING ATMOSPHERIC NEW PARTICLE FORMATION

by

Bryan Richard Bzdek

A dissertation submitted to the Faculty of the University of Delaware in partial fulfillment of the requirements for the degree of Doctor of Philosophy in Chemistry and Biochemistry

Summer 2014

ProQuest LLC.
789 East Eisenhower Parkway
P.O. Box 1346
Ann Arbor, MI 48106 - 1346

CHEMICAL MECHANISMS GOVERNING

ATMOSPHERIC NEW PARTICLE FORMATION

by

Bryan Richard Bzdek

Approved: _____

Murray V. Johnston, III, Ph.D.
Chair of the Department of Chemistry and Biochemistry

Approved: _____

George H. Watson, Ph.D.
Dean of the College of Arts and Sciences

Approved: _____

James G. Richards, Ph.D.
Vice Provost for Graduate and Professional Education

I certify that I have read this dissertation and that in my opinion it meets the academic and professional standard required by the University as a dissertation for the degree of Doctor of Philosophy.

Signed: _____

Murray V. Johnston, III, Ph.D.
Professor in charge of dissertation

I certify that I have read this dissertation and that in my opinion it meets the academic and professional standard required by the University as a dissertation for the degree of Doctor of Philosophy.

Signed: _____

Burnaby Munson, Ph.D.
Member of dissertation committee

I certify that I have read this dissertation and that in my opinion it meets the academic and professional standard required by the University as a dissertation for the degree of Doctor of Philosophy.

Signed: _____

Douglas P. Ridge, Ph.D.
Member of dissertation committee

I certify that I have read this dissertation and that in my opinion it meets the academic and professional standard required by the University as a dissertation for the degree of Doctor of Philosophy.

Signed: _____

George W. Luther, III, Ph.D.
Member of dissertation committee

ACKNOWLEDGMENTS

There are many people to acknowledge. First, I acknowledge my adviser, Prof. Murray Johnston. Obviously, without him none of this work would have been possible. He is an exemplary adviser. He has taught me how to be an effective scientist, and I consider him a role model.

I also thank the members of my committee: Profs. Burnaby Munson, Doug Ridge, and George Luther. They all have provided some very insightful and helpful ideas during my graduate tenure. In particular, I want to give extra thanks to Prof. Ridge, as he was key to all the laboratory studies discussed in this dissertation. He describes rather complicated phenomena in a manner that is both understandable and fascinating. I very much appreciate the many conversations we have had over the years. I also give extra thanks to Prof. Luther, since he played a key role in the background of all the Lewes campaigns.

I thank the members of the Johnston and Ridge groups as well. In particular, I acknowledge Dr. Ross Pennington, since we did three field campaigns together and made a great team. Each of those campaigns had its own unique adventure or catastrophe along the way, but we endured. I also thank Dr. Chris Zordan, who performed all the measurements for the 2007 campaign in Lewes, the results of which feature heavily in this dissertation. I acknowledge as well Joe DePalma, who performed lots of modeling of my experimental work. His work always provides something insightful that we would not necessarily extract from the experiment alone. I thank Andy Horan, who helped substantially on a number of different projects and is

a great person for brainstorming. I also thank Dr. Jeff Spraggins, since he essentially set me up for all the cluster work. Those projects would have been much harder without his help during my first year. Lastly, I thank Dr. Joe Klems for a number of insightful discussions and for generally being a great guy.

I acknowledge a number of collaborators who also have helped me along the way, especially Drs. Julia and Alex Laskin, Dr. Jim Smith, Prof. Peter McMurry, Prof. Dave Hanson, and a number of Finns (too many to name!).

I would be remiss if I did not thank my undergraduate adviser, Prof. Molly McGuire, since I am fairly certain I would not be in graduate school without her help. I was pretty clueless about what to do with my life. I also need to thank Prof. Charles Clapp, since it was he who in an off-handed comment at a departmental barbecue my junior year at Bucknell suggested I join this group. It was a very good suggestion.

I also thank all my teachers throughout the years, since they taught me everything I know. In particular, I will single out Mrs. Paddock and Mr. DeSantis (both my high school chemistry teachers) and Mrs. Tanzola and Mrs. Harrison (who taught me everything I needed to know about life by the end of 5^{th} grade).

I need to thank the people who gave me money. The research described here was funded mainly by NSF. I was lucky to have been individually funded by UD's Center for Critical Zone Research, ACS Division of Analytical Chemistry, and EPA.

Lastly, I thank my friends and family because they are the best people anybody could ask to have in their lives. Most important among them are my grandparents; my parents, Liliane and Richard; and my brother, Kevin. Thank you for teaching me the value of hard work and integrity and for providing me with whatever I needed to achieve my goals. I hope you can at least understand the abstract here.

TABLE OF CONTENTS

LIST OF TABLES

LIST OF FIGURES

ABSTRACT

The goal of this dissertation is to understand the chemistry that governs new particle formation, a ubiquitous and important atmospheric process. New particle formation occurs when gas phase precursors condense to create small molecular clusters on the order of 1 nm diameter. Those clusters must then grow rapidly by uptake of additional species from the gas phase to reach a size around 100 nm diameter where they may serve as a condensation site for water and ultimately serve as the seeds for cloud droplets (cloud condensation nuclei). It is thought that up to 50% of all cloud condensation nuclei arise from new particle formation. However, modelers have substantial difficulty predicting under what conditions new particle formation will occur and what fraction of newly formed particles will ultimately reach the cloud condensation nucleus size range. This predictive difficulty is an important contributor to the uncertainty in aerosol effects on global climate and therefore also contributes to the large uncertainty in anthropogenic effects on climate. In order to reduce these uncertainties, a more precise understanding of how particles nucleate and grow in the atmospheric is required.

In this dissertation, mass spectrometry is used to determine the chemical processes involved in new particle formation. In general, gas phase species such as sulfuric acid, ammonia, amines, and organic matter are thought to be contributors but exactly how and how much each species contributes to the growth of nanoparticles is not well understood. Various mass spectrometric techniques allow for measurement of the chemical composition of clusters and aerosols. Fourier transform ion cyclotron

resonance mass spectrometry (FTICR-MS) and Nano Aerosol Mass Spectrometry (NAMS) are used to study the chemical composition and reactivity of clusters < 3 nm diameter and nanoparticles 10-20 nm diameter, respectively. The FTICR-MS studies are laboratory based, whereas the NAMS studies are field based. Measurements of cluster composition and reactivity using FTICR-MS permit prediction of the composition of ambient molecular clusters, which is important because directly measuring the composition of these clusters in the atmosphere is very challenging. For ambient molecular clusters to become relevant to climate by serving as cloud condensation nuclei, they must grow rapidly. Measurements of 20 nm diameter ambient nanoparticles with NAMS permit determination of the pathways of nanoparticle growth.

Studies of the reactivity of atmospherically relevant ammonium bisulfate clusters with gas phase amines in a FTICR-MS show that amines displace ammonia efficiently in these clusters. Therefore, one would expect aminium bisulfate clusters to be an important component of ambient molecular clusters. These studies also show that bases can add to a cluster in order to neutralize acid, thereby growing the cluster to a larger size, but amines add to clusters much more efficiently than ammonia. Additional FTICR-MS studies suggest that ammonia may not efficiently grow clusters by neutralization because there is an activation barrier to neutralization of sulfuric acid by ammonia in acidic ammonium bisulfate clusters.

Field measurements of nanoparticle elemental composition with NAMS indicate that during new particle formation both organic and inorganic species contribute to growth. Sulfuric acid is shown to be a key contributor to the growth of ambient nanoparticles. Comparison of particle phase sulfur and gas phase sulfuric acid

measurements indicates that sulfuric acid contributes to new particle growth by diffusion limited condensation onto the nanoparticle. Ammonia, rather than amine, is shown to be the key cation that neutralizes sulfuric acid. However, additional nitrogen-containing species are important to growth, and the measurements indicate that this nitrogen contributes to the carbonaceous (organic) portion of the particle. Overall, carbonaceous matter is the largest contributor to nanoparticle growth, and in the locations discussed here must be highly oxidized and contain substantial nitrogen. Silicon is also shown to be a ubiquitous component of ambient nanoparticles, indicating a previously overlooked anthropogenic source of aerosol mass that requires further investigation.

More broadly, this dissertation shows that sulfuric acid adds to both clusters and nanoparticles in a collision limited manner. On the other hand, ammonia uptake in both size regimes may not necessarily occur at a collision limited rate. Finally, additional nitrogen containing compounds are important to new particle formation in both size regimes, but the molecular form of these species is different for each size regime. Amines are important contributors to the growth of molecular clusters, whereas other organic nitrogen species are important to the growth of nanoparticles.

Chapter 1

INTRODUCTION

1.1 Atmospheric Aerosols and Their Relevance

Atmospheric aerosols have deleterious effects on visibility, human health, and global climate. With respect to health, aerosols can trigger myocardial infarction[1-3] and have been linked to lung cancer[4] and adverse pregnancy outcomes.[5] Exposure to ultrafine particles (particles with diameters < 100 nm) is strongly correlated with adverse health effects.[6-8] With respect to global climate, the dominant effect is cooling, either directly through the scattering of incoming solar radiation or indirectly by serving as cloud condensation nuclei that increase cloud albedo and influence precipitation patterns.[9, 10] The current level of scientific understanding of these effects on climate is relatively low, especially compared to the heating caused by greenhouse gases.[11] An improved understanding of these processes, especially the indirect effect, is essential to increase the accuracy of climate change predictions.

Figure 1.1 summarizes the formation of cloud condensation nuclei and their impact on Earth's energy balance. Airborne particles serve as cloud condensation nuclei if they grow into cloud droplets when exposed to an air mass supersaturated with water vapor. While growth is dependent on particle size, composition, and the degree of supersaturation, most particles above about 100 nm diameter are thought to be able to serve as cloud condensation nuclei.[12, 13] Airborne particles in the size range relevant to cloud condensation nuclei can be divided into two main categories:

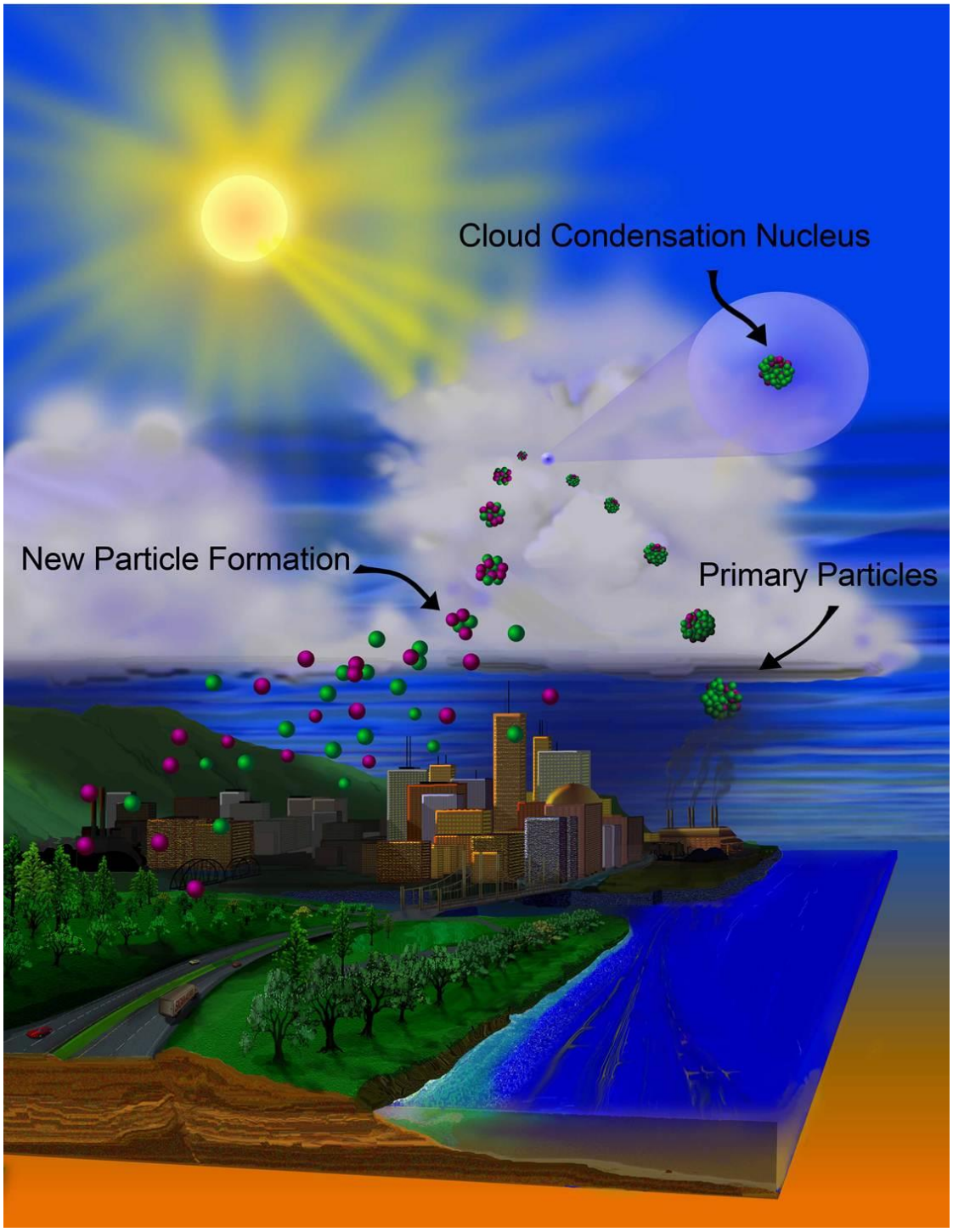

Figure 1.1: The formation of cloud condensation nuclei and their impact on Earth's energy balance. Graphic acknowledgment: Robert Gates.

primary particles and secondary particles arising from new particle formation processes. Primary particles are emitted directly into the atmosphere by natural processes such as sea spray and volcanic action, or by anthropogenic processes such as combustion. Primary particles that are too small to serve directly as cloud condensation nuclei may grow into the relevant size range by condensation of secondary chemical species such as sulfate, nitrate, and organic compounds that have been partially oxidized in the atmosphere. For many years, it was thought that primary particles were the predominant source of cloud condensation nuclei; however, new particle formation recently has been recognized as a potentially significant contributor to cloud condensation nucleus levels.[14-19] New particle formation occurs when gas phase species in the atmosphere come together to form new particles in the low nanometer size range that subsequently grow into the cloud condensation nucleus size range. A recent estimate suggests that 45% of global cloud condensation nuclei are derived from new particle formation.[19] However, there are substantial uncertainties associated with the rates of both primary particle emission and new particle formation, and these uncertainties lead to an even greater uncertainty in the contribution of cloud condensation nuclei to global climate.[20] For this reason, the relationship between new particle formation and climate is a rapidly evolving area of study.

1.2 Atmospheric New Particle Formation

New particle formation is a global phenomenon, with approximately 35% of cloud condensation nuclei arising from new particle formation in the free troposphere and 10% from new particle formation in the boundary layer, mostly over land.[19] New particle formation frequently occurs over the continental boundary layer in regional events that extend hundreds of kilometers.[21-23] Localized new particle formation

occurs in urban and industrial plumes as well as in coastal marine locations. Particle size distributions during new particle formation events are usually obtained with a scanning mobility particle sizer (SMPS). The SMPS consists of a differential mobility analyzer (DMA), which size-selects singly charged particles based on electrical mobility diameter (defined as the diameter of a unit density sphere having the same electrical mobility as the particle of interest), and a condensation particle counter (CPC), which grows particles in a supersaturated vapor to a size that permits individual particles to be detected by light scattering.[24]

Figure 1.2 shows an example of new particle formation over a several day period in Lewes, Delaware.[25] Each day, nucleation occurs shortly after sunrise and particles grow quickly to several tens of nanometers. Growth rates in the 10-20 nm diameter range in Lewes are on the order of 2-10 $nm \cdot hr^{-1}$,[25-27] which are typical of new particle formation events elsewhere around the world.[22] Note that the lower size limit for efficient detection with an SMPS is typically 3 nm diameter. Recent technological advances have made it possible to mobility analyze and detect sub-3 nm diameter clusters.[28] These measurements have shown that a relatively stable pool of clusters in the 1-2 nm diameter size range exists in ambient air at a number concentration of 10^3-10^4 cm^{-3}. The likely chemical components of these clusters can be inferred from knowledge of condensable species in the gas phase. In most ambient observations, the nucleation rate is strongly correlated with the sulfuric acid vapor concentration.[29] However, the precise constituents of the critical cluster for nucleation are unclear since several mechanisms for cluster formation and growth are possible. The predominant cluster formation mechanism is believed to be a ternary process involving sulfuric

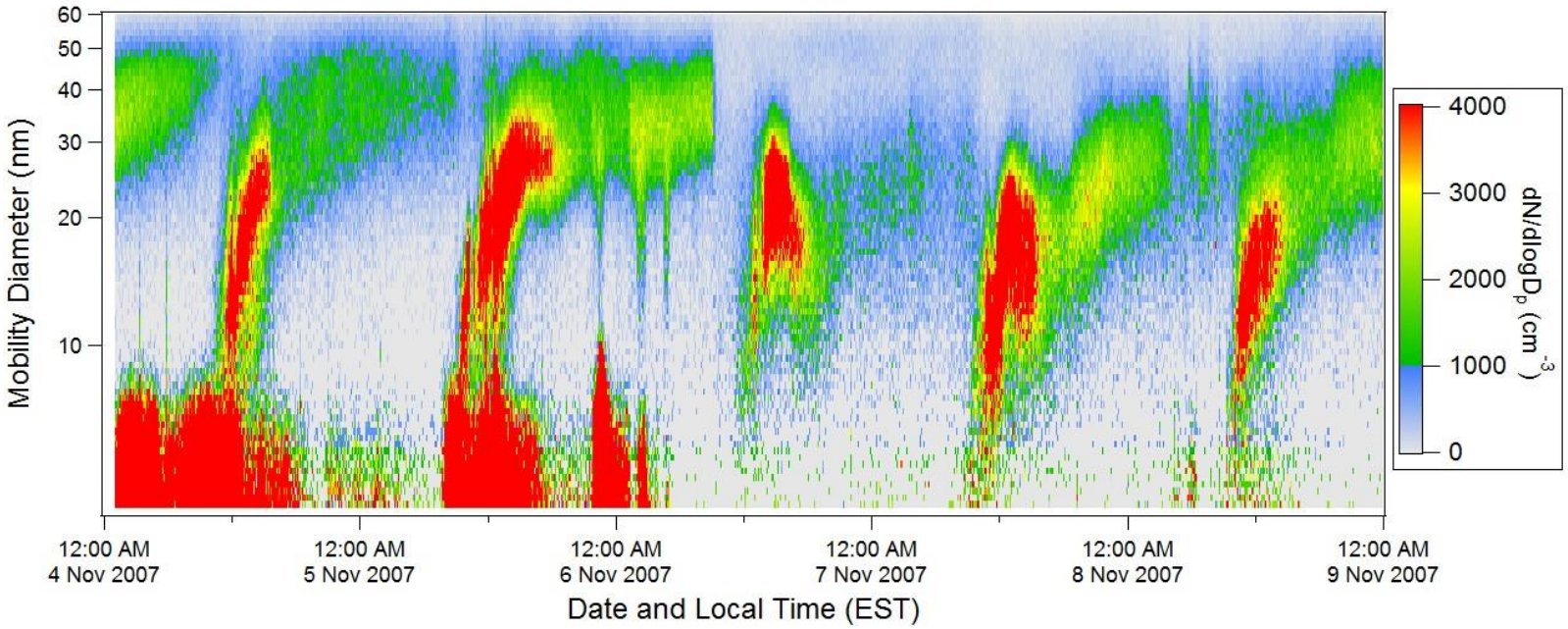

Figure 1.2: SMPS-measured particle size distributions over several days in Lewes, Delaware, when new particle formation was observed.

acid, water, and ammonia.[30-33] Other possible mechanisms include sulfuric acid-water binary nucleation,[30, 34-36] ion-induced nucleation,[37] nucleation via halogen species,[38] and condensation of organic vapors.[39] Recent fieldwork suggests that carboxylic acids and organic bases (e.g. amines) may participate in cluster growth.[40, 41] Recently, two mass spectrometers have been developed to measure the composition of these clusters.[42, 43] Field measurements with these instruments give evidence for sulfuric acid, ammonia, amines, and organic matter playing important roles in cluster composition.[42, 44, 45] The relatively constant ambient concentration of these clusters means that formation and loss rates are similar.

New particle formation events such as the one in Figure 1.2 can occur by activation of the existing cluster pool[28] or by rapid formation of new clusters during activation.[46] Activation requires that the growth rate associated with condensation of gas phase species exceed the loss rate due to processes such as evaporation or scavenging onto pre-existing particles. These conditions are most often met when 1) the concentrations of condensable gases rapidly increase, for example by photochemical processes during the daytime, and/or 2) the pre-existing particle concentration is low, which both favors condensation of gases onto newly formed nanoparticles over larger (and higher surface area) pre-existing particles and decreases the probability of nanoparticle scavenging. Growth rates during new particle formation events are initially on the order of 1-20 $nm \cdot hr^{-1}$, and as a result particles can reach a size appropriate for cloud condensation nucleus activity within one or a few days.[18] If the particle survives this time period, then it contributes to cloud condensation nucleus activity. Analysis of several new particle formation events suggests that up to 20% of the particles in an event eventually become cloud condensation nuclei, which

increases the cloud condensation nucleus concentration above its pre-existing value by a factor of about 4.[18]

1.3 Analytical Challenges Associated with Studying New Particle Formation

Our understanding of new particle formation and its impact on cloud condensation nucleus levels are based mostly on measurements of particle size distributions with time. While these measurements show how new particle formation proceeds, they give no information on the chemical mechanisms by which nucleation and growth occur. Understanding chemical mechanisms requires the development of analytical methods capable of detecting and characterizing the small amount of matter in these particles. In this section, the difficulties associated with chemical analysis of ambient clusters and nanoparticles are illustrated by analogy with well-known analytical methods. Because a high degree of molecular specificity must be determined for an exceedingly small sample size, this discussion focuses on mass spectrometry. Indeed, the most successful approaches described in the literature for ambient nanoparticle chemical analysis involve mass spectrometry.

Ambient particles in the 1-10 nm diameter size range are similar in dimension to individual biomolecules such as peptides or proteins. It is informative to compare the analysis of each by sampling through an atmospheric pressure inlet into a mass spectrometer. Highly sensitive analysis by electrospray ionization might involve spraying a 1 nanomolar solution at a sub-microliter per minute flow rate. Such a source has the potential to produce 10^7 particles (individual biomolecules) per second into the air being sampled through the inlet. In contrast, formation rates for the sub-3 nm clusters are typically < 10 $cm^{-3} \cdot s^{-1}$.[28] Even if a large volume of air is sampled through the inlet, a huge disconnect exists between the number concentration in the

cluster pool and even the most sensitive configuration for biomolecular analysis by atmospheric pressure sampling and analysis. For this reason, direct mass spectrometric analysis of the cluster pool is challenging and has been reported only recently.[42, 43]

Another illustration of the analytical challenge involves collecting a sufficient amount of material for analysis. Typically, on the order of several picograms to a nanogram of material is needed for a conventional mass spectrometric analysis. Collecting this amount of sample during a new particle formation event is possible, but removing interferents may be difficult. The number and mass concentrations of particles in the 10 nm diameter range can exceed 10^3 cm^{-3} and 10^{-15} $g \cdot cm^{-3}$, respectively, during new particle formation, although background levels are much lower. The high mass concentration during new particle formation allows a sufficient amount of material to be collected in only minutes with a high sampling rate (e.g. 5 $L \cdot min^{-1}$). The challenge is to efficiently capture 10 nm diameter particles while rejecting larger particles. Since the mass of a particle scales with the cube of its diameter, capturing even one rogue particle at a large size can compromise the analysis. A similar problem arises if gas phase compounds are inadvertently analyzed, since many relevant compounds have much higher mass concentrations in ambient air than in particulate matter. Fortunately, a method has been developed to size-selectively collect and sensitively analyze ambient nanoparticles,[47] and chemical composition measurements have been reported for collected particles smaller than 10 nm in diameter.[48]

Real-time single particle mass spectrometry has been used for almost two decades to sample and analyze "large" (> 50 nm diameter) particles in ambient air.[49, 50] This method becomes increasingly difficult as the particle size decreases because of

the limited amount of material in the particle to be analyzed. For example, a single 10 nm particle of ammonium sulfate contains less than 10^{-18} g (< 1 attogram) of material, which corresponds to about 4000 "molecules". In principle, this amount of material is detectable by mass spectrometry, but only if near unit ionization efficiency is achieved. The experiment is facilitated by performing elemental rather than molecular analysis, since there are many more atoms than molecules in the particle and high ionization efficiencies are more readily achieved for atoms. Elemental analysis with size-selective particle trapping extends real-time single particle analysis to the 10 nm diameter size range.[51]

1.4 Chemical Mechanism of New Particle Formation

In order for a nucleated particle to ultimately serve as a cloud condensation nucleus, the particle must grow at a rate that is much faster than the rate of coagulation or scavenging to larger particles.[52, 53] Therefore, it is important to understand the chemical mechanisms that govern growth of newly formed nanoparticles to larger sizes.[54]

In general, sulfuric acid, ammonia, amines, and other organic matter are thought to contribute to atmospheric new particle formation. Sulfuric acid is a key contributor to new particle formation,[36, 55-59] although measured nanoparticle nucleation and growth rates are typically much larger than those expected based simply on sulfuric acid and ammonia alone.[52, 60, 61] Field measurements during new particle formation events have shown a correlation between the measured nucleation rate and the sulfuric acid concentration.[29, 62, 63] The important role of sulfuric acid in new particle formation has been validated by measurements of ambient ions and uncharged clusters, as mass spectra of these species indicate an important sulfuric

acid-derived component (bisulfate).[45, 64, 65] Additionally, ambient measurements by the thermal desorption chemical ionization mass spectrometer (TDCIMS), which allows molecular characterization of semivolatile components in collected nanoparticulate samples down to 6 nm in diameter, have indicated the presence of sulfate or bisulfate in newly-formed particles.[40, 41, 48] Much effort has focused on quantifying the contribution of sulfuric acid to particle growth.[52, 61, 66-69] This work has generally focused on relating gas-phase sulfuric acid concentrations to measured particle growth rates during new particle formation events.

Ammonia and, more recently, amines have also emerged as important contributors to new particle formation.[30, 31, 45, 55, 56, 64, 70-75] Both are thought to contribute by lowering the barrier to nucleation with sulfuric acid.[76-79] Amines have been shown to nucleate new particles more efficiently than ammonia.[78] Amines are also proposed to contribute to nanoparticle growth through the formation of aminium-organic acid salts.[40, 41, 80]

Other organic species are also thought to contribute to new particle formation. Indeed, indirect measurements of nanoparticle chemical composition suggest a substantial organic component associated with new particle formation[81-86] and nanoparticle chemical composition measurements during new particle formation have shown that organic species can contribute substantially to growth.[40, 41] Recent modeling studies have also implied that the growth of nanoparticles cannot be explained without a substantial low-volatility organic component.[54, 87-89] Several studies have provided additional important evidence of the critical role of organics to new particle formation.[58, 90-92] In both field and laboratory studies, highly oxidized organic compounds have been shown to cluster with sulfuric acid and are presumed to

lower the energy barrier to nucleation.[44] Modeling studies have shown that multifunctional organics can sufficiently stabilize sulfuric acid in order to promote nucleation[93] and may even adsorb to the surface of small clusters to promote growth.[94] Most recently, a chamber study has shown that large, highly oxidized organic molecules are involved in both the nucleation and growth of new particles.[95-97]

Taken together, this discussion highlights several key uncertainties associated with our understanding of the mechanisms of new particle formation. First, sulfuric acid is clearly important, but exactly how it contributes to nanoparticle growth is not fully resolved. Second, amines may be more efficient than ammonia at enhancing new particle formation, but very little work thus far has quantified neither how bases incorporate into clusters and nanoparticles nor the relative efficiencies of each in promoting new particle growth. Third, organic species appear to be important, but very little is understood about their composition and their quantitative contribution to growth. Fourth, the relative importance of these contributors as clusters grow to nanoparticles has not been well-characterized. These uncertainties exist because (as discussed above) performing chemical composition measurements on clusters and nanoparticles is a challenging analytical problem.[98] This dissertation will directly address these uncertainties in order to provide a quantitative mechanistic description of the channels by which newly formed clusters and nanoparticles may grow.

1.5 Research Approach and Dissertation Goals

The goal of this dissertation is to better understand the chemical mechanisms underlying atmospheric new particle formation using mass spectrometric approaches. The concept of new particle formation is illustrated in Fig. 1.3. In this figure, new

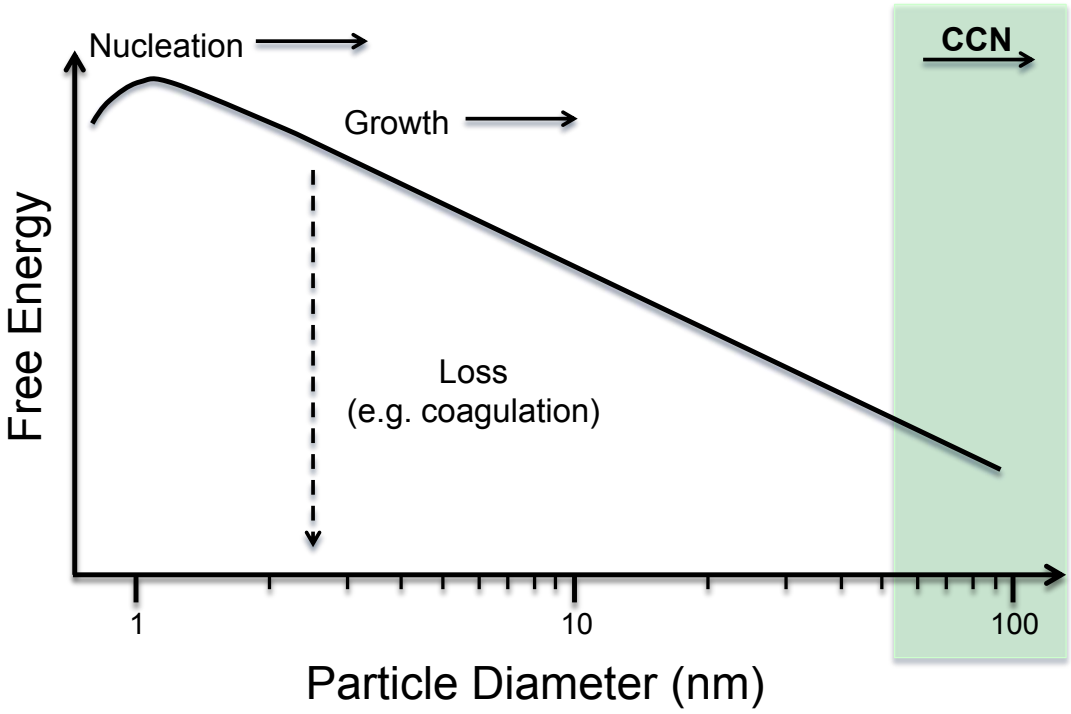

Figure 1.3: New particle formation described as a function of Gibbs free energy. CCN = cloud condensation nucleus.

particle formation is described as a function of Gibbs free energy. Nucleation occurs upon formation of the critical cluster, which is the most unstable (highest energy) cluster along the potential energy surface. After overcoming the nucleation barrier to form the critical cluster, growth is considered to be a downhill process. As discussed earlier, growth must be sufficiently fast so as to avoid particle loss due to scavenging or coagulation. Once particles have grown to ~50-100 nm diameter, they may be activated to serve as cloud condensation nuclei.

Figure 1.4 essentially superimposes the research approach used in this dissertation to study new particle formation onto Fig. 1.3. As discussed earlier, chemical composition analysis over the entire size range relevant to new particle formation is challenging. As a particle grows from the nucleating cluster (1 nm diameter) to the cloud condensation nucleus size range (100 nm), its mass increases 10^6-fold. Therefore, one might expect that different analytical technologies are required to analyze particles as they grow from 1 to 100 nm diameter. Two size regimes important to new particle formation are investigated in this dissertation: 1) small clusters on the order of 1-2 nm diameter and 2) nanoparticles on the order of 10-30 nm diameter. Both of these size regimes are important. Measurements on 1-2 nm diameter clusters gives information important to the very early steps of nanoparticle growth. However, if those clusters are to become atmospherically relevant, they must grow into the cloud condensation nucleus size regime. Measurements on 20 nm diameter nanoparticles provide insight on that growth process. Different analytical approaches are used to access these size regimes. To understand the chemical composition and reactivity of molecular clusters, Fourier transform ion cyclotron

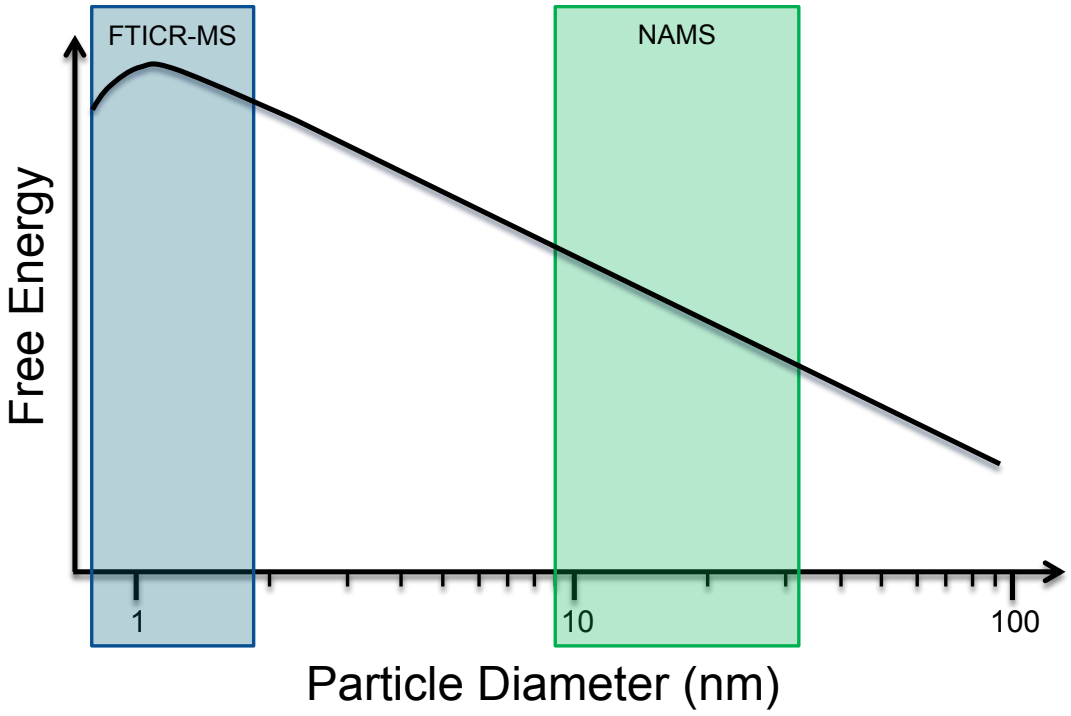

Figure 1.4: Research approach taken in this dissertation superimposed onto the description of new particle formation.

resonance mass spectrometry (FTICR-MS)[99] is used. These measurements are laboratory-based and are aimed at predicting the composition of the ambient sub-3 nm diameter cluster pool. To understand the composition and growth processes relevant on the order of 20 nm diameter, the Nano Aerosol Mass Spectrometer (NAMS)[51, 100, 101] is used. The NAMS measurements described in this dissertation are primarily field-based.

1.5.1 Fourier Transform Ion Cyclotron Resonance Mass Spectrometry

FTICR-MS is used to study the composition and reactivity of clusters relevant to new particle formation that are produced by electrospray ionization. The specific instrument used is a 7T Bruker apex-Qe instrument. The instrument is described in detail in Fig.1.5. The benefits of using FTICR-MS are 1) mass spectra may be obtained at a desired trapping time, easily allowing for the study of ion-molecule reactions, and 2) high resolving power and high mass accuracy mass spectra permit accurate assignment of elemental formulae to the reactant and product ions.

In the experimental setup, charged, atmospherically relevant clusters are produced by electrospray ionization of solutions containing relevant salts, such as ammonium sulfate. The charged clusters enter the mass spectrometer through a glass capillary. Charged clusters are then transferred through an orthogonal ion funnel, where they are focused into an ion beam. Charged clusters then are decelerated and collisionally cooled as they pass through a second ion funnel and into a hexapole, which serves as an ion guide. A desired cluster is mass selected on the basis of its mass-to-charge (*m/z*) ratio in a mass selective quadrupole. The composition-selected clusters are then transferred to a collision cell (hexapole), which also serves as an ion

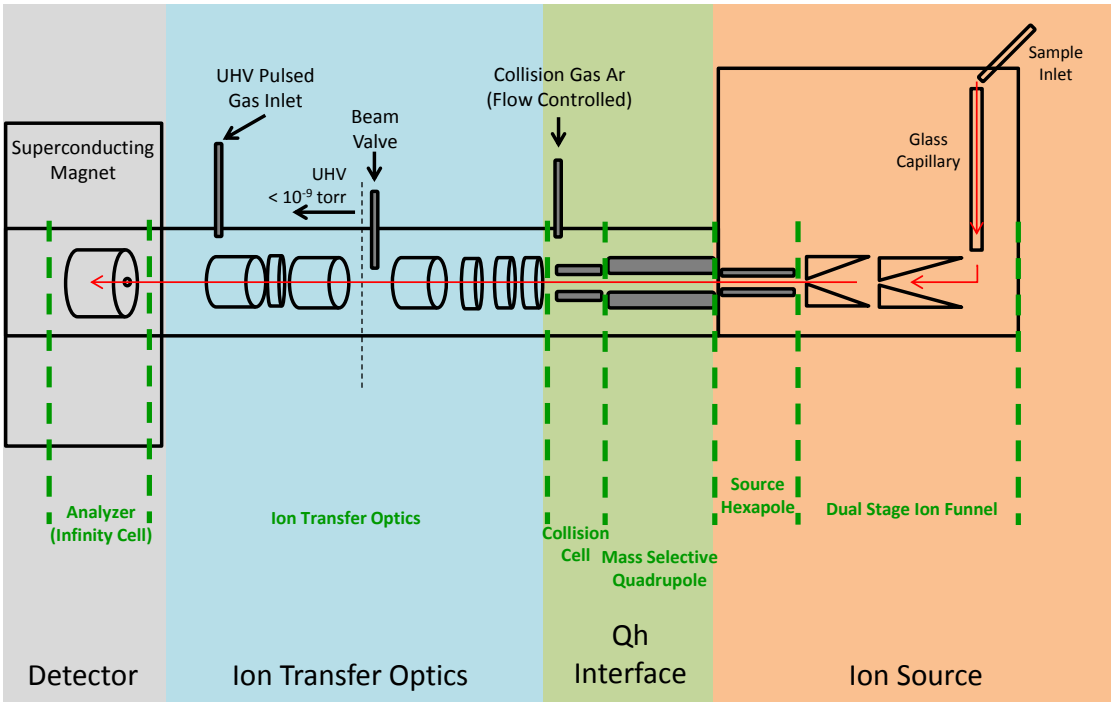

Figure 1.5: Schematic description of the 7T Bruker apex-Qe FTICR-MS used in this dissertation.

accumulation cell. Accumulation times were on the order of 1 sec in the experiments discussed in this dissertation. The pressure in the collision cell was ~1 × 10^{-3} torr. Accumulated, composition-selected clusters are then sent through ion transfer optics and ultimately into the ICR cell (mass analyzer and detector). For this instrument, the Infinity Cell served as the mass analyzer and detector. The ICR cell is located inside the 7T superconducting magnet. The ultra-high vacuum region (ICR cell) was maintained at ~5 × 10^{-10} torr when no reactive gas was intentionally introduced into the system.

Relevant to the ion-molecule reactions discussed in Chapters 3 and 4, atmospherically relevant gases (e.g. ammonia or amines) were introduced from a lecture bottle through Teflon tubing into an external gas reservoir. The pressure in the gas reservoir was generally on the order of 1-5 torr. Neutral reactant gas was introduced to the ICR cell via a high precision variable leak valve that was incorporated into the ultra-high vacuum pulsed valve inlet. By adjusting the variable leak valve, the pressure in the ultra-high vacuum region of the instrument can be set to a constant value. For the ion-molecule reactions described in Chapters 3 and 4, pressure was set to ~4 × 10^{-9} torr. Note that this value represents the value reported by the instrument's ultra-high vacuum ionization gauge, and its accuracy is affected by the chemical identity of the gas introduced into the cell as well as the magnetic field strength. Determination of the absolute gas pressure in the ICR cell is described in Chapter 3. In order to perform ion-molecule reactions, the instrument is operated in the same manner as if one were to perform sustained off-resonance irradiation collision induced dissociation (SORI-CID) experiments. The basic principle of SORI-CID is that ions are excited slightly above or below their resonant frequency, resulting

in an oscillation of the ion kinetic energy with time. This off-resonance excitation is combined with a short, high pressure collision gas pulse.[102-104] Ions are alternately accelerated and decelerated, and fragmentation results from multiple low-energy collisions. For these experiments, SORI-CID was used simply to vary the reaction time in the cell. In this setup, the SORI power was set to 0% (i.e. no off-resonance excitation) and the pulse length was set to the desired reaction time. In this manner, a mass spectrum of ions in the ICR cell may be obtained at a specific trapping time.

For the measurements described in Chapter 6, a specially fabricated 6T FTICR-MS was used.[105] Relevant to those experiments, the FTICR-MS was equipped with surface-induced dissociation (SID). In SID, an ion is collided against a surface at a well-defined collision energy, and some of the ion kinetic energy is rapidly (order of picoseconds) converted to internal energy, resulting in efficient activation and fragmentation.[104, 106] As a result of the large energy deposition into the ion after a single collision, fragmentation products inaccessible by other multiple collision ion activation methods can be accessed. The major benefit of SID is that the energy deposited into an ion is large in magnitude, has a narrow range, and is tunable. This benefit enables precise modeling of the fragmentation energetics.

1.5.2 Nano Aerosol Mass Spectrometry

NAMS was used to study the elemental composition of nanoparticles on the order of 20 nm diameter.[51, 100, 101] The instrumental setup is described in Fig. 1.6. Particles are drawn into an inlet and charged in a unipolar charger,[47] which maximizes the fraction of particles receiving a +1 charge as they are sampled into the instrument. Once the charged particles enter the mass spectrometer, they are collimated and

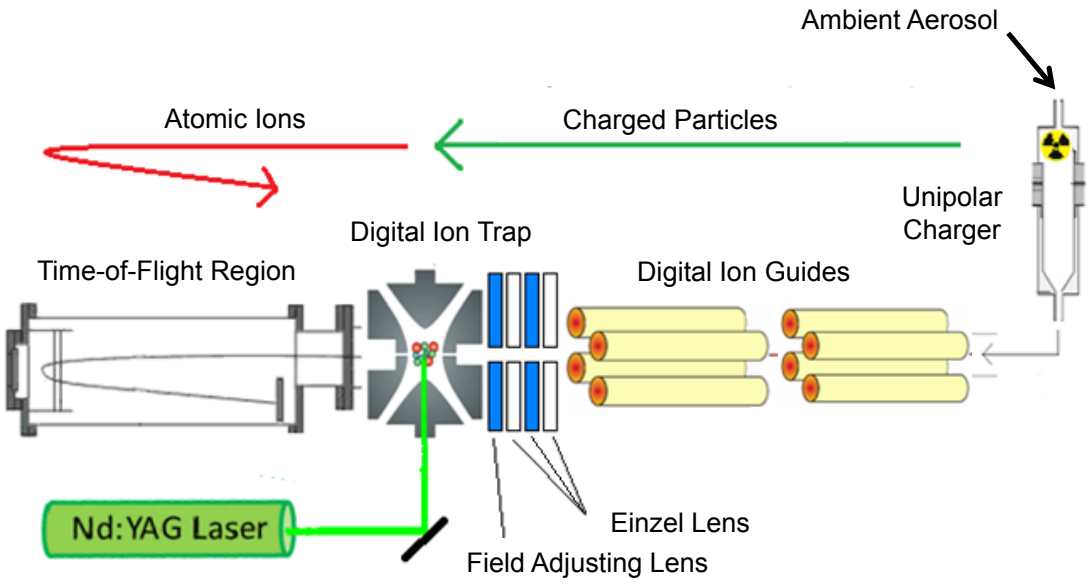

Figure 1.6: Schematic description of the Nano Aerosol Mass Spectrometer.

focused into a digital ion trap. For the results presented in Chapters 7 and 8 and the second portion of Chapter 10, an aerodynamic lens assembly followed by a digital ion guide were used to focus the charged particles. However, for the results presented in Chapter 9 and the first portion of Chapter 10, the aerodynamic lens assembly was replaced with an additional digital ion guide. This instrumental upgrade (accomplished by M. Ross Pennington[107]) resulted in a substantially improved nanoparticle focusing and analysis rate. Charged particles are size-selectively trapped in a digital ion trap on the basis of *m/z*, which can be related to a mass normalized diameter (d_{mn}). The mass normalized diameter is defined as the diameter of a spherical particle having unit density and the same *m/z* as the particle being trapped. Mass normalized diameter can be converted to mobility diameter (d_m, a more commonly used description of particle size) by Eq. (1):

$$d_{mn} = d_m \left(\frac{\rho}{\rho_0}\right)^{1/3} \quad (1)$$

where ρ_0 is a reference density (1 g·cm^{-3}) and ρ is the density of the particle analyzed by NAMS.

Once a charged nanoparticle is size-selectively trapped in the digital ion trap, it is cooled to the center of the trap by an Ar bath gas and then irradiated with a high energy laser pulse (532 nm, 200 mJ·pulse^{-1}, focused to a spot < 100 μm diameter) to create a laser-induced plasma that quantitatively converts all molecular components of the particle to multiply charged positive atomic ions. These ions are then mass analyzed by time-of-flight.

The crucial component of analysis with NAMS is the quantitative conversion of all molecular species to atomic ions. This is accomplished by using a highly focused, high fluence laser that reaches the "complete ionization limit," where the

laser forms a plasma and the particle is quantitatively converted to multiply charged, positive atomic ions.[108-111] This development was first reported by Reents [108, 109] and developed further by Zachariah.[110-114] By this ionization method, one may quantitatively determine the elemental composition of a particle directly from the observed ion signal intensities in the mass spectrum. An additional advantage is an increase in total ion signal from an individual particle, as there are considerably more atoms in a particle than there are molecular species. This advantage improves spectral detection efficiency, as ion signal from smaller particles is significantly enhanced. This method appears to have some morphological and compositional biases, at least for particles > 50 nm diameter. Quantitation of multi-component particles may depend on 1) whether the components exist in a core-shell structure or are internally mixed and 2) the laser absorptivity of each component.[114] It is thought that during the ionization process, the particle initially experiences "soft heating" followed by a hydrodynamic expansion and that ablation and ionization are effectively complete before the laser reaches its peak intensity.[113] Additionally, ions from the surface of the particle are of higher energy than those in the core, resulting in a lower detection efficiency.[113] In addition to determining quantitative elemental composition of a particle, laser-induced plasma analysis may also be used to determine the size of an analyzed particle.[108, 109, 115]

The major advantage of NAMS is that the elemental composition is quantitative: NAMS-measured elemental mole ratios of standard compounds are typically within 10% of their expected values.[116] The disadvantages of NAMS are that the size range for analysis is relatively small (10-30 nm diameter) and all molecular information is lost during particle analysis. To overcome the second disadvantage, a

molecular apportionment algorithm (described in detail in Chapter 7) has been developed based on the major constitutents typically found in ambient nanoparticles in order to place the elemental composition into a molecular context.[25, 117]

1.6 Scope of This Dissertation

As discussed earlier, the goal of this dissertation is to understand the chemical mechanisms governing atmospheric new particle formation. This goal is accomplished by performing laboratory and field measurements addressing two size regimes important to this process. Chapters 2-6 address laboratory measurements aimed primarily at understanding the composition and reactivity of the sub-3 nm cluster pool. The information gained from these chapters enable an improved understanding of how small clusters important to nucleation grow to larger sizes. Chapters 7-10 address field measurements aimed at understanding the growth processes operative from ~10-20 nm diameter. An improved understanding of cluster growth pathways from 10-20 nm diameter is important. If the clusters discussed in Chapters 2-6 are to be climatically relevant, they must grow into the cloud condensation nucleus size range, thereby passing through the 10-20 nm diameter size range.

In specific, Chapter 2 examines the composition of clusters produced by electrospray ionization of atmospherically relevant salts. Chapter 3 examines the reactivity of these ammonium salt clusters with gas phase amines in order to infer the favored composition of clusters in the sub-3 nm cluster pool. Chapter 4 expands on the work discussed in Chapter 3 by exploring size-dependent chemistry of atmospherically relevant salt clusters. Chapter 5 extends the discussion of the previous chapters by examining additional mechanisms by which bases may incorporate into

these clusters. Chapter 6 addresses specifically how clusters may grow out of the cluster pool to larger sizes.

Chapter 7 examines how the composition of 20 nm diameter nanoparticles changes during new particle formation and describes initial work to put those elemental changes into a molecular context. Chapter 8 focuses primarily on sulfuric acid and how it contributes to nanoparticle growth. Chapter 9 describes highly time-resolved measurements of nanoparticle elemental composition, which permit more precise elucidation of the chemical mechanism of new particle formation. Chapter 10 addresses species other than sulfuric acid that are important to nanoparticle growth.

Chapter 11 concludes with a discussion of the overarching trends observed from measurements in both size regimes (clusters and nanoparticles) and puts those observations into context with respect to the mechanism of new particle formation. Remaining knowledge gaps and methods to fill those gaps are also discussed.

1.7 References

1. Nawrot, T. S.; Perez, L.; Kunzli, N.; Munters, E.; Nemery, B., Public health importance of triggers of myocardial infarction: a comparative risk assessment. *Lancet* **2011,** *377* (9767), 732-740.

2. Peters, A.; Dockery, D. W.; Muller, J. E.; Mittleman, M. A., Increased particulate air pollution and the triggering of myocardial infarction. *Circulation* **2001,** *103* (23), 2810-2815.

3. Rich, D. Q.; Ozkaynak, H.; Crooks, J.; Baxter, L.; Burke, J.; Ohman-Strickland, P.; Thevenet-Morrison, K.; Kipen, H. M.; Zhang, J. F.; Kostis, J. B.; Lunden, M.; Hodas, N.; Turpin, B. J., The triggering of myocardial infarction by fine particles is enhanced when particles are enriched in secondary species. *Environ. Sci. Technol.* **2013,** *47* (16), 9414-9423.

4. Raaschou-Nielsen, O.; Andersen, Z. J.; Beelen, R.; Samoli, E.; Stafoggia, M.; Weinmayr, G.; Hoffmann, B.; Fischer, P.; Nieuwenhuijsen, M. J.; Brunekreef, B.; Xun, W. W.; Katsouyanni, K.; Dimakopoulou, K.; Sommar, J.; Forsberg, B.; Modig, L.; Oudin, A.; Oftedal, B.; Schwarze, P. E.; Nafstad, P.; De Faire, U.; Pedersen, N. L.; Östenson, C.-G.; Fratiglioni, L.; Penell, J.; Korek, M.; Pershagen, G.; Eriksen, K. T.; Sørensen, M.; Tjønneland, A.; Ellermann, T.; Eeftens, M.; Peeters, P. H.; Meliefste, K.; Wang, M.; Bueno-de-Mesquita, B.; Key, T. J.; de Hoogh, K.; Concin, H.; Nagel, G.; Vilier, A.; Grioni, S.; Krogh, V.; Tsai, M.-Y.; Ricceri, F.; Sacerdote, C.; Galassi, C.; Migliore, E.; Ranzi, A.; Cesaroni, G.; Badaloni, C.; Forastiere, F.; Tamayo, I.; Amiano, P.; Dorronsoro, M.; Trichopoulou, A.; Bamia, C.; Vineis, P.; Hoek, G., Air pollution and lung cancer incidence in 17 European cohorts: prospective analyses from the European Study of Cohorts for Air Pollution Effects (ESCAPE). *Lancet Oncol.* **2013,** *14* (9), 813-822.

5. Miranda, M. L.; Edwards, S. E.; Chang, H. H.; Auten, R. L., Proximity to roadways and pregnancy outcomes. *J. Expo. Sci. Environ. Epidemiol.* **2013,** *23* (1), 32-38.

6. Gong, H.; Linn, W. S.; Clark, K. W.; Anderson, K. R.; Sioutas, C.; Alexis, N. E.; Cascio, W. E.; Devlin, R. B., Exposures of healthy and asthmatic volunteers to concentrated ambient ultrafine particles in Los Angeles. *Inhal. Toxicol.* **2008,** *20* (6), 533-545.

7. Maudgalya, T.; Genaidy, A.; Weckman, G.; Shell, R.; Karwowski, W.; Wallace, S., A critical appraisal of epidemiological studies investigating the effects of ultrafine particles on human health. *Hum. Fact. Ergon. Man.* **2008,** *18* (3), 358-373.

8. Oberdorster, G.; Oberdorster, E.; Oberdorster, J., Nanotoxicology: An emerging discipline evolving from studies of ultrafine particles. *Environ. Health Perspect.* **2005,** *113* (7), 823-839.

9. Charlson, R. J.; Schwartz, S. E.; Hales, J. M.; Cess, R. D.; Coakley, J. A.; Hansen, J. E.; Hofmann, D. J., Climate forcing by anthropogenic aerosols. *Science* **1992,** *255* (5043), 423-430.

10. Lohmann, U.; Feichter, J., Global indirect aerosol effects: A review. *Atmos. Chem. Phys.* **2005,** *5* (3), 715-737.

11. Solomon, S.; Qin, D.; Manning, M.; Chen, Z.; Marquis, M.; Averyt, K. B.; Tignor, M.; Miller, H. L., *Climate Change 2007: The Physical Science Basis. Contribution of Working Group I to the Fourth Assessment Report of the Intergovernmental Panel on Climate Change*. Cambridge University Press: Cambridge, UK, 2007; p 996.

12. Zelenyuk, A.; Imre, D.; Earle, M.; Easter, R.; Korolev, A.; Leaitch, R.; Liu, P.; Macdonald, A. M.; Ovchinnikov, M.; Strapp, W., In situ characterization of cloud condensation nuclei, interstitial, and background particles using the single particle mass spectrometer, SPLAT II. *Anal. Chem.* **2010,** *82* (19), 7943-7951.

13. Dusek, U.; Frank, G. P.; Hildebrandt, L.; Curtius, J.; Schneider, J.; Walter, S.; Chand, D.; Drewnick, F.; Hings, S.; Jung, D.; Borrmann, S.; Andreae, M. O., Size matters more than chemistry for cloud-nucleating ability of aerosol particles. *Science* **2006,** *312* (5778), 1375-1378.

14. Lihavainen, H.; Kerminen, V. M.; Komppula, M.; Hatakka, J.; Aaltonen, V.; Kulmala, M.; Viisanen, Y., Production of "potential" cloud condensation nuclei associated with atmospheric new-particle formation in northern Finland. *J. Geophys. Res.-Atmos.* **2003,** *108* (D24), 4782, doi: 10.1029/2003jd003887.

15. Laaksonen, A.; Hamed, A.; Joutsensaari, J.; Hiltunen, L.; Cavalli, F.; Junkermann, W.; Asmi, A.; Fuzzi, S.; Facchini, M. C., Cloud condensation nucleus production from nucleation events at a highly polluted region. *Geophys. Res. Lett.* **2005,** *32* (6), L06812, doi: 10.1029/2004gl022092.

16. Kerminen, V. M.; Lihavainen, H.; Komppula, M.; Viisanen, Y.; Kulmala, M., Direct observational evidence linking atmospheric aerosol formation and cloud droplet activation. *Geophys. Res. Lett.* **2005,** *32* (14), L14803, doi: 10.1029/2005gl023130.

17. Ghan, S. J.; Easter, R. C.; Chapman, E. G.; Abdul-Razzak, H.; Zhang, Y.; Leung, L. R.; Laulainen, N. S.; Saylor, R. D.; Zaveri, R. A., A physically based estimate of radiative forcing by anthropogenic sulfate aerosol. *J. Geophys. Res.-Atmos.* **2001,** *106* (D6), 5279-5293, doi: 10.1029/2000JD900503.

18. Kuang, C.; McMurry, P. H.; McCormick, A. V., Determination of cloud condensation nuclei production from measured new particle formation events. *Geophys. Res. Lett.* **2009,** *36* (9), L09822, doi: 10.1029/2009gl037584.

19. Merikanto, J.; Spracklen, D. V.; Mann, G. W.; Pickering, S. J.; Carslaw, K. S., Impact of nucleation on global CCN. *Atmos. Chem. Phys.* **2009,** *9* (21), 8601-8616.

20. Pierce, J. R.; Adams, P. J., Uncertainty in global CCN concentrations from uncertain aerosol nucleation and primary emission rates. *Atmos. Chem. Phys.* **2009,** *9* (4), 1339-1356.

21. Kulmala, M.; Kerminen, V. M., On the formation and growth of atmospheric nanoparticles. *Atmos. Res.* **2008,** *90* (2-4), 132-150.

22. Kulmala, M.; Vehkamaki, H.; Petaja, T.; Dal Maso, M.; Lauri, A.; Kerminen, V. M.; Birmili, W.; McMurry, P. H., Formation and growth rates of ultrafine atmospheric particles: A review of observations. *J. Aerosol Sci.* **2004,** *35* (2), 143-176.

23. Crippa, P.; Pryor, S. C., Spatial and temporal scales of new particle formation events in eastern North America. *Atmos. Environ.* **2013,** *75* (1), 257-264.

24. Kulkarni, P.; Baron, P. A.; Willeke, K., *Aerosol Measurement: Principles, Techniques, and Applications, 3rd Edition*. Wiley-Interscience: New York, 2011.

25. Bzdek, B. R.; Zordan, C. A.; Luther, G. W.; Johnston, M. V., Nanoparticle chemical composition during new particle formation. *Aerosol Sci. Technol.* **2011,** *45* (8), 1041-1048.

26. Bzdek, B. R.; Horan, A. J.; Pennington, M. R.; DePalma, J. W.; Zhao, J.; Jen, C. N.; Hanson, D.; Smith, J. N.; McMurry, P. H.; Johnston, M. V., Quantitative and time-resolved nanoparticle composition measurements during new particle formation. *Faraday Discuss.* **2013,** *165* (1), 25-43.

27. Bzdek, B. R.; Zordan, C. A.; Pennington, M. R.; Luther, G. W.; Johnston, M. V., Quantitative assessment of the sulfuric acid contribution to new particle growth. *Environ. Sci. Technol.* **2012,** *46* (8), 4365-4373.

28. Kulmala, M.; Riipinen, I.; Sipila, M.; Manninen, H. E.; Petaja, T.; Junninen, H.; Dal Maso, M.; Mordas, G.; Mirme, A.; Vana, M.; Hirsikko, A.; Laakso, L.; Harrison, R. M.; Hanson, I.; Leung, C.; Lehtinen, K. E. J.; Kerminen, V. M., Toward direct measurement of atmospheric nucleation. *Science* **2007,** *318* (5847), 89-92.

29. Kuang, C.; McMurry, P. H.; McCormick, A. V.; Eisele, F. L., Dependence of nucleation rates on sulfuric acid vapor concentration in diverse atmospheric locations. *J. Geophys. Res.-Atmos.* **2008,** *113* (D10), D10209, doi: 10.1029/2007jd009253.

30. Ball, S. M.; Hanson, D. R.; Eisele, F. L.; McMurry, P. H., Laboratory studies of particle nucleation: Initial results for H_2SO_4, H_2O, and NH_3 vapors. *J. Geophys. Res.-Atmos.* **1999,** *104* (D19), 23709-23718, doi: 10.1029/1999JD900411.

31. Korhonen, P.; Kulmala, M.; Laaksonen, A.; Viisanen, Y.; McGraw, R.; Seinfeld, J. H., Ternary nucleation of H_2SO_4, NH_3, and H_2O in the atmosphere. *J. Geophys. Res.-Atmos.* **1999,** *104* (D21), 26349-26353, doi: 10.1029/1999JD900784.

32. McMurry, P. H.; Fink, M.; Sakurai, H.; Stolzenburg, M. R.; Mauldin, R. L.; Smith, J.; Eisele, F.; Moore, K.; Sjostedt, S.; Tanner, D.; Huey, L. G.; Nowak, J. B.; Edgerton, E.; Voisin, D., A criterion for new particle formation in the sulfur-rich Atlanta atmosphere. *J. Geophys. Res.-Atmos.* **2005,** *110* (D22), D22s02, doi: 10.1029/2005jd005901.

33. Benson, D. R.; Erupe, M. E.; Lee, S. H., Laboratory-measured H_2SO_4-H_2O-NH_3 ternary homogeneous nucleation rates: Initial observations. *Geophys. Res. Lett.* **2009,** *36* (15), L15818, doi: 10.1029/2009gl038728.

34. Kulmala, M.; Laaksonen, A., Binary nucleation of water sulfuric acid system: Comparison of classical theories with different H_2SO_4 saturation vapor pressures. *J. Chem. Phys.* **1990,** *93* (1), 696-701.

35. Benson, D. R.; Young, L. H.; Kameel, F. R.; Lee, S. H., Laboratory-measured nucleation rates of sulfuric acid and water binary homogeneous nucleation from the SO_2+OH reaction. *Geophys. Res. Lett.* **2008,** *35* (11), L11801, doi: 10.1029/2008gl033387.

36. Young, L. H.; Benson, D. R.; Kameel, F. R.; Pierce, J. R.; Junninen, H.; Kulmala, M.; Lee, S. H., Laboratory studies of H_2SO_4/H_2O binary homogeneous nucleation from the SO_2+OH reaction: Evaluation of the experimental setup and preliminary results. *Atmos. Chem. Phys.* **2008,** *8* (16), 4997-5016.

37. Yu, F. Q.; Turco, R. P., Ultrafine aerosol formation via ion-mediated nucleation. *Geophys. Res. Lett.* **2000,** *27* (6), 883-886, doi: 10.1029/1999GL011151.

38. Hoffmann, T.; O'Dowd, C. D.; Seinfeld, J. H., Iodine oxide homogeneous nucleation: An explanation for coastal new particle production. *Geophys. Res. Lett.* **2001,** *28* (10), 1949-1952, doi: 10.1029/2000GL012399.

39. O'Dowd, C. D.; Aalto, P.; Hameri, K.; Kulmala, M.; Hoffmann, T., Aerosol formation - Atmospheric particles from organic vapours. *Nature* **2002,** *416* (6880), 497-498.

40. Smith, J. N.; Barsanti, K. C.; Friedli, H. R.; Ehn, M.; Kulmala, M.; Collins, D. R.; Scheckman, J. H.; Williams, B. J.; McMurry, P. H., Observations of aminium salts in atmospheric nanoparticles and possible climatic implications. *Proc. Natl. Acad. Sci. U.S.A.* **2010,** *107* (15), 6634-6639.

41. Smith, J. N.; Dunn, M. J.; VanReken, T. M.; Iida, K.; Stolzenburg, M. R.; McMurry, P. H.; Huey, L. G., Chemical composition of atmospheric nanoparticles formed from nucleation in Tecamac, Mexico: Evidence for an important role for organic species in nanoparticle growth. *Geophys. Res. Lett.* **2008,** *35* (4), L04808, doi: 10.1029/2007gl032523.

42. Junninen, H.; Ehn, M.; Petaja, T.; Luosujarvi, L.; Kotiaho, T.; Kostiainen, R.; Rohner, U.; Gonin, M.; Fuhrer, K.; Kulmala, M.; Worsnop, D. R., A high-resolution mass spectrometer to measure atmospheric ion composition. *Atmos. Meas. Tech.* **2010,** *3* (4), 1039-1053.

43. Zhao, J.; Eisele, F. L.; Titcombe, M.; Kuang, C.; McMurry, P. H., Chemical ionization mass spectrometric measurements of atmospheric neutral clusters using the cluster-CIMS. *J. Geophys. Res.-Atmos.* **2010,** *115* (D8), D08205, doi: 10.1029/2009JD012606.

44. Ehn, M.; Kleist, E.; Junninen, H.; Petaja, T.; Lonn, G.; Schobesberger, S.; Dal Maso, M.; Trimborn, A.; Kulmala, M.; Worsnop, D. R.; Wahner, A.; Wildt, J.; Mentel, T. F., Gas phase formation of extremely oxidized pinene reaction products in chamber and ambient air. *Atmos. Chem. Phys.* **2012,** *12* (11), 5113-5127.

45. Zhao, J.; Smith, J. N.; Eisele, F. L.; Chen, M.; Kuang, C.; McMurry, P. H., Observation of neutral sulfuric acid-amine containing clusters in laboratory and ambient measurements. *Atmos. Chem. Phys.* **2011,** *11* (21), 10823-10836.

46. Lehtipalo, K.; Kulmala, M.; Sipila, M.; Petaja, T.; Vana, M.; Ceburnis, R.; Dupuy, R.; O'Dowd, C., Nanoparticles in boreal forest and coastal environment: a comparison of observations and implications of the nucleation mechanism. *Atmos. Chem. Phys.* **2010,** *10* (15), 7009-7016.

47. McMurry, P. H.; Ghimire, A.; Ahn, H. K.; Sakurai, H.; Moore, K.; Stolzenburg, M.; Smith, J. N., Sampling nanoparticles for chemical analysis by low resolution electrical mobility classification. *Environ. Sci. Technol.* **2009,** *43* (13), 4653-4658.

48. Smith, J. N.; Moore, K. F.; Eisele, F. L.; Voisin, D.; Ghimire, A. K.; Sakurai, H.; McMurry, P. H., Chemical composition of atmospheric nanoparticles during nucleation events in Atlanta. *J. Geophys. Res.-Atmos.* **2005,** *110* (D22), D22s03, doi: 10.1029/2005jd005912.

49. Nash, D. G.; Baer, T.; Johnston, M. V., Aerosol mass spectrometry: An introductory review. *Int. J. Mass Spectrom.* **2006,** *258* (1-3), 2-12.

50. Bzdek, B. R.; Pennington, M. R.; Johnston, M. V., Single particle chemical analysis of ambient ultrafine aerosol: A review. *J. Aerosol Sci.* **2012,** *52* (1), 109-120.

51. Wang, S. Y.; Zordan, C. A.; Johnston, M. V., Chemical characterization of individual, airborne sub-10-nm particles and molecules. *Anal. Chem.* **2006,** *78* (6), 1750-1754.

52. Kuang, C.; Riipinen, I.; Sihto, S. L.; Kulmala, M.; McCormick, A. V.; McMurry, P. H., An improved criterion for new particle formation in diverse atmospheric environments. *Atmos. Chem. Phys.* **2010,** *10* (17), 8469-8480.

53. Riipinen, I.; Sihto, S. L.; Kulmala, M.; Arnold, F.; Dal Maso, M.; Birmili, W.; Saarnio, K.; Teinila, K.; Kerminen, V. M.; Laaksonen, A.; Lehtinen, K. E. J., Connections between atmospheric sulphuric acid and new particle formation during QUEST III-IV campaigns in Heidelberg and Hyytiälä. *Atmos. Chem. Phys.* **2007,** *7* (8), 1899-1914.

54. Riipinen, I.; Yli-Juuti, T.; Pierce, J. R.; Petaja, T.; Worsnop, D. R.; Kulmala, M.; Donahue, N. M., The contribution of organics to atmospheric nanoparticle growth. *Nat. Geosci.* **2012,** *5* (7), 453-458.

55. Benson, D. R.; Yu, J. H.; Markovich, A.; Lee, S. H., Ternary homogeneous nucleation of H_2SO_4, NH_3, and H_2O under conditions relevant to the lower troposphere. *Atmos. Chem. Phys.* **2011,** *11* (10), 4755-4766.

56. Berndt, T.; Stratmann, F.; Sipila, M.; Vanhanen, J.; Petaja, T.; Mikkila, J.; Gruner, A.; Spindler, G.; Mauldin, R. L.; Curtius, J.; Kulmala, M.; Heintzenberg, J., Laboratory study on new particle formation from the reaction OH + SO_2: Influence of experimental conditions, H_2O vapour, NH_3 and the amine tert-butylamine on the overall process. *Atmos. Chem. Phys.* **2010,** *10* (15), 7101-7116.

57. Erupe, M. E.; Viggiano, A. A.; Lee, S. H., The effect of trimethylamine on atmospheric nucleation involving H_2SO_4. *Atmos. Chem. Phys.* **2011,** *11* (10), 4767-4775.

58. Metzger, A.; Verheggen, B.; Dommen, J.; Duplissy, J.; Prevot, A. S. H.; Weingartner, E.; Riipinen, I.; Kulmala, M.; Spracklen, D. V.; Carslaw, K. S.; Baltensperger, U., Evidence for the role of organics in aerosol particle formation under atmospheric conditions. *Proc. Natl. Acad. Sci. U.S.A.* **2010,** *107* (15), 6646-6651.

59. Zhang, R. Y.; Wang, L.; Khalizov, A. F.; Zhao, J.; Zheng, J.; McGraw, R. L.; Molina, L. T., Formation of nanoparticles of blue haze enhanced by anthropogenic pollution. *Proc. Natl. Acad. Sci. U.S.A.* **2009,** *106* (42), 17650-17654.

60. Kuang, C.; Chen, M.; Zhao, J.; Smith, J.; McMurry, P. H.; Wang, J., Size and time-resolved growth rate measurements of 1 to 5 nm freshly formed atmospheric nuclei. *Atmos. Chem. Phys.* **2012,** *12* (7), 3573-3589.

61. Stolzenburg, M. R.; McMurry, P. H.; Sakurai, H.; Smith, J. N.; Mauldin, R. L.; Eisele, F. L.; Clement, C. F., Growth rates of freshly nucleated atmospheric particles in Atlanta. *J. Geophys. Res.-Atmos.* **2005,** *110* (D22), D22s05, doi: 10.1029/2005jd005935.

62. Erupe, M. E.; Benson, D. R.; Li, J. M.; Young, L. H.; Verheggen, B.; Al-Refai, M.; Tahboub, O.; Cunningham, V.; Frimpong, F.; Viggiano, A. A.; Lee, S. H., Correlation of aerosol nucleation rate with sulfuric acid and ammonia in Kent, Ohio: An atmospheric observation. *J. Geophys. Res.-Atmos.* **2010,** *115* (D23), D23216, doi: 10.1029/2010jd013942.

63. Nieminen, T.; Manninen, H. E.; Sihto, S. L.; Yli-Juuti, T.; Mauldin, R. L.; Petaja, T.; Riipinen, I.; Kerminen, V. M.; Kulmala, M., Connection of sulfuric acid to atmospheric nucleation in boreal forest. *Environ. Sci. Technol.* **2009,** *43* (13), 4715-4721.

64. Ehn, M.; Junninen, H.; Petaja, T.; Kurten, T.; Kerminen, V. M.; Schobesberger, S.; Manninen, H. E.; Ortega, I. K.; Vehkamaki, H.; Kulmala, M.; Worsnop, D. R., Composition and temporal behavior of ambient ions in the boreal forest. *Atmos. Chem. Phys.* **2010,** *10* (17), 8513-8530.

65. Eisele, F. L.; Lovejoy, E. R.; Kosciuch, E.; Moore, K. F.; Mauldin, R. L.; Smith, J. N.; McMurry, P. H.; Iida, K., Negative atmospheric ions and their potential role in ion-induced nucleation. *J. Geophys. Res.-Atmos.* **2006,** *111* (D4), D04305, doi: 10.1029/2005jd006568.

66. Iida, K.; Stolzenburg, M. R.; McMurry, P. H.; Smith, J. N., Estimating nanoparticle growth rates from size-dependent charged fractions: Analysis of new particle formation events in Mexico City. *J. Geophys. Res.-Atmos.* **2008,** *113* (D5), D05207, doi: 10.1029/2007jd009260.

67. Weber, R. J.; Marti, J. J.; McMurry, P. H.; Eisele, F. L.; Tanner, D. J.; Jefferson, A., Measurements of new particle formation and ultrafine particle growth rates at a clean continental site. *J. Geophys. Res.-Atmos.* **1997,** *102* (D4), 4375-4385, doi: 10.1029/96jd03656.

68. Wehner, B.; Petaja, T.; Boy, M.; Engler, C.; Birmili, W.; Tuch, T.; Wiedensohler, A.; Kulmala, M., The contribution of sulfuric acid and non-volatile compounds on the growth of freshly formed atmospheric aerosols. *Geophys. Res. Lett.* **2005,** *32* (17), L17810, doi: 10.1029/2005gl023827.

69. Weber, R. J.; Marti, J. J.; McMurry, P. H.; Eisele, F. L.; Tanner, D. J.; Jefferson, A., Measured atmospheric new particle formation rates: Implications for nucleation mechanisms. *Chem. Eng. Commun.* **1996,** *151* (1), 53-64.

70. Anderson, K. E.; Siepmann, J. I.; McMurry, P. H.; VandeVondele, J., Importance of the number of acid molecules and the strength of the base for double-ion formation in $(H_2SO_4)_m{\cdot}Base{\cdot}(H2O)_6$ clusters. *J. Am. Chem. Soc.* **2008,** *130* (43), 14144-14147.

71. Chen, M.; Titcombe, M.; Jiang, J.; Jen, C.; Kuang, C.; Fischer, M. L.; Eisele, F. L.; Siepmann, J. I.; Hanson, D. R.; Zhao, J.; McMurry, P. H., Acid–base chemical reaction model for nucleation rates in the polluted atmospheric boundary layer. *Proc. Natl. Acad. Sci. U.S.A.* **2012,** *109* (46), 18713-18718.

72. Dawson, M. L.; Varner, M. E.; Perraud, V.; Ezell, M. J.; Gerber, R. B.; Finlayson-Pitts, B. J., Simplified mechanism for new particle formation from methanesulfonic acid, amines, and water via experiments and ab initio calculations. *Proc. Natl. Acad. Sci. U.S.A.* **2012,** *109* (46), 18719-18724.

73. Hanson, D. R.; Eisele, F. L., Measurement of prenucleation molecular clusters in the NH_3, H_2SO_4, H_2O system. *J. Geophys. Res.-Atmos.* **2002,** *107* (D12), 4158, doi: 10.1029/2001jd001100.

74. Yu, H.; McGraw, R.; Lee, S. H., Effects of amines on formation of sub-3 nm particles and their subsequent growth. *Geophys. Res. Lett.* **2012,** *39* (2), L02807, doi: 10.1029/2011gl050099.

75. Zollner, J. H.; Glasoe, W. A.; Panta, B.; Carlson, K. K.; McMurry, P. H.; Hanson, D. R., Sulfuric acid nucleation: power dependencies, variation with relative humidity, and effect of bases. *Atmos. Chem. Phys.* **2012,** *12* (10), 4399-4411.

76. Kurten, T.; Loukonen, V.; Vehkamaki, H.; Kulmala, M., Amines are likely to enhance neutral and ion-induced sulfuric acid-water nucleation in the atmosphere more effectively than ammonia. *Atmos. Chem. Phys.* **2008,** *8* (14), 4095-4103.

77. Ortega, I. K.; Kurten, T.; Vehkamaki, H.; Kulmala, M., The role of ammonia in sulfuric acid ion induced nucleation. *Atmos. Chem. Phys.* **2008,** *8* (11), 2859-2867.

78. Almeida, J.; Schobesberger, S.; Kurten, A.; Ortega, I. K.; Kupiainen-Maatta, O.; Praplan, A. P.; Adamov, A.; Amorim, A.; Bianchi, F.; Breitenlechner, M.; David, A.; Dommen, J.; Donahue, N. M.; Downard, A.; Dunne, E.; Duplissy, J.; Ehrhart, S.; Flagan, R. C.; Franchin, A.; Guida, R.; Hakala, J.; Hansel, A.; Heinritzi, M.; Henschel, H.; Jokinen, T.; Junninen, H.; Kajos, M.; Kangasluoma, J.; Keskinen, H.; Kupc, A.; Kurten, T.; Kvashin, A. N.; Laaksonen, A.; Lehtipalo, K.; Leiminger, M.; Leppa, J.; Loukonen, V.; Makhmutov, V.; Mathot, S.; McGrath, M. J.; Nieminen, T.; Olenius, T.; Onnela, A.; Petaja, T.; Riccobono, F.; Riipinen, I.; Rissanen, M.; Rondo, L.; Ruuskanen, T.; Santos, F. D.; Sarnela, N.; Schallhart, S.; Schnitzhofer, R.; Seinfeld, J. H.; Simon, M.; Sipila, M.; Stozhkov, Y.; Stratmann, F.; Tome, A.; Trostl, J.; Tsagkogeorgas, G.; Vaattovaara, P.; Viisanen, Y.; Virtanen, A.; Vrtala, A.; Wagner, P. E.; Weingartner, E.; Wex, H.; Williamson, C.; Wimmer, D.; Ye, P.; Yli-Juuti, T.; Carslaw, K. S.; Kulmala, M.; Curtius, J.; Baltensperger, U.; Worsnop, D. R.; Vehkamaki, H.; Kirkby, J., Molecular understanding of sulphuric acid-amine particle nucleation in the atmosphere. *Nature* **2013,** *502* (7471), 359-363.

79. Kirkby, J.; Curtius, J.; Almeida, J.; Dunne, E.; Duplissy, J.; Ehrhart, S.; Franchin, A.; Gagne, S.; Ickes, L.; Kurten, A.; Kupc, A.; Metzger, A.; Riccobono, F.; Rondo, L.; Schobesberger, S.; Tsagkogeorgas, G.; Wimmer, D.; Amorim, A.; Bianchi, F.; Breitenlechner, M.; David, A.; Dommen, J.; Downard,

A.; Ehn, M.; Flagan, R. C.; Haider, S.; Hansel, A.; Hauser, D.; Jud, W.; Junninen, H.; Kreissl, F.; Kvashin, A.; Laaksonen, A.; Lehtipalo, K.; Lima, J.; Lovejoy, E. R.; Makhmutov, V.; Mathot, S.; Mikkila, J.; Minginette, P.; Mogo, S.; Nieminen, T.; Onnela, A.; Pereira, P.; Petaja, T.; Schnitzhofer, R.; Seinfeld, J. H.; Sipila, M.; Stozhkov, Y.; Stratmann, F.; Tome, A.; Vanhanen, J.; Viisanen, Y.; Vrtala, A.; Wagner, P. E.; Walther, H.; Weingartner, E.; Wex, H.; Winkler, P. M.; Carslaw, K. S.; Worsnop, D. R.; Baltensperger, U.; Kulmala, M., Role of sulphuric acid, ammonia and galactic cosmic rays in atmospheric aerosol nucleation. *Nature* **2011,** *476* (7361), 429-433.

80. Barsanti, K. C.; McMurry, P. H.; Smith, J. N., The potential contribution of organic salts to new particle growth. *Atmos. Chem. Phys.* **2009,** *9* (9), 2949-2957.

81. Ehn, M.; Petaja, T.; Birmili, W.; Junninen, H.; Aalto, P.; Kulmala, M., Non-volatile residuals of newly formed atmospheric particles in the boreal forest. *Atmos. Chem. Phys.* **2007,** *7* (3), 677-684.

82. Riipinen, I.; Manninen, H. E.; Yli-Juuti, T.; Boy, M.; Sipila, M.; Ehn, M.; Junninen, H.; Petaja, T.; Kulmala, M., Applying the Condensation Particle Counter Battery (CPCB) to study the water-affinity of freshly-formed 2-9 nm particles in boreal forest. *Atmos. Chem. Phys.* **2009,** *9* (10), 3317-3330.

83. Ristovski, Z. D.; Suni, T.; Kulmala, M.; Boy, M.; Meyer, N. K.; Duplissy, J.; Turnipseed, A.; Morawska, L.; Baltensperger, U., The role of sulphates and organic vapours in growth of newly formed particles in a eucalypt forest. *Atmos. Chem. Phys.* **2010,** *10* (6), 2919-2926.

84. Modini, R. L.; Ristovski, Z. D.; Johnson, G. R.; He, C.; Surawski, N.; Morawska, L.; Suni, T.; Kulmala, M., New particle formation and growth at a remote, sub-tropical coastal location. *Atmos. Chem. Phys.* **2009,** *9* (19), 7607-7621.

85. Vaattovaara, P.; Huttunen, P. E.; Yoon, Y. J.; Joutsensaari, J.; Lehtinen, K. E. J.; O'Dowd, C. D.; Laaksonen, A., The composition of nucleation and Aitken modes particles during coastal nucleation events: evidence for marine secondary organic contribution. *Atmos. Chem. Phys.* **2006,** *6* (12), 4601-4616.

86. Yli-Juuti, T.; Nieminen, T.; Hirsikko, A.; Aalto, P. P.; Asmi, E.; Horrak, U.; Manninen, H. E.; Patokoski, J.; Dal Maso, M.; Petaja, T.; Rinne, J.; Kulmala, M.; Riipinen, I., Growth rates of nucleation mode particles in Hyytiala during 2003-2009: variation with particle size, season, data analysis method and ambient conditions. *Atmos. Chem. Phys.* **2011,** *11* (24), 12865-12886.

87. Donahue, N. M.; Trump, E. R.; Pierce, J. R.; Riipinen, I., Theoretical constraints on pure vapor-pressure driven condensation of organics to ultrafine particles. *Geophys. Res. Lett.* **2011,** *38* (16), L16801, doi: 10.1029/2011gl048115.

88. Pierce, J. R.; Riipinen, I.; Kulmala, M.; Ehn, M.; Petaja, T.; Junninen, H.; Worsnop, D. R.; Donahue, N. M., Quantification of the volatility of secondary organic compounds in ultrafine particles during nucleation events. *Atmos. Chem. Phys.* **2011,** *11* (17), 9019-9036.

89. Riipinen, I.; Pierce, J. R.; Yli-Juuti, T.; Nieminen, T.; Hakkinen, S.; Ehn, M.; Junninen, H.; Lehtipalo, K.; Petaja, T.; Slowik, J.; Chang, R.; Shantz, N. C.; Abbatt, J.; Leaitch, W. R.; Kerminen, V. M.; Worsnop, D. R.; Pandis, S. N.; Donahue, N. M.; Kulmala, M., Organic condensation: a vital link connecting aerosol formation to cloud condensation nuclei (CCN) concentrations. *Atmos. Chem. Phys.* **2011,** *11* (8), 3865-3878.

90. Zhang, R. Y.; Suh, I.; Zhao, J.; Zhang, D.; Fortner, E. C.; Tie, X. X.; Molina, L. T.; Molina, M. J., Atmospheric new particle formation enhanced by organic acids. *Science* **2004,** *304* (5676), 1487-1490.

91. Kulmala, M.; Kontkanen, J.; Junninen, H.; Lehtipalo, K.; Manninen, H. E.; Nieminen, T.; Petäjä, T.; Sipilä, M.; Schobesberger, S.; Rantala, P.; Franchin, A.; Jokinen, T.; Järvinen, E.; Äijälä, M.; Kangasluoma, J.; Hakala, J.; Aalto, P. P.; Paasonen, P.; Mikkilä, J.; Vanhanen, J.; Aalto, J.; Hakola, H.; Makkonen, U.; Ruuskanen, T.; Mauldin, R. L.; Duplissy, J.; Vehkamäki, H.; Bäck, J.; Kortelainen, A.; Riipinen, I.; Kurtén, T.; Johnston, M. V.; Smith, J. N.; Ehn, M.; Mentel, T. F.; Lehtinen, K. E. J.; Laaksonen, A.; Kerminen, V.-M.; Worsnop, D. R., Direct observations of atmospheric aerosol nucleation. *Science* **2013,** *339* (6122), 943-946.

92. Winkler, P. M.; Ortega, J.; Karl, T.; Cappellin, L.; Friedli, H. R.; Barsanti, K.; McMurry, P. H.; Smith, J. N., Identification of the biogenic compounds responsible for size-dependent nanoparticle growth. *Geophys. Res. Lett.* **2012,** *39* (20), L20815, doi: 10.1029/2012gl053253.

93. Donahue, N. M.; Ortega, I. K.; Chuang, W.; Riipinen, I.; Riccobono, F.; Schobesberger, S.; Dommen, J.; Baltensperger, U.; Kulmala, M.; Worsnop, D. R.; Vehkamaki, H., How do organic vapors contribute to new-particle formation? *Faraday Discuss.* **2013,** *165* (1), 91-104.

94. Wang, J.; Wexler, A. S., Adsorption of organic molecules may explain growth of newly nucleated clusters and new particle formation. *Geophys. Res. Lett.* **2013,** *40* (11), 2834-2838, doi: 10.1002/grl.50455.

95. Schobesberger, S.; Junninen, H.; Bianchi, F.; Lönn, G.; Ehn, M.; Lehtipalo, K.; Dommen, J.; Ehrhart, S.; Ortega, I. K.; Franchin, A.; Nieminen, T.; Riccobono, F.; Hutterli, M.; Duplissy, J.; Almeida, J.; Amorim, A.; Breitenlechner, M.; Downard, A. J.; Dunne, E. M.; Flagan, R. C.; Kajos, M.; Keskinen, H.; Kirkby, J.; Kupc, A.; Kürten, A.; Kurtén, T.; Laaksonen, A.; Mathot, S.; Onnela, A.; Praplan, A. P.; Rondo, L.; Santos, F. D.; Schallhart, S.; Schnitzhofer, R.; Sipilä, M.; Tomé, A.; Tsagkogeorgas, G.; Vehkamäki, H.; Wimmer, D.; Baltensperger, U.; Carslaw, K. S.; Curtius, J.; Hansel, A.; Petäjä, T.; Kulmala, M.; Donahue, N. M.; Worsnop, D. R., Molecular understanding of atmospheric particle formation from sulfuric acid and large oxidized organic molecules. *Proc. Natl. Acad. Sci. U.S.A.* **2013,** *110* (43), 17223-17228.

96. Ehn, M.; Thornton, J. A.; Kleist, E.; Sipila, M.; Junninen, H.; Pullinen, I.; Springer, M.; Rubach, F.; Tillmann, R.; Lee, B.; Lopez-Hilfiker, F.; Andres, S.; Acir, I.-H.; Rissanen, M.; Jokinen, T.; Schobesberger, S.; Kangasluoma, J.; Kontkanen, J.; Nieminen, T.; Kurten, T.; Nielsen, L. B.; Jorgensen, S.; Kjaergaard, H. G.; Canagaratna, M.; Maso, M. D.; Berndt, T.; Petaja, T.; Wahner, A.; Kerminen, V.-M.; Kulmala, M.; Worsnop, D. R.; Wildt, J.; Mentel, T. F., A large source of low-volatility secondary organic aerosol. *Nature* **2014,** *506* (7489), 476-479.

97. Zhao, J.; Ortega, J.; Chen, M.; McMurry, P. H.; Smith, J. N., Dependence of particle nucleation and growth on high-molecular-weight gas-phase products during ozonolysis of alpha-pinene. *Atmos. Chem. Phys.* **2013,** *13* (15), 7631-7644.

98. Bzdek, B. R.; Johnston, M. V., New particle formation and growth in the troposphere. *Anal. Chem.* **2010,** *82* (19), 7871-7878.

99. Amster, I. J., Fourier transform mass spectrometry. *J. Mass Spectrom.* **1996,** *31* (12), 1325-1337.

100. Pennington, M. R.; Johnston, M. V., Trapping charged nanoparticles in the nano aerosol mass spectrometer (NAMS). *Int. J. Mass Spectrom.* **2012,** *311* (1), 64-71.

101. Wang, S. Y.; Johnston, M. V., Airborne nanoparticle characterization with a digital ion trap-reflectron time of flight mass spectrometer. *Int. J. Mass Spectrom.* **2006,** *258* (1-3), 50-57.

102. Gauthier, J. W.; Trautman, T. R.; Jacobson, D. B., Sustained off-resonance irradiation for collision-activated dissociation involving Fourier transform mass spectrometry: Collision-activated dissociation technique that emulates infrared multiphoton dissociation. *Anal. Chim. Acta* **1991,** *246* (1), 211-225.

103. Senko, M. W.; Speir, J. P.; McLafferty, F. W., Collisional activation of large multiply-charged ions using Fourier transform mass spectrometry. *Anal. Chem.* **1994,** *66* (18), 2801-2808.

104. Laskin, J.; Futrell, J. H., Activation of large ions in FT-ICR mass spectrometry. *Mass Spectrom. Rev.* **2005,** *24* (2), 135-167.

105. Laskin, J.; Denisov, E. V.; Shukla, A. K.; Barlow, S. E.; Futrell, J. H., Surface-induced dissociation in a Fourier transform ion cyclotron resonance mass spectrometer: Instrument design and evaluation. *Anal. Chem.* **2002,** *74* (14), 3255-3261.

106. Dongre, A. R.; Somogyi, A.; Wysocki, V. H., Surface-induced dissociation: An effective tool to probe structure, energetics and fragmentation mechanisms of protonated peptides. *J. Mass Spectrom.* **1996,** *31* (4), 339-350.

107. Pennington, M. R. An Improved Nano Aerosol Mass Spectrometer for Ambient and Laboratory Measurements. University of Delaware, Newark, DE, 2012.

108. Reents, W. D.; Ge, Z. Z., Simultaneous elemental composition and size distributions of submicron particles in real time using laser atomization/ionization mass spectrometry. *Aerosol Sci. Technol.* **2000,** *33* (1-2), 122-134.

109. Reents, W. D.; Schabel, M. J., Measurement of individual particle atomic composition by aerosol mass spectrometry. *Anal. Chem.* **2001,** *73* (22), 5403-5414.

110. Mahadevan, R.; Lee, D.; Sakurai, H.; Zachariah, M. R., Measurement of condensed-phase reaction kinetics in the aerosol phase using single particle mass spectrometry. *J. Phys. Chem. A* **2002,** *106* (46), 11083-11092.

111. Park, K.; Lee, D.; Rai, A.; Mukherjee, D.; Zachariah, M. R., Size-resolved kinetic measurements of aluminum nanoparticle oxidation with single particle mass spectrometry. *J. Phys. Chem. B* **2005,** *109* (15), 7290-7299.

112. Park, K.; Rai, A.; Zachariah, M. R., Characterizing the coating and size-resolved oxidative stability of carbon-coated aluminum nanoparticles by single-particle mass-spectrometry. *J. Nanopar. Res.* **2006,** *8* (3-4), 455-464.

113. Zhou, L.; Park, K.; Milchberg, H. M.; Zachariah, M. R., Understanding the interaction of an intense laser pulse with nanoparticles: Application to the

quantification of single particle mass spectrometry. *Aerosol Sci. Technol.* **2007,** *41* (9), 818-827.

114. Zhou, L.; Rai, A.; Zachariah, M. R., Component and morphology biases on quantifying the composition of nanoparticles using single-particle mass spectrometry. *Int. J. Mass Spectrom.* **2006,** *258* (1-3), 104-112.

115. Lee, D.; Park, K.; Zachariah, M. R., Determination of the size distribution of polydisperse nanoparticles with single-particle mass spectrometry: The role of ion kinetic energy. *Aerosol Sci. Technol.* **2005,** *39* (2), 162-169.

116. Zordan, C. A.; Pennington, M. R.; Johnston, M. V., Elemental composition of nanoparticles with the Nano Aerosol Mass Spectrometer. *Anal. Chem.* **2010,** *82* (19), 8034-8038.

117. Klems, J. P.; Pennington, M. R.; Zordan, C. A.; McFadden, L.; Johnston, M. V., Apportionment of motor vehicle emissions from fast changes in number concentration and chemical composition of ultrafine particles near a roadway intersection. *Environ. Sci. Technol.* **2011,** *45* (13), 5637-5643.

Chapter 2

SULFURIC ACID CLUSTER DISTRIBUTIONS PRODUCED BY ELECTROSPRAY IONIZATION

2.1 Introduction

The goal of this chapter is to explore the types of clusters that are produced by electrospray ionization of solutions containing sulfuric acid, ammonia, and dimethylamine and use those observations to infer the composition of ambient clusters. Knowledge of how the composition of the resulting clusters changes with the identity of the base (ammonia vs. dimethylamine) and cluster charge (positive ions vs. negative ions) informs about the types of clusters that may be thermodynamically favored. Additionally, comparing the composition of clusters produced by electrospray ionization to the composition of clusters measured in the atmosphere indicates that the electrospray-produced cluster composition is similar to that of ambient clusters and that studies of the reactivities of the clusters produced by electrospray ionization would have atmospheric relevance.

2.2 Experimental Section

Charged ammonium bisulfate clusters were introduced into a 7T Bruker apex-Qe Fourier transform ion cyclotron resonance mass spectrometer (FTICR-MS) by electrospray of an ammonium sulfate (Aldrich, St. Louis, Missouri) solution in 50/50 water/methanol. Charged dimethylammonium bisulfate clusters were produced by electrospray of a dimethylammonium sulfate solution made by combining solutions of

dimethylamine (Fluka, St. Louis, Missouri) in 50/50 methanol/water and H_2SO_4 (Fisher, Pittsburgh, Pennsylvania) in 50/50 methanol/water. For broadband spectra, the solution concentration was 0.05 M. Both positive and negative polarity ions were studied.

2.3 Electrospray Ionization of Ammonium Sulfate and Dimethylammonium Sulfate Solutions

Although the ions produced during electrospray ionization are not necessarily at equilibrium, the species most likely to receive a charge are those that tend to be more stable upon charging. In complex solutions containing several analytes, some chemical species will receive charge preferentially relative to other species in the same solution.[1] Similar to this phenomenon, a solution of ammonium sulfate contains ammonium and sulfate ions that, upon ionization and transfer from the liquid phase to the gas phase, produce an array of unique charged clusters that contain differing numbers of ammonium and bisulfate ions. An analysis of the distribution of charged species produced by electrospray of ammonium sulfate can give an indication of the relative stabilities of ammonium sulfate/ammonium bisulfate clusters that may be expected to be observed in ambient air.

Figure 2.1 provides mass spectra of an ammonium sulfate solution introduced by electrospray into the FTICR-MS operating in (a) positive and (b) negative modes. Interestingly, electrospray of the same solution produces cluster ions of very different composition depending upon polarity. In positive mode, three distinct series of clusters are observed. The first series (indicated in Fig. 2.1a by the letter "a") consists of singly-charged ammonium bisulfate clusters in the form $[(NH_4)_x(HSO_4)_{x-1}]^+$, where all

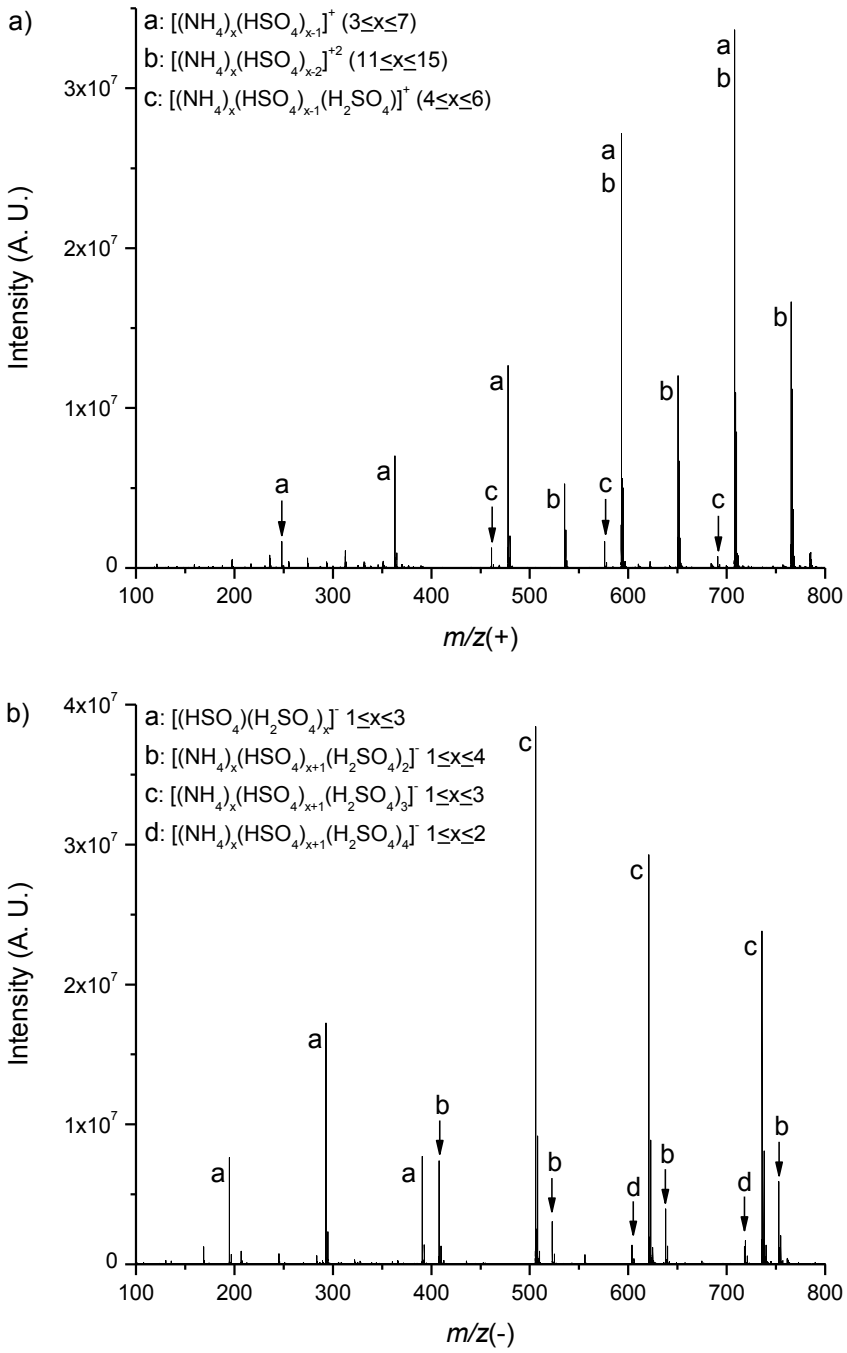

Figure 2.1: Electrospray ionization mass spectra of an ammonium sulfate solution in a) positive and b) negative modes.

sulfuric acid is neutralized to bisulfate. The second series (indicated in Fig. 2.1a by the letter "b") is similar to the first series, as all sulfuric acid is neutralized to bisulfate; however, these clusters are doubly-charged and are in the form $[(NH_4)_x(HSO_4)_{x-2}]^{+2}$. These clusters overall contain one fewer bisulfate ion than the singly-charged clusters, resulting in a +2 charge. The third series (indicated in Fig. 2.1a by the letter "c") consists of clusters where not all sulfuric acid in the clusters is neutralized to bisulfate. In other words, these clusters are more acidic and can be described as being in the form $[(NH_4)_x(HSO_4)_{x-1}(H_2SO_4)]^{+}$.

The three different series of charged clusters observed in positive mode contrast greatly with the charged clusters observed from electrospray of the same solution in negative mode (Fig. 2.1b). For negative ions, four unique series of charged clusters are observed. The first consists of simple clusters of sulfuric acid and bisulfate (i.e. $[(HSO_4)(H_2SO_4)_x]^{-}$, indicated by the letter "a" in Fig. 2.1b). The second, third, and fourth cluster series are all ammonium bisulfate clusters with varying degrees of sulfuric acid neutralization to bisulfate. These clusters can be described by $[(NH_4)_x(HSO_4)_{x+1}(H_2SO_4)_2]^{-}$, $[(NH_4)_x(HSO_4)_{x+1}(H_2SO_4)_3]^{-}$, and $[(NH_4)_x(HSO_4)_{x+1}(H_2SO_4)_4]^{-}$ (indicated by letters "b", "c", and "d", respectively, in Fig. 2.1b). These observations suggest that the presence of ammonium is less favorable in small negatively-charged clusters containing sulfuric acid than for small positively-charged clusters. The electrospray distributions are consistent with observations by Hanson and Eisele (2002),[2] who examined similar negatively-charged clusters at atmospheric pressure and found that the number of ammonium ions in the clusters is generally smaller than the number of sulfur-containing species (sulfuric acid and bisulfate). In Fig. 2.1, the effect of charge on cluster composition decreases as the

cluster size increases. The corollary to this is that both polarity clusters converge towards the same composition (ammonium bisulfate) at larger cluster size. For instance, for positive ions in Fig. 2.1, the ammonium:bisulfate ratio decreases with increasing cluster size, whereas for negative ions, the ammonium:bisulfate ratio increases with increasing cluster size and in both cases approaches a 1:1 ratio. It is interesting that ammonium sulfate appears not to be the preferred composition over the range of cluster sizes examined here. However, at much larger particle sizes, ammonium sulfate eventually becomes preferred. For example, the elemental composition of 25 nm mass normalized diameter ammonium sulfate particles produced by electrospray gives a molar N:S ratio of 2, indicating these particles are composed of ammonium sulfate (N:S = 2), rather than ammonium bisulfate (N:S = 1).[3]

Figure 2.2 presents a comparison of cluster acidity (defined as the number of unneutralized sulfuric acid molecules, n) in positively-charged and negatively-charged ammonium bisulfate and dimethylammonium bisulfate clusters. For a given type of cluster (ammonium bisulfate or dimethylammonium bisulfate) at a given polarity (positive or negative), the relative signal intensities of the different series of ions produced by electrospray are plotted. Note that for positive ions, only singly-charged clusters are considered; for negative ions, only clusters containing ammonium or dimethylammonium are considered (sulfuric acid-bisulfate clusters are not included). For positive ions (Fig. 2.2a-b), clusters tend to be fully neutralized to bisulfate, as for both ammonium bisulfate and dimethylammonium bisulfate clusters the predominant cluster series observed in the mass spectrum is one that contains no unneutralized

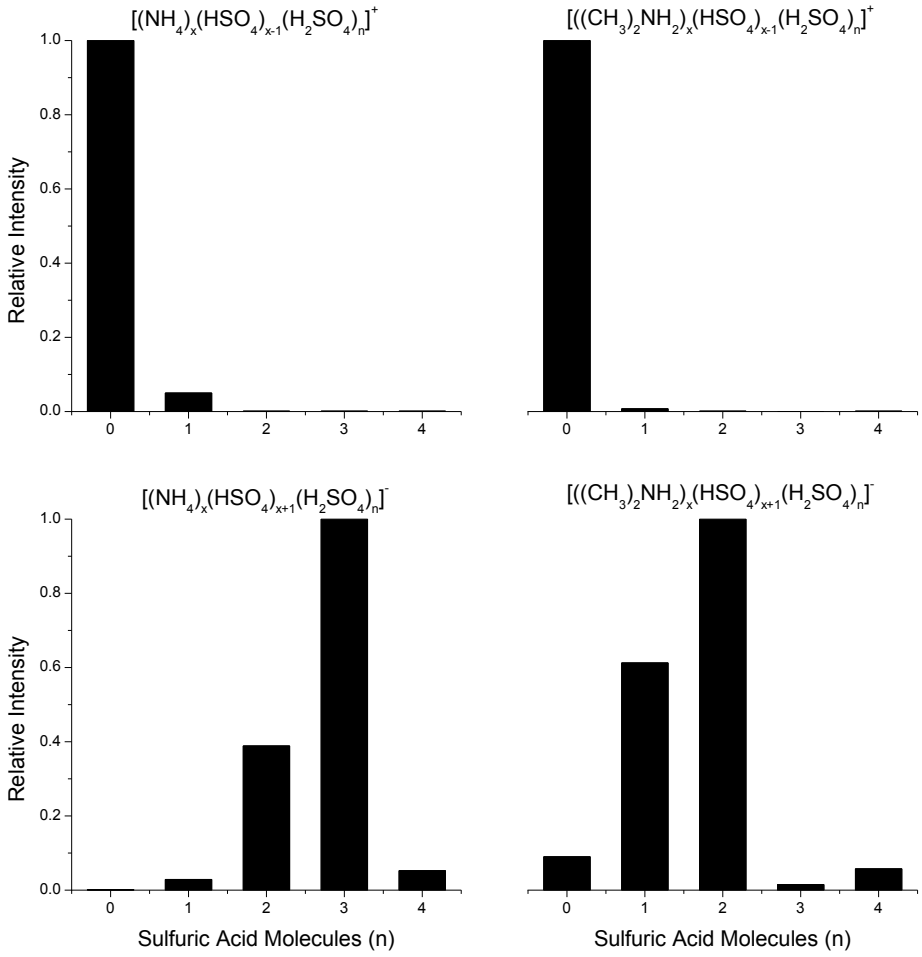

Figure 2.2: Cluster acidity (defined as the number of unneutralized sulfuric acid molecules, n, in a cluster) for clusters formed through electrospray of ammonium sulfate and dimethylammonium sulfate solutions in positive and negative polarities.

sulfuric acid (n = 0). However, the presence of dimethylammonium appears to enhance neutralization to bisulfate better than the presence of ammonium, as in Fig. 2.2b there is less signal intensity from the $[((CH_3)_2NH_2)_x(HSO_4)_{x-1}(H_2SO_4)]^+$ series than from the $[(NH_4)_x(HSO_4)_{x+1}(H_2SO_4)]^+$ series in Fig. 2.2a. The reason for this enhanced neutralization to bisulfate is likely because dimethylamine is a stronger base than ammonia.

Negative ions (Fig. 2.2c-d) show two interesting phenomena. The first observation is that negative ions in general differ significantly in composition relative to positive ions. The second observation is that the composition of ammonium bisulfate negative ions is different than the composition of dimethylammonium bisulfate negative ions, despite the similarity between the two in positive mode. Specifically, negative ions tend to be much more acidic (fewer sulfuric acid molecules neutralized to bisulfate) than positive ions. Whereas in positive mode the predominant cluster series for both types of clusters contains no unneutralized sulfuric acid (n = 0), the most intense series of negatively-charged ammonium bisulfate clusters contains three unneutralized sulfuric acid molecules (n = 3; Fig. 2.2c) and the most intense series of negatively-charged dimethylammonium bisulfate clusters contains two unneutralized sulfuric acid molecules (n = 2; Fig. 2.2d). These observations also indicate that for negatively-charged clusters, dimethylammonium enhances neutralization of sulfuric acid to bisulfate better than ammonium. Again, this can be attributed to dimethylamine's stronger basicity.

The clusters examined in this work are produced by the dissociation of larger, metastable species as they travel to the ICR cell and not simply by charge transfer to a previously neutral cluster (see Chapter 4).[4] Nonetheless, the clusters that are

eventually trapped in the cell are stable. The stability of these clusters was examined by performing experiments where an isolated cluster was held for varying periods of time in the ICR cell with no reactant gas or with a small pressure of unreactive argon collision gas (see Chapter 3).[5] This experiment indicated no change in the cluster distribution with time, indicating that trapped clusters are relatively stable under vacuum. Additionally, it should be noted that not all clusters observed in a broadband mass spectrum can be isolated for reactivity studies. One reason for this relates to how these clusters are formed: because these clusters are formed from larger, metastable ions, isolation of a particular ion with sufficient intensity depends on which larger ions are selected in the quadrupole and how those ions dissociate on the way to the ICR cell. Finally, sodium substitution for ammonium or dimethylammonium is frequently observed (although significantly more sodium substitution is observed for the dimethylammonium-substituted clusters). Sodium is a ubiquitous contaminant; however these clusters are usually easily ignored, as the experimental method allows one to exclude isolation of the sodium-substituted clusters. Sodium-substituted clusters were excluded from further study because they are not atmospherically relevant.

Analysis of the ions produced from electrospray ionization of ammonium sulfate and dimethylammonium sulfate solutions in both positive and negative modes combined with a consideration of the constraints discussed above give an indication of the most likely (most favorable) charged species to be formed.

2.4 Atmospheric Implications

This study examined the distribution of charged species produced by electrospray of ammonium sulfate in both positive and negative polarities. The ions

produced by electrospray give an indication of what charged species might be expected in ambient air within the constraints discussed above. Recent advances in instrumentation to measure charged clusters in ambient air permit comparison of the electrospray ionization mass spectra to ambient ion spectra. Specifically, the atmospheric pressure interface time-of-flight mass spectrometer (APi-TOF) permits detection of either positively- or negatively-charged ions up to 2000 *m/z*.[6, 7] APi-TOF analysis of nebulized sulfuric acid mixed with laboratory air[6] yielded a spectrum with some prominent peaks at *m/z* values that correspond to those dominant negatively-charged ammonium bisulfate series observed in this work from electrospray of an ammonium sulfate solution. Ambient measurements of negative ions < 500 *m/z* during the daytime are dominated by sulfuric acid-bisulfate clusters (e.g. $[HSO_4]^-$, $[(HSO_4)(H_2SO_4)]^-$, $[(HSO_4)(H_2SO_4)_2]^-$, and $[(HSO_4)(H_2SO_4)_3]^-$). Nonetheless, signal from negatively-charged clusters containing ammonium has also been detected (e.g. $[(NH_4)(HSO_4)_2(H_2SO_4)_2]^-$).[7] These ambient observations confirm the hypothesis that bases will not be observed in low *m/z* negative ion clusters. APi-TOF measurements and the results of these electrospray experiments are also consistent with observations of ambient ions using a flow opposed drift tube coupled to a quadrupole mass analyzer, which indicated that sulfuric acid-bisulfate clusters dominate the low *m/z* range.[8]

For negative ions, amine-ammonia chemistry will only be evident and important in larger charged clusters (> 400 *m/z*), which appear to be much lower in concentration than the low *m/z* clusters and therefore harder to detect. However, as illustrated in Fig. 2.1, amine-ammonia chemistry is likely to influence even the smallest positive ions. Therefore, these types of clusters should be more evident in

ambient positive ion spectra than in ambient negative ion spectra. Ambient positive ion spectra, though, are quite complex,[6, 7] as there are many other chemical species in the atmosphere competing for a limited amount of charge. Observation of positively-charged ammonium-aminium bisulfate clusters may be obscured by competition with other (non-salt) species for charge or even simply by the vast number of positively-charged ambient species.

There are two important limitations to these experiments. First, this work examines the composition of charged clusters. However, in the atmosphere, uncharged clusters are thought to dominate over charged clusters.[8, 9] The results presented here indicate that the composition of ambient clusters can depend significantly on polarity. Therefore, a major focus of future work should be the composition of uncharged clusters. Whether the composition of the smallest ambient uncharged clusters would be more similar to positive ions, negative ions, or neither is an important unanswered question in atmospheric chemistry. Second, the role of particulate water is not addressed, as these experiments take place under vacuum. Different experimental methods will be required to address these limitations in future work.

Reproduced in part from: B. R. Bzdek, D. P. Ridge, and M. V. Johnston, "Amine reactivity with charged sulfuric acid clusters," *Atmospheric Chemistry and Physics*, **2011**, *11* (16), 8735-8743.

2.5 References

1. Oss, M.; Kruve, A.; Herodes, K.; Leito, I., Electrospray ionization efficiency scale of organic compounds. *Anal. Chem.* **2010,** *82* (7), 2865-2872.

2. Hanson, D. R.; Eisele, F. L., Measurement of prenucleation molecular clusters in the NH_3, H_2SO_4, H_2O system. *J. Geophys. Res.-Atmos.* **2002,** *107* (D12), 4158, doi: 10.1029/2001jd001100.

3. Zordan, C. A.; Pennington, M. R.; Johnston, M. V., Elemental composition of nanoparticles with the Nano Aerosol Mass Spectrometer. *Anal. Chem.* **2010,** *82* (19), 8034-8038.

4. Bzdek, B. R.; Ridge, D. P.; Johnston, M. V., Size-dependent reactions of ammonium bisulfate clusters with dimethylamine. *J. Phys. Chem. A* **2010,** *114* (43), 11638-11644.

5. Bzdek, B. R.; Ridge, D. P.; Johnston, M. V., Amine exchange into ammonium bisulfate and ammonium nitrate nuclei. *Atmos. Chem. Phys.* **2010,** *10* (8), 3495-3503.

6. Junninen, H.; Ehn, M.; Petaja, T.; Luosujarvi, L.; Kotiaho, T.; Kostiainen, R.; Rohner, U.; Gonin, M.; Fuhrer, K.; Kulmala, M.; Worsnop, D. R., A high-resolution mass spectrometer to measure atmospheric ion composition. *Atmos. Meas. Tech.* **2010,** *3* (4), 1039-1053.

7. Ehn, M.; Junninen, H.; Petaja, T.; Kurten, T.; Kerminen, V. M.; Schobesberger, S.; Manninen, H. E.; Ortega, I. K.; Vehkamaki, H.; Kulmala, M.; Worsnop, D. R., Composition and temporal behavior of ambient ions in the boreal forest. *Atmos. Chem. Phys.* **2010,** *10* (17), 8513-8530.

8. Eisele, F. L.; Lovejoy, E. R.; Kosciuch, E.; Moore, K. F.; Mauldin, R. L.; Smith, J. N.; McMurry, P. H.; Iida, K., Negative atmospheric ions and their potential role in ion-induced nucleation. *J. Geophys. Res.-Atmos.* **2006,** *111* (D4), D04305, doi: 10.1029/2005jd006568.

9. Kulmala, M.; Riipinen, I.; Sipila, M.; Manninen, H. E.; Petaja, T.; Junninen, H.; Dal Maso, M.; Mordas, G.; Mirme, A.; Vana, M.; Hirsikko, A.; Laakso, L.; Harrison, R. M.; Hanson, I.; Leung, C.; Lehtinen, K. E. J.; Kerminen, V. M., Toward direct measurement of atmospheric nucleation. *Science* **2007,** *318* (5847), 89-92.

Chapter 3

AMINE EXCHANGE INTO POSITIVELY-CHARGED AMMONIUM BISULFATE AND AMMONIUM NITRATE NUCLEI

3.1 Introduction

The goal of this chapter is to examine the reactivity of small positively-charged ammonium bisulfate and ammonium nitrate clusters (similar to those discussed in Chapter 2) with different amine gases. This goal was accomplished by performing ion-molecule reactions in a Fourier transform ion cyclotron resonance mass spectrometer (FTICR-MS), fitting the resulting reaction profiles to kinetic models, and determining reaction probabilities. The results of this work indicate that amines efficiently incorporate into these small clusters by displacement of ammonia. On the other hand, ammonia cannot efficiently incorporate into small aminium bisulfate clusters. These observations are atmospherically relevant because they indicate that even low amine concentrations can have a substantial impact on ambient cluster composition. Therefore, one would expect that a substantial component of the sub-3 nm cluster pool (out of which new particles grow during atmospheric new particle formation) consists of aminium bisulfate clusters, even if those clusters were initially formed as ammonium bisulfate clusters.

3.2 Experimental Section

Singly-charged ammonium bisulfate clusters were introduced to a 7T Bruker apex-Qe FTICR-MS operating in the positive mode by electrospray of a 0.5 mM

solution of ammonium sulfate (Aldrich, St. Louis, Missouri) in 50/50 methanol/water. Electrospray produced an array of singly-charged ammonium bisulfate clusters of different sizes. For the clusters examined in this chapter, there was no evidence in the mass spectra for formation of multiply-charged clusters. Ions of a specific cluster of interest were mass selected and accumulated in a quadrupole. Ions were then transferred to the ICR cell, where they were allowed to react to completion with a constant pressure of either dimethylamine (DMA) or trimethylamine (TMA) gas (Matheson Tri-Gas, Basking Ridge, New Jersey) that was introduced to the ICR cell via a leak valve. The reverse reaction, exposure of an aminium salt cluster to ammonia gas, was also studied. A solution of aminium sulfate (0.5 mM in 50/50 methanol/water) was made by mixing equal proportions of solutions of 2.0 mM amine (monomethylamine, MMA: Sigma-Aldrich, St. Louis, Missouri; DMA and TMA: Fluka, St. Louis, Missouri) in 50/50 methanol/water and 1.0 mM H_2SO_4 (Fisher, Pittsburgh, Pennsylvania) in 50/50 methanol/water. Singly-charged aminium bisulfate clusters were introduced to the instrument by electrospray of this solution and were allowed to react with ammonia gas (Matheson Tri-Gas, Basking Ridge, New Jersey). Solutions that contained both aminium and ammonium sulfate were made, and singly-charged ammonium bisulfate clusters partially substituted with amine were isolated and reacted with both amine and ammonia gas in order to more directly study later substitutions. The same procedure was performed for ammonium nitrate (Aldrich, St. Louis, Missouri). The aminium nitrate solution was made by combining equal proportions of 2.0 mM amine and 1.0 mM nitric acid (Fisher, Pittsburgh, Pennsylvania).

A mass spectrum of ions in the ICR cell can be obtained at a specific trapping time. FTICR-MS provides high accuracy mass-to-charge (*m/z*) measurements, which allows for unique elemental formulae to be assigned to reactant and product ions. A plot of ion abundance as a function of trapping time (reaction profile) reveals the progress of the sequential substitution reactions. In some of the more exothermic reactions, the reactant molecule induces a more complicated decomposition rather than displacing a single ligand. These minor reaction-induced decomposition channels increase in importance with the difference in proton affinity between the incoming and departing ligands. The induced decompositions are not enhanced by adding unreactive argon collision gas. With the exception of one case (ammonium nitrate with TMA), reaction-induced decomposition was too small to affect the quantitative kinetic analysis of the predominant simple displacements. The data were fit to the kinetic models using the simplex method of non-linear fitting embodied in the Solver function of the Microsoft Excel program.

Obtaining second order rate constants required knowledge of the absolute pressure of gas in the ICR cell. However, the ICR cell pressure reading given by the ionization gauge did not correspond to the true gas pressure in the cell because of effects associated with the external magnetic field and the polarizability of the gas being measured. The absolute gas pressure was determined by the equation:

$$P_{\text{True}} = P_{\text{gauge}} \times K_{\text{magnet}} \times \left(\frac{\alpha_{\text{N}_2}}{\alpha_{\text{gas}}} \right) \tag{1}$$

where P_{True} is the true ICR cell pressure, P_{gauge} is the pressure reading on the ionization gauge, K_{magnet} is an empirical correction factor for the effect of the magnet on the pressure reading, and α is the polarizability of a gas. The ionization gauge is

calibrated for N_2, so to obtain the pressure for another gas, the ratio of the polarizability of N_2 to the polarizability of the gas used is required.[1]

3.3 Results and Discussion

3.3.1 Reaction Rate Constants and Free Energy Changes

Figure 3.1 presents a typical reaction profile and statistical fit for substitution of amine for ammonia in an ammonium salt cluster, in this case the reaction of DMA gas with $[(NH_4)_3(HSO_4)_2]^+$, the "3-2" ammonium bisulfate cluster. Because the pressure of DMA gas was maintained at a constant level during the experiment, pseudo first order kinetics may be assumed. A linear dependence of the pseudo first order rate constant on reactant gas pressure was confirmed by varying (e.g. doubling) the gas pressure. The observed change in the pseudo first order rate constants increased linearly with pressure as expected. The data were fit to equations obtained by assuming sequential pseudo first order reactions. For example, the three step mechanism in Eq. (2) for reactions of the 3-2 ammonium bisulfate cluster involves rate constants proportional to the fixed pressure of DMA.

$$[(NH_4)_3(HSO_4)_2]^+ \xrightarrow{k_1} [(NH_4)_2(HDMA)(HSO_4)_2]^+ \xrightarrow{k_2} [(NH_4)(HDMA)_2(HSO_4)_2]^+ \xrightarrow{k_3} [(HDMA)_3(HSO_4)_2]^+ \quad (2)$$

This mechanism gives rise to Eqs. (3)-(5) for the time-dependent concentrations of the reactants, intermediates, and product.

$$A_1 = A_0 e^{-k_1 t} \quad (3)$$

$$A_2 = \frac{k_1 A_0}{k_2 - k_1}\left(e^{-k_1 t} - e^{-k_2 t}\right) \quad (4)$$

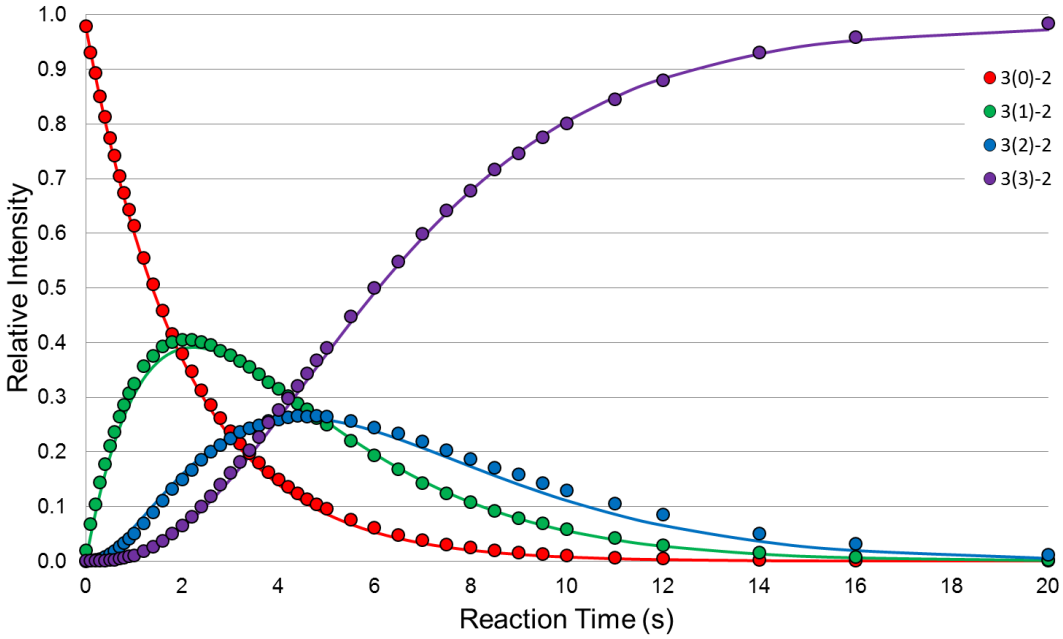

Figure 3.1: Reaction profile and statistical fit for the reaction of the 3-2 ammonium bisulfate cluster with DMA. Circles represent experimental data; lines represent statistical fits to pseudo first order kinetics. Each step in the sequential reaction is represented by a different color, as indicated in the legend. Cluster assignment in the legend is given as *a*(*b*)-*c*, where *a* represents the number of ammonium ions initially in the unreacted cluster, *b* represents the progress of the displacement reaction (i.e. the number of ammonium ions that have been displaced by DMA), and *c* represents the number of bisulfate ions in the cluster.

$$A_3 = k_1 k_2 A_0 \left(\frac{e^{-k_1 t}}{(k_2 - k_1)(k_3 - k_1)} + \frac{e^{-k_2 t}}{(k_1 - k_2)(k_3 - k_2)} + \frac{e^{-k_3 t}}{(k_1 - k_3)(k_2 - k_3)} \right) \quad (5)$$

where t is the reaction time (seconds); A_0 is the relative intensity of $[(NH_4)_3(HSO_4)_2]^+$ at t=0; A_1, A_2, and A_3 are the relative intensities of $[(NH_4)_3(HSO_4)_2]^+$, $[(NH_4)_2(HDMA)(HSO_4)_2]^+$, and $[(NH_4)(HDMA)_2(HSO_4)_2]^+$ at time t, respectively; and k_1, k_2, and k_3 are the pseudo first order rate constants for each respective substitution of amine for ammonia.

Fitting these equations simultaneously to the data gives pseudo first order rate constants for each successive substitution. As a check of the procedure, ammonium bisulfate clusters partially substituted with DMA were produced by electrospray of a solution containing ammonia, amine, and sulfuric acid. Exposing the partially substituted clusters to DMA gas allowed each substitution step to be measured directly and successive substitutions to be determined by statistical fit of the reaction profile. The results are shown in Table 3.1. In each case, the pseudo first order rate constants obtained from the partially substituted clusters were within experimental error of the rate constants determined from the reaction profile of the original ammonium bisulfate cluster. The averages and standard deviations of all data for each substitution in the 3-2 cluster are given in Table 3.2.

Table 3.1: Pseudo first order rate constants obtained for the substitution of pure 3-2 ammonium bisulfate as well as for the partially substituted cluster with DMA.

	Pseudo first order rate constant (s^{-1})		
Initial Substitution	k_1	k_2	k_3
$[(NH_4)_3(HSO_4)_2]^+ \rightarrow [(NH_4)_2(HDMA)(HSO_4)_2]^+$	0.49 ± 0.03	0.41 ± 0.03	0.44 ± 0.05
$[(NH_4)_2(HDMA)(HSO_4)_2]^+ \rightarrow [(NH_4)(HDMA)_2(HSO_4)_2]^+$		0.40 ± 0.01	0.42 ± 0.01
$[(NH_4)(HDMA)_2(HSO_4)_2]^+ \rightarrow [(HDMA)_3(HSO_4)_2]^+$			0.43 ± 0.02

Table 3.2: Data summary for the substitution of DMA for NH_3 in the 3-2 ammonium bisulfate cluster and for the substitution of NH_3 for DMA in the 3-2 dimethylammonium bisulfate cluster.

Substitution with DMA[a]	Pseudo first order rate constant (s^{-1})	Second order rate constant ($cm^3 \cdot molec^{-1} \cdot s^{-1}$)	K	ΔG ($kJ \cdot mol^{-1}$)	Collisional Rate Constant ($cm^3 \cdot molec^{-1} \cdot s^{-1}$)	Uptake Coefficient (γ)
$[(NH_4)_3(HSO_4)_2]^+ \rightarrow [(NH_4)_2(HDMA)(HSO_4)_2]^+$	0.49 ± 0.03	$1.1 \pm 0.3 \times 10^{-9}$	> 1500	< -18	$1.3 \pm 0.3 \times 10^{-9}$	0.85 ± 0.26
$[(NH_4)_2(HDMA)(HSO_4)_2]^+ \rightarrow [(NH_4)(HDMA)_2(HSO_4)_2]^+$	0.41 ± 0.02	$9.3 \pm 3.0 \times 10^{-10}$	> 620	< -16	$1.3 \pm 0.3 \times 10^{-9}$	0.72 ± 0.22
$[(NH_4)(HDMA)_2(HSO_4)_2]^+ \rightarrow [(HDMA)_3(HSO_4)_2]^+$	0.43 ± 0.03	$9.7 \pm 3.0 \times 10^{-10}$	> 26000	< -25	$1.3 \pm 0.3 \times 10^{-9}$	0.75 ± 0.23
Substitution with NH_3[b]						
$[(HDMA)_3(HSO_4)_2]^+ \rightarrow [(NH_4)(HDMA)_2(HSO_4)_2]^+$	$< 5 \times 10^{-4}$	$< 3.8 \pm 1.1 \times 10^{-14}$	$< 4 \times 10^{-5}$	> 25	$2.0 \pm 0.4 \times 10^{-9}$	$< 1.9 \times 10^{-5}$
$[(NH_4)(HDMA)_2(HSO_4)_2]^+ \rightarrow [(NH_4)_2(HDMA)(HSO_4)_2]^+$	$< 1.8 \times 10^{-3}$	$< 1.5 \pm 0.5 \times 10^{-12}$	$< 1.6 \times 10^{-3}$	> 16	$2.0 \pm 0.4 \times 10^{-9}$	$< 7.6 \times 10^{-4}$
$[(NH_4)_2(HDMA)(HSO_4)_2]^+ \rightarrow [(NH_4)_3(HSO_4)_2]^+$	$< 9 \times 10^{-4}$	$< 7.5 \pm 2.3 \times 10^{-13}$	$< 7 \times 10^{-4}$	> 18	$2.0 \pm 0.4 \times 10^{-9}$	$< 3.8 \times 10^{-4}$

[a]Pressure: $1.2 \pm 0.2 \times 10^{-8}$ torr.

[b]Pressure: For $[(HDMA)_3(HSO_4)_2]^+$: $3.7 \pm 0.7 \times 10^{-7}$ torr; for $[(NH_4)(HDMA)_2(HSO_4)_2]^+$ and $[(NH_4)_2(HDMA)(HSO_4)_2]^+$: $3.4 \pm 0.7 \times 10^{-8}$ torr.

In order to calculate a second order rate constant (k_{II}), one must divide the pseudo first order rate constant (k_I) by the pressure of gas in the cell (P_{gas}):

$$k_{II} = \frac{k_I}{P_{gas}} \tag{6}$$

Values for the second order rate constants are also provided in Table 3.2. It is important to note that while the error assigned to the second order rate constant is 30%, the uncertainty associated with the pseudo first order rate constants is relatively small (< 10%). The larger error results from an uncertainty of 20% assigned to the measurement of the absolute pressure rather than imprecision in the observed reaction rates.

To probe the reverse reaction, 3-2 dimethylammonium bisulfate clusters were introduced to the ICR cell and allowed to react with gaseous NH_3. However, no reaction was observed even when the gas pressure was increased as high as possible and the reaction time extended to as long a period as possible. Therefore, only upper limits of rates for this reaction could be obtained. These values were estimated by multiplying the baseline noise in the mass spectrum by a factor of three and setting that equal to the intensity of the product substituted cluster and are provided in Table 3.2.

Thermodynamic values, or limits on thermodynamic values, were determined from the second order rate constants. The equilibrium constant, K, for the reaction is given by:

$$K = \frac{k_{II,\,forward}}{k_{II,\,reverse}} \tag{7}$$

and the Gibbs free energy change, ΔG, is given by:

$$\Delta G = -RT \ln K \tag{8}$$

where R is the gas constant and T is temperature (298 K).

Table 3.2 gives K and ΔG values for substitution of DMA for NH_3 in the 3-2 ammonium bisulfate cluster. Clearly substitution of amine for ammonia is thermodynamically favorable; upper limits of ΔG values are quite negative.

3.3.2 Uptake Coefficients (Reaction Probabilities)

Determination of an uptake coefficient for a reaction requires knowledge of the collision rate. The collision rate between an ion and a (polar) molecule can be estimated in one of two ways. The capture collision model[2] assumes an ion-induced dipole force between the ion (salt cluster) and molecule (reactant gas). As a result of this force, capture, a spiral inward towards zero separation, will occur at some critical impact parameter resulting in a collision between the two species. The spiraling trajectories become less important as the ion and/or molecule involved in the collision increase in size or as the relative velocity between the two increases. In these cases, the ion and molecule are more likely to impact each other before the attractive force significantly deflects their trajectories, and the collision rate is better approximated by a hard sphere model. However, for the range of conditions used in this work (small clusters with collision radii $\leq$ 10 Å; low velocities), the capture collision model is probably the more appropriate approach. In general, for the clusters discussed in this chapter, the hard sphere model would result in smaller calculated collision rates (due to smaller calculated collision cross sections), resulting in larger uptake coefficients, which ultimately would result in unrealistic uptake coefficients (i.e. > 1). This further supports the use of the capture collision model to calculate the collision rate.

The capture collision rate constant as parameterized by Su and Chesnavich,[3] k_{SC}, is calculated from the ratio k_{SC}/k_L. The Langevin rate constant, k_L, is given by:

$$k_L = 2.342Z\left(\frac{\alpha'}{\mu'}\right)^{1/2} \times 10^{-9}\,\mathrm{cm^3 \cdot molec^{-1} \cdot s^{-1}} \quad (9)$$

where Z is the number of charges on the ion, α' is the volume polarizability (Å^3) of the colliding molecule, and μ' is the reduced mass of the colliding pair in atomic mass units. Note that the volume polarizability values used were as follows: 2.35 Å^3 for NH_3, 6.49 Å^3 for DMA, and 7.97 Å^3 for TMA.[4] The capture collision rate constant can then be determined by:

$$k_{SC} = \frac{k_{SC}}{k_L} \times k_L \quad (10)$$

where k_{SC}/k_L is given by:

$$\frac{k_{SC}}{k_L} = 0.9754 + \frac{\left(\tau/\sqrt{2} + 0.509\right)^2}{10.526} \qquad 0 < \tau \le 2\sqrt{2} \quad (11)$$

$$\frac{k_{SC}}{k_L} = 0.62 + 0.3371\tau \qquad 2\sqrt{2} \le \tau \quad (12)$$

and τ is a dimensionless parameter described by the equation

$$\tau = 85.11\mu_D'\left(\frac{1}{\alpha' T}\right)^{1/2} \quad (13)$$

where μ_D' is the dipole moment of the molecule in Debye (D) and T is the temperature in K. In general, Eq. (11) was appropriate when an amine gas was used, as the dipole moment for DMA is 1.01 D and for TMA is 0.612 D.[4] Eq. (12) was appropriate for reaction with ammonia gas, which has a dipole moment of 1.471 D.[4]

Uptake coefficients (γ) were determined by the equation:

$$\gamma = \frac{k_{II}}{k_{SC}} \tag{14}$$

Table 3.2 provides collisional rate constants and uptake coefficients for both the substitution of DMA for NH_3 in 3-2 ammonium bisulfate and the substitution of NH_3 for DMA in 3-2 dimethylammonium bisulfate. Since the reverse reaction was not observed, only upper estimates of uptake coefficients were possible. Substitution kinetics and energetics are discussed in more detail below.

3.3.3 Bisulfate Clusters

The procedures described above were performed for bisulfate clusters of several different sizes and compositions. Not only were ammonium bisulfate clusters investigated, but also the substitution of one amine for another in different aminium bisulfate clusters was studied so as to determine the favorability of one amine versus another in a bisulfate salt. ΔG values for substitution in bisulfate clusters are provided in Table 3.3, while uptake coefficients for these reactions are provided in Table 3.4.

Table 3.3: ΔG values ($kJ \cdot mol^{-1}$) for the substitution reactions of bisulfate clusters at 298 K.

	Sub. 1	Sub. 2	Sub. 3	Sub. 4
$[(NH_4)_2(HSO_4)]^+$ with DMA	< -15	< -23		
$[(NH_4)_3(HSO_4)_2]^+$ with DMA	< -18	< -16	< -25	
$[(NH_4)_4(HSO_4)_3]^+$ with DMA	< -17	< -15	< -12	< -27
$[(NH_4)_2(HSO_4)]^+$ with TMA	< -14	< -21		
$[(NH_4)_3(HSO_4)_2]^+$ with TMA	< -7.0	< -7.7	< -15	
$[(NH_4)_4(HSO_4)_3]^+$ with TMA	< -13			
$[(HDMA)_2(HSO_4)]^+$ with TMA	-14.0 ± 0.7	-9.5 ± 0.5		
$[(HDMA)_3(HSO_4)_2]^+$ with TMA	-1.1 ± 0.1	-0.37 ± 0.02	7.9 ± 0.4	

Table 3.4: Uptake coefficients for the substitution reactions of bisulfate clusters.

	γ_1	γ_2	γ_3	γ_4
$[(NH_4)_2(HSO_4)]^+$ with DMA	1.05 ± 0.26	0.97 ± 0.24		
$[(NH_4)_3(HSO_4)_2]^+$ with DMA	0.85 ± 0.22	0.72 ± 0.18	0.75 ± 0.19	
$[(NH_4)_4(HSO_4)_3]^+$ with DMA	0.61 ± 0.15	0.56 ± 0.14	0.58 ± 0.15	0.83 ± 0.21
$[(HMMA)_2(HSO_4)]^+$ with DMA	1.05 ± 0.26	0.70 ± 0.18		
$[(HMMA)_3(HSO_4)_2]^+$ with DMA	0.82 ± 0.20	0.71 ± 0.18	0.64 ± 0.16	
$[(HMMA)_4(HSO_4)_3]^+$ with DMA	0.85 ± 0.21	0.80 ± 0.20	0.69 ± 0.17	0.66 ± 0.16
$[(HTMA)_2(HSO_4)]^+$ with DMA	$8.6 \pm 2.2 \times 10^{-3}$	$1.8 \pm 0.5 \times 10^{-3}$		
$[(HTMA)_3(HSO_4)_2]^+$ with DMA	0.51 ± 0.13	0.22 ± 0.05	0.18 ± 0.05	
$[(NH_4)_2(HSO_4)]^+$ with TMA	0.90 ± 0.26	0.65 ± 0.26		
$[(NH_4)_3(HSO_4)_2]^+$ with TMA	0.66 ± 0.26	0.45 ± 0.26	0.57 ± 0.26	
$[(NH_4)_4(HSO_4)_3]^+$ with TMA	0.64 ± 0.26	0.48 ± 0.26	0.39 ± 0.26	1.07 ± 0.26
$[(HMMA)_2(HSO_4)]^+$ with TMA	1.07 ± 0.27	0.54 ± 0.13		
$[(HMMA)_3(HSO_4)_2]^+$ with TMA	0.75 ± 0.19	0.60 ± 0.15	0.39 ± 0.10	
$[(HMMA)_4(HSO_4)_3]^+$ with TMA	0.76 ± 0.19	0.69 ± 0.17	0.55 ± 0.14	0.13 ± 0.03
$[(HDMA)_2(HSO_4)]^+$ with TMA	0.62 ± 0.15	0.47 ± 0.12		
$[(HDMA)_3(HSO_4)_2]^+$ with TMA	0.33 ± 0.08	0.30 ± 0.07	0.025 ± 0.006	
$[(HDMA)_4(HSO_4)_3]^+$ with TMA	0.36 ± 0.09	0.050 ± 0.013	0.014 ± 0.004	$3.9 \pm 1.0 \times 10^{-3}$
$[(HMMA)_2(HSO_4)]^+$ with NH_3	$< 1.1 \times 10^{-3}$	$< 1.7 \times 10^{-3}$		
$[(HMMA)_3(HSO_4)_2]^+$ with NH_3	$3 \pm 1 \times 10^{-4}$	$< 3.1 \times 10^{-4}$	$< 3 \times 10^{-4}$	
$[(HMMA)_4(HSO_4)_3]^+$ with NH_3	$< 1.0 \times 10^{-4}$	$< 8 \times 10^{-5}$	$< 4 \times 10^{-4}$	$< 4 \times 10^{-4}$

Table 3.4 continued.

	γ_1	γ_2	γ_3	γ_4
$[(HDMA)_2(HSO_4)]^+$ with NH_3	$< 6 \times 10^{-5}$	$< 1.6 \times 10^{-3}$		
$[(HDMA)_3(HSO_4)_2]^+$ with NH_3	$< 1.9 \times 10^{-5}$	$< 8 \times 10^{-4}$	$< 4 \times 10^{-4}$	
$[(HDMA)_4(HSO_4)_3]^+$ with NH_3	$< 1.2 \times 10^{-5}$	$< 3.0 \times 10^{-3}$	$< 8 \times 10^{-4}$	$< 5 \times 10^{-4}$
$[(HTMA)_2(HSO_4)]^+$ with NH_3	$< 9 \times 10^{-5}$	$< 1.7 \times 10^{-3}$		
$[(HTMA)_3(HSO_4)_2]^+$ with NH_3	$< 6 \times 10^{-4}$	$< 1.1 \times 10^{-2}$	$< 2.1 \times 10^{-2}$	
$[(HTMA)_4(HSO_4)_3]^+$ with NH_3				$< 1.9 \times 10^{-3}$

It is evident based on ΔG values that substitution of amine for ammonia is highly favorable. Since the reverse reaction (substitution of ammonia for amine) was not observed, only upper limits for ΔG were determined. However, in the case of substitution of TMA for DMA in dimethylammonium bisulfate, both the forward and reverse reactions were observed, so actual ΔG values were determined. One general conclusion based on these thermodynamic results is that reaction is favorable when substitution occurs by a more polarizable species. Table 3.5 provides proton affinity and enthalpy of solvation values for ammonia and the aliphatic amines. By comparing ΔG values to proton affinity differences, it appears that proton affinity is a good guide for determining the favorability of substitution in most cases. However, since measurements were not absolute for the ammonium bisulfate clusters, exactly how good of a guide proton affinity values may be is uncertain, but initial substitution of TMA for DMA in 2-1 dimethylammonium bisulfate gives a ΔG value (14.0 ± 0.7 $kJ \cdot mol^{-1}$) close to the difference in proton affinity between DMA and TMA (20 $kJ \cdot mol^{-1}$). However, in the 3-2 dimethylammonium bisulfate cluster, substitution of TMA for DMA becomes unfavorable after the second substitution, which is what would be predicted based on enthalpy of solvation values. DMA solvates better than TMA; therefore, based on enthalpy of solvation values, substitution should be unfavorable. The unfavorability may also be due to steric interactions between TMA and the cluster as well as the loss of one hydrogen bond that occurs upon substitution of TMA. Therefore, while proton affinity may be a good predictor for initial substitution, enthalpy of solvation may be a better predictor for subsequent substitutions. Recent computational work indicates that the thermodynamics of

substitution are governed by the relative differences in gas phase basicity and cluster binding efficiency for each base.[5]

Table 3.5: Proton affinity and enthalpy of solvation values for NH_3 and the aliphatic amines.[4]

	Proton Affinity ($kJ \cdot mol^{-1}$)	Enthalpy of Solvation ($kJ \cdot mol^{-1}$)
NH_3	853.6	-35.4
MMA	899.0	-45.3
DMA	929.5	-53.1
TMA	948.9	-52.7

An examination of the uptake coefficients for bisulfate clusters agrees with this analysis. In the case of ammonium bisulfate clusters reacting with amine, uptake coefficients are close to unity, indicating that substitution occurs near the collision rate. The same is true for the reaction of monomethylammonium bisulfate with both DMA and TMA. In general, the first substitution occurred the fastest. Subsequent substitutions, while still quite fast, were slightly slower. This behavior can be explained by collisions of amine with the cluster occurring in places where substitution had already occurred, resulting in no net reaction. This trend does not appear to apply for the final substitution of the 4-3 ammonium bisulfate cluster with amine, as this substitution occurs more quickly than previous substitutions. This observation may arise because enough internal energy has been built up in the cluster to allow for a rearrangement to occur, making substitution more facile. However, it must be noted that the uncertainties associated with these uptake coefficients are relatively large, so one must be cautious in making any definite conclusions. In the case of trimethylammonium bisulfate reacting with DMA, substitution in the 2-1

cluster is unfavorable, which would be predicted based on proton affinity values. For the 3-2 cluster, though, substitution is observed, which would be predicted based on enthalpy of solvation values. Overall, later substitutions in a cluster occurred more quickly when reacting with DMA than TMA, likely due to steric hindrance with TMA.

3.3.4 Nitrate Clusters

Substitution kinetics and thermodynamics were also investigated for nitrate clusters. Thermodynamic results are provided in Table 3.6; kinetic results are provided in Table 3.7. In general, nitrate clusters were more difficult to study than bisulfate clusters. Ammonium nitrate volatilizes at low temperatures, so obtaining a stable ion signal for one cluster was a challenging problem. Clusters also appeared to be less strongly bound, so energetic substitutions in some cases introduced moderate to significant cluster dissociation. Significant cluster dissociation was evident for the 3-2 ammonium nitrate cluster reacting with TMA; however this cluster appeared to dissociate to the analogous 2-1 cluster at a rate close to collision rate. Additionally, both the 4-3 monomethylammonium and dimethylammonium nitrate clusters appeared to dissociate upon their final substitution with TMA. Rate constants (and, therefore, uptake coefficients) were not ascertained for the final substitution because these species were not observed. However, it appears that substitution did occur for this step, as significant cluster dissociation was observed at this point in the reaction, which is the opposite of what is normally observed upon the final substitution (that is, virtually no cluster dissociation is observed). Overall, results from nitrate clusters were in agreement with results from bisulfate clusters. Of particular note is that ΔG values for the substitution of TMA for DMA in 2-1 dimethylammonium nitrate are in

agreement within experimental error to the ΔG values for the analogous substitution in dimethylammonium bisulfate.

Therefore, it appears that amines displace ammonia at or near collision rate for small bisulfate and nitrate clusters. Initial substitution is generally favorable when a species with higher proton affinity displaces one with lower proton affinity.

Table 3.6: ΔG values ($kJ \cdot mol^{-1}$) for the substitution reactions of nitrate clusters at 298 K.

	Sub. 1	Sub. 2	Sub. 3
$[(NH_4)_3(NO_3)]^+$ with DMA			< -24
$[(HDMA)_2(NO_3)]^+$ with TMA	-13.7 ± 0.7	-9.9 ± 0.5	

3.3.5 Reaction of Ions versus Neutrals

It should be noted that in order to study these small clusters using mass spectrometry, they must exist as charged species. Nonetheless, one would expect that these results would also apply to neutral clusters, which appear to be dominant in the atmosphere.[6] Within one specific cluster size, there generally were no large (i.e. order of magnitude) differences in the observed rate constants from one substitution to the next, which would be indicative of charge playing an important role in the reaction. Additionally, the differences in substitution rate constants for clusters of different sizes (i.e. 2-1 ammonium bisulfate vs. 3-2 ammonium bisulfate vs. 4-3 ammonium bisulfate) were minimal. If charge were playing an important role in these reactions, significant differences from one size cluster to the next would be apparent; however, since this was not observed, it is likely that charge played a minimal role in these substitution reactions.

Table 3.7: Uptake coefficients for the substitution reactions of nitrate clusters.

	γ_1	γ_2	γ_3	γ_4
$[(NH_4)_3(NO_3)_2]^+$ with DMA	0.53 ± 0.21	0.50 ± 0.17	0.68 ± 0.12	
$[(HMMA)_2(NO_3)]^+$ with DMA	0.86 ± 0.25	0.55 ± 0.18		
$[(HMMA)_3(NO_3)_2]^+$ with DMA	0.77 ± 0.21	0.66 ± 0.17	0.47 ± 0.12	
$[(HTMA)_2(NO_3)]^+$ with DMA	$6.4 \pm 1.9 \times 10^{-3}$	$2.0 \pm 0.6 \times 10^{-3}$		
$[(NH_4)_3(NO_3)_2]^+$ with TMA[a]	0.40 ± 0.12			
$[(HMMA)_2(NO_3)]^+$ with TMA	0.84 ± 0.25	0.59 ± 0.18		
$[(HMMA)_3(NO_3)_2]^+$ with TMA	0.71 ± 0.21	0.55 ± 0.17	0.39 ± 0.12	
$[(HMMA)_4(NO_3)_3]^+$ with TMA[b]	0.76 ± 0.23	0.57 ± 0.17	0.43 ± 0.13	xx
$[(HDMA)_2(NO_3)]^+$ with TMA	0.60 ± 0.18	0.40 ± 0.12		
$[(HDMA)_3(NO_3)_2]^+$ with TMA	0.22 ± 0.07	0.16 ± 0.05	0.016 ± 0.006	
$[(HDMA)_4(NO_3)_3]^+$ with TMA[b]	0.13 ± 0.04	0.025 ± 0.008	$5.6 \pm 1.7 \times 10^{-3}$	xx
$[(HMMA)_3(NO_3)_2]^+$ with NH_3	$< 2.2 \times 10^{-4}$		$< 0.029 \pm 0.009$	
$[(HDMA)_2(NO_3)]^+$ with NH_3	$< 1.0 \times 10^{-4}$			
$[(HDMA)_3(NO_3)_2]^+$ with NH_3	$< 2.5 \times 10^{-5}$			
$[(HTMA)_2(NO_3)]^+$ with NH_3	$< 9 \times 10^{-5}$			

[a]Breakup of the 3-2 cluster to the 2-1 cluster was quite significant. The uptake coefficient represents the rate of cluster breakup to the 2-1 cluster compared to the collisional rate constant.

[b]For these 4-3 clusters, the final substitution of TMA appeared to induce cluster breakup.

3.4 Atmospheric Implications

The results of this work have important atmospheric implications. These clusters have diameters that are about 1-2 nanometers, which fall into the size range of the stable pool of clusters that have been implicated in new particle formation.[6] For a 1-nm diameter cluster exposed to an ambient amine level of 1 ppb, i.e. near an amine source, the collision rate would be on the order of 30 s^{-1}. Based on the near unity uptake coefficients measured in this work, complete conversion of ammonium to aminium in the cluster would be expected to occur in less than a second. If the ambient amine concentration were in the low ppt level, i.e. further away from an amine source, complete conversion still would be expected within several seconds to minutes. These results suggest that if salt clusters are a component of the sub-3 nm cluster pool, they are likely to be aminium salts rather than ammonium salts, even if they were initially formed as ammonium salts. Ammonium salt clusters would be expected to persist only when 1) the formation rate of new clusters exceeds the cluster collision rate with amine or 2) the growth rate of a cluster by collision with ammonia exceeds the cluster collision rate with amine.

Reproduced in part from: B. R. Bzdek, D. P. Ridge, and M. V. Johnston, "Amine exchange into ammonium bisulfate and ammonium nitrate nuclei," *Atmospheric Chemistry and Physics*, **2010**, *10* (8), 3495-3503.

3.5 References

1. Bartmess, J. E.; Georgiadis, R. M., Empirical methods for determination of ionization gauge relative sensitivities for different gases. *Vacuum* **1983,** *33* (3), 149-153.

2. Ridge, D. P., Ion-Molecule Collision Theory. In *The Encyclopedia of Mass Spectrometry*, Armentrout, P. B., Ed. Elsevier: San Diego, CA, 2003; Vol. Volume I: Theory and Ion Chemistry, pp 1-8.

3. Su, T.; Chesnavich, W. J., Parametrization of the ion-polar molecule collision rate constant by trajectory calculations. *J. Chem. Phys.* **1982,** *76* (10), 5183-5185.

4. Lide, D. R., (ed.), *CRC Handbook of Chemistry and Physics, 90th Edition (Internet Version 2010)*. CRC Press/Taylor Francis: Boca Raton, FL, 2010.

5. DePalma, J. W.; Bzdek, B. R.; Doren, D. J.; Johnston, M. V., Structure and energetics of nanometer size clusters of sulfuric acid with ammonia and dimethylamine. *J. Phys. Chem. A* **2012,** *116* (3), 1030-1040.

6. Kulmala, M.; Riipinen, I.; Sipila, M.; Manninen, H. E.; Petaja, T.; Junninen, H.; Dal Maso, M.; Mordas, G.; Mirme, A.; Vana, M.; Hirsikko, A.; Laakso, L.; Harrison, R. M.; Hanson, I.; Leung, C.; Lehtinen, K. E. J.; Kerminen, V. M., Toward direct measurement of atmospheric nucleation. *Science* **2007,** *318* (5847), 89-92.

Chapter 4

SIZE-DEPENDENT REACTIONS OF AMMONIUM BISULFATE CLUSTERS WITH DIMETHYLAMINE

4.1 Introduction

The goal of this chapter is to extend the work on small positively-charged ammonium bisulfate clusters described in Chapter 3 to much larger clusters. Specifically, the size-dependent reactivity of positively-charged ammonium bisulfate clusters with dimethylamine (DMA) gas is explored. This work is accomplished by performing ion-molecule reactions in a Fourier transform ion cyclotron resonance mass spectrometer (FTICR-MS), fitting the resulting reaction profiles to pseudo first order kinetic models, and determining reaction probabilities. The results of this work indicate that DMA displaces ammonia very efficiently on the surface of the cluster, but that this displacement is much slower for ammonia encapsulated in the core of a cluster. These results are consistent with preliminary measurements of amine-ammonia exchange in 20-30 nm diameter ammonium sulfate particles. Additionally, another mechanism of amine incorporation into these clusters is identified: amines can also add to the cluster in order to neutralize acid. In this case, amine can add to larger clusters to neutralize bisulfate towards sulfate. These observations are atmospherically relevant because they permit one to infer the composition of ambient clusters in the sub-3 nm cluster pool. Based on the observations discussed in this chapter, aminium salts would be expected to be an important component of that cluster pool.

Additionally, these observations indicate that the rate and mechanism of amine incorporation can depend upon cluster size.

4.2 Experimental Section

The experimental setup is similar to that in previous work on amine exchange in smaller ammonium bisulfate clusters (see Chapter 3).[1] Charged ammonium bisulfate clusters were introduced to a 7T Bruker Apex-Qe Fourier transform ion cyclotron resonance mass spectrometer (FTICR-MS) operating in the positive mode by electrospray of a 0.5 mM solution of ammonium sulfate (Aldrich, St. Louis, Missouri) in 70/30 acetonitrile/water. Electrospray produced an array of clusters that were predominantly singly charged. Ions for a specific cluster of interest were mass selected and accumulated in a quadrupole. Ions were then transferred to the ICR cell where they were exposed to a constant pressure of DMA gas (Matheson Tri-Gas, Basking Ridge, New Jersey) at $2.4 \pm 0.5 \times 10^{-8}$ torr that was introduced to the cell via a leak valve. Whereas multiply charged clusters were observed in the mass spectrum at the same exact mass as singly charged clusters, multiply charged clusters were easily and quantitatively differentiated from the singly charged clusters by the presence of isotopic peaks at fractional mass-to-charge (*m/z*) ratios, which cannot arise from a singly charged cluster. Analysis of the abundance of these fractional *m/z* peaks determined the intensity of the multiply charged clusters to be generally less than 3% of the total ion signal (> 97% singly charged clusters). Therefore, the effect of multiply charged clusters on kinetic analysis was minimal. Additionally, singly charged dimethylammonium bisulfate clusters were introduced to the FTICR-MS by electrospray of a dimethylammonium sulfate solution (0.5 mM in 50/50 methanol/water) made by combining equal proportions of solutions of 2.0 mM DMA

(Fluka, St. Louis, Missouri) in 50/50 methanol/water and 1.0 mM H_2SO_4 (Fisher, Pittsburgh, Pennsylvania) in 50/50 methanol/water. Isolated dimethylammonium bisulfate clusters were exposed to DMA gas in order to study the kinetics of DMA addition to the clusters. Finally, ammonium and dimethylammonium bisulfate clusters were exposed to ammonia gas (Matheson Tri-Gas, Basking Ridge, New Jersey) at 1.0 $\pm$ 0.2 $\times$ 10^{-7} torr to determine the kinetics of ammonia addition to the clusters.

A mass spectrum of ions in the ICR cell can be obtained at a specific trapping time. FTICR-MS provides high resolution and accuracy *m/z* measurements, which allow for the assignment of unique elemental formulae to reactant and product ions. A plot of ion abundance as a function of trapping time (reaction profile) reveals the progress of the sequential reactions. Since the substitution reaction is exothermic,[1] each incoming DMA molecule induces decomposition of the cluster as well as the displacement of a single ligand. These minor reaction-induced decomposition channels are not enhanced by introducing unreactive argon collision gas to the ICR cell. As will be discussed later, the reaction-induced decomposition was too small to affect quantitative kinetic analysis of the predominant simple displacements. All data were fit to the kinetic models using the simplex method of non-linear fitting embodied in the Solver function of the Microsoft Excel program.

Determination of second order rate constants required knowledge of the absolute pressure of gas in the ICR cell. However, due to effects associated with the magnet and the polarizability of the gas being measured, the ICR cell pressure reading given by the ionization gauge did not correspond to the true ICR cell pressure. The absolute gas pressure in the ICR cell was determined by in the manner described in Chapter 3.

4.3 Results and Discussion

4.3.1 Amine Substitution into Ammonium Bisulfate Clusters

The sequential displacement of ammonia by DMA in ammonium bisulfate clusters is described by the scheme below:

$$[(NH_4)_x(HSO_4)_{x-1}]^+ + (CH_3)_2NH \xrightarrow{k_1} [(NH_4)_{x-1}((CH_3)_2NH_2)(HSO_4)_{x-1}]^+ + NH_3$$
$$[(NH_4)_{x-1}((CH_3)_2NH_2)(HSO_4)_{x-1}]^+ + (CH_3)_2NH \xrightarrow{k_2} [(NH_4)_{x-2}((CH_3)_2NH_2)_2(HSO_4)_{x-1}]^+ + NH_3$$
$$[(NH_4)_{x-2}((CH_3)_2NH_2)_2(HSO_4)_{x-1}]^+ + (CH_3)_2NH \xrightarrow{k_3} [(NH_4)_{x-3}((CH_3)_2NH_2)_3(HSO_4)_{x-1}]^+ + NH_3$$
$$\cdots \xrightarrow{k_x} [((CH_3)_2NH_2)_x(HSO_4)_{x-1}]^+ + NH_3$$

Figure 4.1 presents representative mass spectra for the sequential displacement of ammonia by DMA in $[(NH_4)_8(HSO_4)_7]^+$ (the "8-7" ammonium bisulfate cluster) at a) 0 sec and b) 10 sec after exposure to DMA. Cluster assignments are given in the form *a*(*b*)-*c*-*d*, where *a* represents the number of ammonium ions initially in the unreacted cluster, *b* represents the progress of the displacement reaction (i.e. the number of ammonium ions that have been displaced by DMA), *c* represents the number of bisulfate ions in the cluster, and *d* (indicated when nonzero) represents the number of neutral DMA molecules that have added onto the cluster (not displacement). The addition of DMA to a cluster is described by the equation:

$$[((CH_3)_2NH_2)_x(HSO_4)_{x-1}]^+ + (CH_3)_2NH \xrightarrow{k_{add}} [((CH_3)_2NH_2)_x(HSO_4)_{x-1}((CH_3)_2NH)]^+ \quad (1)$$

Additionally, clusters substituted with sodium are indicated with the "Na-" prefix.

At 0 sec reaction time (Fig. 4.1a), the predominant peak is that of the pure 8-7 ammonium bisulfate cluster (8(0)-7) at *m/z* 822.991, for which mass selection was performed in the quadrupole. Mass selection was accomplished by setting the *m/z* of

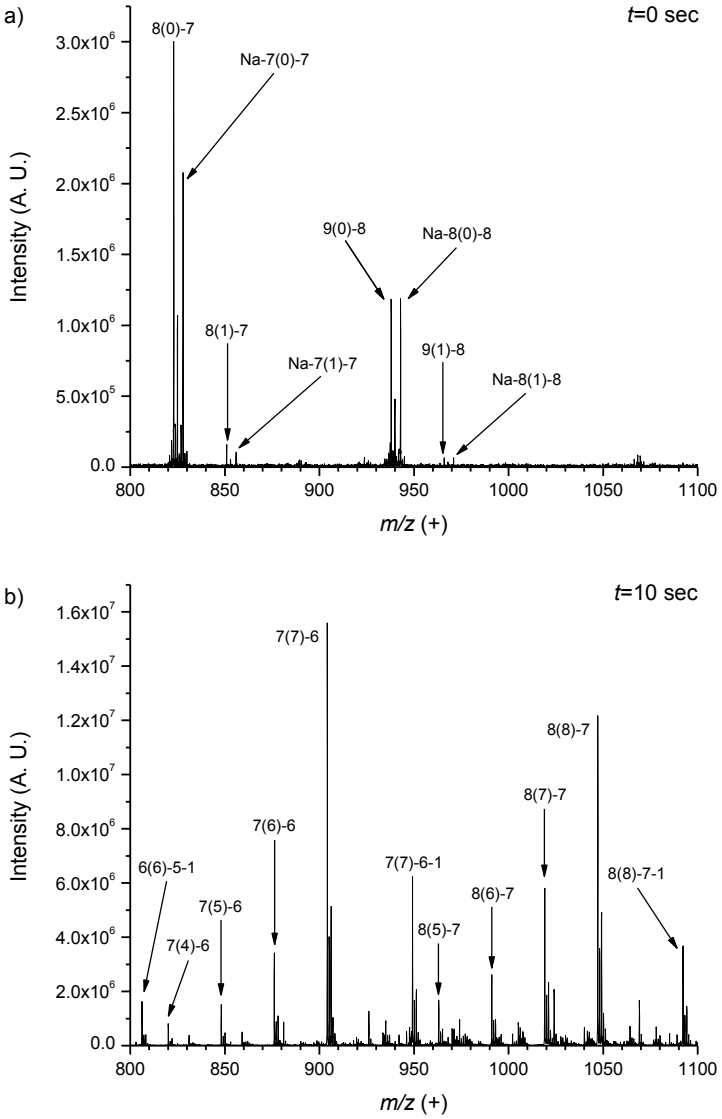

Figure 4.1: Mass spectra for the reaction of 8-7 ammonium bisulfate with DMA at a) *t*=0 sec and b) *t*=10 sec reaction time. Cluster ions are identified in the form *a*(*b*)-*c*-*d*, where *a* represents the number of ammonium ions initially in the unreacted cluster, *b* represents the progress of the reaction (i.e. the number of ammonium ions that have been displaced by DMA), *c* represents the number of bisulfate ions in the cluster, and *d* (indicated when nonzero) represents the number of neutral DMA molecules that have added onto the cluster (not displacement). Ions containing sodium are indicated by the "Na-" prefix.

interest to that of the 9-8 cluster (*m/z* 937.985). Although a relatively small amount of the 9-8 cluster (9(0)-8) is isolated, the predominant ion isolated corresponds to the 8-7 cluster, likely due to decomposition of metastable 9-8 clusters during isolation. For all examined clusters, isolation was accomplished by selecting for a cluster larger by one ammonium bisulfate neutral, [$(NH_4)(HSO_4)$]. Some of the 7-6 cluster (not present in the displayed *m/z* range) is also isolated in small intensity. Additionally, clusters where a sodium ion has replaced an ammonium ion (Na-7(0)-7 and Na-8(0)-8) were observed. Finally, a very small amount of the first DMA substitution for each cluster (8(1)-7, Na-7(1)-7, 9(1)-8, and Na-8(1)-8) was detected owing to residual DMA in the system. As the reaction progresses (Fig. 4.1b), ion intensity for each sequential substitution builds, reaches a maximum value, and subsequently decreases as the different substitution products are formed and react away (e.g. 8(5)-7, 8(6)-7, 8(7)-7), eventually resulting in the fully-substituted dimethylammonium bisulfate cluster (8(8)-7). In this case, as was the case for most clusters studied, the addition of a single DMA molecule to the fully-substituted cluster (8(8)-7-1) was also observed at the end of the reaction.

In addition to signal from *m/z* values corresponding to the cluster of interest, also present is signal from the partially- and fully-substituted 7-6 cluster. The signal for this cluster in part comes from the small amount of it that was isolated initially, but also from decomposition of the 8-7 cluster as a result of the exothermic displacements. Previous work (Chapter 3) has indicated that initial substitution of DMA for ammonia is governed by the difference in proton affinity values between the incoming and departing ligands, while subsequent substitutions may be governed by the difference in solvation enthalpies between the two.[1] For the reaction of DMA with ammonium

bisulfate, initial displacement is highly favorable ($\Delta G^{o} < -16$ kJ·mol^{-1}).[1] Since these displacements take place in near-vacuum conditions, there is no sink for the energy that is released from the substitution. As a result, this released energy induces decomposition of the cluster through the loss of an ammonium bisulfate neutral. Throughout the course of the reaction, the summed intensity of all 8-7 clusters decreased by about 30% relative to the summed intensity of all 7-6 clusters. As discussed later, this decrease in intensity of the 8-7 clusters is too small to significantly affect the kinetic analysis. Unidentified peaks in both spectra are relatively small in intensity and, in fact, comprise less than 20% of the total ion signal in Fig. 4.1b. While the identity of these peaks is unknown, they appear to arise from dimethylammonium bisulfate associating with pump oil or some other organic impurity in the system. For instance, in Fig. 4.1b ions at *m/z* 926.166 and 1069.175 (the two most prominent unidentified peaks) are both singly charged and differ by a *m/z* value that corresponds to the exact mass of a dimethylammonium bisulfate neutral, [$((CH_3)_2NH_2)(HSO_4)$]; however, the isotope distribution does not correspond to one that would contain a significant amount of sulfur (small M+2 peak) and instead resembles an isotope distribution for a species that contains a significant amount of carbon (large M+1 peak). Additionally, a low sulfur content for these ions is suggested by their relatively large positive mass defects. These unidentified peaks play little to no role in the kinetics of exchange. Finally, as is evident in the spectrum at t=10 sec, the overall ion intensity increases with increasing reaction time. This increase is due to collisional cooling of ions to the center of the ICR cell, and is taken into account in the kinetic analysis through the use of relative, rather than absolute, ion intensities.

A reaction profile for sequential reactions occurring in a given cluster is created by plotting the relative abundance of each step compared to total cluster abundance. Because the DMA pressure was maintained at a constant level, these data can be fit to pseudo first order kinetics. Integration of the rate equations for a series of j sequential pseudo first order reactions gives:

$$A_{\mathrm{i}} = k_1 k_2 \ldots k_{\mathrm{i}-1} A_0 \left(\sum_{\mathrm{j}=1}^{\mathrm{i}} \alpha_{\mathrm{j}} e^{-k_{\mathrm{j}} t} \right) \tag{2}$$

where A_{i} is the relative intensity of the i^{th} product in the reaction sequence; k_1, k_2, k_3, etc. represent the pseudo first order rate constants for the sequential reaction steps; and

$$\alpha_{\mathrm{j}} = \frac{1}{\prod_{\mathrm{n}=1}^{\mathrm{i}} \left(k_{\mathrm{n}} - k_{\mathrm{j}} \right)} \qquad \text{where } \mathrm{n} \neq \mathrm{j} \tag{3}$$

Figure 4.2 presents the reaction profile and statistical fits to pseudo first order kinetics for the 8-7 cluster. Symbols represent experimental data, while solid lines represent the statistical fits. The ammonium bisulfate cluster (8(0)-7) is exposed to DMA gas at t=0 sec and the relative intensities of it and the eight sequential displacements of ammonia (8(1)-7, 8(2)-7, 8(3)-7, 8(4)-7, 8(5)-7, 8(6)-7, 8(7)-7, and 8(8)-7) change as a function of exposure time. Addition of DMA to the fully substituted cluster was also observed (8(8)-7-1). While the first several displacements appear to be very fast, signal intensity builds up before the final substitution and the DMA addition (8(7)-7 and 8(8)-7) indicating that these steps are slower than the previous steps. The fit of the kinetic model to the data was less sensitive to the rate constants for the initial "fast" processes (k_1-k_7) than to the rate constants for the final "slow" steps (k_8 and k_{add}). The uncertainties in k_1 to k_7 are therefore larger than those

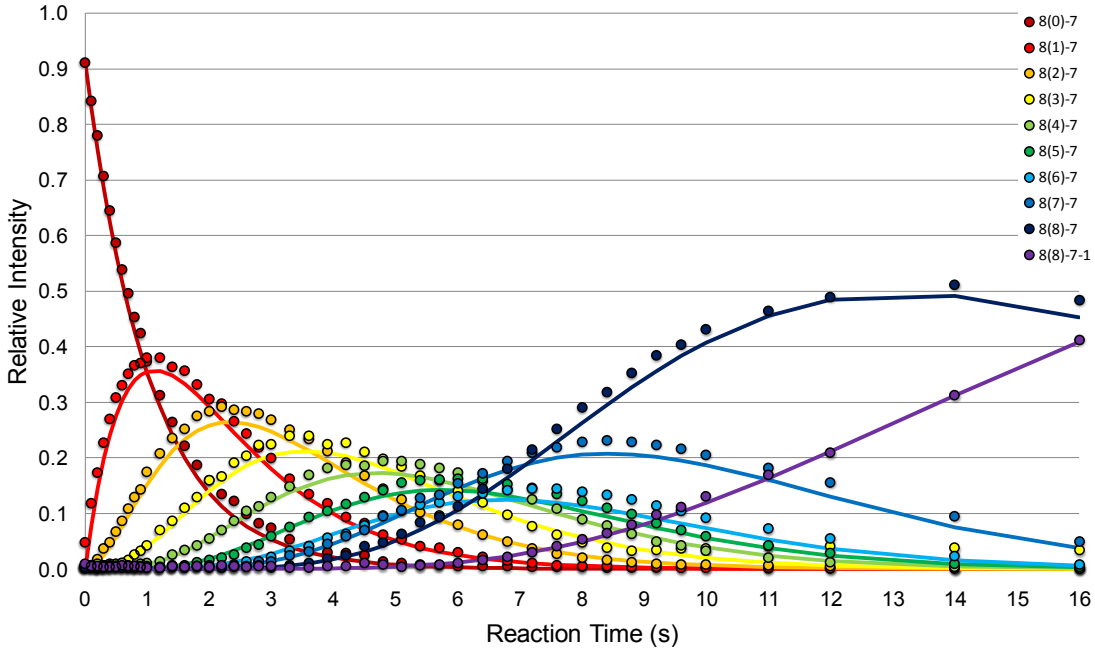

Figure 4.2: Reaction profile for the reaction of 8-7 ammonium bisulfate with DMA. Circles represent experimental data; lines represent statistical fits to pseudo first order kinetics. Each step in the sequential reactions is represented by a different color as indicated in the legend. The cluster notation is the same as in Fig. 4.1.

for k_8 and k_{add}, but the magnitudes of k_1 to k_7 are quite large and similar to one another. Pseudo first order rate constants for the 8-7 cluster are provided in Table 4.1. For the 8-7 cluster, pseudo first order rate constants for the "fast" steps (k_1-k_7) ranged from 0.74 to 0.99 s^{-1}, while the slow steps (k_8 and k_{add}) had pseudo first order rate constants of 0.51 ± 0.02 s^{-1} and 0.098 ± 0.005 s^{-1}, respectively. Second order rate constants, obtained by dividing the pseudo first order rate constant by the absolute gas pressure in the cell, are also provided in Table 4.1.

Because the collisional radius for the 8-7 cluster and a DMA molecule is likely much larger than 10 Å, the hard sphere model would be appropriate to determine the theoretical collisional rate constant, which would be used to determine uptake coefficients (reaction probabilities, γ) for these reactions. However, determining an accurate value for the collisional radius for this cluster is not trivial, as its size and structure at a molecular level are not known. Any estimation of the collisional radius (and collisional cross section) would result in large uncertainties in the calculated uptake coefficients. In previous work, though, ammonia displacement by amine was found to be collision-limited, with rate constants similar to those observed for k_1-k_7 in this work (see Chapter 3).[1] Therefore, relative uptake coefficients, which are determined by dividing the pseudo first order rate constant for each step by the pseudo first order rate constant for the fastest step observed for that cluster, are calculated. The implicit assumption is that the fastest rate constant is equal or close to the collisional rate constant. Relative uptake coefficients for the 8-7 cluster are provided in Table 4.1. An examination of the relative uptake coefficients indicates that the "fast" steps occur near collision rate. However, the final substitution step (k_8) has a lower relative uptake coefficient than the earlier steps.

Table 4.1: Pseudo first order rate constants, second order rate constants, and relative uptake coefficients for the reaction of 8-7 ammonium bisulfate with DMA (P_{DMA}: $2.4 \pm 0.5 \times 10^{-8}$ torr).

Reaction Step	Pseudo First Order Rate Constant (s^{-1})	Second Order Rate Constant ($cm^3 \cdot molec^{-1} \cdot s^{-1}$)	Relative Uptake Coefficient, γ
k_1	0.86 ± 0.07	$1.0 \pm 0.2 \times 10^{-9}$	0.87 ± 0.26
k_2	0.76 ± 0.06	$9.2 \pm 1.8 \times 10^{-10}$	0.77 ± 0.23
k_3	0.74 ± 0.04	$9.0 \pm 1.8 \times 10^{-10}$	0.75 ± 0.23
k_4	0.77 ± 0.04	$9.3 \pm 1.8 \times 10^{-10}$	0.78 ± 0.23
k_5	0.83 ± 0.04	$1.0 \pm 0.2 \times 10^{-9}$	0.84 ± 0.25
k_6	0.92 ± 0.05	$1.1 \pm 0.2 \times 10^{-9}$	0.94 ± 0.28
k_7	0.99 ± 0.05	$1.2 \pm 0.2 \times 10^{-9}$	1.00 ± 0.30
k_8	0.51 ± 0.02	$6.1 \pm 1.2 \times 10^{-10}$	0.51 ± 0.15
k_{add}	0.098 ± 0.005	$1.2 \pm 0.2 \times 10^{-10}$	0.10 ± 0.03

A slow final substitution step was observed for many ammonium bisulfate clusters. Figure 4.3 presents a summary of relative uptake coefficients for the final substitution step (γ_{sub}) in a given cluster (filled squares) as a function of cluster size (the number of bisulfate ions in the cluster). Second order rate constants (empty triangles) are also provided on the opposite axis. For relatively small clusters (the 2-1 cluster through the 6-5 cluster), γ_{sub} is close to unity. However, beginning with the 7-6 and 8-7 clusters, γ_{sub} decreases slightly. For the 9-8 cluster, γ_{sub} is nearly an order of magnitude lower than for the smaller clusters. Finally, for the 10-9 and 11-10 clusters, the final substitution step was not observed at all. Based on spectral noise, the relative uptake coefficients for that step are more than two orders of magnitude lower than for initial substitution. Pseudo first and second order rate constants, as well as relative uptake coefficients for all substitutions in all clusters examined, are provided in Table 4.2.

As mentioned earlier, during the course of the sequential substitution reactions, the ion intensity for the 8-7 cluster decreased relative to that for the 7-6 cluster. Decomposition to smaller clusters occurred in similar magnitude for all studied substitution reactions. These minor decomposition pathways, however, are too small to affect quantitative kinetic analysis of the substitution reaction pathway. As an example, for the 8-7 ammonium bisulfate cluster after 10 sec reaction time with DMA, the summed intensity of all 8-7 clusters decreases by about 30% relative to the summed intensity of all 7-6 clusters. A model was created to test the effect of cluster decomposition on the results. In this model, the rate for a simple displacement (8(0)-7 to 8(1)-7) was set to a value consistent with those calculated from the fit of

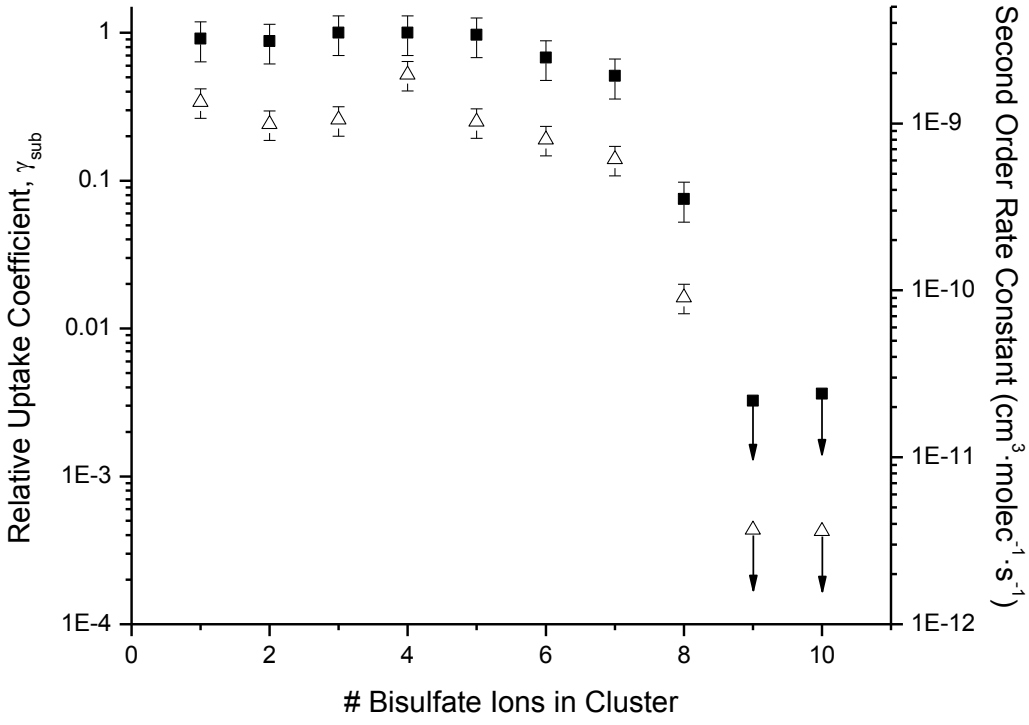

Figure 4.3: A plot of relative uptake coefficients and second order rate constants for the displacement of the final ammonium ion by DMA in ammonium bisulfate clusters of increasing size. Filled squares represent relative uptake coefficient values; empty triangles represent second order rate constant values. Arrows pointing down from data points indicate that substitution was not observed, so maximum possible values are reported.

Table 4.2: Pseudo first order rate constants, second order rate constants, and relative uptake coefficients for the displacement of ammonia by DMA in ammonium bisulfate clusters. Note that data presented in Fig. 4.3 for clusters smaller than the 5-4 cluster are given in Chapter 3.[1] DMA gas pressure was $2.4 \pm 0.5 \times 10^{-8}$ torr for all clusters except the 9-8 cluster, where DMA gas pressure was $1.2 \pm 0.2 \times 10^{-8}$ torr. The "<" sign indicates that no product was detected; maximum rates were determined based upon the noise levels in the spectra.

	Pseudo first Order Rate Constant (s^{-1})	Second Order Rate Constant ($cm^3 \cdot molec^{-1} \cdot s^{-1}$)	Relative Uptake Coefficient, γ
5-4 Cluster			
k_1	0.69 ± 0.02	$8.1 \pm 1.6 \times 10^{-10}$	0.41 ± 0.12
k_2	0.54 ± 0.02	$6.4 \pm 1.3 \times 10^{-10}$	0.32 ± 0.10
k_3	0.66 ± 0.01	$7.7 \pm 1.5 \times 10^{-10}$	0.40 ± 0.12
k_4	0.98 ± 0.02	$1.2 \pm 0.2 \times 10^{-9}$	0.58 ± 0.17
k_5	1.67 ± 0.05	$2.0 \pm 0.4 \times 10^{-9}$	1.00 ± 0.30
k_{add}	0.043 ± 0.001	$5.0 \pm 1.0 \times 10^{-11}$	0.026 ± 0.008
6-5 Cluster			
k_1	0.69 ± 0.08	$8.2 \pm 1.6 \times 10^{-10}$	0.80 ± 0.24
k_2	0.58 ± 0.05	$6.9 \pm 1.4 \times 10^{-10}$	0.68 ± 0.20
k_3	0.57 ± 0.05	$6.8 \pm 1.4 \times 10^{-10}$	0.66 ± 0.20
k_4	0.71 ± 0.05	$8.3 \pm 1.7 \times 10^{-10}$	0.82 ± 0.25
k_5	0.85 ± 0.08	$1.0 \pm 0.2 \times 10^{-9}$	0.99 ± 0.30
k_6	0.86 ± 0.10	$1.0 \pm 0.2 \times 10^{-9}$	1.00 ± 0.30
k_{add}	0.058 ± 0.003	$6.8 \pm 1.4 \times 10^{-11}$	0.07 ± 0.02
7-6 Cluster			
k_1	0.84 ± 0.03	$1.0 \pm 0.2 \times 10^{-9}$	0.84 ± 0.25
k_2	0.67 ± 0.03	$7.9 \pm 1.6 \times 10^{-10}$	0.67 ± 0.20
k_3	0.67 ± 0.04	$7.9 \pm 1.6 \times 10^{-10}$	0.67 ± 020
k_4	0.67 ± 0.04	$7.8 \pm 1.6 \times 10^{-10}$	0.67 ± 020
k_5	0.79 ± 0.05	$1.0 \pm 0.2 \times 10^{-9}$	0.79 ± 0.24
k_6	1.00 ± 0.09	$1.2 \pm 0.2 \times 10^{-9}$	1.00 ± 0.30
k_7	0.68 ± 0.04	$8.0 \pm 1.6 \times 10^{-10}$	0.68 ± 0.20
k_{add}	0.080 ± 0.002	$9.5 \pm 1.9 \times 10^{-11}$	0.08 ± 0.02
8-7 Cluster			
k_1	0.86 ± 0.07	$1.0 \pm 0.2 \times 10^{-9}$	0.87 ± 0.26
k_2	0.76 ± 0.06	$9.2 \pm 1.8 \times 10^{-10}$	0.77 ± 0.23
k_3	0.74 ± 0.04	$9.0 \pm 1.8 \times 10^{-10}$	0.75 ± 0.23
k_4	0.77 ± 0.04	$9.3 \pm 1.8 \times 10^{-10}$	0.78 ± 0.23
k_5	0.83 ± 0.04	$1.0 \pm 0.2 \times 10^{-9}$	0.84 ± 0.25
k_6	0.92 ± 0.05	$1.1 \pm 0.2 \times 10^{-9}$	0.94 ± 0.28
k_7	0.99 ± 0.05	$1.2 \pm 0.2 \times 10^{-9}$	1.00 ± 0.30
k_8	0.51 ± 0.02	$6.1 \pm 1.2 \times 10^{-10}$	0.51 ± 0.15

Table 4.2 continued.

	Pseudo first Order Rate Constant (s^{-1})	Second Order Rate Constant ($cm^3 \cdot molec^{-1} \cdot s^{-1}$)	Relative Uptake Coefficient, γ
k_{add}	0.098 ± 0.005	$1.2 \pm 0.2 \times 10^{-10}$	0.10 ± 0.03
9-8 Cluster			
k_1	0.49 ± 0.02	$1.2 \pm 0.2 \times 10^{-9}$	1.00 ± 0.30
k_2	0.45 ± 0.01	$1.1 \pm 0.2 \times 10^{-9}$	0.91 ± 0.27
k_3	0.41 ± 0.02	$1.0 \pm 0.2 \times 10^{-9}$	0.85 ± 0.26
k_4	0.39 ± 0.03	$9.7 \pm 1.9 \times 10^{-10}$	0.80 ± 0.24
k_5	0.39 ± 0.04	$9.6 \pm 1.9 \times 10^{-10}$	0.79 ± 0.24
k_6	0.42 ± 0.05	$1.0 \pm 0.2 \times 10^{-9}$	0.86 ± 0.26
k_7	0.41 ± 0.03	$1.0 \pm 0.2 \times 10^{-9}$	0.84 ± 0.25
k_8	0.43 ± 0.04	$1.1 \pm 0.2 \times 10^{-9}$	0.87 ± 0.26
k_9	0.04 ± 0.01	$9.1 \pm 1.8 \times 10^{-11}$	0.08 ± 0.02
k_{add}	0.054 ± 0.001	$1.3 \pm 0.3 \times 10^{-10}$	0.10 ± 0.03
10-9 Cluster			
k_1	0.99 ± 0.06	$1.2 \pm 0.2 \times 10^{-9}$	1.00 ± 0.30
k_2	0.93 ± 0.06	$1.1 \pm 0.2 \times 10^{-9}$	0.94 ± 0.28
k_3	0.95 ± 0.06	$1.1 \pm 0.2 \times 10^{-9}$	0.96 ± 0.29
k_4	0.92 ± 0.09	$1.1 \pm 0.2 \times 10^{-9}$	0.93 ± 0.28
k_5	0.91 ± 0.05	$1.1 \pm 0.2 \times 10^{-9}$	0.92 ± 0.28
k_6	0.91 ± 0.03	$1.1 \pm 0.2 \times 10^{-9}$	0.92 ± 0.28
k_7	0.88 ± 0.10	$1.0 \pm 0.2 \times 10^{-9}$	0.89 ± 0.27
k_8	0.93 ± 0.04	$1.1 \pm 0.2 \times 10^{-9}$	0.94 ± 0.28
k_9	0.91 ± 0.04	$1.1 \pm 0.2 \times 10^{-9}$	0.92 ± 0.28
k_{10}	< 0.003	$< 4.0 \times 10^{-13}$	$< 3.5 \times 10^{-4}$
k_{add}	0.11 ± 0.01	$1.3 \pm 0.3 \times 10^{-10}$	0.11 ± 0.03
11-10 Cluster			
k_1	0.79 ± 0.10	$9.5 \pm 1.9 \times 10^{-10}$	1.00 ± 0.30
k_2	0.72 ± 0.09	$8.7 \pm 1.7 \times 10^{-10}$	0.92 ± 0.38
k_3	0.65 ± 0.08	$7.8 \pm 1.6 \times 10^{-10}$	0.82 ± 0.25
k_4	0.62 ± 0.07	$7.4 \pm 1.4 \times 10^{-10}$	0.78 ± 0.23
k_5	0.61 ± 0.08	$7.4 \pm 1.4 \times 10^{-10}$	0.77 ± 0.23
k_6	0.63 ± 0.08	$7.4 \pm 1.5 \times 10^{-10}$	0.79 ± 0.24
k_7	0.64 ± 0.07	$7.7 \pm 1.5 \times 10^{-10}$	0.81 ± 0.24
k_8	0.63 ± 0.05	$7.5 \pm 1.5 \times 10^{-10}$	0.79 ± 0.24
k_9	0.58 ± 0.05	$7.0 \pm 1.4 \times 10^{-10}$	0.73 ± 0.22
k_{10}	0.55 ± 0.06	$6.6 \pm 1.3 \times 10^{-10}$	0.69 ± 0.21
k_{11}	< 0.003	$< 3.6 \times 10^{-12}$	< 0.004
k_{add}	0.10 ± 0.01	$1.2 \pm 0.2 \times 10^{-10}$	0.12 ± 0.04

experimental data (e.g. 0.95 s^{-1}). A second pathway was also modeled, where the overall intensity of the cluster would decrease over 10 sec to 70% of its original value. The combined effect of the two competing pathways were then fit to the pseudo first order rate law. Under these conditions, which can be considered extreme conditions since only one substitution is considered, the calculated rate constant changed by only 20%, which is much smaller than the order-of-magnitude changes observed during the final substitution step as the cluster size increases. It is also notable that these decomposition pathways are only significant during the displacements, as exchange is very exothermic. At long reaction times (after most or all ammonia has been displaced from the cluster), relative cluster intensities remain stable.

The dramatic decrease in relative uptake coefficient for the final substitution step that is observed with increasing cluster size relates directly to the structure of the cluster. At small cluster sizes, all ammonium ions are exposed to incoming DMA molecules, allowing for facile exchange. However, as cluster size increases or perhaps as a result of multiple displacements by DMA, an ammonium ion can be trapped in an inaccessible region of the cluster. Therefore, while the "surface" exchange occurs at collision rate, reaction in the "core" is much slower.

4.3.2 Amine Addition onto Dimethylammonium Bisulfate Clusters

In addition to simple substitution, DMA-substituted clusters containing three or more bisulfate ions exhibited some more complicated behavior, as DMA was observed to add onto these substituted clusters, as illustrated in Eq. (1). The addition of DMA onto dimethylammonium bisulfate clusters was studied in two ways. In the first method, mass selected ammonium bisulfate clusters were exposed to DMA gas. Near the end of the reaction, DMA would add onto either the fully substituted or

mostly substituted cluster, depending on the rate of the final substitution step. Rates for this addition were determined simultaneously while fitting for the substitution steps (see Fig. 4.2). In the second method, mass selected dimethylammonium bisulfate clusters were exposed to a constant pressure of DMA gas in order to directly measure the rate for DMA addition.

Figure 4.4 presents a plot summarizing the measured relative uptake coefficients for DMA addition (γ_{add}) as a function of cluster size. Empty triangles represent values measured by exposure of ammonium bisulfate clusters to DMA, while filled squares represent values measured by direct analysis of dimethylammonium bisulfate clusters. Relative uptake coefficient values were determined by comparing the observed rate constant for addition to the fastest substitution step observed for a specific cluster. Rate constants are provided in Tables 4.2 (from substitution) and 4.3 (from direct analysis). While no DMA addition is observed for the 2-1 and 3-2 clusters ($\gamma_{add} < 10^{-3}$), DMA addition occurs at a very slow rate for the 4-3 cluster ($\gamma_{add} = 4 \pm 1 \times 10^{-3}$). For clusters larger than the 4-3 cluster, DMA addition occurs consistently at a relative uptake coefficient value close to 0.1. For the 5-4, 6-5, 7-6, and 8-7 clusters, the relative uptake coefficient value for addition ($\gamma_{add} \approx 0.1$) is still much slower than that for the final substitution step ($0.5 \leq \gamma_{sub} \leq 1.0$). Therefore, addition was only observed after the cluster was fully substituted with DMA. However, in the case of the 9-8 cluster, the relative uptake coefficients for substitution and for addition are nearly the same (γ_{sub} and γ_{add} for both near 0.1) and, in fact, substitution and addition are observed simultaneously during the reaction. Finally, for larger clusters (i.e. the 10-9 and 11-10 clusters), the relative uptake

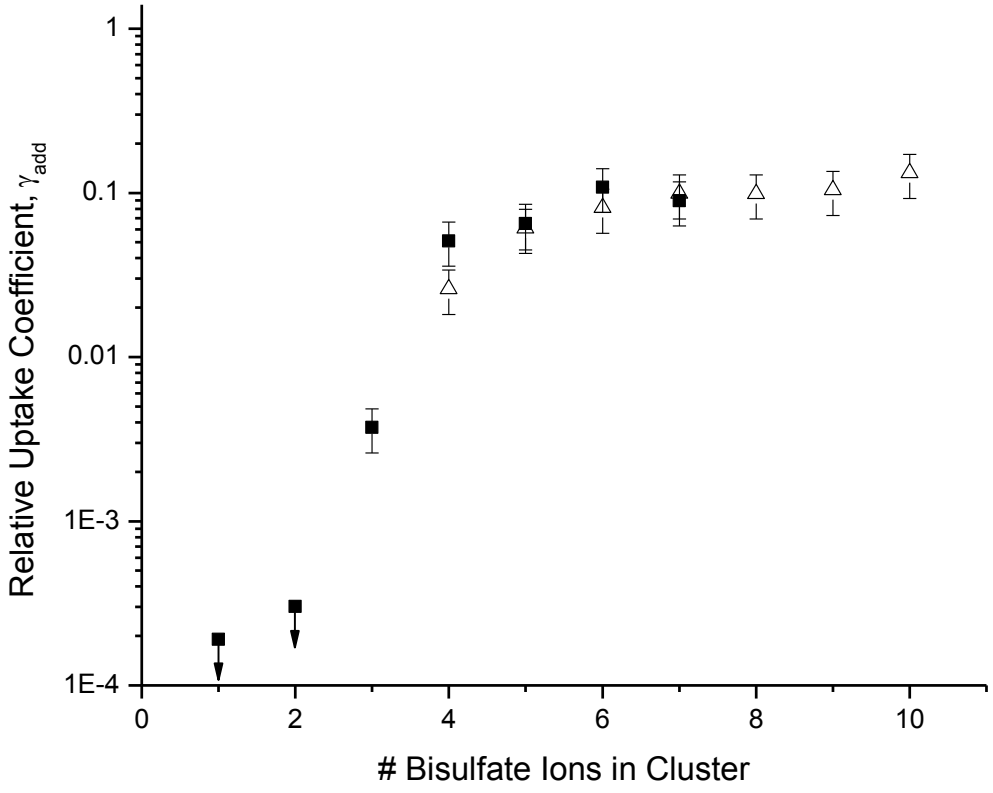

Figure 4.4: A plot of relative uptake coefficients for the addition of a DMA molecule as a function of dimethylammonium bisulfate cluster size. Filled squares represent values determined through the direct analysis of a dimethylammonium bisulfate cluster. Empty triangles represent values determined through the exposure of ammonium bisulfate to DMA. Arrows pointing downward from data points indicate that addition was not observed, so maximum possible values are reported.

Table 4.3: Pseudo first order rate constants, second order rate constants, and relative uptake coefficients for the addition of DMA to a dimethylammonium bisulfate cluster introduced directly into the instrument by electrospray. Relative uptake coefficients are determined relative to the fastest step for that cluster's substitution reaction. DMA gas pressure was $2.4 \pm 0.5 \times 10^{-8}$ torr for all clusters. The "<" sign indicates that no product was detected; maximum rates were determined based upon the noise levels in the spectra.

	Pseudo First Order Rate Constant (s^{-1})	Second Order Rate Constant ($cm^3 \cdot molec^{-1} \cdot s^{-1}$)	Relative Uptake Coefficient, γ_{add}
2-1 Cluster			
$k_{add(1)}$	$< 1.9 \times 10^{-4}$	$< 2.2 \times 10^{-13}$	$< 1.9 \times 10^{-4}$
3-2 Cluster			
$k_{add(1)}$	$< 3.0 \times 10^{-4}$	$< 3.6 \times 10^{-13}$	$< 3.0 \times 10^{-4}$
4-3 Cluster			
$k_{add(1)}$	0.0037 ± 0.0007	$4.4 \pm 0.9 \times 10^{-12}$	0.004 ± 0.001
5-4 Cluster			
$k_{add(1)}$	0.086 ± 0.006	$1.0 \pm 0.2 \times 10^{-10}$	0.05 ± 0.02
$k_{add(2)}$	$< 8.0 \times 10^{-4}$	$< 9.9 \times 10^{-13}$	$< 5 \times 10^{-4}$
6-5 Cluster			
$k_{add(1)}$	0.06 ± 0.04	$6.6 \pm 1.3 \times 10^{-11}$	0.07 ± 0.02
$k_{add(2)}$	0.003 ± 0.002	$3.8 \pm 0.8 \times 10^{-12}$	0.004 ± 0.001
7-6 Cluster			
$k_{add(1)}$	0.107 ± 0.006	$1.3 \pm 0.3 \times 10^{-10}$	0.11 ± 0.03
$k_{add(2)}$	< 0.005	$< 6.4 \times 10^{-12}$	< 0.006
8-7 Cluster			
$k_{add(1)}$	0.090 ± 0.002	$1.1 \pm 0.2 \times 10^{-10}$	0.09 ± 0.03
$k_{add(2)}$	< 0.006	$< 6.9 \times 10^{-12}$	< 0.006

coefficient value for addition of DMA ($\gamma_{add} \approx 0.1$) is significantly greater than that for the final substitution step ($\gamma_{sub} < 10^{-2}$). Therefore, only the addition of DMA to the mostly substituted clusters (one ammonium ion remaining) is observed. It is notable that whenever a cluster was studied by both methods, the observed rate constants were similar in value, further suggesting that the rate constant values obtained from the sequential displacement reactions are the result of adequate statistical fits to pseudo first order kinetics.

The addition of a second DMA molecule was observed directly in one case, while for other clusters upper limits for this rate constant were determined. These values are provided in Table 4.3. For the 5-4 cluster, the relative uptake coefficient for the addition of a second DMA molecule was $< 5 \pm 2 \times 10^{-4}$, which is two orders of magnitude below that observed for the first addition ($5 \pm 2 \times 10^{-2}$). A second DMA addition was directly observed for the 6-5 cluster ($\gamma = 4 \pm 1 \times 10^{-3}$). The relative uptake coefficient for the second DMA addition is more than an order of magnitude slower than that for the first DMA addition ($7 \pm 2 \times 10^{-2}$). While a second DMA addition was not observed for the 7-6 and 8-7 clusters, upper limits for the relative uptake coefficient are similar to that observed for the 6-5 cluster ($\gamma < 6 \pm 2 \times 10^{-3}$).

These results suggest that dimethylammonium bisulfate is the favored composition for small (2-1 and 3-2) clusters, while di-dimethylammonium sulfate becomes more favorable as the cluster size increases.

4.3.3 Ammonia Addition onto Ammonium and Dimethylammonium Bisulfate Clusters

The addition of ammonia onto both ammonium and dimethylammonium bisulfate clusters was also investigated in this work. For both types of clusters, ammonia was

never observed to add onto an existing cluster. Upper limits for the relative uptake coefficients were determined by fitting to the noise and those rate constants were compared to the fastest observed substitution (with DMA) rate constant for a specific cluster. Upper limits for rate constants and relative uptake coefficients for the addition of ammonia to ammonium bisulfate and dimethylammonium bisulfate are summarized in Tables 4.4 and 4.5, respectively. In the case of ammonium bisulfate, the upper limit for the relative uptake coefficient ranged from $1.1 \pm 0.3 \times 10^{-5}$ to $8.3 \pm 2.5 \times 10^{-3}$, depending on the amount of noise in the spectrum. For dimethylammonium bisulfate exposed to ammonia gas, the upper limit for ammonia addition ranged from $7.8 \pm 2.3 \times 10^{-6}$ in the case of high signal-to-noise (S/N) to $1.1 \pm 0.3 \times 10^{-3}$ in the case of low S/N. Also notable is that for dimethylammonium bisulfate clusters reacting with ammonia gas, ammonia was never observed to displace DMA in the cluster. Table 4.6 provides upper limits for the rate constants and relative uptake coefficients for the displacement of DMA by ammonia. Upper limits for relative uptake coefficients ranged from $1.6 \pm 0.5 \times 10^{-5}$ for high S/N to $8.9 \pm 2.4 \times 10^{-4}$ for low S/N. These observations indicate that over the range of cluster sizes studied (2-1 to 12-11 ammonium bisulfate clusters), ammonium bisulfate is the favored cluster composition. Additionally, over the range of dimethylammonium bisulfate clusters studied (2-1 to 6-5 clusters) ammonia will neither displace DMA nor will it add onto the cluster.

4.3.4 Amine-Ammonia Exchange in 20-30 nm Diameter Nanoparticles

This chapter thus far has discussed in detail measurements of the size-dependent reactivity of ammonium bisulfate clusters with DMA. Small clusters react to completion because all ammonium ions are on the surface of the cluster, whereas

Table 4.4: Pseudo first order rate constants, second order rate constants, and relative uptake coefficients for the addition of ammonia to ammonium bisulfate clusters. Relative uptake coefficients are determined relative to the fastest step for that cluster's substitution reaction with DMA. Ammonia gas pressure was $1.0 \pm 0.2 \times 10^{-7}$ torr. No product was detected in any of these experiments; the given values are the maximum possible values based on noise levels in the spectra.

	Pseudo First Order Rate Constant (s^{-1})	Second Order Rate Constant ($cm^3 \cdot molec^{-1} \cdot s^{-1}$)	Relative Uptake Coefficient, γ_{add}
2-1 Cluster k_{add}	$< 5.3 \times 10^{-4}$	$< 1.5 \times 10^{-13}$	$< 3.5 \times 10^{-4}$
3-2 Cluster k_{add}	$< 9.4 \times 10^{-5}$	$< 2.7 \times 10^{-14}$	$< 8.2 \times 10^{-5}$
4-3 Cluster k_{add}	$< 1.0 \times 10^{-4}$	$< 2.9 \times 10^{-14}$	$< 9.3 \times 10^{-5}$
5-4 Cluster k_{add}	$< 2.1 \times 10^{-5}$	$< 5.9 \times 10^{-15}$	$< 1.1 \times 10^{-5}$
6-5 Cluster k_{add}	$< 1.1 \times 10^{-4}$	$< 3.1 \times 10^{-14}$	$< 9.9 \times 10^{-5}$
7-6 Cluster k_{add}	$< 1.74 \times 10^{-3}$	$< 4.9 \times 10^{-13}$	$< 1.4 \times 10^{-3}$
8-7 Cluster k_{add}	$< 4.1 \times 10^{-4}$	$< 1.2 \times 10^{-13}$	$< 3.3 \times 10^{-4}$
9-8 Cluster k_{add}	$< 3.8 \times 10^{-4}$	$< 1.1 \times 10^{-13}$	$< 3.1 \times 10^{-4}$
10-9 Cluster k_{add}	$< 1.00 \times 10^{-3}$	$< 2.8 \times 10^{-13}$	$< 8.3 \times 10^{-3}$
11-10 Cluster k_{add}	$< 1.6 \times 10^{-3}$	$< 4.5 \times 10^{-13}$	$< 1.6 \times 10^{-3}$
12-11 Cluster k_{add}	$< 2.6 \times 10^{-3}$	$< 7.4 \times 10^{-13}$	$< 2.7 \times 10^{-3}$

Table 4.5: Pseudo first order rate constants, second order rate constants, and relative uptake coefficients for the addition of ammonia to dimethylammonium bisulfate clusters introduced directly by electrospray. Relative uptake coefficients are determined relative to the fastest step for that cluster's substitution reaction with DMA. Ammonia gas pressure was $1.0 \pm 0.2 \times 10^{-7}$ torr. No product was detected in any of these experiments; the given values are the maximum possible values based on noise levels in the spectra.

	Pseudo First Order Rate Constant (s^{-1})	Second Order Rate Constant ($cm^3 \cdot molec^{-1} \cdot s^{-1}$)	Relative Uptake Coefficient, γ_{add}
2-1 Cluster k_{add}	$< 4.5 \times 10^{-5}$	$< 1.3 \times 10^{-14}$	$< 3.0 \times 10^{-5}$
3-2 Cluster k_{add}	$< 1.2 \times 10^{-5}$	$< 3.4 \times 10^{-15}$	$< 1.0 \times 10^{-5}$
4-3 Cluster k_{add}	$< 8.5 \times 10^{-6}$	$< 2.4 \times 10^{-15}$	$< 7.8 \times 10^{-6}$
5-4 Cluster k_{add}	$< 4.4 \times 10^{-5}$	$< 1.3 \times 10^{-14}$	$< 3.6 \times 10^{-5}$
6-5 Cluster k_{add}	$< 1.2 \times 10^{-3}$	$< 3.4 \times 10^{-13}$	$< 1.1 \times 10^{-3}$

Table 4.6: Pseudo first order rate constants, second order rate constants, and relative uptake coefficients for displacement of DMA by ammonia in dimethylammonium bisulfate clusters. Relative uptake coefficients are determined relative to the fastest step for that cluster's substitution reaction with DMA. Ammonia gas pressure was $1.0 \pm 0.2 \times 10^{-7}$ torr. No product was detected in any of these experiments; the given values are the maximum possible values based on noise levels in the spectra.

	Pseudo First Order Rate Constant (s^{-1})	Second Order Rate Constant ($cm^3 \cdot molec^{-1} \cdot s^{-1}$)	Relative Uptake Coefficient, γ_{sub}
2-1 Cluster[a]			
k_1	$< 4.1 \times 10^{-4}$	$< 1.3 \times 10^{-13}$	$< 8.7 \times 10^{-5}$
3-2 Cluster[a]			
k_1	$< 5.0 \times 10^{-4}$	$< 3.8 \times 10^{-14}$	$< 3.4 \times 10^{-4}$
4-3 Cluster			
k_1	$< 1.7 \times 10^{-5}$	$< 4.8 \times 10^{-15}$	$< 1.6 \times 10^{-5}$
5-4 Cluster			
k_1	$< 5.0 \times 10^{-5}$	$< 1.4 \times 10^{-14}$	$< 2.5 \times 10^{-5}$
6-5 Cluster			
k_1	$< 8.5 \times 10^{-4}$	$< 2.4 \times 10^{-13}$	$< 8.9 \times 10^{-4}$

[a]From Chapter 3.[1]

larger clusters do not react to completion because ammonium ions can become encapsulated in the core of the cluster, impeding exchange. This could suggest that as the particle size becomes larger, the relative importance of amine chemistry decreases.

One method to investigate this phenomenon further is to perform flow tube experiments where ammonium sulfate nanoparticles are mixed with a gas phase amine flow and the resulting nanoparticle composition is measured in a time-dependent manner with aerosol mass spectrometry. The reactivity of ammonium sulfate aerosol can then be studied as a function of relative humidity (and, therefore, aerosol phase). This experiment was attempted and the key challenges and main observations of those experiments are summarized below. Note that this work is still in progress. For the work described in this section, nanoparticle chemical composition was measured with the Nano Aerosol Mass Spectrometer (NAMS), which provides quantitative elemental composition of individual size-selected nanoparticles in the 10-30 nm diameter size range.[2-4]

Nanoparticles were generated by atomization of an aqueous ammonium sulfate solution (~0.5 mM) and sent through a particle dryer. Aerosol was then size-selected in an electrostatic classifier (model 3080, TSI, Inc. St. Paul, Minnesota), sent through a specially constructed, segmented flow tube similar to that used previously for the study of nitric acid uptake onto sodium chloride particles (see dissertation of Thomas D. Saul[5]).[6, 7] In the flow tube, aerosol mixes with gas phase DMA (from a calibrated permeation tube: Kin-Tek, LaMarque, Texas), the concentration of which was quantified using extractive electrospray.[8] DMA gas flow to or from the flow tube was via ¼" outer diameter Teflon tubing. At the exit of the flow tube, particles were sampled into a scanning mobility particle sizer (SMPS, condensation particle counter

model 3788, TSI, Inc., St. Paul, Minnesota) for size distribution analysis and into the NAMS for elemental analysis. Time-dependent, quantitative elemental composition would permit determination of uptake coefficients, as the relative fraction of carbon (from DMA) would increase as more DMA was incorporated into the nanoparticles. Note that aerosols entering the flow tube needed to pass through a Polonium-210 neutralizer in order to minimize particle loss. Also, at the outlet of the flow tube, a Nafion dryer was used to strip away the reactive amine before entering NAMS.

Several challenges arose in the execution of this experiment. First, atomization of "pure" ammonium sulfate produced aerosol that contained a small amount of carbon impurity. Note that this small impurity has also been observed by others.[9] Although this impurity could not be completely eliminated, it could be reduced substantially through careful cleaning of the setup. A second challenge was that silicone tubing in the setup apparently emitted vapors that interfered with the gas phase amine measurement and also possibly the particle composition measurement. Silicone tubing is known to be a source of contaminant vapors.[10, 11] In order to minimize this impact, all silicone tubing was removed from the setup. Wherever possible, ¼" outer diameter copper tubing was used. For the SMPS systems used, the silicone tubing was replaced with stainless steel. This change to metal tubing seemed to make a substantial difference, as the extractive electrospray mass spectra indicated that the impurity (around 59 *m/z*) was eliminated and gas phase DMA (at 46.5 *m/z*) and trimethylamine (at 60.1 *m/z*) appeared in greater abundance as each portion of the entire apparatus (flow tube, SMPS, etc.) was systematically investigated. Note that even silicone tubing in the SMPS setup used *before* introduction of DMA to the flow tube still resulted in an overwhelming contaminant signal that was inconveniently

close to that of the trimethylamine standard (making its identification as a contaminant challenging) and apparently overwhelmed all other ion signals from the amines (resulting in an inability to quantify them). Because of time constraints when performing these experiments, it was not confirmed whether the replacement of silicone tubing resulted in a decrease in NAMS-measured carbon contamination.

When size-selected ammonium sulfate aerosol was sent through the flow tube and ultimately into NAMS, N/S elemental ratios were close to 2, indicative of ammonium sulfate (2 NH_4^+: 1 SO_4^{-2}), and the carbon mole fraction was generally 2-5%, indicating little if any DMA. Upon introduction of DMA vapor to the flow tube, no change in nanoparticle composition was observed. The gas phase DMA concentration was increased, but no measured change in composition was observed. Eventually, air was blown over concentrated aqueous DMA solutions up to ~2.5×10^{-2} M, with no apparent change in elemental composition (i.e. no change in the carbon mole fraction). Eventually, the amine appeared to flood the system, resulting in a very large (~23%) measured carbon mole fraction, even when no DMA was introduced. It is possible that DMA was pumped away initially, trapped in the pump oil and waste lines, and managed to continuously recontaminate the system. Shortly after these measurements were performed, NAMS was taken to Lewes, Delaware, for a field campaign, and all tubing and pump oil were changed, which eliminated this contamination. Initially, 20 nm diameter nanoparticles were investigated. Once no reaction was observed with 20 nm diameter nanoparticles, 30 nm diameter nanoparticles were then investigated. Again, no exchange was apparent from the mass spectra.

These results appear to imply that for particles in this size range, amine-ammonia exchange is inhibited and proceeds at a rate that is several orders of magnitude slower than for small clusters. The small amount of carbon measured is consistent with only surface exchange. However, this has not been rigorously investigated. Additionally, it is not fully apparent why this would be the case, as relative humidity was ~80-90%, well above the deliquescence point for ammonium sulfate. In other words, the aerosol was a liquid droplet, which one may expect to react more easily with DMA than a solid particle. Note that preliminary experiments by other group members where polydisperse ammonium sulfate aerosol was reacted with DMA in the flow tube, collected on a filter, and analyzed by time-of-flight secondary ion mass spectrometry (TOF-SIMS) indicated that after reaction a substantial amount of ammonia remained in these (liquid) particles, further providing support that exchange is very slow in larger particles.

Future work will require better quantification of the gas phase DMA concentration (made possible by the systematic removal of all silicone tubing). Additionally, it will be necessary to examine reactivity in larger particles. This can be accomplished by using the Rapid Single Particle Mass Spectrometer (RSMS)[12] but equipping it with the same ionization setup as in NAMS (Nd:YAG laser tightly focused to create a plasma) rather than simple laser desorption ionization at 193 nm with an ArF excimer laser. In this manner, quantitative elemental composition of particles on the order of 50 nm or larger can be obtained. Such studies would be useful to better understanding the limitations to amine uptake onto nanoparticles.

4.4 Atmospheric Implications

Much effort has been devoted to characterizing the composition of the stable critical cluster in aerosol nucleation,[13-19] which determines the particle nucleation rate. However, comparatively little work has been done to elucidate potential size-dependent reaction mechanisms from the critical cluster size up to the smallest detectable particle diameter (3 nm) and beyond, which is an equally important subject, as cluster growth governs what fraction of the nuclei form detectable particles and possibly lead to cloud condensation nucleus production. This study examined the size-dependent chemistry of clusters from the probable critical cluster size (1-2 acid molecules) to much larger clusters (up to 11 acid molecules), all of which fall into the ambient sub-3 nm diameter pool of clusters.[20]

Ambient amine levels can vary considerably depending upon proximity to the amine source, though they are usually orders of magnitude lower than ambient ammonia levels. Major amine sources include animal husbandry,[21] biomass burning,[22] and the marine environment.[23] In proximity to a source, amine levels can be greater than 1 ppb and can even exceed 100 ppb;[24] however, amine levels can be orders of magnitude lower away from a source (e.g. low ppt). For a 1 nm diameter cluster exposed to 1 ppb amine (near a source), the collision rate is on the order of 30 s^{-1}, suggesting that complete displacement of ammonia by amine would occur within 1 sec. Away from an amine source (low ppt level), complete exchange would still occur within seconds to minutes. On the other hand, displacement of amine by ammonia would not be expected to occur, despite higher ammonia concentrations and a correspondingly greater collision rate. Therefore, these findings provide additional evidence to suggest that ambient sub-3 nm diameter bisulfate clusters will be ammonium salts, rather than ammonium salts, even if they were initially formed as

ammonium salts. The results of this work also illustrate that the rate and pathway of amine incorporation into ambient particles change with particle size. Preliminary work examining amine exchange into much larger 20-30 nm diameter ammonium sulfate nanoparticles suggests that amine uptake is hindered, which is consistent with the core-shell chemistry observed for the molecular cluster studies. This observation suggests that as the particle size becomes larger, the importance of amine chemistry relative to ammonia chemistry decreases. Additional work is needed to fully characterize these processes and to explore the possible role of particulate water.

These findings are also of interest to the broader field of ion-molecule chemistry. While gas-phase solvation of ions, such as hydration of the sulfate anion, have been studied,[25, 26] reactions of "ionic" (salt) clusters are poorly understood.[27] The work presented here, along with that from a previous study (see Chapter 3),[1] are the first systematic studies of such processes.

4.5 References

1. Bzdek, B. R.; Ridge, D. P.; Johnston, M. V., Amine exchange into ammonium bisulfate and ammonium nitrate nuclei. *Atmos. Chem. Phys.* **2010,** *10* (8), 3495-3503.

2. Pennington, M. R.; Johnston, M. V., Trapping charged nanoparticles in the nano aerosol mass spectrometer (NAMS). *Int. J. Mass Spectrom.* **2012,** *311* (1), 64-71.

3. Wang, S. Y.; Johnston, M. V., Airborne nanoparticle characterization with a digital ion trap-reflectron time of flight mass spectrometer. *Int. J. Mass Spectrom.* **2006,** *258* (1-3), 50-57.

4. Wang, S. Y.; Zordan, C. A.; Johnston, M. V., Chemical characterization of individual, airborne sub-10-nm particles and molecules. *Anal. Chem.* **2006,** *78* (6), 1750-1754.

5. Saul, T. D. Reactive Uptake of Nitric Acid onto Sub-Micron Sea Salt Across a Wide Range of Relative Humidities. University of Delaware, Newark, DE, 2010.

6. Saul, T. D.; Tolocka, M. P.; Johnston, M. V., Reactive uptake of nitric acid onto sodium chloride aerosols across a wide range of relative humidities. *J. Phys. Chem. A* **2006,** *110* (24), 7614-7620.

7. Tolocka, M. P.; Saul, T. D.; Johnston, M. V., Reactive uptake of nitric acid into aqueous sodium chloride droplets using real-time single-particle mass spectrometry. *J. Phys. Chem. A* **2004,** *108* (14), 2659-2665.

8. Horan, A. J.; Gao, Y.; Hall, W. A.; Johnston, M. V., Online characterization of particles and gases with an ambient electrospray ionization source. *Anal. Chem.* **2012,** *84* (21), 9253-9258.

9. Zhou, S.; Shiraiwa, M.; McWhinney, R. D.; Poschl, U.; Abbatt, J. P. D., Kinetic limitations in gas-particle reactions arising from slow diffusion in secondary organic aerosol. *Faraday Discuss.* **2013,** *165* (1), 391-406.

10. Timko, M. T.; Yu, Z. H.; Kroll, J. H.; Jayne, J. T.; Worsnop, D. R.; Miake-Lye, R. C.; Onasch, T. B.; Liscinsky, D.; Kirchstetter, T. W.; Destaillats, H.; Holder, A. L.; Smith, J. D.; Wilson, K. R., Sampling artifacts from conductive silicone tubing. *Aerosol Sci. Technol.* **2009,** *43* (9), 855-865.

11. Yu, Y.; Alexander, M. L.; Perraud, V.; Bruns, E. A.; Johnson, S. N.; Ezell, M. J.; Finlayson-Pitts, B. J., Contamination from electrically conductive silicone tubing during aerosol chemical analysis. *Atmos. Environ.* **2009,** *43* (17), 2836-2839.

12. Bzdek, B. R.; Pennington, M. R.; Johnston, M. V., Single particle chemical analysis of ambient ultrafine aerosol: A review. *J. Aerosol Sci.* **2012,** *52* (1), 109-120.

13. Anderson, K. E.; Siepmann, J. I.; McMurry, P. H.; VandeVondele, J., Importance of the number of acid molecules and the strength of the base for double-ion formation in $(H_2SO_4)_m \cdot Base \cdot (H2O)_6$ clusters. *J. Am. Chem. Soc.* **2008,** *130* (43), 14144-14147.

14. Kuang, C.; McMurry, P. H.; McCormick, A. V.; Eisele, F. L., Dependence of nucleation rates on sulfuric acid vapor concentration in diverse atmospheric locations. *J. Geophys. Res.-Atmos.* **2008,** *113* (D10), D10209, doi: 10.1029/2007jd009253.

15. Kulmala, M.; Lehtinen, K. E. J.; Laaksonen, A., Cluster activation theory as an explanation of the linear dependence between formation rate of 3nm particles and sulphuric acid concentration. *Atmos. Chem. Phys.* **2006,** *6* 787-793.

16. Metzger, A.; Verheggen, B.; Dommen, J.; Duplissy, J.; Prevot, A. S. H.; Weingartner, E.; Riipinen, I.; Kulmala, M.; Spracklen, D. V.; Carslaw, K. S.; Baltensperger, U., Evidence for the role of organics in aerosol particle formation under atmospheric conditions. *Proc. Natl. Acad. Sci. U.S.A.* **2010,** *107* (15), 6646-6651.

17. Nieminen, T.; Manninen, H. E.; Sihto, S. L.; Yli-Juuti, T.; Mauldin, R. L.; Petaja, T.; Riipinen, I.; Kerminen, V. M.; Kulmala, M., Connection of sulfuric acid to atmospheric nucleation in boreal forest. *Environ. Sci. Technol.* **2009,** *43* (13), 4715-4721.

18. Sipila, M.; Berndt, T.; Petaja, T.; Brus, D.; Vanhanen, J.; Stratmann, F.; Patokoski, J.; Mauldin, R. L.; Hyvarinen, A. P.; Lihavainen, H.; Kulmala, M., The role of sulfuric acid in atmospheric nucleation. *Science* **2010,** *327* (5970), 1243-1246.

19. Zhang, R. Y.; Wang, L.; Khalizov, A. F.; Zhao, J.; Zheng, J.; McGraw, R. L.; Molina, L. T., Formation of nanoparticles of blue haze enhanced by anthropogenic pollution. *Proc. Natl. Acad. Sci. U.S.A.* **2009,** *106* (42), 17650-17654.

20. Kulmala, M.; Riipinen, I.; Sipila, M.; Manninen, H. E.; Petaja, T.; Junninen, H.; Dal Maso, M.; Mordas, G.; Mirme, A.; Vana, M.; Hirsikko, A.; Laakso, L.; Harrison, R. M.; Hanson, I.; Leung, C.; Lehtinen, K. E. J.; Kerminen, V. M.,

Toward direct measurement of atmospheric nucleation. *Science* **2007,** *318* (5847), 89-92.

21. Schade, G. W.; Crutzen, P. J., Emission of aliphatic amines from animal husbandry and their reactions: Potential source of N_2O and HCN. *J. Atmos. Chem.* **1995,** *22* (3), 319-346.

22. Lobert, J. M.; Scharffe, D. H.; Hao, W.; Kuhlbusch, T. A.; Warneck, P.; Crutzen, P. J., Experimental evaluation of biomass burning emissions: nitrogen and carbon containing compounds. In *Global Biomass Burning: Atmospheric, Climatic and Biospheric Implications*, Levine, J. S., Ed. MIT Press: Cambridge, MA, 1991.

23. Van Neste, A.; Duce, R. A.; Lee, C., Methylamines in the marine atmosphere. *Geophys. Res. Lett.* **1987,** *14* (7), 711-714.

24. Rabaud, N. E.; Ebeler, S. E.; Ashbaugh, L. L.; Flocchini, R. G., Characterization and quantification of odorous and non-odorous volatile organic compounds near a commercial dairy in California. *Atmos. Environ.* **2003,** *37* (7), 933-940.

25. Blades, A. T.; Kebarle, P., Sequential hydration energies of the sulfate ion, from determinations of the equilibrium constants for the gas-phase reactions: $SO_4(H_2O)_n^{2-} = SO_4(H_2O)_{n-1}^{2-} + H_2O$. *J. Phys. Chem. A* **2005,** *109* (37), 8293-8298.

26. Wong, R. L.; Williams, E. R., Dissociation of $SO_4^{2-}(H_2O)_n$ clusters, n=3-17. *J. Phys. Chem. A* **2003,** *107* (50), 10976-10983.

27. Wu, R. H.; McMahon, T. B., Structures, energetics, and dynamics of gas phase ions studied by FTICR and HPMS. *Mass Spectrom. Rev.* **2009,** *28* (4), 546-585.

Chapter 5

REACTIVITY OF POSITIVELY-CHARGED AMMONIUM METHANESULFONATE AND NEGATIVELY-CHARGED SULFURIC ACID CLUSTERS WITH DIMETHYLAMINE GAS

5.1 Introduction

Chapters 3 and 4 examined the reactivity of positively-charged bisulfate and nitrate clusters. For these clusters, the dominant mechanism of amine incorporation was by substitution for another base. In this chapter, the goal is to study the reactivity of two different types of clusters with ammonia and dimethylamine. The first type consists of positively-charged clusters containing methanesulfonic acid. These clusters are interesting because methanesulfonic acid can be considered a more "organic" acid, so a study of these clusters would provide information on how clusters with organic acids may impact reactivity. Additionally, these clusters tend to be more acidic. The second type of cluster consists of negatively-charged clusters containing sulfuric acid. These clusters are interesting because their composition is very different from positively-charged clusters: they are extremely acidic (see Chapter 2). Similar to the previous chapters, their reactivity with dimethylamine and ammonia gases is investigated using Fourier transform ion cyclotron resonance mass spectrometry (FTICR-MS). The results expand upon our understanding of the reactivity of these clusters. Bases can incorporate into clusters via two mechanisms: 1) substitution of one base for another and 2) addition to the cluster to neutralize acid. In every instance, addition is always slower than substitution. These observations imply that in the

atmosphere, small clusters 1) are likely to be aminium salts, rather than ammonium salts and 2) may grow to larger sizes more efficiently by addition of dimethylamine than by addition of ammonia.

5.2 Experimental Section

The experimental setup is similar to that in previous work examining amine exchange into ammonium bisulfate and ammonium nitrate clusters (see Chapters 3 and 4).[1, 2] For methanesulfonate clusters, 1.0 mM ammonium methanesulfonate and 1.0 mM dimethylammonium methanesulfonate solutions each in 50/50 methanol/water were prepared by combining solutions of ammonia (Acros, Geel, Belgium) and methanesulfonic acid (Lancaster, Ward Hill, Massachusetts) or dimethylamine (Fluka, St. Louis, Missouri) and methanesulfonic acid. For sulfuric acid clusters, 1.0 mM solutions of ammonium sulfate (Aldrich, St. Louis, Missouri) and 1.0 mM dimethylammonium sulfate were prepared in 50/50 methanol/water. Singly-charged clusters were introduced to a 7T Bruker apex-Qe FTICR-MS by electrospray of the desired solution. Electrospray produces an array of clusters with different compositions. A specific cluster was isolated by mass selection and accumulation in a quadrupole. Ions were then transferred to the ICR cell where they were exposed to a constant pressure of dimethylamine gas (Matheson Tri-Gas, Basking Ridge, New Jersey) at $2.4 \pm 0.5 \times 10^{-8}$ torr that was introduced to the cell via a leak valve. Isolated clusters were exposed to dimethylamine gas in order to examine the mechanisms and kinetics of dimethylamine incorporation to the clusters. Additionally, some clusters were exposed to ammonia gas (Matheson Tri-Gas, Basking Ridge, New Jersey) at $1.0 \pm 0.2 \times 10^{-7}$ torr to determine the mechanisms and kinetics of ammonia incorporation into these clusters. Electrospray of the dimethylammonium sulfate solution in negative

mode produced complicated spectra due to substitution by sodium for dimethylamine. Negatively-charged dimethylammonium bisulfate clusters were unstable upon mass selection; therefore, no kinetic data were obtained for exposure of these clusters to dimethylamine or ammonia gas.

A mass spectrum of ions in the ICR cell can be obtained at a specific trapping time. FTICR-MS provides high resolving power and high accuracy mass-to-charge (*m/z*) measurements, allowing for the assignment of unique elemental formulae to reactant and product ions. A plot of ion abundance as a function of trapping time (reaction profile) reveals the progress of the sequential reactions. In some of the more exothermic reactions, the reactant molecule induces a more complicated decomposition rather than displacement alone. As discussed later, these reaction-induced decomposition channels do not significantly affect quantitative kinetic analysis of the predominant simple displacements. All data were fit to the kinetic models using the simplex method of non-linear fitting embodied in the Solver function of the Microsoft Excel program. Second order rate constants were determined from gas pressure measurements in the ICR cell, as discussed elsewhere (see Chapters 3 and 4).[1, 2] Collisional rate constants were determined using the capture collision model (see Chapter 3).[3]

5.3 Results and Discussion

This chapter examines reactions of two types of clusters. The first series of clusters discussed here consists of positively-charged methanesulfonate salt clusters. The second series of clusters discussed here consists of negatively-charged sulfuric acid salt clusters. An examination of the mechanisms and kinetics of amine and

ammonia incorporation into these clusters is beneficial because in general these clusters tend to be substantially more acidic than those examined in Chapters 3 and 4.

5.3.1 Reactions of Positively-Charged Ammonium Methanesulfonate Clusters

5.3.1.1 Amine Substitution into Ammonium Methanesulfonate Clusters

Electrospray of an ammonium methanesulfonate solution produces a wide array of ammonium methanesulfonate clusters, which can be described by the number of cations, anions, and additional species they contain. Clusters described in this work are referred to in the form *a*(*b*)-*c*-*d*, where *a* is the number of ammonium ions initially in the unreacted cluster, *b* represents the number of ammonium ions that have been displaced by dimethylamine, *c* represents the number of methanesulfonate ions in the cluster, and *d* (indicated when nonzero) represents the number of unneutralized methanesulfonic acid molecules attached to the cluster. For this experiment, electrospray of an ammonium methanesulfonate solution produced mainly singly-charged 2(0)-1, 3(0)-2, 4(0)-3, and 5(0)-4, 6(0)-5, and 7(0)-6 clusters. However, depending upon instrumental parameters, isolation of these clusters sometimes resulted in isolation of clusters containing unneutralized methanesulfonic acid. Additionally, as discussed in Chapter 4,[2] mass selection of a specific cluster usually resulted in isolation of a smaller cluster produced by spontaneous dissociation of one ammonium methanesulfonate neutral. Displacement in an ammonium methanesulfonate cluster containing an unneutralized methanesulfonic acid molecule can be described by Scheme 1. Note that for the displacement reactions, the unneutralized methanesulfonic acid molecule can be considered a spectator, as it is still observed (unaltered) at the completion of the reaction.

SCHEME 1

$$[(NH_4^+)_x(CH_3SO_3^-)_{x-1}(CH_3SO_3H)]^+ + (CH_3)_2NH \xrightarrow{k_1}$$

$$[(NH_4^+)_{x-1}((CH_3)_2NH_2^+)(CH_3SO_3^-)_{x-1}(CH_3SO_3H)]^+ + NH_3 \quad \text{(a)}$$

$$[(NH_4^+)_{x-1}((CH_3)_2NH_2^+)(CH_3SO_3^-)_{x-1}(CH_3SO_3H]^+ + (CH_3)_2NH \xrightarrow{k_2}$$

$$[(NH_4^+)_{x-2}((CH_3)_2NH_2^+)_2(CH_3SO_3^-)_{x-1}(CH_3SO_3H)]^+ + NH_3 \quad \text{(b)}$$

$$[(NH_4^+)_{x-2}((CH_3)_2NH_2^+)_2(CH_3SO_3^-)_{x-1}(CH_3SO_3H)]^+ + (CH_3)_2NH \xrightarrow{k_3} \cdots \xrightarrow{k_x}$$

$$[((CH_3)_2NH_2^+)_x(CH_3SO_3^-)_{x-1}(CH_3SO_3H)]^+ + NH_3 \quad \text{(c)}$$

Figure 5.1 presents mass spectra for $[(NH_4^+)_2(CH_3SO_3^-)(CH_3SO_3H)]^+$ (the "2-1-1" cluster because it contains two ammonium ions, one methanesulfonate ion, and one neutral methanesulfonic acid molecule) exposed to dimethylamine gas at a) 0 sec and b) 7 sec reaction time. At 0 sec reaction time (Figure 5.1a), the predominant peak is that of 2(0)-1-1 ammonium methanesulfonate at 227.037 *m/z*, for which mass selection was performed in the quadrupole. Additionally present is a small amount of the first substitution product (2(1)-1-1) at 255.068 *m/z* which results from residual dimethylamine in the instrument. At 7 sec reaction time (Figure 5.1b), almost all ammonium ions have been displaced by dimethylamine in the cluster. The predominant product ion is the fully displaced cluster (2(2)-1-1) at 283.099 *m/z*; however, a small amount of the 2(1)-1-1 cluster remains. Finally, signal from a 3(3)-2 dimethylammonium methanesulfonate cluster is observed at 328.157 *m/z*. This cluster arises from the addition of a dimethylamine molecule to the 2(2)-1-1 cluster in order to neutralize the remaining acid, effectively causing the 2(2)-1-1 cluster to grow to a

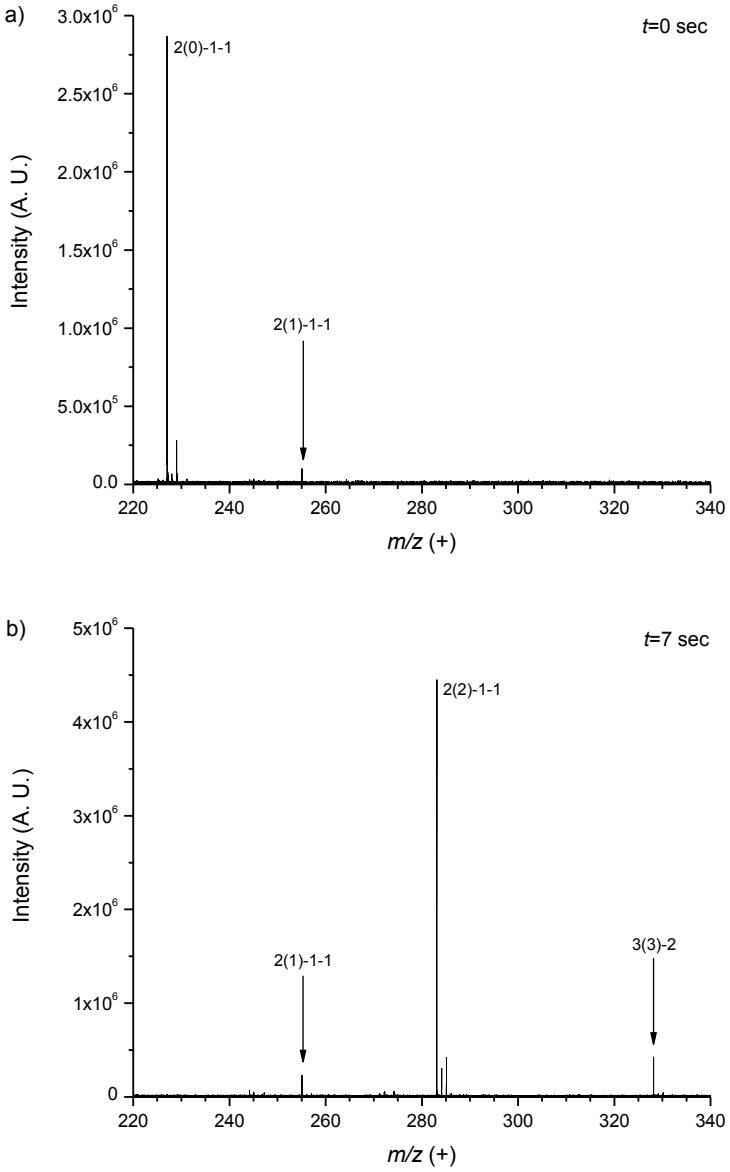

Figure 5.1: Mass spectra for the reaction of 2-1-1 ammonium methanesulfonate with dimethylamine at a) t=0 sec and b) t=7 sec reaction time. Notation for cluster ions is in the form $a(b)$-c-d, where a represents the number of ammonium ions initially in the unreacted cluster, b represents the number of ammonium ions that have been displaced by dimethylamine, c represents the number of methanesulfonate ions in the cluster, and d represents the number of unneutralized methanesulfonic acid molecules that are also present in the cluster.

larger size cluster, 3(3)-2. This addition of dimethylamine to the 2(2)-1-1 cluster is described by Scheme 2.

SCHEME 2

$$[((CH_3)_2NH_2^+)_2(CH_3SO_3^-)(CH_3SO_3H)]^+ + (CH_3)_2NH \xrightarrow{k_{add}}$$

$$[((CH_3)_2NH_2^+)_3(CH_3SO_3^-)_2]^+$$

A reaction profile is created by plotting the relative abundance of each reaction step against exposure time. Pseudo first order kinetics applies to these reactions because the pressure of the reactant gas was constant during the experiment. A fit of the reaction profile to pseudo first order kinetics allows for quantitative determination of the rate constants for these sequential reactions. Integration of the rate equations for a series of *j* sequential pseudo first order reactions gives:

$$A_i = k_1 k_2 \ldots k_{i-1} A_0 \left(\sum_{j=1}^{i} \alpha_j e^{-k_j t} \right) \tag{1}$$

where A_i is the relative intensity of the i^{th} product in the reaction sequence; k_1, k_2, k_3, etc. represent the pseudo first order rate constants for the sequential reaction steps; and:

$$\alpha_j = \frac{1}{\prod_{n=1}^{i} (k_n - k_j)} \qquad \text{where } n \neq j \tag{2}$$

Figure 5.2 presents the reaction profile (symbols) and statistical fit to pseudo first order kinetics (lines) for the 2-1-1 cluster exposed to dimethylamine gas. As was evident in the mass spectrum, at 0 sec reaction time, the 2(0)-1-1 cluster is the predominant ion observed. However, with increasing dimethylamine exposure time,

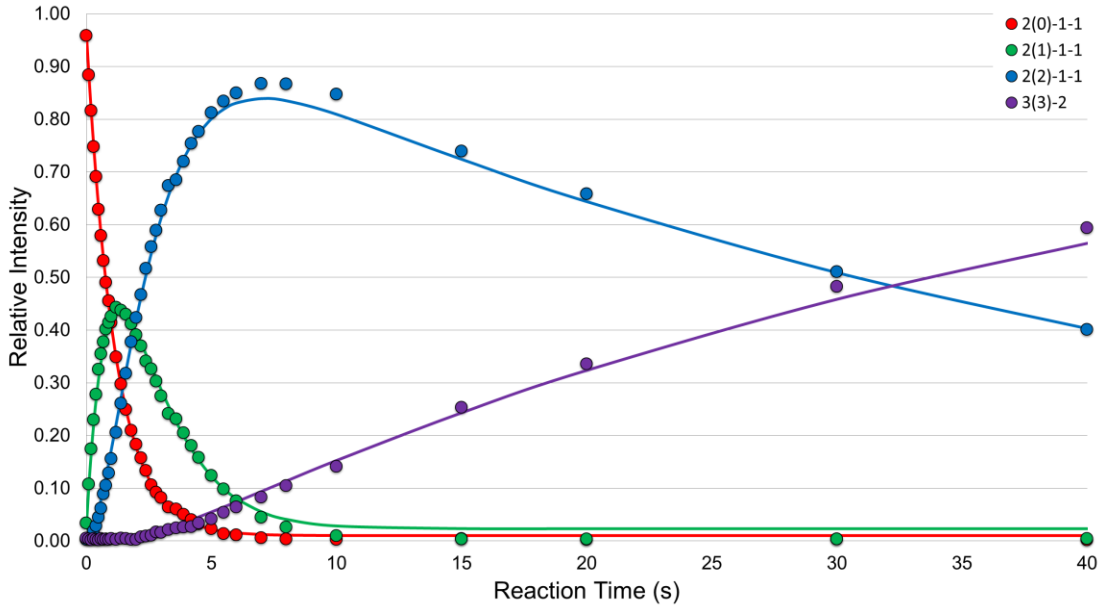

Figure 5.2: Reaction profile (symbols) and statistical fit to pseudo first order kinetics (lines) for the reaction of the 2-1-1 ammonium methanesulfonate cluster to dimethylamine. Each step in the sequential reactions is represented by a different color, as indicated in the legend. Cluster ion notation is the same as in Fig. 5.1. $P_{dimethylamine}$: $2.4 \pm 0.5 \times 10^{-8}$ torr.

ammonia is sequentially displaced by dimethylamine to produce the 2(1)-1-1 and 2(2)-1-1 clusters. After complete substitution by dimethylamine to form the 2(2)-1-1 cluster, an additional dimethylamine molecule is observed to slowly neutralize the remaining methanesulfonic acid, effectively forming the 3(3)-2 dimethylammonium methanesulfonate cluster. For the reaction of the 2-1-1 ammonium methanesulfonate cluster with dimethylamine, pseudo first order rate constants for the two substitution steps were $k_1 = 0.79 \pm 0.08$ s^{-1} and $k_2 = 0.58 \pm 0.06$ s^{-1}. For the addition step (k_{add}), the pseudo first order rate constant was $2.2 \pm 0.2 \times 10^{-2}$ s^{-1}.

Second order rate constants and reactive uptake coefficients were determined in the manner described in Chapter 3.[1] The clusters examined in this work are relatively small and likely have collisional radii < 10 Å. Therefore, the capture collision model, which assumes an ion-induced dipole force between the ion (salt cluster) and molecule (reactant gas) that results in a spiral inward towards zero separation, was used to determine the collisional rate constant.[3] For the 2-1-1 ammonium methanesulfonate cluster, uptake coefficients for substitution were $\gamma_1 = 0.68 \pm 0.20$ and $\gamma_2 = 0.51 \pm 0.15$, whereas the uptake coefficient for the addition step was $\gamma_{add} = 2.0 \pm 0.6 \times 10^{-2}$. These values indicate that the substitution steps are quite fast, but the addition (acid neutralization) step is more than an order of magnitude slower than substitution.

This same analysis was performed on several ammonium methanesulfonate clusters. The substitution kinetics in clusters of various sizes are discussed first, followed by discussion of the kinetics of addition to the clusters. Table 5.1 presents reactive uptake coefficients for the substitution reaction steps in 2-1 to 6-5 ammonium

Table 5.1: Reactive uptake coefficients for the substitution reaction steps of ammonium methanesulfonate clusters with dimethylamine.

Cluster	γ_1	γ_2	γ_3	γ_4	γ_5	γ_6
2-1	0.88 ± 0.26	0.81 ± 0.24				
2-1-1	0.68 ± 0.20	0.51 ± 0.15				
3-2	0.56 ± 0.17	0.41 ± 0.12	0.35 ± 0.11			
5-4	0.58 ± 0.17	0.61 ± 0.18	0.56 ± 0.17	0.48 ± 0.14	0.21 ± 0.06	
6-5	0.57 ± 0.17	0.53 ± 0.16	0.55 ± 0.17	0.55 ± 0.17	0.47 ± 0.14	0.21 ± 0.06

methanesulfonate clusters. Also included are reactive uptake coefficient values for the substitution steps in the 2-1-1 cluster. Note that no information is provided for the 4-3 ammonium methanesulfonate cluster nor for ammonium methanesulfonate clusters containing an additional unneutralized methanesulfonic acid larger than the 2-1-1 cluster, as it was not possible to isolate and react these clusters in appreciable intensity in the ICR cell. In general, reactive uptake coefficients were very fast, indicating a high probability of exchange when the cluster collided with an amine molecule. Also notable is that for the 2-1 and the 2-1-1 clusters, the reactive uptake coefficients are within experimental error of each other. One trend observed in most clusters is a slow decrease in the magnitude of the reaction probability for each subsequent substitution step in a cluster, although in most cases the values are still very similar and fast. However, for the 5-4 and 6-5 ammonium methanesulfonate clusters, the rate of the final substitution step decreases by more than a factor of two. Such observations suggest that these clusters are large enough to have a structure that could impede access of an incoming dimethylamine molecule to the final ammonium ion, either as a result of the initial structure of the ammonium methanesulfonate cluster or from structural changes in the cluster resulting from sequential amine substitution. Such a phenomenon has been previously observed in bisulfate clusters (see Chapter 4);[2] however, since no clusters larger than the 6-5 cluster were efficiently isolated and no known molecular structure for these clusters exists, it is not possible to determine exactly the cause of this decrease in the final substitution step. Pseudo first order rate constants, second order rate constants, and reactive uptake coefficients for all examined reactions of ammonium methanesulfonate clusters with dimethylamine are provided in Table 5.2.

Table 5.2: Pseudo first order rate constants, second order rate constants, and reactive uptake coefficients for all reactions of ammonium methanesulfonate and dimethylammonium methanesulfonate clusters exposed to dimethylamine or ammonia.

A. Exposure of Ammonium Methanesulfonate Clusters to Dimethylamine[a] (Substitution/Addition)			
Cluster	Pseudo First Order Rate Constant (s^{-1})	Second Order Rate Constant ($cm^3 \cdot molec^{-1} \cdot s^{-1}$)	Reactive Uptake Coefficient (γ)
2-1 Cluster			
k_1	1.07 ± 0.14	$1.2 \pm 0.4 \times 10^{-9}$	0.88 ± 0.26
k_2	0.97 ± 0.14	$1.1 \pm 0.3 \times 10^{-9}$	0.81 ± 0.24
2-1-1 Cluster			
k_1	0.79 ± 0.08	$9.0 \pm 2.7 \times 10^{-10}$	0.68 ± 0.20
k_2	0.58 ± 0.06	$6.7 \pm 2.0 \times 10^{-10}$	0.51 ± 0.15
k_{add}	$2.2 \pm 0.2 \times 10^{-2}$	$2.5 \pm 0.8 \times 10^{-11}$	$2.0 \pm 0.6 \times 10^{-2}$
3-2 Cluster			
k_1	0.65 ± 0.10	$7.4 \pm 2.2 \times 10^{-10}$	0.56 ± 0.17
k_2	0.47 ± 0.07	$5.4 \pm 1.6 \times 10^{-10}$	0.41 ± 0.12
k_3	0.40 ± 0.04	$4.6 \pm 1.4 \times 10^{-10}$	0.35 ± 0.11
5-4 Cluster			
k_1	0.65 ± 0.06	$7.4 \pm 2.2 \times 10^{-10}$	0.58 ± 0.17
k_2	0.67 ± 0.06	$7.7 \pm 2.3 \times 10^{-10}$	0.61 ± 0.18
k_3	0.62 ± 0.05	$7.1 \pm 2.1 \times 10^{-10}$	0.56 ± 0.17

Table 5.2 continued.

Cluster	Pseudo First Order Rate Constant (s^{-1})	Second Order Rate Constant ($cm^3 \cdot molec^{-1} \cdot s^{-1}$)	Reactive Uptake Coefficient (γ)
k_4	0.53 ± 0.06	$6.0 \pm 1.8 \times 10^{-10}$	0.48 ± 0.14
k_5	0.23 ± 0.03	$2.6 \pm 0.8 \times 10^{-10}$	0.21 ± 0.06
6-5 Cluster			
k_1	0.62 ± 0.07	$7.1 \pm 2.1 \times 10^{-10}$	0.57 ± 0.17
k_2	0.58 ± 0.07	$6.7 \pm 2.0 \times 10^{-10}$	0.53 ± 0.16
k_3	0.60 ± 0.07	$6.9 \pm 2.1 \times 10^{-10}$	0.55 ± 0.17
k_4	0.61 ± 0.07	$6.9 \pm 2.1 \times 10^{-10}$	0.55 ± 0.17
k_5	0.51 ± 0.05	$5.9 \pm 1.8 \times 10^{-10}$	0.47 ± 0.14
k_6	0.23 ± 0.02	$2.6 \pm 0.8 \times 10^{-10}$	0.21 ± 0.06

B. Exposure of Dimethylammonium Methanesulfonate Clusters to Ammonia[b] (Substitution)

Cluster	Pseudo First Order Rate Constant (s^{-1})	Second Order Rate Constant ($cm^3 \cdot molec^{-1} \cdot s^{-1}$)	Reactive Uptake Coefficient (γ)
$[((CH_3)_2NH_2^+)_2(CH_3SO_3^-)]^+$	$< 2.4 \times 10^{-5}$	$< 7.2 \times 10^{-15}$	$< 3.6 \times 10^{-6}$
$[((CH_3)_2NH_2^+)_3(CH_3SO_3^-)_2]^+$	$< 1.3 \times 10^{-4}$	$< 4.0 \times 10^{-14}$	$< 2.0 \times 10^{-5}$
$[((CH_3)_2NH_2^+)_4(CH_3SO_3^-)_2(HSO_4^-)]^+$	$< 1.1 \times 10^{-4}$	$< 3.2 \times 10^{-14}$	$< 1.6 \times 10^{-5}$
$[((CH_3)_2NH_2^+)_5(CH_3SO_3^-)_3(HSO_4^-)]^+$	$< 2.8 \times 10^{-4}$	$< 8.4 \times 10^{-14}$	$< 4.3 \times 10^{-5}$

Table 5.2 continued.

C. Exposure of Dimethylammonium Methanesulfonate Clusters to Dimethylamine[a] (Addition)

Cluster	Pseudo First Order Rate Constant (s^{-1})	Second Order Rate Constant ($cm^3 \cdot molec^{-1} \cdot s^{-1}$)	Reactive Uptake Coefficient (γ)
$[((CH_3)_2NH_2^+)_2(CH_3SO_3^-)(CH_3SO_3H)]^+$	$2.2 \pm 0.2 \times 10^{-2}$	$2.5 \pm 0.8 \times 10^{-11}$	$2.0 \pm 0.6 \times 10^{-2}$
$[((CH_3)_2NH_2^+)_2(CH_3SO_3^-)]^+$	$< 3.7 \times 10^{-5}$	$< 4.2 \times 10^{-14}$	$< 3.1 \times 10^{-5}$
$[((CH_3)_2NH_2^+)_3(CH_3SO_3^-)_2]^+$	$< 8.9 \times 10^{-6}$	$< 1.0 \times 10^{-14}$	$< 7.8 \times 10^{-6}$
$[((CH_3)_2NH_2^+)_4(CH_3SO_3^-)_2(HSO_4^-)]^+$	$1.8 \pm 0.2 \times 10^{-3}$	$2.1 \pm 0.6 \times 10^{-12}$	$1.6 \pm 0.5 \times 10^{-3}$
$[((CH_3)_2NH_2^+)_5(CH_3SO_3^-)_3(HSO_4^-)]^+$	$< 1.6 \times 10^{-3}$	$< 1.9 \times 10^{-12}$	$< 1.5 \times 10^{-3}$

D. Exposure of Ammonium and Dimethylammonium Methanesulfonate Clusters to Ammonia[b] (Addition)

Cluster	Pseudo First Order Rate Constant (s^{-1})	Second Order Rate Constant ($cm^3 \cdot molec^{-1} \cdot s^{-1}$)	Reactive Uptake Coefficient (γ)
$[(NH_4^+)_2(CH_3SO_3^-)(CH_3SO_3H)]^+$	$1.61 \pm 0.04 \times 10^{-2}$	$5.2 \pm 1.0 \times 10^{-12}$	$2.6 \pm 0.3 \times 10^{-3}$
$[((CH_3)_2NH_2^+)_2(CH_3SO_3^-)]^+$	$< 3.0 \times 10^{-5}$	$< 8.8 \times 10^{-15}$	$< 4.4 \times 10^{-6}$
$[((CH_3)_2NH_2^+)_3(CH_3SO_3^-)_2]^+$	$< 4.4 \times 10^{-6}$	$< 1.3 \times 10^{-15}$	$< 6.6 \times 10^{-7}$
$[((CH_3)_2NH_2^+)_4(CH_3SO_3^-)_2(HSO_4^-)]^+$	$< 1.2 \times 10^{-4}$	$< 3.5 \times 10^{-14}$	$< 1.8 \times 10^{-5}$
$[((CH_3)_2NH_2^+)_5(CH_3SO_3^-)_3(HSO_4^-)]^+$	$< 1.6 \times 10^{-4}$	$< 4.6 \times 10^{-14}$	$< 2.4 \times 10^{-5}$

[a] $P_{dimethylamine}$: $2.4 \pm 0.5 \times 10^{-8}$ torr.
[b] $P_{ammonia}$: $1.0 \pm 0.2 \times 10^{-7}$ torr.

As mentioned earlier, in some of the more exothermic reactions, the reactant molecule induced a more complicated decomposition rather than simply displacing a single ligand. Decomposition of methanesulfonate clusters appears to be more significant than for previously studied bisulfate clusters (see Chapters 3 and 4), suggesting that methanesulfonate clusters are less strongly bound than bisulfate clusters. The magnitude of decomposition from a larger cluster to a smaller cluster depended upon the extent of reaction. For instance, decomposition to a smaller cluster was more significant in the first substitution step than in the final substitution step. In order to examine more quantitatively the effect of cluster decomposition on the measured rate constants, a model was created where the magnitude of cluster decomposition varied depending upon the progress of the reaction.[2] In the model, cluster decomposition was assumed to decrease the cluster ion intensity by a factor similar to that observed experimentally, typically 20-30% over a time period of about 1 sec. The model showed that fitting the experimental data (e.g. Fig. 5.2) without taking cluster decomposition into account gave measured rate constants that were larger than the actual rate constants. Typically, the actual rate constants were about 30-40% smaller than the measured values for the first or second substitution steps, but there was no difference between measured and actual rate constants for later substitution steps or for addition. The modeling results suggest that the slight decrease in reactive uptake coefficient for the first few steps may be an artifact of cluster decomposition. However, the slow final substitution step observed for the 5-4 and 6-5 clusters cannot be an artifact of cluster decomposition.

The displacement of dimethylamine by ammonia in dimethylammonium methanesulfonate clusters was examined in addition to the displacement of ammonia

by dimethylamine in ammonium methanesulfonate clusters. Pseudo first order rate constants, second order rate constants, and reactive uptake coefficients for the dimethylamine displacement in 2-1 and 3-2 dimethylammonium methanesulfonate are provided in Table 5.2. Ammonia was never observed to displace amine in these reactions; reactive uptake coefficients were $< 2.0 \times 10^{-5}$. However, upper limits for these reactions still permit calculation of thermodynamic properties, such as equilibrium constants and Gibbs free energy (ΔG^{o}) values. For the final substitution step in the 2-1 and 3-2 clusters, ΔG^{o} was < -29.6 and < -23.1 kJ·mol^{-1}, respectively, which indicates that the substitution process is extremely favorable. Such favorability compares well with thermodynamic values obtained for ammonium bisulfate and ammonium nitrate clusters.[1]

5.3.1.2 Addition of Dimethylamine or Ammonia to Dimethylammonium and Ammonium Methanesulfonate Clusters

In addition to simple substitution, dimethylamine and ammonia were observed to add onto some dimethylammonium and ammonium methanesulfonate clusters. Table 5.3 presents uptake coefficients for addition of ammonia to the 2(0)-1-1 cluster and addition of dimethylamine to the 2(2)-1-1 cluster. Dimethylamine added to the 2(2)-1-1 cluster, forming the 3(3)-2 cluster, whereas ammonia added to the 2(0)-1-1 cluster, forming the 3(0)-2 cluster. These addition reactions are interesting because they can be construed as particle growth pathways whereby an acid in the particle is neutralized by an incoming base molecule. Addition of dimethylamine to the 2(2)-1-1 cluster occurred with a reactive uptake coefficient (γ_{add}) of $2.0 \pm 0.6 \times 10^{-2}$, which was nearly an order of magnitude greater than that for addition of ammonia to the 2(0)-1-1 cluster

Table 5.3: Reactive uptake coefficients for the addition of dimethylamine or ammonia to some methanesulfonate and bisulfate clusters.

Initial Cluster	γ_{add} (Dimethylamine)	γ_{add} (Ammonia)
$[(NH_4^+)_2(CH_3SO_3^-)(CH_3SO_3H)]^+$		$2.6 \pm 0.8 \times 10^{-3}$
$[((CH_3)_2NH_2^+)_2(CH_3SO_3^-)(CH_3SO_3H)]^+$	$2.0 \pm 0.6 \times 10^{-2}$	
$[(CH_3)_2NH_2^+)_2(HSO_4^-)]^+$ [a]	$< 1.9 \times 10^{-4}$	$< 3.0 \times 10^{-5}$
$[(CH_3)_2NH_2^+)_3(HSO_4^-)_2]^+$ [a]	$< 3.0 \times 10^{-4}$	$< 1.0 \times 10^{-5}$
$[(NH_4^+)_2(HSO_4^-)]^+$ [a]		$< 3.5 \times 10^{-4}$
$[(NH_4^+)_3(HSO_4^-)_2]^+$ [a]		$< 8.2 \times 10^{-5}$

[a]From Chapter 4.[2]

(γ_{add} = 2.6 ± 0.8 × 10^{-3}). Table 5.3 also provides γ_{add} values for addition to some previously examined bisulfate clusters in the same size (*m/z*) range as these methanesulfonate clusters.[2] For bisulfate clusters, neither dimethylamine nor ammonia was observed to add onto the relevant 2-1 clusters, making the uptake coefficients at least two orders of magnitude smaller than the corresponding methanesulfonate clusters. These observations may relate in part to pKa values for the acids. The pKa of the acidic proton in methanesulfonic acid is -2.[4] However, bisulfate is much less acidic; the pKa for the loss of its proton to form the sulfate anion is +2.[5] These experimental observations are consistent with differences in pKa values for these acids. It should be noted that dimethylamine has been observed to add onto large dimethylammonium bisulfate clusters (see Chapter 4), and the uptake coefficients are comparable to γ_{add} for small methanesulfonate clusters.[2]

Neither dimethylamine nor ammonia added onto the 2-1 or 3-2 dimethylammonium methanesulfonate clusters, making $\gamma_{add} < 3.1 \times 10^{-5}$, or at least three orders of magnitude smaller than for the corresponding 2-1-1 clusters (Table 5.2). These results are not surprising since neither the 2-1 nor the 3-2 cluster has excess acid that can be neutralized by the incoming base molecule.

5.3.1.3 Substitution and Addition to Mixed Methanesulfonate-Bisulfate Clusters

In addition to the clusters discussed above, electrospray of a dimethylammonium methanesulfonate solution produced mixed clusters of the form $[((CH_3)_2NH_2^+)_4(CH_3SO_3^-)_2(HSO_4^-)]^+$ and $[((CH_3)_2NH_2^+)_5(CH_3SO_3^-)_3(HSO_4^-)]^+$. When these clusters were exposed to ammonia gas, dimethylamine was never displaced by ammonia. Reactive uptake coefficients for the displacement were $< 4.3 \times 10^{-5}$ (Table 5.2). Dimethylamine was observed to add onto the 4-3 mixed dimethylammonium

methanesulfonate-bisulfate cluster ($\gamma_{add} = 1.6 \pm 0.5 \times 10^{-3}$). This value is somewhat slower than that observed for dimethylamine addition to 4-3 dimethylammonium bisulfate ($\gamma_{add} = 4 \pm 1 \times 10^{-3}$).[2] For the 5-4 mixed methanesulfonate-bisulfate cluster, the upper limit for dimethylamine addition was 1.5×10^{-3} (Table 5.2), whereas for the 5-4 dimethylammonium bisulfate cluster, $\gamma_{add} = 5.0 \pm 2.0 \times 10^{-2}$.[2] Addition to the bisulfate clusters therefore occurred at rates that were more than an order of magnitude faster than addition to the mixed methanesulfonate-bisulfate clusters. The slower rates of the mixed methanesulfonate-bisulfate clusters may be a consequence of methanesulfonate ions shielding the bisulfate ion from the incoming dimethylamine molecule. As with the corresponding bisulfate clusters, ammonia was not observed to add onto either the 4-3 or 5-4 mixed clusters (Table 5.2).

5.3.1.4 Comparison of Positively-Charged Methanesulfonate Clusters to Other Positively-Charged Clusters

The substitution kinetics and thermodynamics of amines for ammonia in ammonium bisulfate, ammonium nitrate, and ammonium methanesulfonate clusters have now been investigated (see Chapters 3 and 4).[1, 2] Whereas bisulfate and nitrate are acid ions that may have global significance in particle formation and growth, methanesulfonic acid is an acid that may be important to the growth of particles in the marine environment. The observed behavior for all three salts is similar: displacement of ammonia by amine is thermodynamically favorable and very fast (near unit reaction probability). Table 5.4 presents a summary of reactive uptake coefficients for exchange in different-sized clusters of all three types of salts. Although exchange in the methanesulfonate clusters (a bulkier acid) appears to be somewhat slower than in

Table 5.4: Substitution uptake coefficient ranges for ammonium methanesulfonate, ammonium bisulfate, and ammonium nitrate clusters exposed to dimethylamine.

Cluster	Ammonium Methanesulfonate	Ammonium Bisulfate	Ammonium Nitrate
2-1	0.81-0.88	0.97-1.05[a]	
3-2	0.35-0.56	0.72-0.86[a]	0.55-0.86[a]
4-3		0.56-0.83[b]	
5-4	0.21-0.61	0.32-1.00[b]	
6-5	0.21-0.57	0.66-1.00[b]	

[a]From Chapter 3.[1]
[b]From Chapter 4.[2]

bisulfate or nitrate clusters, it is still quite fast, implying that regardless of the acid in the cluster, amine will easily displace ammonia, at least on the surface of the particle. For both methanesulfonate and bisulfate clusters, the final substitution step can be much slower than the initial substitution step, suggesting that exchange is more difficult in the core than on the surface. Finally, addition of a base (ammonia or amine) to a cluster occurs only in order to neutralize the remaining acid in the cluster.

5.3.2 Reactivity of Negatively-Charged Ammonium Bisulfate Clusters

In Chapters 3 and 4, as well as the first portion of this chapter, only positively-charged clusters were investigated. Here, negatively-charged ammonium bisulfate and sulfuric acid-bisulfate clusters are investigated with respect to their reactivity with bases for the first time. The results are complementary to those presented above and provide important information about the mechanisms of base incorporation into charged clusters.

The two series of clusters were analyzed in the kinetics experiments. The first series consisted of the sulfuric acid-bisulfate clusters ($[(HSO_4)(H_2SO_4)_x]^-$), which occurred at low *m/z* values and contained no ammonium. The second series was the most abundant series of negative ions observed and was of the form $[(NH_4)_x(HSO_4)_{x+1}(H_2SO_4)_3]^-$. For these ammonium bisulfate clusters, three specific clusters were isolated and exposed to dimethylamine in order to elucidate the kinetics of amine substitution and amine addition to the cluster: a cluster containing one ammonium ion, $[(NH_4)(HSO_4)_2(H_2SO_4)_3]^-$; a cluster containing two ammonium ions, $[(NH_4)_2(HSO_4)_3(H_2SO_4)_3]^-$; and a cluster containing three ammonium ions, $[(NH_4)_3(HSO_4)_4(H_2SO_4)_3]^-$. Two unique chemical reactions occurred upon exposure of

these clusters to dimethylamine: 1) dimethylamine substitution for ammonia and 2) dimethylamine addition to the cluster.

The substitution reaction can be described by Scheme 3. Note that in Scheme 3, the unneutralized sulfuric acid molecules serve essentially as a spectator to the reaction.

SCHEME 3

$$[(NH_4)_x(HSO_4)_{x+1}(H_2SO_4)_3]^- + (CH_3)_2NH \xrightarrow{k_1}$$

$$[(NH_4)_{x-1}((CH_3)_2NH_2)(HSO_4)_{x+1}(H_2SO_4)_3]^- + NH_3 \quad \text{(a)}$$

$$[(NH_4)_{x-1}((CH_3)_2NH_2)(HSO_4)_{x+1}(H_2SO_4)_3]^- + (CH_3)_2NH \xrightarrow{k_2}$$

$$[(NH_4)_{x-2}((CH_3)_2NH_2)_2(HSO_4)_{x+1}(H_2SO_4)_3]^- + NH_3 \quad \text{(b)}$$

$$[(NH_4)_{x-2}((CH_3)_2NH_2)_2(HSO_4)_{x+1}(H_2SO_4)_3]^- + (CH_3)_2NH \xrightarrow{k_3} \cdots \xrightarrow{k_x}$$

$$[((CH_3)_2NH_2)_x(HSO_4)_{x+1}(H_2SO_4)_3]^- + NH_3 \quad \text{(c)}$$

Scheme 4 describes the addition reaction, whereby a dimethylamine can add to the cluster, effectively neutralizing the sulfuric acid to bisulfate and growing the cluster to a larger size.

SCHEME 4

$$[((CH_3)_2NH_2)_x(HSO_4)_{x+1}(H_2SO_4)_3]^- + (CH_3)_2NH \xrightarrow{k_{add1}}$$

$$[((CH_3)_2NH_2)_{x+1}(HSO_4)_{x+2}(H_2SO_4)_2]^- \quad \text{(a)}$$

$$[((CH_3)_2NH_2)_{x+1}(HSO_4)_{x+2}(H_2SO_4)_2]^- + (CH_3)_2NH \xrightarrow{k_{add2}}$$

$$[((CH_3)_2NH_2)_{x+2}(HSO_4)_{x+3}(H_2SO_4)]^- \quad \text{(b)}$$

$$[((CH_3)_2NH_2)_{x+2}(HSO_4)_{x+3}(H_2SO_4)]^- + (CH_3)_2NH \xrightarrow{k_{add3}}$$

$$[((CH_3)_2NH_2)_{x+3}(HSO_4)_{x+4}]^- \quad \text{(c)}$$

The kinetics experiment is similar to previous work on positive ions (see Chapters 3 and 4).[1, 2, 6] An ammonium bisulfate cluster is isolated by mass selection in the quadrupole of the mass spectrometer. The isolated cluster is then transferred to the ICR cell, where it is exposed to dimethylamine gas at constant pressure. Reaction time is varied, and time-dependent mass spectra are recorded. A reaction profile is created by plotting the relative abundance of each reaction step against exposure time. Pseudo first order kinetics applies to these reactions because the pressure of the reactant gas is constant during the experiment. A fit of the reaction profile to pseudo first order kinetics allows for quantitative determination of the rate constants for the sequential substitution and addition reactions.

Figure 5.3 presents the reaction profile (symbols) and statistical fit to pseudo first order kinetics (lines) for $[(NH_4)(HSO_4)_2(H_2SO_4)_3]^-$ exposed to dimethylamine gas. At time t=0 sec, the initial cluster is the predominant ion observed, which is expected as no reaction should have occurred. With increasing exposure time to dimethylamine, ammonia is displaced by dimethylamine. Next, dimethylamine adds sequentially to the cluster, eventually neutralizing all sulfuric acid molecules to bisulfate. For the $[(NH_4)(HSO_4)_2(H_2SO_4)_3]^-$ cluster, the reactive uptake coefficient (reaction probability, γ) for substitution (i.e. Scheme 3) is $\gamma_{sub} = 0.24 \pm 0.07$. For the sequential addition steps (i.e. Scheme 4), the reactive uptake coefficients are $\gamma_{add1} = 0.13 \pm 0.04$, $\gamma_{add2} = 0.10 \pm 0.03$, and $\gamma_{add3} = 2.1 \pm 0.6 \times 10^{-2}$.

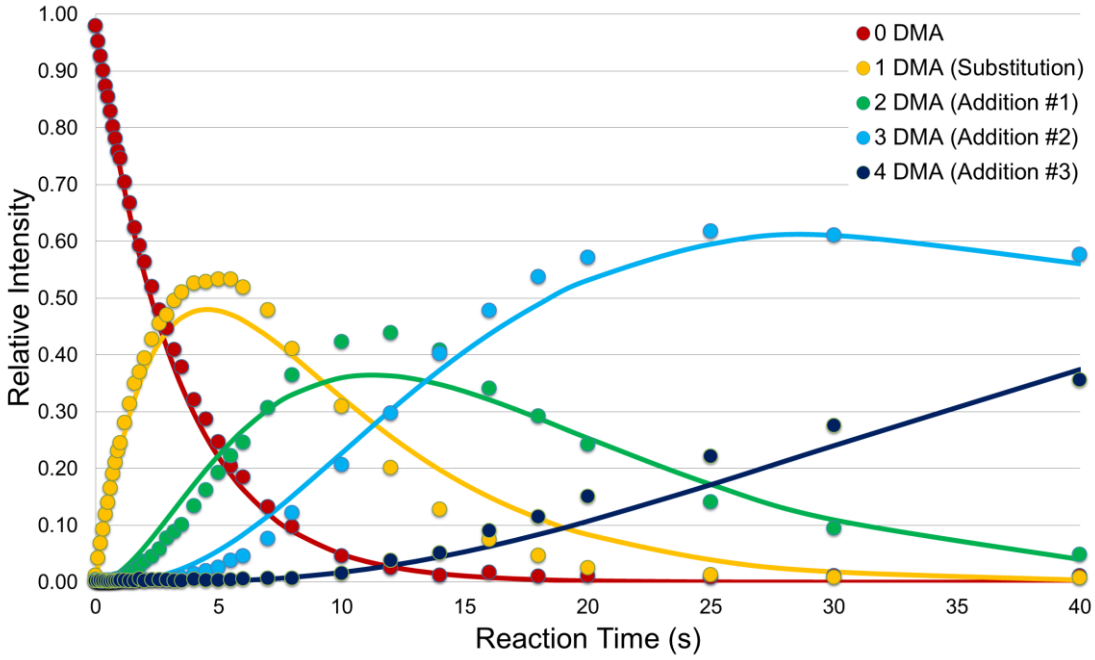

Figure 5.3: Reaction profile (symbols) and statistical fit to pseudo first order kinetics (lines) for exposure of $[(NH_4)(HSO_4)_2(H_2SO_4)_3]^-$ to dimethylamine gas. $P_{dimethylamine}$: $2.4 \pm 0.5 \times 10^{-8}$ torr.

Table 5.5 presents pseudo first order rate constants, second order rate constants, and reactive uptake coefficients for exposure of negatively-charged ammonium bisulfate clusters to dimethylamine. For clusters containing ammonium, substitution steps are fairly fast, with $\gamma_{sub} \geq 0.24$. These values for substitution are somewhat slower than those observed for positive ions, where γ_{sub} for ammonium ions on the cluster surface is typically greater than 0.50 (see Chapters 3 and 4).[1, 2, 6] The lower uptake coefficients are probably due to a decrease in the frequency of potentially reactive collisions (i.e. collision between the cluster and the amine would need to occur near the ammonium ion, but since fewer ammonium ions are in the cluster, there are more collisions where reaction would not occur). This helps to explain the observed increase in uptake coefficient for substitution as cluster size (and the number of reactive sites) increases. The initial addition step is typically slower than the substitution steps by about a factor of two. The second addition step is slightly slower than the first. However, the final addition step (to neutralize all sulfuric acid to bisulfate) is significantly slower than the first two addition steps for all studied clusters. Future computational work investigating the thermodynamics and structure of these clusters would be beneficial in explaining these experimental observations. Based on the kinetic results, amine substitution for ammonia is facile. Addition is relatively fast and results in further neutralization of the cluster to bisulfate than what can be accomplished by just ammonium.

In addition to negatively-charged ammonium bisulfate clusters, the kinetics of dimethylamine addition to two sulfuric acid-bisulfate clusters, specifically $[(HSO_4)(H_2SO_4)]^-$ and $[(HSO_4)(H_2SO_4)_2]^-$, were examined. Dimethylamine was not

Table 5.5: Pseudo first order rate constants, second order rate constants, and uptake coefficients for reaction of dimethylamine with negatively-charged ammonium bisulfate clusters. $P_{dimethylamine}$: $2.4 \pm 0.5 \times 10^{-8}$ torr.

Cluster	Reaction Step	Pseudo First Order Rate Constant (s^{-1})	Second Order Rate Constant ($cm^3 \cdot molec^{-1} \cdot s^{-1}$)	Uptake Coefficient, γ
$[(HSO_4)(H_2SO_4)]^-$	Addition	$< 1.1 \times 10^{-5}$	$< 1.3 \times 10^{-14}$	$< 9.7 \times 10^{-6}$
$[(HSO_4)(H_2SO_4)_2]^-$	Addition	$1.2 \pm 0.2 \times 10^{-3}$	$1.4 \pm 0.3 \times 10^{-12}$	$1.0 \pm 0.3 \times 10^{-3}$
$[(NH_4)(HSO_4)_2(H_2SO_4)_3]^-$	Substitution	0.26 ± 0.03	$3.1 \pm 0.6 \times 10^{-10}$	0.24 ± 0.07
	Addition 1	0.14 ± 0.01	$1.7 \pm 0.3 \times 10^{-10}$	0.13 ± 0.04
	Addition 2	0.11 ± 0.01	$1.3 \pm 0.3 \times 10^{-10}$	0.10 ± 0.03
	Addition 3	$2.2 \pm 0.3 \times 10^{-2}$	$2.6 \pm 0.5 \times 10^{-11}$	$2.1 \pm 0.6 \times 10^{-2}$
$[(NH_4)_2(HSO_4)_3(H_2SO_4)_3]^-$	Substitution 1	0.48 ± 0.08	$5.6 \pm 1.1 \times 10^{-10}$	0.44 ± 0.13
	Substitution 2	0.38 ± 0.06	$4.5 \pm 0.9 \times 10^{-10}$	0.36 ± 0.11
	Addition 1	0.19 ± 0.03	$2.2 \pm 0.4 \times 10^{-10}$	0.17 ± 0.05
	Addition 2	0.13 ± 0.02	$1.6 \pm 0.3 \times 10^{-10}$	0.13 ± 0.04
	Addition 3	$3.6 \pm 0.5 \times 10^{-2}$	$4.2 \pm 0.8 \times 10^{-11}$	$3.4 \pm 1.0 \times 10^{-2}$
$[(NH_4)_3(HSO_4)_4(H_2SO_4)_3]^-$	Substitution 1	0.56 ± 0.06	$6.6 \pm 1.3 \times 10^{-10}$	0.53 ± 0.16
	Substitution 2	0.51 ± 0.07	$6.0 \pm 1.2 \times 10^{-10}$	0.48 ± 0.14
	Substitution 3	0.43 ± 0.06	$5.1 \pm 1.0 \times 10^{-10}$	0.41 ± 0.12
	Addition 1	0.23 ± 0.02	$2.3 \pm 0.5 \times 10^{-10}$	0.22 ± 0.07
	Addition 2	0.13 ± 0.01	$1.2 \pm 0.2 \times 10^{-10}$	0.12 ± 0.04
	Addition 3	$7.0 \pm 0.7 \times 10^{-2}$	$6.8 \pm 1.4 \times 10^{-11}$	$6.7 \pm 2.0 \times 10^{-2}$

observed to add onto the $[(HSO_4)(H_2SO_4)]^-$ cluster ($\gamma_{add} < 9.7 \times 10^{-6}$); however dimethylamine did add to the $[(HSO_4)(H_2SO_4)_2]^-$ cluster, though at a rate that was an order of magnitude slower than the slowest addition step in the ammonium-containing clusters ($\gamma_{add} = 1.0 \pm 0.3 \times 10^{-3}$). These observations suggest that for negatively-charged sulfuric acid-bisulfate clusters in this size range, the incorporation of amine is not kinetically favorable. These observations agree with recent computational modeling that suggests similar negatively-charged sulfuric acid-bisulfate clusters containing dimethylamine are not thermodynamically stable.[7]

The reactivity of these same clusters was examined upon exposure to ammonia gas. Table 5.6 provides pseudo first order rate constants, second order rate constants, and reactive uptake coefficients for exposure of the three ammonium bisulfate clusters and the two sulfuric acid-bisulfate clusters to ammonia. Ammonia added to neither the $[(HSO_4)(H_2SO_4)]^-$ cluster ($\gamma_{add} < 8.1 \times 10^{-5}$) nor the $[(HSO_4)(H_2SO_4)_2]^-$ cluster ($\gamma_{add} < 5.3 \times 10^{-4}$). For ammonium-containing clusters, ammonia did not add onto the $[(NH_4)(HSO_4)_2(H_2SO_4)_3]^-$ cluster ($\gamma_{add} < 9.9 \times 10^{-4}$), but did add to the $[(NH_4)_2(HSO_4)_3(H_2SO_4)_3]^-$ and $[(NH_4)_3(HSO_4)_4(H_2SO_4)_3]^-$ clusters ($\gamma_{add} = 5.1 \pm 1.5 \times 10^{-3}$ and $1.2 \pm 0.4 \times 10^{-2}$, respectively). Addition was slow, so only the first addition step was observed. The addition rates for ammonia to these clusters are more than one order of magnitude slower than those for the first addition of dimethylamine to the dimethylammonium-substituted clusters. The measured kinetics for ammonia addition to the $[(HSO_4)(H_2SO_4)]^-$ and $[(HSO_4)(H_2SO_4)_2]^-$ clusters compares favorably with quantum chemical calculations performed previously on these clusters. Ortega et al. (2008)[8] performed calculations that suggest the presence of ammonia is unfavorable in

Table 5.6: Pseudo first order rate constants, second order rate constants, and uptake coefficients for reaction of ammonia with negatively-charged ammonium bisulfate clusters.[a]

Cluster	Reaction Step	Pseudo First Order Rate Constant (s^{-1})	Second Order Rate Constant ($cm^3 \cdot molec^{-1} \cdot s^{-1}$)	Uptake Coefficient, γ
$[(HSO_4)(H_2SO_4)]^-$	Addition	$< 5.1 \times 10^{-4}$	$< 1.6 \times 10^{-13}$	$< 8.1 \times 10^{-5}$
$[(HSO_4)(H_2SO_4)_2]^-$	Addition	$< 3.3 \times 10^{-3}$	$< 1.1 \times 10^{-12}$	$< 5.3 \times 10^{-4}$
$[(NH_4)(HSO_4)_2(H_2SO_4)_3]^-$	Addition	$< 6.1 \times 10^{-3}$	$< 1.9 \times 10^{-12}$	$< 9.9 \times 10^{-4}$
$[(NH_4)_2(HSO_4)_3(H_2SO_4)_3]^-$	Addition	$3.1 \pm 0.1 \times 10^{-2}$	$1.0 \pm 0.2 \times 10^{-11}$	$5.1 \pm 1.5 \times 10^{-3}$
$[(NH_4)_3(HSO_4)_4(H_2SO_4)_3]^-$	Addition	$7.1 \pm 0.2 \times 10^{-2}$	$2.3 \pm 0.5 \times 10^{-11}$	$1.2 \pm 0.4 \times 10^{-2}$

[a] $P_{ammonia}$: $1.0 \pm 0.2 \times 10^{-7}$ torr.

the $[(HSO_4)(H_2SO_4)]^-$ cluster, which agrees with the kinetics observations, as the uptake coefficient was $< 8.1 \times 10^{-5}$. They also predict that the favorability for ammonium in these clusters increases with increasing cluster size, as demonstrated here. These results also compare favorably to Hanson and Eisele (2002),[9] who observed that that uncharged clusters < 300 *m/z* did not contain ammonia upon ionization, whereas larger clusters did contain ammonia.

5.4 Conclusions and Atmospheric Implications

In this work, the reactivity of positively-charged clusters containing methanesulfonic acid as well as the reactivity of negatively-charged clusters containing sulfuric acid with dimethylamine and ammonia gases was examined. Two mechanisms of base uptake were observed: 1) displacement of one base by another and 2) addition to neutralize acid. Importantly, addition was always slower than displacement.

An important consideration in this work is the role of charge in these reactions. The collision rate between a charged cluster and a neutral molecule is much larger than the collision rate between a neutral cluster and neutral molecule owing to ion-dipole interaction. This is the reason why collision rate constants were calculated in this work using the collision capture model. Because the collision rate is faster, small charged clusters in ambient air are likely to react faster (i.e. larger rate constants) than their neutral counterparts. The collision rate enhancement due to ion-dipole interaction decreases as the cluster size increases and becomes insignificant for clusters above about 1 nm in diameter.[3] For large clusters, the collision rate is dependent only on size, not charge. A separate question is the role of charge beyond a simple enhancement of the collision rate. The reactive uptake coefficients determined in this

and previous work (Chapter 3)[1] for the initial substitution step are independent of cluster size. These results suggest that charge does not play a significant role in altering the substitution or addition reaction mechanisms – the differences between neutral and ionic cluster reaction rates are due to the collision rate enhancement alone.

For the methanesulfonate clusters, the substitution reaction rates suggest that ambient sub-3 nm diameter salt clusters (no matter the identity of the acidic counter ion) are likely to be aminium salts rather than ammonium salts. Methanesulfonic acid is has recently been shown to efficiently nucleate new particles in the presence of dimethylamine, but not in the presence of ammonia.[10] Additionally, several studies have observed the presence of amines, ammonia, and methanesulfonic acid in larger particles.[11-15] The results of this work indicate that amine will quickly displace ammonia on the surfaces of large particles in marine air that contain neutralized ammonium salts. The acidity of the particle may be a complicating factor, as the rate of the acid neutralization (addition) step can increase with particle size,[2] suggesting a potential for competition between the two reaction pathways at larger particle size.

The addition process studied in this work could be considered a potential growth pathway in the atmosphere, whereby a cluster containing excess acid is neutralized by incoming base. Of particular note are the 2-1-1 ammonium and dimethylammonium methanesulfonate clusters, where addition of dimethylamine occurs nearly an order of magnitude faster than addition of ammonia. Such a difference may translate to a higher rate of particle growth by amines relative to ammonia if the amine and ammonia levels are comparable. For example, in the NW Arabian Sea, aliphatic amines have been observed at concentrations within an order of

magnitude of ammonia,[16] suggesting that amines could compete favorably with ammonia in particle growth at small particle size.

For the sulfuric acid-containing clusters, the kinetics results have important atmospheric implications, especially since many of these charged clusters may be present in ambient air (see Chapter 2). Because substitution is nearly collision-limited for the negatively-charged ammonium bisulfate clusters, and because these results agree very well with those of positively-charged clusters (see Chapters 3 and 4),[1, 2, 6] ammonium salt clusters in the 1-2 nm size range whether charged or not would be expected to quickly react with amine to form aminium salts upon atmospheric collision of the ammonium salt with the gas-phase amine. Finally, the kinetics of ammonia addition to these clusters is 1-2 orders of magnitude slower than both mechanisms of dimethylamine incorporation into the cluster (substitution and addition). Therefore, when ambient concentrations of ammonia and amine are comparable, amine chemistry will likely compete favorably with ammonia chemistry.

Reproduced in part with permission from: Bryan R. Bzdek, Douglas P. Ridge, and Murray V. Johnston, "Reactivity of methanesulfonic acid salt clusters relevant to marine air," *Journal of Geophysical Research – Atmospheres*, **2011**, *116* (D3), D03301, doi: 10.1029/2010JD015217.

Reproduced in part from: B. R. Bzdek, D. P. Ridge, and M. V. Johnston, "Amine reactivity with charged sulfuric acid clusters," *Atmospheric Chemistry and Physics*, **2011**, *11* (16), 8735-8743.

5.5 References

1. Bzdek, B. R.; Ridge, D. P.; Johnston, M. V., Amine exchange into ammonium bisulfate and ammonium nitrate nuclei. *Atmos. Chem. Phys.* **2010,** *10* (8), 3495-3503.

2. Bzdek, B. R.; Ridge, D. P.; Johnston, M. V., Size-dependent reactions of ammonium bisulfate clusters with dimethylamine. *J. Phys. Chem. A* **2010,** *114* (43), 11638-11644.

3. Ridge, D. P., Ion-Molecule Collision Theory. In *The Encyclopedia of Mass Spectrometry*, Armentrout, P. B., Ed. Elsevier: San Diego, CA, 2003; Vol. Volume I: Theory and Ion Chemistry, pp 1-8.

4. Serjeant, E. P.; Dempsey, B., *Ionisation Constants of Organic Acids in Aqueous Solution*. Pergamon Press: Oxford, 1979.

5. Perrin, D. D., *Ionisation Constants of Inorganic Acids and Bases in Aqueous Solution*. Pergamon Press: Oxford, 1982.

6. Bzdek, B. R.; Ridge, D. P.; Johnston, M. V., Reactivity of methanesulfonic acid salt clusters relevant to marine air. *J. Geophys. Res.-Atmos.* **2011,** *116* (D3), D03301, doi: 10.1029/2010JD015217.

7. Kurten, T.; Petaja, T.; Smith, J.; Ortega, I. K.; Sipila, M.; Junninen, H.; Ehn, M.; Vehkamaki, H.; Mauldin, L.; Worsnop, D. R.; Kulmala, M., The effect of H_2SO_4-amine clustering on chemical ionization mass spectrometry (CIMS) measurements of gas-phase sulfuric acid. *Atmos. Chem. Phys.* **2011,** *11* (6), 3007-3019.

8. Ortega, I. K.; Kurten, T.; Vehkamaki, H.; Kulmala, M., The role of ammonia in sulfuric acid ion induced nucleation. *Atmos. Chem. Phys.* **2008,** *8* (11), 2859-2867.

9. Hanson, D. R.; Eisele, F. L., Measurement of prenucleation molecular clusters in the NH_3, H_2SO_4, H_2O system. *J. Geophys. Res.-Atmos.* **2002,** *107* (D12), 4158, doi: 10.1029/2001jd001100.

10. Dawson, M. L.; Varner, M. E.; Perraud, V.; Ezell, M. J.; Gerber, R. B.; Finlayson-Pitts, B. J., Simplified mechanism for new particle formation from methanesulfonic acid, amines, and water via experiments and ab initio calculations. *Proc. Natl. Acad. Sci. U.S.A.* **2012,** *109* (46), 18719-18724.

11. Facchini, M. C.; Decesari, S.; Rinaldi, M.; Carbone, C.; Finessi, E.; Mircea, M.; Fuzzi, S.; Moretti, F.; Tagliavini, E.; Ceburnis, D.; O'Dowd, C. D., Important source of marine secondary organic aerosol from biogenic amines. *Environ. Sci. Technol.* **2008,** *42* (24), 9116-9121.

12. Gaston, C. J.; Pratt, K. A.; Qin, X. Y.; Prather, K. A., Real-time detection and mixing state of methanesulfonate in single particles at an inland urban location during a phytoplankton bloom. *Environ. Sci. Technol.* **2010,** *44* (5), 1566-1572.

13. Kolaitis, L. N.; Bruynseels, F. J.; Vangrieken, R. E.; Andreae, M. O., Determination of methanesulfonic acid and non-sea-salt sulfate in single marine aerosol particles. *Environ. Sci. Technol.* **1989,** *23* (2), 236-240.

14. Muller, C.; Iinuma, Y.; Karstensen, J.; van Pinxteren, D.; Lehmann, S.; Gnauk, T.; Herrmann, H., Seasonal variation of aliphatic amines in marine sub-micrometer particles at the Cape Verde islands. *Atmos. Chem. Phys.* **2009,** *9* (24), 9587-9597.

15. Sorooshian, A.; Padro, L. T.; Nenes, A.; Feingold, G.; McComiskey, A.; Hersey, S. P.; Gates, H.; Jonsson, H. H.; Miller, S. D.; Stephens, G. L.; Flagan, R. C.; Seinfeld, J. H., On the link between ocean biota emissions, aerosol, and maritime clouds: Airborne, ground, and satellite measurements off the coast of California. *Global Biogeochem. Cycles* **2009,** *23* (4), GB4007, doi: 10.1029/2009gb003464.

16. Gibb, S. W.; Mantoura, R. F. C.; Liss, P. S., Ocean-atmosphere exchange and atmospheric speciation of ammonia and methylamines in the region of the NW Arabian Sea. *Global Biogeochem. Cycles* **1999,** *13* (1), 161-177.

Chapter 6

FRAGMENTATION AND GROWTH ENERGETICS OF CLUSTERS RELEVANT TO ATMOSPHERIC NEW PARTICLE FORMATION

6.1 Introduction

Chapters 3-5 examined the reactivity of charged molecular clusters that are relevant to atmospheric new particle formation. The results provided important information that mainly helps to predict the composition of clusters in the ambient sub-3 nm cluster pool. However, this work did not directly address how clusters grow out of that cluster pool to larger sizes, which is a prerequisite for new particle formation to be atmospherically relevant. The goal of this chapter is to more directly study how clusters grow. This goal is accomplished by isolating a positively-charged ammonium bisulfate cluster, fragmenting that cluster, modeling the fragmentation, and assuming that growth is the reverse of fragmentation. In other words, the energetics of cluster dissociation are studied to infer the energetics of cluster growth. Time- and collision energy-resolved cluster fragmentation is accomplished using Fourier transform ion cyclotron resonance mass spectrometry (FTICR-MS) equipped with surface-induced dissociation (SID). The experimental data are then fit to a Rice-Ramsperger-Kassel-Marcus Quasi-Equilibrium Theory (RRKM/QET) model. The results of the RRKM/QET modeling are compared to thermodynamic values obtained from computational modeling. Cluster fragmentation occurs by two pathways: 1) a two-step pathway whereby the cluster sequentially loses ammonia followed by sulfuric acid and 2) and one-step pathway whereby the cluster loses an ammonium

bisulfate molecule. With respect to growth, these observations suggest that atmospheric clusters grow by first adding sulfuric acid and then adding ammonia, which is what would be expected from thermodynamic modeling.[1] The dissociation threshold for loss of ammonia from the cluster is larger than the thermodynamic value. On the other hand, the dissociation threshold for loss of sulfuric acid from the cluster is consistent with the thermodynamic value. In terms of cluster growth, these results suggest that sulfuric acid adds to a cluster in a collision limited manner, but ammonia must overcome an activation barrier in order to incorporate into growing clusters. These conclusions are consistent with the ion-molecule reaction results discussed in Chapters 3-5 and are consistent with measurements made by other groups. The concept of an activation barrier along individual chemical pathways during new particle formation has substantial importance: it requires a rethinking of the ways new particle formation is modeled, as normally the process is only considered from a thermodynamic perspective.

6.2 Experimental Section

6.2.1 Surface-Induced Dissociation Experiments

SID experiments were conducted using a specially fabricated 6T FTICR-MS described in detail elsewhere.[2] A 5 mM ammonium sulfate (Sigma-Aldrich, St. Louis, Missouri) solution in 50/50 water/methanol was electrosprayed in the positive mode at atmospheric pressure to produce positively charged ammonium bisulfate clusters of the form $[(NH_4)_x(HSO_4)_{x-1}]^+$. These charged clusters were transferred into the vacuum system via an electrodynamic ion funnel.[3] Two quadrupoles following the ion funnel provide collisional focusing and mass selection of the ion of interest. Because the

charged clusters studied in this experiment are metastable, mass selection of a particular cluster of interest was accomplished by setting the mass-selecting quadrupole to pass a cluster larger than the desired cluster.[4] The cluster selected by the quadrupole then decomposes in the octopole, where the desired precursor ion is isolated. The identity of the precursor is confirmed by transferring the ions in the octopole to the ICR cell in the absence of a collision potential and obtaining a mass spectrum. In the SID sequence, mass-selected clusters were accumulated, extracted from the accumulation octopole, transferred into the ICR cell (which is offset at a selected collision potential), and allowed to collide with the SID target at the selected collision energy. The kinetic energy of the ions colliding with the surface is varied by adjusting the dc offset applied to the ICR cell. The SID target is introduced through a vacuum interlock assembly and is positioned at the rear trapping plate of the ICR cell. Scattered positive ions were captured by raising the potentials on the front and rear trapping plates at the conclusion of the transfer time. Time-resolved mass spectra were acquired by varying the delay between the gated trapping and the excitation/detection event (reaction delay). In this experiment, reaction delays of 1 ms, 5 ms, 10 ms, and 50 ms were examined. Immediately following the reaction delay, ions were excited through a broadband chirp and detected. The collision energy was the potential applied to the rear trapping plate and the SID target relative to that applied to the accumulation octopole. The SID target was a 1-dodecanethiol self-assembled monolayer surface prepared on a single gold {111} crystal (Monocrystals, Richmond Heights, Ohio) using a standard procedure. The target was cleaned in an ultraviolet cleaner (Model 135500, Boekel Industries Inc., Feasterville, Pennsylvania) for 10 minutes and allowed to stand in a 98% 1-dodecanethiol solution (Sigma-Aldrich, St. Louis,

Missouri) for 8-12 hours. The target was removed from the thiol solution and ultrasonically washed in ethanol for 10 minutes to remove extra layers. A modular FTICR data acquisition system was used to control the voltages and timing of the ion source, transfer optics, and ion manipulations in the ICR cell.[5, 6] Survival curves and time-resolved fragmentation efficiency curves (TFECs) were constructed from experimental mass spectra by plotting the relative abundance of the precursor ion and its fragments as a function of collision energy at each reaction delay.

6.2.2 RRKM Modeling

Survival curves and TFECs were modeled using an RRKM/QET formalism described previously.[7, 8] Briefly, the microcanonical rate coefficient $k(E)$ is calculated using the microcanonical RRKM/QET expression:

$$k(E) = \frac{\sigma W^{\ddagger}(E-E_0)}{h\rho(E)} \quad (1)$$

where $\rho(E)$ is the density of states of the reactant, $W^{\ddagger}(E\text{-}E_0)$ is the sum of states of the transition state, E_0 is the critical energy, h is Planck's constant, and σ is the reaction path degeneracy. The breakdown graph, a collection of breakdown curves (BDC) representing the fragmentation probability of the precursor ion into a particular reaction channel as a function of the internal energy of the precursor ion (E) and the reaction delay (t_r), was calculated using the appropriate equations of formal kinetics derived for a particular reaction scheme. Because of the long reaction delay times involved in these experiments, radiative cooling of the excited ions was incorporated into the kinetics scheme.[9]

The internal energy deposition function was described by the following analytical expression:[7, 8]

$$P(E, E_{coll}) = \frac{1}{C}(E - \Delta)^l exp\left(-\frac{(E-\Delta)}{f(E_{coll})}\right) \quad (2)$$

where l and Δ are parameters obtained from reference ions, C=$\Gamma(l+1)[f(E_{coll})]^{l+1}$ is a normalization factor, and $f(E_{coll})$ has the form:

$$f(E_{coll}) = A_2 E_{coll}^2 + A_1 E_{coll} + E_{th}/(l+1) \quad (3)$$

where A_1 and A_2 are parameters obtained from reference ions, E_{th} is the thermal energy of the ensemble of ions prior to ion activation, and E_{coll} is the collision energy.

The normalized signal intensity for a particular reaction channel is given by:

$$I_i(E_{coll}) = \int_0^\infty BDC_i(E, t_r)P(E, E_{coll})dE \quad (4)$$

Calculated TFECs were constructed using this described procedure and then were compared to the experimental data. The same energy deposition function was used for all reaction delays, and the fitting parameters were varied until the best fit to the experimental curves was obtained. The model also considers energy partitioning into the neutral fragments.[8, 10] The fitting parameters included critical energies (E_0) and activation entropies ($\Delta S^{\ddagger}$) for all reaction channels. The parameters (l, Δ, A_1, and A_2) characterizing the energy deposition function [Eqs. (2) and (3)] were determined by fitting the experimental survival curves for protonated leucine enkephalin (YGGFL) and its derivative (RYGGFL), for which the dissociation parameters are already known.[11, 12] In order to ensure fits did not converge to local minima, each model was fit using random starting points for E_0 and $\Delta S^{\ddagger}$. Additionally, experimental data points were systematically removed in order to examine the effect on the RRKM/QET model fits. The purpose of doing this was to elucidate the effect of experimental scatter on the resulting model fits. For instance, in one iteration of this exercise, every fifth experimental data point was removed. Although this exercise resulted in a broader range of E_0 values (which are reported in the tables), the

conclusions obtained from the RRKM/QET model fits do not change. Parameters were also individually fixed to expected thermodynamic values while the rest were varied in order to ensure that certain thermodynamic values (see below) could or could not accurately explain the experimental data. Finally, the data were modeled such that pathways present in the $[(NH_4)_6(HSO_4)_5]^+$ SID experiment as well as in the $[(NH_4)_5(HSO_4)_4]^+$ SID experiment were included in the modeling of the $[(NH_4)_5(HSO_4)_4]^+$ SID experiment. In this manner, redundant pathways were analyzed by two different models. E_0 values for identical fragmentation pathways were consistent between the two models.

6.2.3 Computational Procedure

All computational work was performed by Joseph W. DePalma, another group member. Structures and energetics of the precursor and product ions discussed in this work were calculated using a method previously described.[13] Briefly, initial positively charged cluster geometries were constructed from individual optimized molecules of ammonia and sulfuric acid and then optimized to a minimum at the AM1 level of theory[14] using the HyperChem 8.0.8 GUI-based molecular modeling package.[15] Monte Carlo conformational searches were performed in the NVT ensemble using HyperChem 8.0.8 to generate a test set of configurations for further optimizations. Of the 4000 structures generated for every cluster studied, the ten most energetically favorable structures were selected for full optimization with AM1. The most stable structure for a given cluster from the AM1/Monte Carlo method was further optimized with the PW91 functional[16, 17] using the 6-31++G(d,p) basis set as implemented in Gaussian 09 (version C.01).[18] For selected clusters, further energy refinement was performed using MP2[19] with the aug-cc-pVTZ basis set[20] at the PW91/6-31++G(d,p)

geometries for each optimized cluster with the zero-point corrrections from PW91 applied. Note that the computational values derived for these clusters are consistent with experimental thermodynamic values determined by Froyd and Lovejoy (2012)[21] to which the SID experimental values are compared. Raw energy data are provided in Table 6.1.

Table 6.1: Thermochemical parameters for all clusters. All values are in hartrees and calculated at gas phase standard state of 1 atm and 298 K. 1 hartree = 27.2116 eV. ZPE = Zero point energy.

Molecular Cluster or Molecule	$E_{electronic}$ (PW91)	$E_{electronic}$ (MP2)	ZPE (PW91)
$[(NH_4^+)(HSO_4^-)]$	-756.714796	-755.901875	0.072987
$[(NH_4^+)_2(HSO_4^-)]^+$	-813.652698	-812.763187	0.124409
$[(NH_4^+)_2(HSO_4^-)(H_2SO_4)]^+$	-1513.830516	-1512.21669	0.163448
$[(NH_4^+)_3(HSO_4^-)_2]^+$	-1570.416762	-1568.72236	0.202684
$[(NH_4^+)_3(HSO_4^-)_2(H_2SO_4)]^+$	-2270.593488	-2268.16689	0.242117
$[(NH_4^+)_4(HSO_4^-)_3]^+$	-2327.184889	-2324.67346	0.280334
$[(NH_4^+)_5(HSO_4^-)_4]^+$	-3083.954882	N/A	0.357987
$[(NH_4^+)_6(HSO_4^-)_5]^+$	-3840.716016	N/A	0.436480
H_2SO_4	-700.144548	-699.414695	0.036816
NH_3	-56.538531	-56.456628	0.033692

6.3 Results and Discussion

Electrospray ionization of an ammonium sulfate solution in the positive mode produces an array of positively charged clusters predominantly in the form $[(NH_4)_x(HSO_4)_{x-1}]^+$.[22] In this study the fragmentation energetics of two specific ammonium bisulfate clusters, $[(NH_4)_6(HSO_4)_5]^+$ and $[(NH_4)_5(HSO_4)_4]^+$, were studied by energy-resolved FTICR-SID. Each cluster was isolated and then impacted against a surface at precisely known collision energies. The resulting fragmentation patterns

were modeled using an RRKM/QET formalism to determine threshold energies for dissociation.

6.3.1 Surface-Induced Dissociation of $[(NH_4)_6(HSO_4)_5]^+$

Figure 6.1 presents the fragmentation pathway for $[(NH_4)_6(HSO_4)_5]^+$. Upon collision with the surface, this cluster immediately and completely fragments to $[(NH_4)_3(HSO_4)_2]^+$. Then, as collision energy increases, two subsequent fragmentation pathways are observed. The first is a stepwise pathway whereby $[(NH_4)_3(HSO_4)_2]^+$ loses an ammonia molecule to form the acidic cluster $[(NH_4)_2(HSO_4)(H_2SO_4)]^+$ and then loses a sulfuric acid molecule to form $[(NH_4)_2(HSO_4)]^+$. The second pathway is a one-step loss of an ammonium bisulfate molecule from $[(NH_4)_3(HSO_4)_2]^+$ to form $[(NH_4)_2(HSO_4)]^+$. These two distinct fragmentation pathways have been observed in fragmentation studies of other salt clusters.[23, 24] Note that a stepwise fragmentation pathway whereby sulfuric acid loss occurs first followed by ammonia loss was not observed. Such a pathway would result in the formation of $[(NH_4)_2(HSO_4)(NH_3)]^+$, which has a unique mass-to-charge ratio that was not observed in the mass spectra.

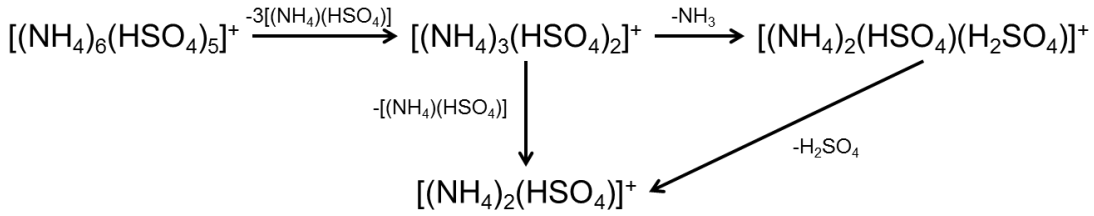

Figure 6.1: Scheme presenting the fragmentation pathway for $[(NH_4)_6(HSO_4)_5]^+$.

Figure 6.2 presents the time-resolved fragmentation efficiency curves (TFECs) for SID of $[(NH_4)_6(HSO_4)_5]^+$ (given by the symbols) as a function of SID collision energy and reaction delay. As mentioned previously, although the $[(NH_4)_6(HSO_4)_5]^+$ cluster was isolated at the start of the experiment, upon SID it immediately and completely fragments to $[(NH_4)_3(HSO_4)_2]^+$. Therefore, the relative abundance of $[(NH_4)_6(HSO_4)_5]^+$ is zero even at low collision energy. $[(NH_4)_3(HSO_4)_2]^+$ is at 100% relative abundance at collision energies below 70 eV but with increasing collision energy fragments and eventually approaches zero relative abundance at high collision energy. Meanwhile, the final product ion, $[(NH_4)_2(HSO_4)]^+$, initially has no abundance, but with increasing collision energy (E_{coll} > 90 eV) increases in relative abundance and ultimately constitutes nearly 100% of the total ion signal at high collision energies. The more acidic product, $[(NH_4)_2(HSO_4)(H_2SO_4)]^+$, which is the intermediate product in the two-step fragmentation pathway and represents the loss of an ammonia molecule from $[(NH_4)_3(HSO_4)_2]^+$, increases in abundance with increasing collision energy beginning around E_{coll} = 70 eV, reaches a maximum relative abundance at E_{coll} = 90-100 eV, and then decreases at higher collision energies as the cluster fragments by loss of a sulfuric acid molecule to form the final product ion, $[(NH_4)_2(HSO_4)]^+$.

Fits to RRKM/QET modeling at each reaction delay are given by the lines in Fig. 6.2. The model was developed using the appropriate equations of formal kinetics derived for the reaction described by Fig. 6.1. Although there is some scatter in the experimental data, the fits reasonably reproduce the experimental results. The RRKM/QET model used incorporates only E_0 and $\Delta S^{\ddagger}$ as adjustable parameters. As previously mentioned in the Experimental Section, in order to ensure that scatter

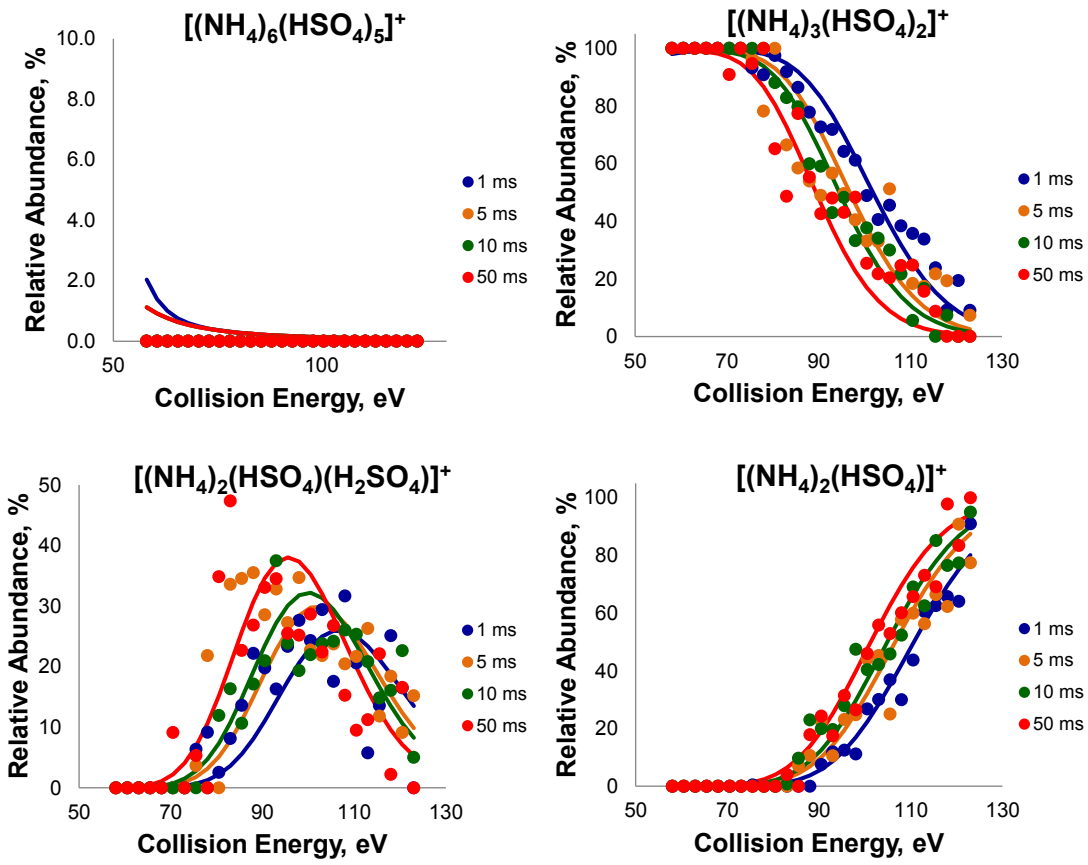

Figure 6.2: Time- and collision energy-resolved fragmentation efficiency curves (symbols) and RRKM/QET model fits (lines) for surface-induced dissociation of $[(NH_4)_6(HSO_4)_5]^+$. Note the different y-axis scales.

among the experimental data did not bias the RRKM/QET model fit, data points were systematically removed to examine the effects on the model fits. The E_0 and $\Delta S^{\ddagger}$ values did not significantly change. Results from all fits are included in the tables.

Table 6.2 presents the results of the RRKM/QET model fit to the experimental data for $[(NH_4)_6(HSO_4)_5]^+$, as well as thermodynamic values obtained from computational modeling and an experimental study of the precursor and product ions. Because the initial fragmentation of $[(NH_4)_6(HSO_4)_5]^+$ to $[(NH_4)_3(HSO_4)_2]^+$ was not observed experimentally, the model results for this step are not interpreted, since presumably the precursor ion was "hot" (i.e. contained a high, non-thermal initial internal energy distribution). The data in Table 6.2 suggest several interesting conclusions. First, the loss of ammonia from $[(NH_4)_3(HSO_4)_2]^+$ to form $[(NH_4)_2(HSO_4)(H_2SO_4)]^+$ has an experimental E_0 in the range 1.80 ± 0.23 eV whereas the thermodynamic value is much lower at 1.15-1.20 eV. Similarly, for the step involving loss of an ammonium bisulfate molecule from $[(NH_4)_3(HSO_4)_2]^+$ to form $[(NH_4)_2(HSO_4)]^+$, the experimental E_0 is 1.85 ± 0.25 eV, whereas the thermodynamic E_0 value is again much lower at 1.20-1.42 eV. These results suggest a reverse activation barrier exists for ammonia and ammonium bisulfate molecule losses. Furthermore, the $\Delta S^{\ddagger}$ values observed for these reaction pathways are close to 0 e.u. within experimental error (the model fit is relatively insensitive to the magnitude of $\Delta S^{\ddagger}$), indicating that for the loss of ammonia and loss of ammonium bisulfate molecule the fragmentation proceeds through a relatively tight transition state. These findings are consistent with the presence of a reverse activation barrier for these fragmentation channels (i.e. a barrier to the association of the two fragments).

Table 6.2: Summary of RRKM/QET model fits to experimental data and thermodynamic values for fragmentation of $[(NH_4)_6(HSO_4)_5]^+$.

Fragmentation Step	$[(NH_4)_6(HSO_4)_5]^+ \rightarrow [(NH_4)_3(HSO_4)_2]^+$	$[(NH_4)_3(HSO_4)_2]^+ \rightarrow [(NH_4)_2(HSO_4)(H_2SO_4)]^+$	$[(NH_4)_3(HSO_4)_2]^+ \rightarrow [(NH_4)_2(HSO_4)]^+$	$[(NH_4)_2(HSO_4)(H_2SO_4)]^+ \rightarrow [(NH_4)_2(HSO_4)]^+$
Neutral Loss	$3[(NH_4)_3(HSO_4)_3]$	NH_3	$[(NH_4)(HSO_4)]$	H_2SO_4
E_0 (eV, this work)	1.57 ± 1.07	1.80 ± 0.23	1.85 ± 0.25	1.15 ±0.09
E_0 (eV, PW91/6-31++G(d,p))[a]	3.81	1.15	1.20	0.84
E_0 (eV, MP2/aug-cc-pVTZ)[a]		1.18	1.42	1.00
E_0 (eV, experimental)[b]		1.20		1.05
$\Delta S^{\ddagger}$ (e.u., this work)[c]	n.s.[d]	1.12 ± 6.23	0.78 ± 6.52	n.s.[d]

[a] $E_0 = E_{electronic} + E_{zero\ point}$. [b] Thermodynamic values from Froyd and Lovejoy (2012).[21] [c] e.u. = entropy unit = $cal \cdot mol^{-1} \cdot K^{-1}$, at 450 K. $\Delta S^{\ddagger}$ had a wide range of values among the model fits. [d] n.s. = model fits are not sensitive to this parameter.

For sulfuric acid loss from $[(NH_4)_2(HSO_4)(H_2SO_4)]^+$, the experimental E_0 is 1.15 ± 0.09, which is close to the thermodynamic value (0.84-1.05 eV), suggesting that little if any reverse activation barrier exists. The absence of reverse activation barrier is consistent with previous work on the sulfuric acid dimer that suggests its formation is kinetically (i.e. diffusion) limited.[25, 26] Note that the RRKM/QET formalism used to model the experimental results does not explicitly include reverse activation barrier along this fragmentation pathway. In other words, the model does not account for the lower potential well between the ammonia loss and sulfuric acid loss steps. Including such an activation barrier would cause the model fit to be highly uncertain since its accuracy would depend upon the energy partitioning description and the partitioning of the reverse activation barrier into vibrational excitation, neither of which is well known. Based on the previous studies and the relatively good agreement between the experiment and theory, it is assumed that only a very small fraction of the reverse activation barrier is partitioned into the vibrational degrees of freedom of the ionic fragment and that the rest is converted into kinetic energy.

6.3.2 Surface-Induced Dissociation of $[(NH_4)_5(HSO_4)_4]^+$

SID of the smaller $[(NH_4)_5(HSO_4)_4]^+$ cluster exhibited more complex fragmentation patterns. Figure 6.3 presents the fragmentation pattern of $[(NH_4)_5(HSO_4)_4]^+$. First, the precursor ion fragmented to two different product ions, $[(NH_4)_4(HSO_4)_3]^+$ and $[(NH_4)_3(HSO_4)_2]^+$. As a result, there are more steps involved in the fragmentation of this cluster than for $[(NH_4)_6(HSO_4)_5]^+$. The fragmentation of $[(NH_4)_5(HSO_4)_4]^+$ is described by Fig. 6.3a. $[(NH_4)_5(HSO_4)_4]^+$ fragments to $[(NH_4)_4(HSO_4)_3]^+$ and $[(NH_4)_3(HSO_4)_2]^+$. $[(NH_4)_4(HSO_4)_3]^+$ then can lose an ammonia

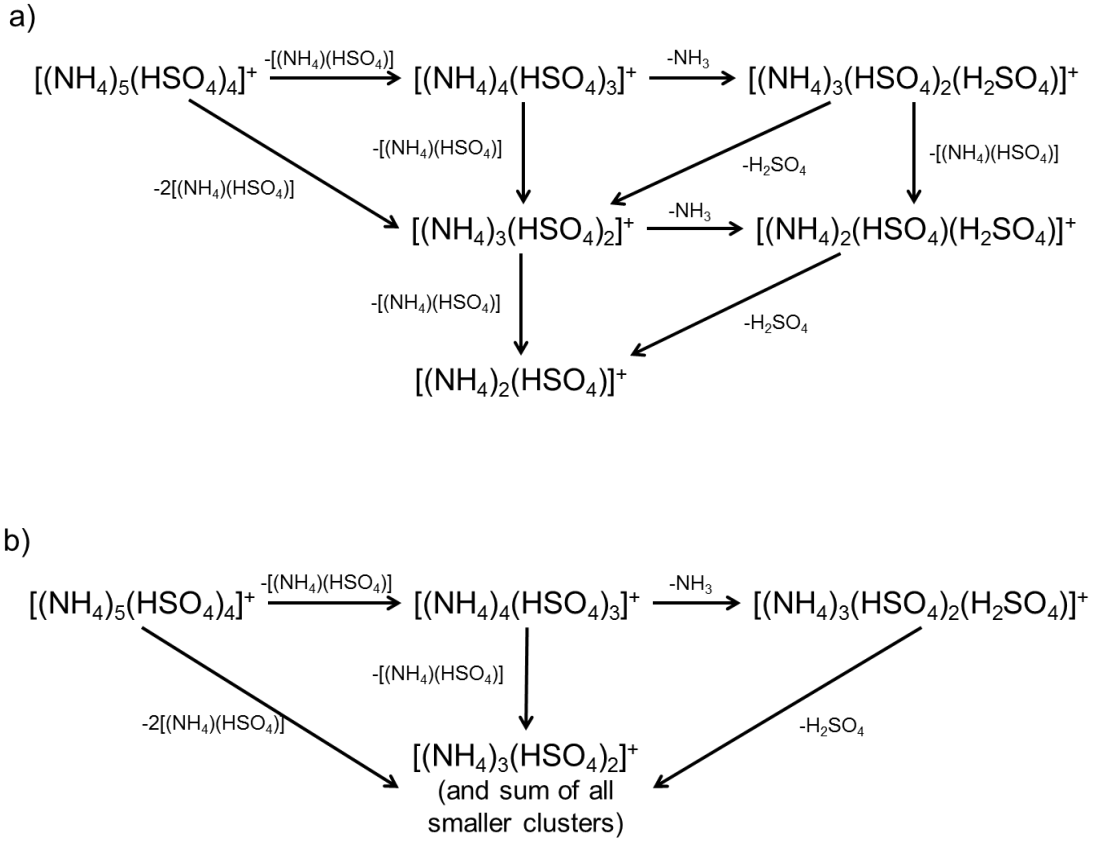

Figure 6.3: Schemes describing the fragmentation pattern of $[(NH_4)_5(HSO_4)_4]^+$. a) Complete fragmentation scheme. b) Simplified fragmentation scheme, where the signal for $[(NH_4)_3(HSO_4)_2]^+$ is summed with all smaller clusters.

molecule to form $[(NH_4)_3(HSO_4)_2(H_2SO_4)]^+$ and then a sulfuric acid molecule to form $[(NH_4)_3(HSO_4)_2]^+$, or it can fragment to $[(NH_4)_3(HSO_4)_2]^+$ in one step via loss of an ammonium bisulfate molecule. The $[(NH_4)_3(HSO_4)_2]^+$ cluster then fragments in the manner discussed in the previous section. Additionally, it is possible for $[(NH_4)_3(HSO_4)_2(H_2SO_4)]^+$ to fragment to $[(NH_4)_2(HSO_4)(H_2SO_4)]^+$ in one step by loss of an ammonium bisulfate molecule. In the RRKM/QET modeling of the fragmentation energetics, the fragmentation was considered in the manner described by Fig. 6.3b, where the signal for $[(NH_4)_3(HSO_4)_2]^+$ is summed with all smaller clusters, since the fragmentation as described by Fig. 6.3a was too complex to model. In this way, only five pathways are considered, most significantly the ammonia loss from $[(NH_4)_4(HSO_4)_3]^+$, the sulfuric acid loss from $[(NH_4)_3(HSO_4)_2(H_2SO_4)]^+$, and the ammonium bisulfate molecule loss from $[(NH_4)_4(HSO_4)_3]^+$.

Figure 6.4 presents the experimental TFECs and fit to the RRKM/QET model using Fig. 6.3b to describe the fragmentation. Even at low collision energies, most of the $[(NH_4)_5(HSO_4)_4]^+$ cluster fragments to $[(NH_4)_4(HSO_4)_3]^+$ and $[(NH_4)_3(HSO_4)_2]^+$; however, there is still a small abundance of $[(NH_4)_5(HSO_4)_4]^+$. There is some abundance of $[(NH_4)_4(HSO_4)_3]^+$ which initially increases in intensity as the residual $[(NH_4)_5(HSO_4)_4]^+$ fragments but above E_{coll} = ~60 eV begins to lose intensity as it fragments to $[(NH_4)_3(HSO_4)_2(H_2SO_4)]^+$ and $[(NH_4)_3(HSO_4)_2]^+$. $[(NH_4)_3(HSO_4)_2(H_2SO_4)]^+$ increases from zero abundance due to fragmentation of $[(NH_4)_4(HSO_4)_3]^+$, reaches a maximum abundance around E_{coll} = 65 eV, and then decreases in abundance as it fragments to $[(NH_4)_3(HSO_4)_2]^+$ by loss of a sulfuric acid molecule. Finally, $[(NH_4)_3(HSO_4)_2]^+$ begins with a relatively large abundance and then

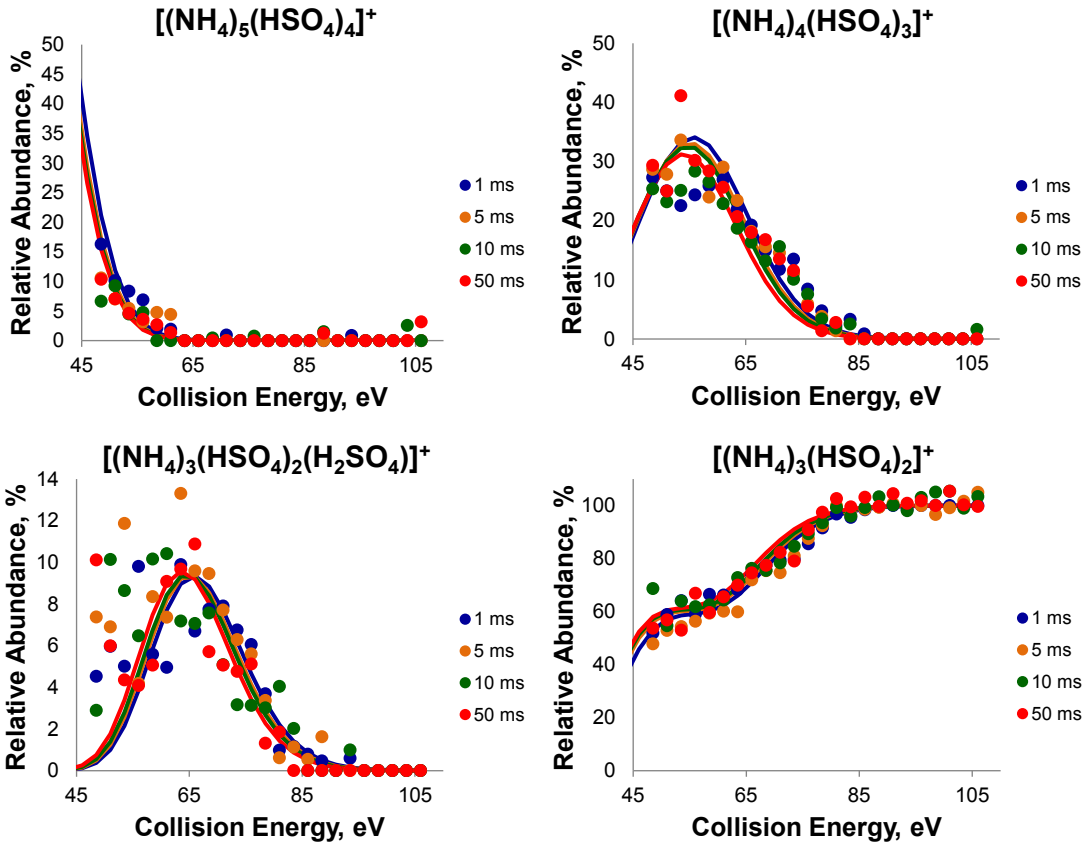

Figure 6.4: Time- and collision energy-resolved fragmentation efficiency curves (symbols) and RRKM/QET model fits (lines) for surface-induced dissociation of $[(NH_4)_5(HSO_4)_4]^+$. Note the different y-axis scales.

increases to 100% abundance as larger clusters fragment. Again, despite some scatter in the experimental data and the complexity of the fragmentation scheme, the RRKM/QET model captures the main fragmentation trends.

Table 6.3 gives RRKM/QET model fits to the experimental data for the SID of $[(NH_4)_5(HSO_4)_4]^+$ as well as thermodynamic values. Because the intensity of $[(NH_4)_5(HSO_4)_4]^+$ is so low even at low collision energy in the experiment, no interpretation of the fragmentations of this cluster to $[(NH_4)_4(HSO_4)_3]^+$ or $[(NH_4)_3(HSO_4)_2]^+$ is attempted. Loss of an ammonia molecule from $[(NH_4)_4(HSO_4)_3]^+$ requires an experimental E_0 of 2.13 ± 0.21 eV, which is much higher than the thermodynamic value (1.12-1.32 eV). Similarly, the loss of the ammonium bisulfate molecule from $[(NH_4)_4(HSO_4)_3]^+$ requires 2.03 ± 0.31 eV, which is also higher than the thermodynamic value (1.21-1.32 eV). These observations suggest the presence of a reverse activation barrier in both of these cases. For the sulfuric acid loss from $[(NH_4)_3(HSO_4)_2(H_2SO_4)]^+$, the experimental E_0 (0.84 ± 0.11 eV) is within the range of thermodynamic values (0.80-0.95 eV), suggesting that there is no reverse activation barrier. $\Delta S^{\ddagger}$ values were very high and variable for this cluster (always much greater than zero), which is a result of the reduced time dependence in the dataset for this cluster.

It is notable that the same three pathways (ammonia loss, sulfuric acid loss, and ammonium bisulfate molecule loss) are observed for the fragmentation of both clusters. Additionally, E_0 values for the same pathway in each cluster are consistent. In both clusters a reverse activation barrier is required to explain the ammonia and ammonium bisulfate molecule loss pathways. The difference in $\Delta S^{\ddagger}$ for ammonia and

Table 6.3: Summary of RRKM/QET model fits to experimental data and thermodynamic values for fragmentation of $[(NH_4)_5(HSO_4)_4]^+$.

Fragmentation Step	$[(NH_4)_5(HSO_4)_4]^+ \rightarrow [(NH_4)_4(HSO_4)_3]^+$	$[(NH_4)_5(HSO_4)_4]^+ \rightarrow [(NH_4)_3(HSO_4)_2]^+$	$[(NH_4)_4(HSO_4)_3]^+ \rightarrow [(NH_4)_3(HSO_4)_2(H_2SO_4)]^+$	$[(NH_4)_4(HSO_4)_3]^+ \rightarrow [(NH_4)_3(HSO_4)_2]^+$	$[(NH_4)_3(HSO_4)_2(H_2SO_4)]^+ \rightarrow [(NH_4)_3(HSO_4)_2]^+$
Neutral Loss	$[(NH_4)(HSO_4)]$	$2[(NH_4)_2(HSO_4)_2]$	NH_3	$[(NH_4)(HSO_4)]$	H_2SO_4
E_0 (eV, this work)	1.87 ± 0.48	1.74 ± 0.49	2.13 ± 0.21	2.03 ± 0.31	0.84 ± 0.11
E_0 (eV, PW91/6-31++G(d,p))[a]	1.38	2.70	1.32	1.32	0.80
E_0 (eV, MP2/aug-cc-pVTZ)[a]			1.24	1.21	0.74
E_0 (eV, experimental)[b]			1.12		0.95
$\Delta S^{\ddagger}$ (e.u., this work)[c]	>> 0	>> 0	>> 0	>> 0	>> 0

[a] $E_0 = E_{electronic} + E_{zero\ point}$. [b] Thermodynamic values from Froyd and Lovejoy (2012).[21] [c] e.u. = entropy unit = $cal \cdot mol^{-1} \cdot K^{-1}$, at 450 K. $\Delta S^{\ddagger}$ had a wide range of very positive values among the model fits.

ammonium bisulfate molecule loss from $[(NH_4)_3(HSO_4)_2]^+$ (where $\Delta S^{\ddagger}$ is near 0 e.u.) and from $[(NH_4)_4(HSO_4)_3]^+$ (where $\Delta S^{\ddagger}$ is much greater than 0 e.u.) suggests that as cluster size increases, the transition state becomes less constrained.

6.3.3 Potential Energy Surfaces

SID of the two positively charged ammonium bisulfate clusters examined in this study suggest two unique pathways for cluster fragmentation. One is a two-step pathway whereby a cluster first loses an ammonia molecule and then loses a sulfuric acid molecule, whereas the other is a one-step pathway proceeding via the loss of an ammonium bisulfate molecule. RRKM/QET modeling of the experimental results and the electronic structure calculations provide information on the energetics and dynamics of these fragmentation channels.

Figure 6.5a presents a potential energy surface describing the stepwise ammonia and sulfuric acid losses. As discussed previously, the experimental E_0 values for the ammonia loss pathways are higher than the thermodynamic values. If one were to consider cluster growth to be the reverse of cluster fragmentation, ammonia addition to neutralize the sulfuric acid must overcome an activation barrier, whereas sulfuric acid addition is close to barrierless. This observation is generally consistent with measured ammonia addition kinetics to acidic clusters in Chapter 5. The presence of an activation barrier probably arises because cluster binding is strong and is mostly due to electrostatic interactions.[13] As a result, when the ammonia molecule interacts with a cluster-bound sulfuric acid molecule to form ionic ammonium bisulfate within the cluster, a rearrangement of the electrostatic interactions, including a charge separation between the two species, must occur. Such a rearrangement of the

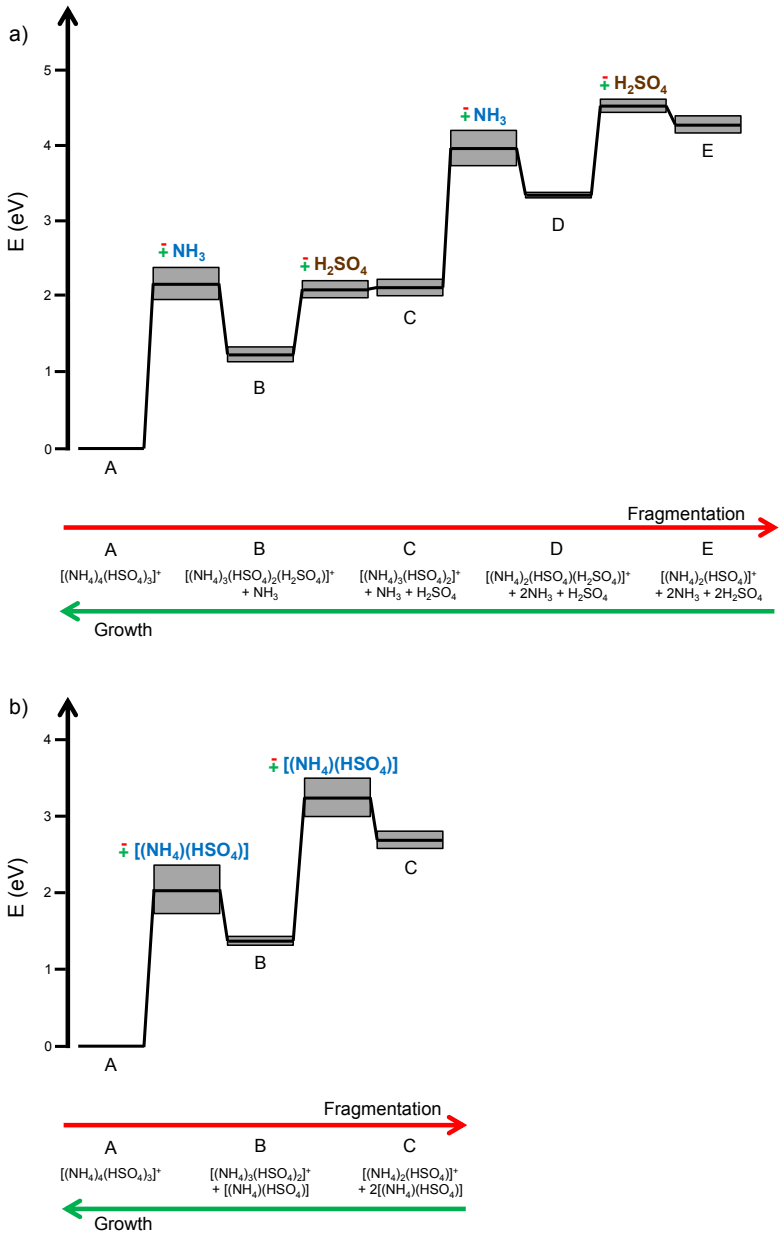

Figure 6.5: Potential energy surfaces for the (a) two-step sequential ammonia-sulfuric acid loss pathway and (b) one-step ammonium bisulfate molecule loss from pathway. Lines show the average value. Gray boxes show ranges. Letters (A, B, C, D, and E) indicate thermodynamic values. In the absence of reverse activation barriers, the fragmentation process would begin from the energy level marked A to the level marked B, etc. Between these levels are shown barrier heights marked with the outgoing/incoming molecule.

electrostatic interactions in the cluster structure is analogous to surface reconstruction in surface science.

Figure 6.5b presents a potential energy surface describing the one-step fragmentation pathway, whereby the cluster loses an ammonium bisulfate molecule.For this pathway, the experimental E_0 values were higher than the thermodynamic value determined by computational chemistry. If one were to consider the reverse pathway, cluster growth by accretion of ammonium bisulfate molecules, these results suggest that to add an ammonium bisulfate molecule to the growing cluster, one must overcome an activation barrier. The presence of a barrier to the addition of the ammonium bisulfate molecule suggests that a substantial rearrangement of the cluster structure must occur in order for the addition to occur. This explanation is in qualitative agreement with structural modeling of these clusters performed previously by Joseph W. DePalma, as the structure and electrostatic interactions change significantly as the cluster grows from $[(NH_4)_2(HSO_4)]^+$ to $[(NH_4)_3(HSO_4)_2]^+$ to $[(NH_4)_4(HSO_4)_3]^+$.[13] However, this pathway may not be atmospherically relevant, as the ambient concentration of the ammonium bisulfate molecule is expected to be very low.[27] The activation barrier heights presented in this work are very high, so the reader is cautioned against a quantitative interpretation of the barrier height. The activation barrier height should be considered qualitative rather than quantitative because energy partitioning is not fully considered in its determination.

6.3.4 Atmospheric Implications

In the atmosphere, nucleating clusters are thought to be composed of sulfuric acid, ammonia, amines, and water. However, the early steps of new particle formation

are poorly understood, especially in terms of the chemical mechanisms for cluster growth. Nonetheless, laboratory studies have found that the growth of sulfuric acid-ammonia clusters proceeds by an ammonium bisulfate coordinate (1:1 ratio of H_2SO_4: NH_3), though whether this growth occurs in one step or two steps was not rigorously investigated.[21, 28]

The implications concerning the existence of an activation barrier to sulfuric acid neutralization by ammonia may be significant with respect to cluster distributions to be expected in the atmosphere and in laboratory experiments that mimic atmospheric conditions. In the atmosphere, ammonia concentrations are typically two orders of magnitude higher than sulfuric acid concentrations.[29] As a result, the height of the activation barrier and the ambient concentrations will dictate the extent of cluster neutralization. Figure 6.6 illustrates three possible scenarios where the reaction kinetics have been modeled taking into account the differences in atmospheric concentrations of sulfuric acid and ammonia as well as the height of the activation barrier for ammonia addition to an acidic cluster. Sulfuric acid uptake is assumed to be barrierless in these examples. The barrier height was used to calculate an expected uptake coefficient (γ_{NH3}) by:

$$\gamma_{NH_3} = e^{-\frac{E_{RAB}}{kT}} \quad (5)$$

where k is the Boltzmann constant and T is temperature.

Figure 6.6a illustrates a limiting scenario where E_{RAB} = 0 eV (γ_{NH3} = 1). In this case, both sulfuric acid addition and the subsequent ammonia addition occur with unit probability. However, because the ammonia concentration is typically two orders of magnitude higher than sulfuric acid, the apparent rate for ammonia addition would be

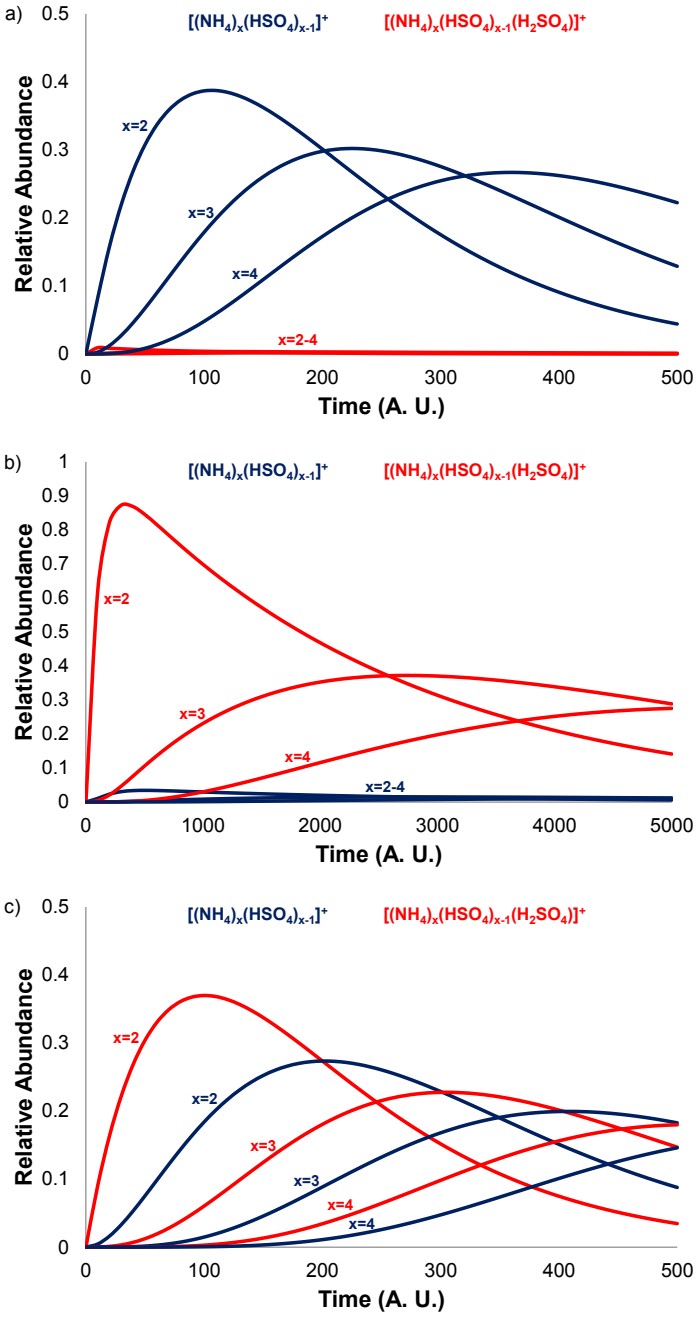

Figure 6.6: Modeled cluster distributions assuming $[NH_3] = 100\times[H_2SO_4]$, $\gamma_{H2SO4} = 1$, and (a) $E_{RAB} = 0$ eV, (b) $E_{RAB} = 0.2$ eV, and (c) $E_{RAB} = 0.1$ eV for ammonia addition. Blue lines are clusters neutralized to bisulfate; red lines are acidic clusters (one unneutralized sulfuric acid molecule). Each line indicates sequential values of x beginning with an arbitrary initial cluster (x=2).

two orders of magnitude higher than the rate of sulfuric acid addition. As illustrated in Fig. 6.6a, this scenario results in neutralized clusters (blue lines) dominating over acidic clusters (red lines).

Figure 6.6b illustrates a second limiting scenario where E_{RAB} = 0.2 eV (γ_{NH3} = 10^{-4}). In this case, uptake of ammonia is four orders of magnitude slower than uptake of sulfuric acid. Despite the higher concentration of ammonia, the rate of ammonia addition will still be two orders of magnitude slower than sulfuric acid addition. As shown in Fig. 6.6b, the result is that acidic clusters dominate over neutralized clusters. Also significant for this limiting scenario is the much longer timescale to cluster growth, as the neutralization step is very slow.

Figure 6.6c presents an intermediate scenario where E_{RAB} = 0.1 eV (γ_{NH3} = 10^{-2}). In this case, although the uptake coefficient for ammonia is two orders of magnitude lower than for sulfuric acid, the larger abundance of ammonia can overcome the kinetic barrier to addition. As a result, the relative rates for sulfuric acid and ammonia addition are the same. As shown in Fig. 6.6c, the result is that both acidic and neutralized clusters have significant abundance. Such a scenario is in qualitative agreement with a recent chamber study examining new particle formation with the ammonia-sulfuric acid system.[28] The above analysis illustrates the concept that the cluster distribution is strongly dependent on E_{RAB} even though all individual steps are thermodynamically strongly favorable.[13, 21]

6.4 Conclusions

In this work, an RRKM/QET model was applied to time- and collision energy-resolved fragmentation by SID of positively charged ammonium bisulfate clusters. The experimental results indicate two distinct fragmentation pathways: 1) a two-step

fragmentation whereby ammonia and sulfuric acid are sequentially lost from the cluster and 2) a one-step fragmentation whereby an ammonium bisulfate molecule is lost from the cluster. RRKM/QET modeling of the experimental SID data indicates that the critical energies for loss of an ammonia molecule and loss of an ammonium bisulfate molecule from a cluster are larger than the thermodynamic values. If one were to consider cluster growth to be the reverse of cluster fragmentation, the results suggest that an activation barrier must be overcome in order to neutralize sulfuric acid in a small cluster with ammonia. The implication therefore is that the reaction probability for neutralization by ammonia in an acidic cluster will be much less than unity though the observed distribution and composition of clusters will be strongly dependent on the barrier height and relative concentrations of the gaseous sulfuric acid and ammonia. These results also suggest an activation barrier to the addition of the ammonium bisulfate molecule. The presence of an activation barrier to ammonia incorporation in principle could be experimentally tested in a nucleation experiment if the molecular ions are monitored and the ammonia concentration is varied. These results indicate that cluster growth in the ammonia-sulfuric acid system is probably not collision limited due to the presence of activation barriers along the potential energy surface. Such a result is consistent with the measured ammonia addition kinetics to acidic clusters described in Chapter 5. Models of atmospheric particle nucleation and growth typically focus on free energy differences among clusters of different sizes and do not consider activation barriers to growth processes in much, if any, detail.[30-33] The results presented here suggest that it may be appropriate to incorporate activation barrier into models of new particle formation. Indeed, these observations may be broadly applicable to studies of heterogeneous

nanoparticle/cluster growth, as the concept of activation barriers along individual chemical steps may be important to consider in understanding such processes.

There are some important limitations to this work that will require further investigation. The activation barrier height, cluster polarity effects, and role of water are not quantified. Additionally, the cluster size-dependence of the barrier is not well-defined. An important question to address is whether an activation barrier can exist in larger clusters and whether that may affect observed kinetics. Finally, this work only addresses ammonium bisulfate clusters. Whether amines would exhibit similar behavior as ammonia or could lower the activation barrier to sulfuric acid neutralization and thereby facilitate higher cluster growth rates is an open question. A reduced activation barrier associated with amines may help to explain the enhanced nucleation rates observed in laboratory studies of sulfuric acid-amine nucleation.

6.5 References

1. Olenius, T.; Kupiainen-Määttä, O.; Ortega, I. K.; Kurtén, T.; Vehkamäki, H., Free energy barrier in the growth of sulfuric acid–ammonia and sulfuric acid–dimethylamine clusters. *J. Chem. Phys.* **2013,** *139* (8), 084312, doi: 10.1063/1.4819024.

2. Laskin, J.; Denisov, E. V.; Shukla, A. K.; Barlow, S. E.; Futrell, J. H., Surface-induced dissociation in a Fourier transform ion cyclotron resonance mass spectrometer: Instrument design and evaluation. *Anal. Chem.* **2002,** *74* (14), 3255-3261.

3. Shaffer, S. A.; Tang, K. Q.; Anderson, G. A.; Prior, D. C.; Udseth, H. R.; Smith, R. D., A novel ion funnel for focusing ions at elevated pressure using electrospray ionization mass spectrometry. *Rapid Commun. Mass Spectrom.* **1997,** *11* (16), 1813-1817.

4. Bzdek, B. R.; Ridge, D. P.; Johnston, M. V., Size-dependent reactions of ammonium bisulfate clusters with dimethylamine. *J. Phys. Chem. A* **2010,** *114* (43), 11638-11644.

5. Mize, T. H.; Taban, I.; Duursma, M.; Seynen, M.; Konijnenburg, M.; Vijftigschild, A.; Doornik, C. V.; Rooij, G. V.; Heeren, R. M. A., A modular data and control system to improve sensitivity, selectivity, speed of analysis, ease of use, and transient duration in an external source FTICR-MS. *Int. J. Mass Spectrom.* **2004,** *235* (3), 243-253.

6. Taban, L. M.; van der Burgt, Y. E. M.; Duursma, M.; Takats, Z.; Seynen, M.; Konijnenburg, M.; Vijftigschild, A.; Attema, I.; Heeren, R. M. A., A novel workflow control system for Fourier transform ion cyclotron resonance mass spectrometry allows for unique on-the-fly data-dependent decisions. *Rapid Commun. Mass Spectrom.* **2008,** *22* (8), 1245-1256.

7. Laskin, J.; Byrd, M.; Futrell, J., Internal energy distributions resulting from sustained off-resonance excitation in FTMS. I. Fragmentation of the bromobenzene radical cation. *Int. J. Mass Spectrom.* **2000,** *195* (1), 285-302.

8. Laskin, J.; Futrell, J., Internal energy distributions resulting from sustained off-resonance excitation in Fourier transform ion cyclotron resonance mass spectrometry. II. Fragmentation of the 1-bromonaphthalene radical cation. *J. Phys. Chem. A* **2000,** *104* (23), 5484-5494.

9. Dunbar, R. C., Infrared radiative cooling of gas-phase ions. *Mass Spectrom. Rev.* **1992,** *11* (4), 309-339.

10. Laskin, J.; Denisov, E.; Futrell, J., A comparative study of collision-induced and surface-induced dissociation. 1. Fragmentation of protonated dialanine. *J. Am. Chem. Soc.* **2000,** *122* (40), 9703-9714.

11. Laskin, J., Energetics and dynamics of fragmentation of protonated leucine enkephalin from time-and energy-resolved surface-induced dissociation studies. *J. Phys. Chem. A* **2006,** *110* (27), 8554-8562.

12. Laskin, J.; Yang, Z.; Song, T.; Lam, C.; Chu, I. K., Effect of the basic residue on the energetics, dynamics, and mechanisms of gas-phase fragmentation of protonated peptides. *J. Am. Chem. Soc.* **2010,** *132* (45), 16006-16016.

13. DePalma, J. W.; Bzdek, B. R.; Doren, D. J.; Johnston, M. V., Structure and energetics of nanometer size clusters of sulfuric acid with ammonia and dimethylamine. *J. Phys. Chem. A* **2012,** *116* (3), 1030-1040.

14. Dewar, M. J. S.; Zoebisch, E. G.; Healy, E. F.; Stewart, J. J. P., The development and use of quantum mechanical molecular models. 76. AM1: A new general purpose quantum mechanical molecular model. *J. Am. Chem. Soc.* **1985,** *107* (13), 3902-3909.

15. *HyperChem Professional 8.0.8*, Hypercube, Inc.: Gainesville, FL, 2010.

16. Perdew, J. P.; Burke, K.; Wang, Y., Generalized gradient approximation for the exchange-correlation hole of a many-electron system. *Phys. Rev. B* **1996,** *54* (23), 16533-16539.

17. Perdew, J. P.; Chevary, J. A.; Vosko, S. H.; Jackson, K. A.; Pederson, M. R.; Singh, D. J.; Fiolhais, C., Atoms, molecules, solids, and surfaces: Appplications of the generalized gradient approximation for exchange and correlation. *Phys. Rev. B* **1992,** *46* (11), 6671-6687.

18. Frisch, M. J.; Trucks, G. W.; Schlegel, H. B.; Scuseria, G. E.; Robb, M. A.; Cheeseman, J. R.; Scalmani, G.; Barone, V.; Mennucci, B.; Petersson, G. A.; Nakatsuji, H.; Caricato, M.; Li, X.; Hratchian, H. P.; Izmaylov, A. F.; Bloino, J.; Zheng, G.; Sonnenberg, J. L.; Hada, M.; Ehara, M.; Toyota, K.; Fukuda, R.; Hasegawa, J.; Ishida, M.; Nakajima, T.; Honda, Y.; Kitao, O.; Naka, H.; Vreven, T.; J. A. Montgomery, J.; Peralta, J. E.; Ogliaro, F.; Bearpark, M.; Heyd, J. J.; Brothers, E.; Kudin, K. N.; Staroverov, V. N.; Keith, T.; Kobayashi, R.; Normand, J.; Raghavachari, K.; Rendell, A.; Burant, J. C.; Iyengar, S. S.; Tomasi, J.; Cossi, M.; Rega, N.; Millam, J. M.; Klene, M.; Knox, J. E.; Cross, J. B.; Bakken, V.; Adamo, C.; Jaramillo, J.; Gomperts, R.; Stratmann, R. E.; Yazyev, O.; Austin, A. J.; Cammi, R.; Pomelli, C.;

Ochterski, J. W.; Martin, R. L.; Morokuma, K.; Zakrzewski, V. G.; Voth, G. A.; Salvador, P.; Dannenberg, J. J.; Dapprich, S.; Daniels, A. D.; Farkas, O.; Foresman, J. B.; Ortiz, J. V.; Cioslowski, J.; Fox, D. J. *Gaussian 09, revision C.01*, Gaussian, Inc.: Wallingford, CT, 2010.

19. Moller, C.; Plesset, M. S., Note on an approximation treatment for many-electron systems. *Phys. Rev.* **1934,** *46* (7), 0618-0622.

20. Dunning, T. H., Gaussian basis sets for use in correlated molecular calculations. I. The atoms boron through neon and hydrogen. *J. Chem. Phys.* **1989,** *90* (2), 1007-1023.

21. Froyd, K. D.; Lovejoy, E. R., Bond energies and structures of ammonia-sulfuric acid positive cluster ions. *J. Phys. Chem. A* **2012,** *116* (24), 5886-5899.

22. Bzdek, B. R.; Ridge, D. P.; Johnston, M. V., Amine reactivity with charged sulfuric acid clusters. *Atmos. Chem. Phys.* **2011,** *11* (16), 8735-8743.

23. Zhou, M.; Huang, C.; Wysocki, V. H., Surface-induced dissociation of ion mobility-separated noncovalent complexes in a quadrupole/time-of-flight mass spectrometer. *Anal. Chem.* **2012,** *84* (14), 6016-23.

24. Wysocki, V. H.; Jones, C. M.; Galhena, A. S.; Blackwell, A. E., Surface-induced dissociation shows potential to be more informative than collision-induced dissociation for structural studies of large systems. *J. Am. Soc. Mass Spectrom.* **2008,** *19* (7), 903-913.

25. Kurten, T.; Kuang, C. A.; Gomez, P.; McMurry, P. H.; Vehkamaki, H.; Ortega, I.; Noppel, M.; Kulmala, M., The role of cluster energy nonaccommodation in atmospheric sulfuric acid nucleation. *J. Chem. Phys.* **2010,** *132* (2), 024304, doi: 10.1063/1.3291213.

26. Petaja, T.; Sipila, M.; Paasonen, P.; Nieminen, T.; Kurten, T.; Ortega, I. K.; Stratmann, F.; Vehkamaki, H.; Berndt, T.; Kulmala, M., Experimental observation of strongly bound dimers of sulfuric acid: Application to nucleation in the atmosphere. *Phys. Rev. Lett.* **2011,** *106* (22), doi: 10.1103/PhysRevLett.106.228302.

27. Kurten, T.; Petaja, T.; Smith, J.; Ortega, I. K.; Sipila, M.; Junninen, H.; Ehn, M.; Vehkamaki, H.; Mauldin, L.; Worsnop, D. R.; Kulmala, M., The effect of H_2SO_4-amine clustering on chemical ionization mass spectrometry (CIMS) measurements of gas-phase sulfuric acid. *Atmos. Chem. Phys.* **2011,** *11* (6), 3007-3019.

28. Kirkby, J.; Curtius, J.; Almeida, J.; Dunne, E.; Duplissy, J.; Ehrhart, S.; Franchin, A.; Gagne, S.; Ickes, L.; Kurten, A.; Kupc, A.; Metzger, A.; Riccobono, F.; Rondo, L.; Schobesberger, S.; Tsagkogeorgas, G.; Wimmer, D.; Amorim, A.; Bianchi, F.; Breitenlechner, M.; David, A.; Dommen, J.; Downard, A.; Ehn, M.; Flagan, R. C.; Haider, S.; Hansel, A.; Hauser, D.; Jud, W.; Junninen, H.; Kreissl, F.; Kvashin, A.; Laaksonen, A.; Lehtipalo, K.; Lima, J.; Lovejoy, E. R.; Makhmutov, V.; Mathot, S.; Mikkila, J.; Minginette, P.; Mogo, S.; Nieminen, T.; Onnela, A.; Pereira, P.; Petaja, T.; Schnitzhofer, R.; Seinfeld, J. H.; Sipila, M.; Stozhkov, Y.; Stratmann, F.; Tome, A.; Vanhanen, J.; Viisanen, Y.; Vrtala, A.; Wagner, P. E.; Walther, H.; Weingartner, E.; Wex, H.; Winkler, P. M.; Carslaw, K. S.; Worsnop, D. R.; Baltensperger, U.; Kulmala, M., Role of sulphuric acid, ammonia and galactic cosmic rays in atmospheric aerosol nucleation. *Nature* **2011,** *476* (7361), 429-433.

29. Finlayson-Pitts, B. J.; Pitts, J. N., *Chemistry of the Upper and Lower Atmosphere*. Academic Press: New York, 2000.

30. McGrath, M. J.; Olenius, T.; Ortega, I. K.; Loukonen, V.; Paasonen, P.; Kurten, T.; Kulmala, M.; Vehkamaki, H., Atmospheric Cluster Dynamics Code: a flexible method for solution of the birth-death equations. *Atmos. Chem. Phys.* **2012,** *12* (5), 2345-2355.

31. Kulmala, M., Dynamical atmospheric cluster model. *Atmos. Res.* **2010,** *98* (2-4), 201-206.

32. Zhang, R.; Khalizov, A.; Wang, L.; Hu, M.; Xu, W., Nucleation and growth of nanoparticles in the atmosphere. *Chem. Rev.* **2012,** *112* (3), 1957-2011.

33. Chen, M.; Titcombe, M.; Jiang, J.; Jen, C.; Kuang, C.; Fischer, M. L.; Eisele, F. L.; Siepmann, J. I.; Hanson, D. R.; Zhao, J.; McMurry, P. H., Acid–base chemical reaction model for nucleation rates in the polluted atmospheric boundary layer. *Proc. Natl. Acad. Sci. U.S.A.* **2012,** *109* (46), 18713-18718.

Chapter 7

NANOPARTICLE CHEMICAL COMPOSITION DURING NEW PARTICLE FORMATION

7.1 Introduction

Chapters 2-6 discussed laboratory measurements addressing the composition and reactivity of clusters relevant to atmospheric new particle formation. Those experiments gave valuable information important to inferring the composition of atmospheric clusters < 3 nm diameter as well as how < 3 nm clusters may grow to larger sizes. This chapter reports field measurements of 20 nm diameter nanoparticle elemental composition during new particle formation using the Nano Aerosol Mass Spectrometer (NAMS). Two measurement campaigns are discussed: one in Lewes, Delaware, during the autumn and another in Wilmington, Delaware, during the summer. Lewes is a rural/coastal site that was not impacted by many anthropogenic sources during the period of the campaign. Wilmington is an urban location heavily impacted by anthropogenic activities. Observations at both of these sites provide important information about how nanoparticles can grow from ~10–20 nm diameter. Such knowledge is necessary to elucidate the chemical mechanisms of nanoparticle growth, which is important if the sub-3 nm diameter clusters discussed in Chapters 2-6 are to become atmospherically relevant. NAMS measurements indicate that during new particle formation, elements associated with inorganic species (e.g. sulfur and nitrogen) increase in relative abundance, whereas elements associated with organic species (e.g. carbon) decrease in relative abundance.

7.2 Experimental Section

The first field campaign was conducted at the Hugh R. Sharp Campus of the University of Delaware in Lewes, Delaware (38°47'02" N, 75°09'39" W) from 15 October 2007 to 12 November 2007. The campus is located on the Delaware Bay, which is at the outlet of the Delaware River to the Atlantic Ocean. The field site is situated about 800 m south of the Delaware Bay, 3 km west of the Atlantic Ocean, and is adjacent (< 50 m) to a large salt marsh on the west. This site is the location of a previous campaign to study gas-phase sulfur emissions and to perform a SO_2 intercomparison experiment.[1, 2] The site is occasionally impacted by SO_2 emissions from a coal-fired power plant 23 km to the south-southwest. The second field campaign was conducted from 1 July 2009 to 15 July 2009 in Wilmington, Delaware (39°44'23" N, 75°33'27" W) as part of the ULTRAfine Aerosol Characterization Experiment (ULTRACE). The field site in Wilmington represents an urban environment that has been described previously and has been the subject of several field campaigns.[3-8]

Ambient particle composition measurements were accomplished using NAMS, which gives a quantitative measure of the elemental composition of individual size-selected nanoparticles in the 7-30 nm size range.[9, 10] Particles were sampled through an inlet approximately 6 m above the ground. Inside NAMS, particles flow through a series of aerodynamic and electrodynamic focusing elements and then are size-selectively captured in an ion trap. Particles are irradiated with a high energy pulsed laser beam to reach the so-called "complete ionization limit," where a plasma is formed. Each particle is completely disintegrated into positively-charged atomic ions that are mass analyzed by time-of-flight. The relative intensities of these ions give the elemental composition. For standard compounds, the elemental mole ratios obtained

by NAMS are typically within 10% of their expected values.[11] The sampled particle size range is selected by the frequency applied to the ring electrode of the ion trap. For the Lewes campaign, NAMS sampled 21 nm mass normalized diameter particles, which (assuming a spherical particle and 1.7 $g \cdot cm^{-3}$ density) corresponds to a mobility diameter of about 18 nm. For the Wilmington campaign, NAMS sampled 25 nm mass normalized diameter particles, which corresponds to a mobility diameter of about 21 nm. For singly-charged spherical particles, the mass normalized diameter equals the mobility diameter multiplied by the cube root of the density.[9]

In addition to particle composition measurements, particle size distributions were monitored throughout the campaign by a scanning mobility particle sizer (SMPS; electrostatic classifier model 3080, condensation particle counter model 3025a, TSI, Inc., St. Paul, Minnesota). For the Lewes campaign only, a unipolar, rather than a bipolar, charger was used to charge the sampled particles entering the SMPS in order to increase the number of charged particles for NAMS analysis. (The experimental setup for this study required particles entering the SMPS and NAMS to be charged by the same device.) An empirical correction to the obtained particle size distribution was applied in order to account for the difference in charging efficiency between the chargers. Because of the possibility of particles > 20 nm mobility diameter taking on multiple charges when using a unipolar charger,[12] growth rate estimates are only given to one significant figure. Note that the use of the unipolar charger has little effect on mass spectrometric measurements, as the size of particle analyzed is determined by a mass-to-charge (*m/z*) ratio. A doubly-charged particle could be analyzed at the same *m/z* as a singly-charged one; however, since mass is proportional to the cube of diameter, this doubly-charged particle would have a mass normalized diameter only a

few nm larger than the desired singly-charged particle. Additionally, since analysis is performed on a particle-by-particle basis, rather than on a mass basis, the contribution of these particles to average particle composition is relatively small.

Particle molecular composition is inferred from elemental composition. The goal is to put the elemental composition into molecular context based on the major constituents that are typically found in ambient nanoparticles: sulfate, nitrate, ammonium, and carbonaceous matter. Accordingly, the molecular apportionment algorithm partitions the elemental composition into the three inorganic species based on elemental abundances of S, N, and O and into organic (carbonaceous) matter based on C and residual O after removing contributions to inorganic species. No attempt is made to apportion the elemental composition into other inorganic species (e.g. metal oxides) because no other inorganic ions are consistently detected in Lewes. The one exception is silicon dioxide, which is apportioned owing to the occasional detection of a small silicon elemental composition (see Chapter 10).[7]

The apportionment algorithm used in this work is summarized in Table 7.1. Note that the apportionment algorithm described below should not be considered to be strictly correct with respect to the chemical forms of all molecular species in the nanoparticles. Each step in the apportionment algorithm relies on an assumption about the chemical form of the element being apportioned. However, for the campaigns discussed in this chapter, there were no other measurements against which the NAMS measurements could be compared. The goal is simply to put the elemental composition into a molecular context based upon the types of molecular species usually observed in atmospheric aerosols.

Table 7.1: Molecular apportionment of the elemental composition measured by NAMS.

Start:	Total Integrated Elemental Signals (sum of all charge states) for C, O, N, S, Si
Step 1.	Remove particles having >90% N, S, or Si and classify as unrealistic or un-interpretable compositions. Remove particles having >90% O and classify as particulate water. Only the remaining particles move forward to step 2.
Step 2.	Apportion all S plus stoichiometric amount of O (=4S) to SO_4^{-2}. (If insufficient O remains from step 1, classify remaining S as residual S.)
Step 3.	Apportion N (up to $2S_{non\text{-}residual}$ from step 1) to NH_4^+.
Step 4.	Apportion all Si plus stoichiometric O (=2Si) to SiO_2. (If insufficient O remains from step 2, classify remaining Si as residual Si.)
Step 5.	Apportion remaining N from step 3 plus stoichiometric O (=3N/2) as NH_4NO_3. (If insufficient O remains from step 4, classify remaining N as residual N.)
Step 6.	Apportion remaining O from step 5 plus all C to carbonaceous matter; calculate O/C elemental ratio from these values.
Step 7.	Report mole fractions of SO_4^{-2}, NO_3^-, NH_4^+, SiO_2, carbonaceous matter, residual elements from steps 2-6. Calculate mass fractions from the mole fractions.

In the apportionment algorithm, sulfur and silicon are assumed to be in oxidized forms (sulfate, silicon dioxide). Nitrogen is assumed to be in cationic form (the algorithm assumes ammonium) until all sulfate is neutralized. Thereafter, any remaining nitrogen (Excess N = N-2S) is assumed to be in the form of ammonium nitrate. Finally, carbon and any residual oxygen are assigned to carbonaceous matter. The apportionment scheme does not assume any oxidation state for the carbon in the particle. However, the O/C ratio for carbonaceous matter in a particle will permit determination of the average carbon oxidation state in the particle.

This apportionment therefore makes the following assumptions (which will be critically evaluated in later chapters) about the chemical form of each element:

1. S is assumed to be in the form of sulfate. In Chapters 8 and 9, this assumption will be tested and shown to be a reasonable assumption.
2. All nitrogen in excess of that required to neutralize sulfuric acid (Excess N = N-2S) is assumed here to be in the form of NH_4NO_3. As will be illustrated in Chapters 9 and 10, this assumption is not always reasonable.
3. Si is assumed to be in the form of SiO_2. Chapter 10 will address this assumption directly. Although this assumption may not be entirely correct, the molecular form of Si usually will not substantially affect the interpretation of the results.

Organic compounds containing heteroatoms, for example organosulfates and organonitrates, are not considered in the apportionment scheme. The "inorganic" portion of these species would be apportioned to sulfate or nitrate with the organic component being apportioned to carbonaceous matter. In terms of cationic nitrogen

species, both cationic ammonium and aminium species would be partitioned to ammonium by the apportionment scheme. Whereas amine nitrogen would correctly be apportioned to the cation, the organic portion would be apportioned to carbonaceous matter.

Particle mass spectra consisting of $\geq$ 90% atomic (molar) area of a single non-carbon atom are deemed to represent unrealistic (or at least un-interpretable) particle compositions and are not subjected to molecular apportionment. These particles typically represent less than 0.1% of total particles in a dataset. Particles consisting of $\geq$ 90% atomic area of oxygen are tabulated separately as particulate water. For some particles that are subjected to molecular apportionment, there is not enough oxygen to assign all of the sulfur, silicon, and nitrogen to the corresponding molecular species. In these cases, the residual N, Si, and S signals are tabulated as "unapportioned" elemental composition. Typically, unapportioned matter represents less than about 5% of the elemental content of an ambient particle dataset. Unapportioned matter and removed particles arise primarily from pulse-to-pulse variations of the laser ablation process, which cause some particle mass spectra to deviate substantially from the true chemical composition.[11]

The molecular apportionment algorithm is used in these early chapters to put the elemental data into a molecular context because there are few measurements against which the NAMS data may be compared. A broader understanding of the molecular species important to nanoparticle growth will be developed in later chapters. However, the refinement of the molecular apportionment algorithm accomplished in the later chapters still gives conclusions in agreement with those described in Chapters 7 and 8.

7.3 Results and Discussion

7.3.1 NAMS Measurements during a Campaign in Lewes in Autumn 2007

New particle formation events were frequently observed at the field site. Figure 7.1 presents the SMPS-measured particle size distribution as a function of time for a five-day period (4-9 November 2007) during which new particle formation was observed every day. SMPS measurements were made on 23 days during the entire study period (15 October-12 November), and new particle formation events were observed on 13 of those days. Although detailed meteorological data from the field site is unavailable, some information was gained through HYSPLIT back trajectories and from meteorological data at a NOAA station approximately 3 km to the east of the site. Particle event days were usually sunny with no precipitation, whereas non-event days were cloudy with occasional precipitation. These observations suggest new particle formation was photochemically driven. Note that 6 November had significant cloudiness and some precipitation during parts of the day, which may have truncated the event. The air masses carrying particle events examined by NAMS were tracked using HYSPLIT.[13] These air masses were of continental origin from regions north and west of the site, having passed over the Washington, D.C.; Baltimore, Maryland; and/or Philadelphia, Pennsylvania, metropolitan areas. It is unlikely that emissions from the coal-fired power plant located 23 km to the south-southwest influenced these events, as air masses carrying the events uniformly arrived from the north and west of the site, and local wind directions measured 3 km from the site also were from the north and west. Wind speeds during these events ranged from 2-8 $km \cdot h^{-1}$. As illustrated in Fig. 7.1, new particle formation typically occurred in the late morning (9:00 a.m.-12:00 p.m. local time) with the abrupt appearance of particles < 10 nm

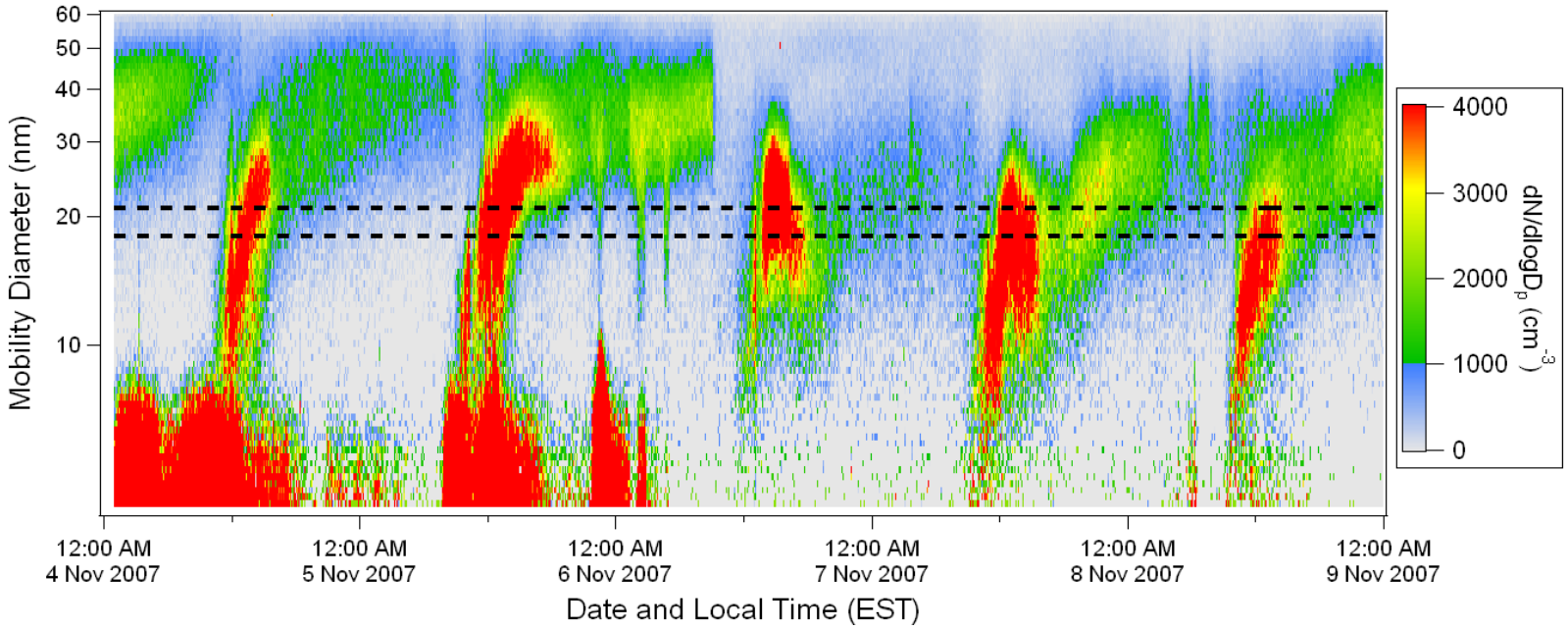

Figure 7.1: SMPS-measured contour plot of the particle size distribution for 4-9 November 2007. The dotted lines indicate the range of nanoparticle mobility diameters analyzed by NAMS.

mobility diameter followed by growth to a final mobility diameter ~40 nm. Growth rates from 10 to 25 nm mobility diameter were estimated by plotting the most intense (mode) particle diameter against local time. These data were fit linearly, and the growth rate for the event was estimated by solving the first derivative of the fit. NAMS was operational on seven of the 13 event days observed by SMPS. The results presented herein focus on those specific days (20, 21, 28 October and 4, 5, 8, 11 November). Growth rates (from 10-25 nm mobility diameter) for these days ranged from 2-6 $nm \cdot h^{-1}$ (median: 3 $nm \cdot h^{-1}$) and are provided in Table 7.2.

Table 7.2: Particle growth rates from 10-25 nm mobility diameter during the analyzed new particle formation events.

Event Date	Particle Growth Rate ($nm \cdot h^{-1}$)
20 October	3
21 October	6
28 October	3
4 November	4
5 November	2
8 November	2
11 November	2

The growth rates observed during this study are similar to those observed during many other studies of new particle formation.[14] Notably, the range of growth rates in Lewes (2-6 $nm \cdot h^{-1}$) is within the range typically observed in Hyytiälä, Finland, a remote boreal environment that has been extensively studied.[15, 16] However, the growth rates are much lower than those reported at a coastal site in Mace Head, Ireland (15-180 $nm \cdot h^{-1}$)[15, 17] and an urban site in Tecamac, Mexico (15-40 $nm \cdot h^{-1}$).[18] One potential explanation for the difference in growth rates is that different mechanisms are involved in new particle formation in these environments; however, this hypothesis would require much further exploration.

Figure 7.2 provides an average mass spectrum of particles analyzed by NAMS during a particle event (11:00 a.m.-3:30 p.m. local time) on 8 November, which is representative of the particle composition during new particle formation in Lewes. As discussed previously, the high irradiance of the laser pulse forms a plasma that disintegrates the particle into multiply-charged atomic ions. The relative signal intensities of these atomic ions give a quantitative measure of the particle elemental composition. The "limited" (i.e. unit) mass resolving power of NAMS results in some complications in interpretation of the mass spectrum, as isobaric ion signals are present at 4 *m/z* (C^{+3} and O^{+4}) and 8 *m/z* (O^{+2} and S^{+4}). A method was developed to deconvolute these isobaric ion signals.[11] Figure 7.2 also provides a pie chart that gives the relative elemental mole fractions of all particles during this event.

NAMS analysis of event days showed only small changes in average particle composition on-event compared to off-event (i.e. particle composition during the same day but before and/or after the event). Figure 7.3a illustrates how the elemental mole fractions of different elements increased or decreased in intensity during new particle formation events compared to off-event. All studied events are included in this figure, with the exception of 4 November, as no particles were analyzed off-event on this day. Median values are given by the bar, whereas the range over all studied days is given by the whiskers. These changes are related by the percent change in the elemental mole fraction on-event versus off-event. The most obvious compositional changes are a decrease in the carbon mole fraction and an increase in the nitrogen mole fraction. The median decrease in the carbon mole fraction during events was ~25%, whereas the nitrogen mole fraction increased by ~16%. These changes are of a magnitude

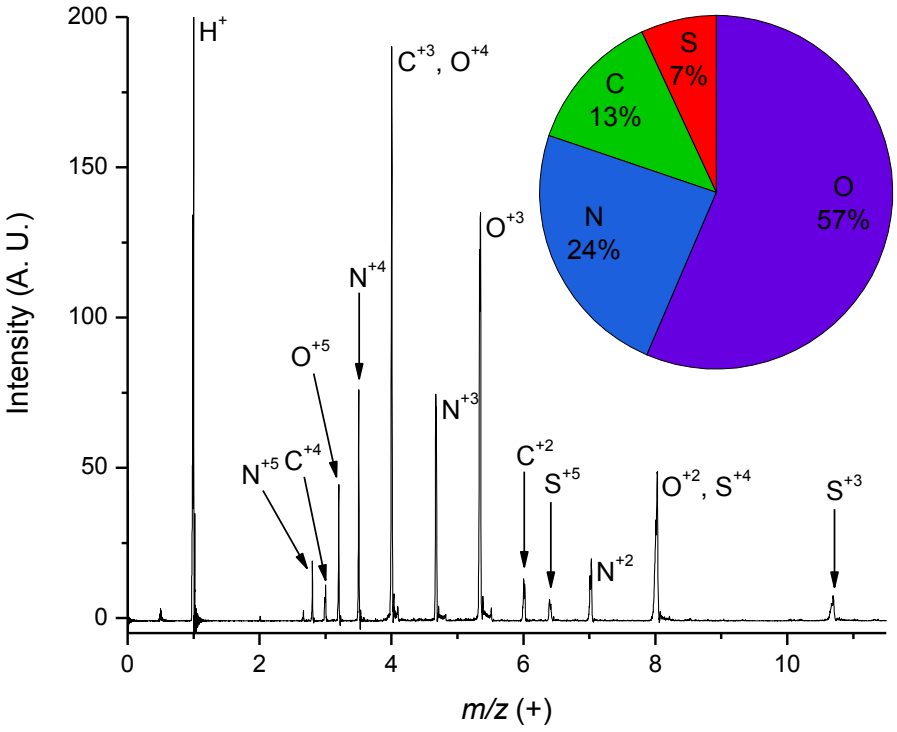

Figure 7.2: Average mass spectrum of particles analyzed by NAMS during the new particle formation event on 8 November 2007 (11:00 a.m.-3:30 p.m. local time). The pie chart gives the elemental mole fractions during this period.

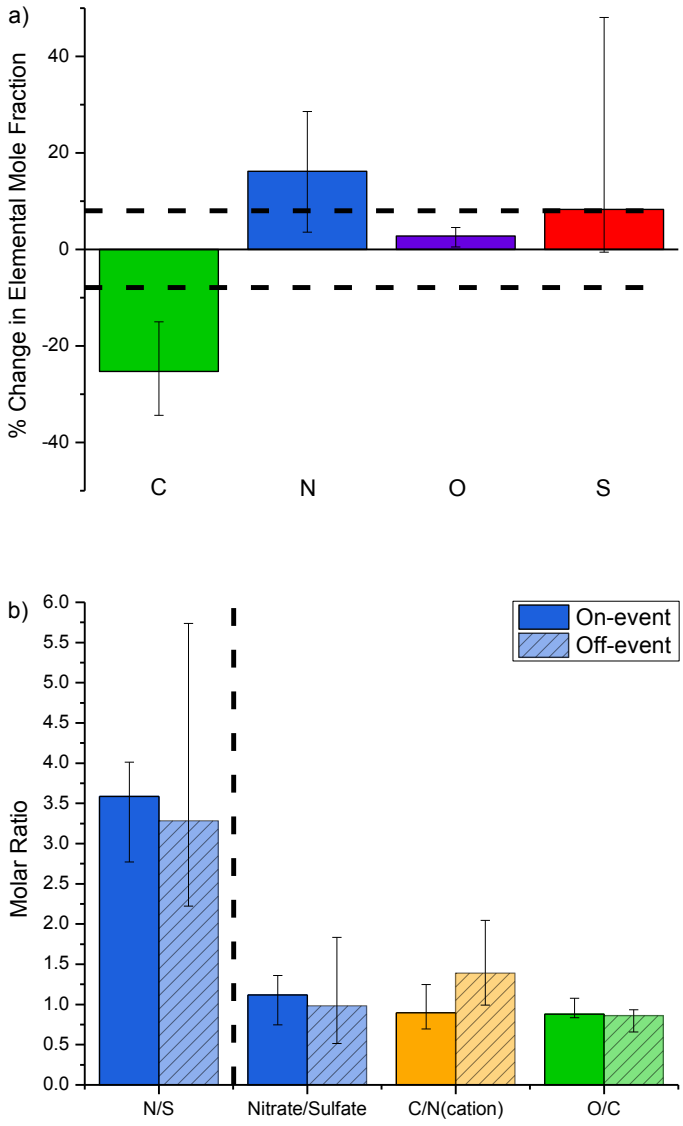

Figure 7.3: a) Comparison of the percent change in elemental mole fraction on- versus off-event. b) Comparison of the change in the molar ratios N/S, NO_3^- /SO_4^{-2}, C/N_{cation}, and O/C ratios on- versus off-event. The dotted line separates elemental ratios determined directly by NAMS (to the left) from molecular ratios inferred from the apportionment scheme (to the right). For both a) and b), median values for event days analyzed by NAMS are given by the bar. Whiskers indicate the range of values for individual days. The event on 4 November is excluded from these plots, as particle composition was not measured off-event on this day. In a), the dotted lines represent the uncertainty in elemental mole fraction measured by NAMS.

greater than the uncertainty associated with elemental composition analysis (indicated by the dotted lines in Fig. 7.2), as NAMS typically measures elemental mole ratios to within ±10%, which corresponds to an uncertainty of ~7% for individual elemental mole fractions.[11] Changes to oxygen and sulfur mole fractions were much smaller and the changes may be within the uncertainty assigned to these values, with a median increase of 3% for oxygen and 8% for sulfur during new particle formation. Note that the sulfur mole fraction in particles was always very low ($\leq$ 7% of the total elemental composition, see Table 7.3). As a result, small changes in the measured elemental sulfur mole fraction in the particles on-event relative to off-event (i.e. from 7% to 5% of the particle) sometimes translated to large percent changes in the sulfur mole fraction. This was not a complicating factor for the other elements, as their mole fractions were always much larger. The increase in nitrogen mole fraction coupled with the decrease in carbon mole fraction suggests an enhanced inorganic component to the particles during new particle formation. Table 7.3 provides particle composition on- and off-event for all studied events. A 10% uncertainty is assigned to the molar ratios.[11]

Comparison of changes in specific elemental ratios can provide some insight into changes in particle composition during new particle formation. For instance, the ratio of the number of moles of N to the number of moles of S (N/S) permits one to infer particle acidity, as two moles of N (as ammonium) would be required to fully neutralize one mole of S (as sulfate). Therefore, a molar N/S ratio < 2 indicates that not all sulfate is neutralized (acidic aerosol), whereas a molar N/S ratio $\geq$ 2 indicates that sufficient N exists to neutralize all S. Figure 7.3b presents the median N/S ratio

Table 7.3: Average on-event and off-event elemental mole fractions on new particle formation event days. Molar N/S, NO_3^-/SO_4^{-2}, C/N_{cation}, and O/C ratios indicate changes in average particle composition during events. The final column provides the number of particles analyzed in each data set. Median values exclude 4 November, where particle composition was not measured off-event.[a]

Event Date	Type	%C	%N	%O	%S	N/S	NO_3^-/SO_4^{-2}	C/N_{cation}	O/C	# particles
20 October	On-event	18 ± 1	20 ± 1	54 ± 4	7.3 ± 0.5	2.8 ± 0.3	0.75 ± 0.08	1.3 ± 0.1	0.84 ± 0.08	2717
	Off-event (a.m./p.m.)	25 ± 2	16 ± 1	52 ± 4	7.1 ± 0.5	2.2 ± 0.2	0.51 ± 0.05	2.1 ± 0.2	0.70 ± 0.07	198
21 October	On-event	14 ± 1	24 ± 2	54 ± 4	7.0 ± 0.5	3.5 ± 0.4	1.0 ± 0.1	0.88 ± 0.09	0.85 ± 0.09	1944
	Off-event (a.m./p.m.)	22 ± 2	20 ± 1	52 ± 4	6.4 ± 0.4	3.1 ± 0.3	0.81 ± 0.08	1.6 ± 0.2	0.66 ± 0.07	198
28 October	On-event	15 ± 1	23 ± 2	55 ± 4	7.3 ± 0.5	3.2 ± 0.3	0.90 ± 0.09	0.91 ± 0.09	0.88 ± 0.09	3997
	Off-event (p.m. only)	22 ± 2	18 ± 1	53 ± 4	6.5 ± 0.5	2.8 ± 0.3	0.80 ± 0.08	1.7 ± 0.2	0.85 ± 0.09	1617
4 November	On-event	14 ± 1	24 ± 2	56 ± 4	5.8 ± 0.4	4.2 ± 0.4	1.5 ± 0.2	0.90 ± 0.09	1.0 ± 0.1	338
5 November	On-event	12 ± 1	27 ± 2	55 ± 4	6.7 ± 0.5	4.0 ± 0.4	1.3 ± 0.1	0.70 ± 0.07	0.89 ± 0.09	615
	Off-event (a.m./p.m.)	15 ± 1	26 ± 2	55 ± 4	4.5 ± 0.3	5.7 ± 0.6	1.8 ± 0.2	0.99 ± 0.10	0.86 ± 0.09	78
8 November	On-event	13 ± 1	24 ± 2	57 ± 4	6.5 ± 0.5	3.7 ± 0.4	1.2 ± 0.1	0.81 ± 0.08	1.1 ± 0.1	497
	Off-event (a.m./p.m.)	16 ± 1	23 ± 2	55 ± 4	6.6 ± 0.5	3.5 ± 0.4	1.2 ± 0.1	1.1 ± 0.1	0.93 ± 0.09	183
11 November	On-event	15 ± 1	24 ± 2	55 ± 4	6.1 ± 0.4	3.9 ± 0.4	1.4 ± 0.1	0.98 ± 0.10	0.95 ± 0.10	1034
	Off-event (a.m./p.m.)	17 ± 1	22 ± 2	55 ± 4	6.1 ± 0.4	3.6 ± 0.4	1.2 ± 0.1	1.2 ± 0.1	0.91 ± 0.09	617
Median:	On-event	15 ± 1	24 ± 2	55 ± 4	6.8 ± 0.5	3.6 ± 0.4	1.1 ± 0.1	0.90 ± 0.09	0.89 ± 0.09	
	Off-event	20 ± 1	21 ± 1	54 ± 4	6.5 ± 0.5	3.3 ± 0.3	0.99 ± 0.10	1.4 ± 0.1	0.86 ± 0.09	

[a]Typically, on-event and off-event time periods each consist of four to five hours of measurements during the event day (10 hours total per event). The off-event time periods are typically split evenly between before (a.m.) and after (p.m.) the event.

on-event and off-event (left of the dotted line). The event on 4 November is excluded because particle composition was not measured off-event. Except for one day (5 November), N/S always increased during the event relative to off-event, implicating nitrogen-containing species as playing an important role in the event. Additionally, these results indicate that the aerosol (both on- and off-event) is fully neutralized according to the apportionment mechanism (Table 7.1), as N/S is always much greater than two (2 NH_4^+:1 SO_4^{-2}). Table 7.3 gives the molar N/S ratio for each event.

A molecular apportionment (Table 7.1) scheme was also applied to the elemental composition data in order to infer changes in nanoparticle molecular composition. As discussed earlier, Excess N (all N not required to neutralize sulfuric acid, = N-2S) is assumed to be in the molecular form of NH_4NO_3. Molar NO_3^-/SO_4^{-2}, C/N_{cation}, and O/C ratios are calculated. NO_3^-/SO_4^{-2} is moles of nitrate divided by moles of sulfate obtained from apportionment, C/N_{cation} is the moles of carbon (not apportioned to any molecular species in the algorithm) divided by the moles of nitrogen apportioned to ammonium, and O/C is the oxygen to carbon elemental ratio for carbonaceous matter in the particle.

In the apportionment scheme, nitrogen is apportioned to ammonium or both ammonium and ammonium nitrate depending on the amount of sulfur (assumed to be entirely sulfate) in the particle. Once all sulfate is neutralized (2 NH_4^+: 1 SO_4^{-2}), ammonium and nitrate are apportioned in a 1:1 molar ratio (1 NH_4^+: 1 NO_3^-). In this apportionment, N_{cation} represents a lower limit to the molar cationic nitrogen content of the particle. This value would increase if N served as cation to another acid, such as an organic acid, rather than as nitrate. If one assumes that all C exists as part of N-containing species (as opposed to organic acids or oxidized carbon species), the

C/N_{cation} ratio provides an upper limit for amine content in the particle. If organic acids are present, C/N_{cation} would decrease; if some N were incorrectly apportioned to nitrate, N_{cation} would increase, resulting in a decrease in C/N_{cation}.

Figure 7.3b summarizes NO_3^-/SO_4^{-2}, C/N_{cation}, and O/C (right of the dotted line) on- and off-event for six events analyzed by NAMS. Table 7.3 gives these values for each event. Not surprisingly, NO_3^-/SO_4^{-2} and N/S track each other. NO_3^-/SO_4^{-2} always increased during new particle formation, except for the event on 5 November. NO_3^-/SO_4^{-2} ratios indicate that both species are significant and sometimes equally important components of the aerosol on a molar basis, as NO_3^-/SO_4^{-2} values ranged from 0.7 to 1.4 during new particle formation. This range of values is in qualitative agreement with TDCIMS measurements of nitrate and sulfate ion signal intensities during new particle formation in Tecamac, Mexico, and Hyytiälä, Finland.[19, 20] In Lewes, C/N_{cation} always decreased relative to off-event composition during new particle formation. The increases in N/S and NO_3^-/SO_4^{-2}, coupled with the observed decrease in C/N_{cation} suggest an increase of inorganic components during new particle formation in Lewes. In particular, these results implicate additional nitrogen-containing species (apportioned here to ammonium nitrate) as playing important roles in the events, as the nitrogen content increases during new particle formation while carbon content decreases. This important role of nitrogen will be explored further in Chapters 9 and 10.

Whereas changes in N/S, NO_3^-/SO_4^{-2}, and C/N_{cation} suggest an important role of nitrogen-containing species in addition to ammonium during new particle formation in Lewes, one cannot exclude the possibility that amines are also important components of these particles. This is evidenced by a substantial carbon mole fraction (see Figure

7.2). For example, the median value of C/N_{cation} is 0.90 during new particle formation events. If one assumes that monomethylamine (CH_3NH_2; C/N = 1:1) is the only amine present, then up to 90% of the N_{cation} could be composed of monomethylammonium. If one assumes that trimethylamine ($(CH_3)_3N$; C/N = 3:1) is the only amine present in the particle, then up to 30% of the N_{cation} could consist of trimethylammonium. These values should only be considered as upper limits for amine content. Actual amine content could be much lower but would require quantitative molecular composition measurements.

It is noteworthy that the O/C ratio only slightly increased during new particle formation and that it was always very high (> 0.8) during new particle formation, which indicates a significant component of highly oxidized organics in these particles. The exact character of organic species in these nanoparticles is uncertain, as NAMS only gives the elemental composition. It is possible, for example, that much of the carbonaceous species contributing to the higher C/N_{cation} ratio off-event is the result of organics partitioning to the particle phase, whereas during particle events the overall character of the organic material shifts to amines and/or organic acids.

The NAMS data provide important insight into nanoparticle composition during new particle formation. The elemental compositions on- versus off-event are quite similar, suggesting that decreases observed in ultrafine particle volatility and hygroscopicity during new particle formation[19, 21-24] are either linked to subtle changes in particle composition (e.g. a thin coating on the particle surface) or to shifts in the character of the organic content (e.g. an enhanced amine/organic acid component). In this regard, TDCIMS measurements in Tecamac and Hyytiälä show that the relative ion signals of individual molecular species can change by a factor of two or more

during new particle formation.[19, 20] Note that the NAMS spectra did not indicate the presence of any higher atomic weight species such as Na, Cl, or I that might influence the physical properties of the particles. However, the sensitivity of the instrument to these elements has not been fully explored. The observations presented here are for several event days over the period of a month, whereas most discussions of new particle formation in the literature tend to focus on only one day in specific. The consistency in observations from one event to the next suggests that these results are representative of Lewes, Delaware, in autumn.

7.3.2 NAMS Measurements during a Campaign in Wilmington in Summer 2009

NAMS was also deployed to an urban site in Wilmington, Delaware, during summertime. New particle formation events were observed on four days during this campaign. For these events, growth rates were significantly higher than those observed in Lewes and ranged from 6 to 10 $nm \cdot h^{-1}$ (Table 7.4). Figure 7.4 illustrates the median change in elemental composition during the events relative to periods before and after the events. Whiskers represent the range of values for individual events. Similar to Lewes, the carbon content decreased during events, though in Wilmington the decrease was much more significant. Additionally, oxygen, nitrogen, and sulfur all increased during events. These observations are consistent with those in Lewes, as particles appear to have enhanced concentrations of the inorganic species during new particle formation. In Wilmington, however, changes in sulfur content appear to be the most significant. Apportionment of the elemental data to molecular species indicates that sulfate constituted 41-46% of the particle mass, whereas nitrate (proxy for Excess N) constituted only 7-8% of the mass. The low apportioned nitrate content is

Table 7.4: Properties of new particle formation events in Wilmington.

Event Date	Growth Rate ($nm \cdot h^{-1}$)
1 July	9
8 July	6
10 July	10
14 July	6

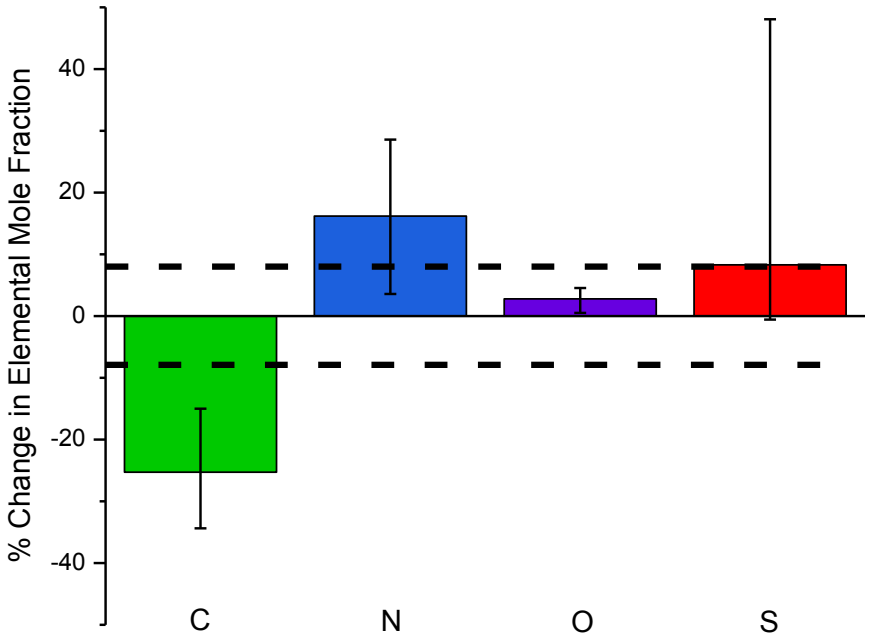

Figure 7.4: Comparison of the percent change in elemental mole fraction on-event relative to off-event (before and after the event) for new particle formation events in Wilmington. Dotted lines indicate the uncertainty in the NAMS elemental mole fraction measurement.

consistent with the observation that particles in Wilmington tended to be more acidic than those in Lewes, as indicated by N/S elemental ratios less than 2 (Table 7.5). Ammonium accounted for 11-12% of the particle mass, and organics were 25-36% of the particle mass. Overall, the observations in Wilmington are consistent with those from Lewes.

Table 7.5: Chemical composition data during new particle formation ("On") and before/after new particle formation ("Off") in Wilmington, Delaware.

			Mole Fraction					Mole Ratio
Date		# Particles	C	O	N	S	Si	N/S
1 July	On	347	22%	51%	16%	12%	0.33%	1.4
	Off	225	43%	41%	9.9%	5.2%	1.7%	1.9
8 July	On	428	27%	48%	15%	9.3%	0.12%	1.6
	Off	270	34%	42%	15%	8.9%	0.38%	1.6
10 July	On	683	17%	53%	17%	12%	0.69%	1.5
	Off	304	42%	41%	10%	6.2%	1.3%	1.6
14 July	On	173	24%	49%	16%	11%	0.15%	1.4
	Off	526	31%	45%	14%	8.9%	0.61%	1.6

7.4 Conclusions

In conclusion, NAMS measurements were performed in two separate environments, one rural/coastal and one urban, to determine quantitatively the elemental composition of ambient nanoparticles during new particle formation events. In both environments, the chemical composition shifted towards elements indicative of a higher inorganic content. Generally, both sulfur and nitrogen mole fractions increased in relative abundance, whereas carbon mole fraction decreased in relative abundance. Application of a molecular apportionment algorithm designed to place the

elemental composition in a molecular context indicates the relative contributions of different molecular species to nanoparticle growth during new particle formation. Based on the apportioned data, sulfate can explain a considerable portion, but not all, of the observed particle growth. Future work is needed to assess more quantitatively the specific changes in molecular composition during new particle formation and in particular to explore the role of nitrogen (in the molecular forms of ammonium, aminium, nitrate, or organic nitrogen) in particle growth in Lewes.

7.5 References

1. Luther, G. W.; Stecher, H. A., Preface: Historical background. *J. Geophys. Res.-Atmos.* **1997,** *102* (D13), 16215-16217, doi: 10.1029/96JD03986.

2. Stecher, H. A.; Luther, G. W.; MacTaggart, D. L.; Farwell, S. O.; Crosley, D. R.; Dorko, W. D.; Goldan, P. D.; Beltz, N.; Krischke, U.; Luke, W. T.; Thornton, D. C.; Talbot, R. W.; Lefer, B. L.; Scheuer, E. M.; Benner, R. L.; Wu, J. G.; Saltzman, E. S.; Gallagher, M. S.; Ferek, R. J., Results of the gas-phase sulfur intercomparison experiment (GASIE): Overview of experimental setup, results and general conclusions. *J. Geophys. Res.-Atmos.* **1997,** *102* (D13), 16219-16236, doi: 10.1029/97JD01362.

3. Dreyfus, M. A.; Johnston, M. V., Rapid sampling of individual organic aerosol species in ambient air with the photoionization aerosol mass spectrometer. *Aerosol Sci. Technol.* **2008,** *42* (1), 18-27.

4. Klems, J. P.; Pennington, M. R.; Zordan, C. A.; Johnston, M. V., Ultrafine particles near a roadway intersection: Origin and apportionment of fast changes in concentration. *Environ. Sci. Technol.* **2010,** *44* (20), 7903-7907.

5. Klems, J. P.; Pennington, M. R.; Zordan, C. A.; McFadden, L.; Johnston, M. V., Apportionment of motor vehicle emissions from fast changes in number concentration and chemical composition of ultrafine particles near a roadway intersection. *Environ. Sci. Technol.* **2011,** *45* (13), 5637-5643.

6. Reinard, M. S.; Adou, K.; Martini, J. M.; Johnston, M. V., Source characterization and identification by real-time single particle mass spectrometry. *Atmos. Environ.* **2007,** *41* (40), 9397-9409.

7. Zordan, C. A.; Wang, S.; Johnston, M. V., Time-resolved chemical composition of individual nanoparticles in urban air. *Environ. Sci. Technol.* **2008,** *42* (17), 6631-6636.

8. Klems, J. P.; Zordan, C. A.; Pennington, M. R.; Johnston, M. V., Chemical composition of ambient nanoparticles on a particle-by-particle basis. *Anal. Chem.* **2012,** *84* (5), 2253-2259.

9. Wang, S. Y.; Johnston, M. V., Airborne nanoparticle characterization with a digital ion trap-reflectron time of flight mass spectrometer. *Int. J. Mass Spectrom.* **2006,** *258* (1-3), 50-57.

10. Wang, S. Y.; Zordan, C. A.; Johnston, M. V., Chemical characterization of individual, airborne sub-10-nm particles and molecules. *Anal. Chem.* **2006,** *78* (6), 1750-1754.

11. Zordan, C. A.; Pennington, M. R.; Johnston, M. V., Elemental composition of nanoparticles with the Nano Aerosol Mass Spectrometer. *Anal. Chem.* **2010,** *82* (19), 8034-8038.

12. McMurry, P. H.; Ghimire, A.; Ahn, H. K.; Sakurai, H.; Moore, K.; Stolzenburg, M.; Smith, J. N., Sampling nanoparticles for chemical analysis by low resolution electrical mobility classification. *Environ. Sci. Technol.* **2009,** *43* (13), 4653-4658.

13. Draxler, R. R.; Rolph, G. D. *HYSPLIT (HYbrid Single-Particle Lagrangian Integrated Trajectory) Model access via NOAA ARL READY Website (http://ready.arl.noaa.gov/HYSPLIT.php)*, NOAA Air Resources Laboratory: Silver Spring, MD, 2013.

14. Kulmala, M.; Vehkamaki, H.; Petaja, T.; Dal Maso, M.; Lauri, A.; Kerminen, V. M.; Birmili, W.; McMurry, P. H., Formation and growth rates of ultrafine atmospheric particles: A review of observations. *J. Aerosol Sci.* **2004,** *35* (2), 143-176.

15. Dal Maso, M.; Kulmala, M.; Lehtinen, K. E. J.; Makela, J. M.; Aalto, P.; O'Dowd, C. D., Condensation and coagulation sinks and formation of nucleation mode particles in coastal and boreal forest boundary layers. *J. Geophys. Res.-Atmos.* **2002,** *107* (D15), 8097, doi: 10.1029/2001jd001053.

16. Dal Maso, M.; Kulmala, M.; Riipinen, I.; Wagner, R.; Hussein, T.; Aalto, P. P.; Lehtinen, K. E. J., Formation and growth of fresh atmospheric aerosols: eight years of aerosol size distribution data from SMEAR II, Hyytiala, Finland. *Boreal Environ. Res.* **2005,** *10* (5), 323-336.

17. O'Dowd, C. D.; Yoon, Y. J.; Junkerman, W.; Aalto, P.; Kulmala, M.; Lihavainen, H.; Viisanen, Y., Airborne measurements of nucleation mode particles I: coastal nucleation and growth rates. *Atmos. Chem. Phys.* **2007,** *7* (6), 1491-1501.

18. Iida, K.; Stolzenburg, M. R.; McMurry, P. H.; Smith, J. N., Estimating nanoparticle growth rates from size-dependent charged fractions: Analysis of new particle formation events in Mexico City. *J. Geophys. Res.-Atmos.* **2008,** *113* (D5), D05207, doi: 10.1029/2007jd009260.

19. Smith, J. N.; Barsanti, K. C.; Friedli, H. R.; Ehn, M.; Kulmala, M.; Collins, D. R.; Scheckman, J. H.; Williams, B. J.; McMurry, P. H., Observations of aminium salts in atmospheric nanoparticles and possible climatic implications. *Proc. Natl. Acad. Sci. U.S.A.* **2010,** *107* (15), 6634-6639.

20. Smith, J. N.; Dunn, M. J.; VanReken, T. M.; Iida, K.; Stolzenburg, M. R.; McMurry, P. H.; Huey, L. G., Chemical composition of atmospheric nanoparticles formed from nucleation in Tecamac, Mexico: Evidence for an important role for organic species in nanoparticle growth. *Geophys. Res. Lett.* **2008,** *35* (4), L04808, doi: 10.1029/2007gl032523.

21. Ehn, M.; Petaja, T.; Birmili, W.; Junninen, H.; Aalto, P.; Kulmala, M., Non-volatile residuals of newly formed atmospheric particles in the boreal forest. *Atmos. Chem. Phys.* **2007,** *7* (3), 677-684.

22. Asmi, E.; Frey, A.; Virkkula, A.; Ehn, M.; Manninen, H. E.; Timonen, H.; Tolonen-Kivimaki, O.; Aurela, M.; Hillamo, R.; Kulmala, M., Hygroscopicity and chemical composition of Antarctic sub-micrometre aerosol particles and observations of new particle formation. *Atmos. Chem. Phys.* **2010,** *10* (9), 4253-4271.

23. Dusek, U.; Frank, G. P.; Curtius, J.; Drewnick, F.; Schneider, J.; Kurten, A.; Rose, D.; Andreae, M. O.; Borrmann, S.; Poschl, U., Enhanced organic mass fraction and decreased hygroscopicity of cloud condensation nuclei (CCN) during new particle formation events. *Geophys. Res. Lett.* **2010,** *37* (3), L03804, doi: 10.1029/2009gl040930.

24. Riipinen, I.; Manninen, H. E.; Yli-Juuti, T.; Boy, M.; Sipila, M.; Ehn, M.; Junninen, H.; Petaja, T.; Kulmala, M., Applying the Condensation Particle Counter Battery (CPCB) to study the water-affinity of freshly-formed 2-9 nm particles in boreal forest. *Atmos. Chem. Phys.* **2009,** *9* (10), 3317-3330.

Chapter 8

QUANTITATIVE ASSESSMENT OF THE SULFURIC ACID CONTRIBUTION TO NEW PARTICLE GROWTH

8.1 Introduction

Chapter 7 examined how the composition of nanoparticles changed during new particle formation events in two environments. In this chapter, changes in nanoparticle elemental composition are quantitatively linked to gas phase concentrations. Specifically, the sulfur mole fraction measured by the Nano Aerosol Mass Spectrometer (NAMS) can be used to quantitatively describe the gas phase sulfuric acid concentration during a new particle formation event. The capability to link the two relies critically on the assumption that the molecular form of particle phase sulfur is sulfuric acid. This assumption is evaluated and shown to be reasonable in this chapter. Linking gas and particle phase composition (in this case gas phase sulfuric acid to particle phase sulfur) is very significant, as it explicitly defines the mechanism for sulfuric acid uptake onto nanoparticles and thereby solves one key mechanism governing new particle growth. With such knowledge in hand, modelers are also enabled to explore the effect of changes in gas phase sulfuric acid concentrations on nanoparticle growth rates and the resulting impacts on climate.

8.2 Experimental Section

Nanoparticle chemical composition and particle size distribution measurements were performed at two field sites: one in Lewes, Delaware, from 15 October 2007 to

12 November 2007 and the other in Wilmington, Delaware, from 1 July 2009 to 15 July 2009. Detailed descriptions of the field sites and measurement campaigns are discussed in Chapter 7.

Ambient nanoparticle chemical composition measurements were performed by NAMS, which gives a quantitative measure of the elemental composition of individual size-selected nanoparticles in the 7-30 nm diameter size range.[1, 2] The operating principles of NAMS have been described in detail in Chapters 1 and 7. In the Lewes study, 21 nm mass normalized diameter particles were sampled throughout the campaign;[3] in the Wilmington study, 25 nm mass normalized diameter particles were sampled throughout the campaign.[4]

Particle size distributions were measured in both campaigns using a scanning mobility particle sizer (electrostatic classifier model 3080, condensation particle counter model 3025a, TSI, Inc., St. Paul, Minnesota). Growth rates from 10 to 25 nm diameter during new particle formation events were determined by plotting the most intense (mode) particle diameter against local time. These data were fit linearly, and the growth rate for a particular event was estimated by solving the first derivative of the linear fit.

8.3 Results and Discussion

The main observations regarding changes in nanoparticle elemental composition during new particle formation in Lewes were discussed in Chapter 7.[3] Briefly, during events, nanoparticle elemental composition shifted towards a more inorganic content: nitrogen content increased by ~15% whereas carbon content decreased by ~25%. Oxygen content remained about the same and during some events

sulfur content increased but the median change was within the uncertainty assigned to NAMS measurements (10%).

Figure 8.1a presents an average mass spectrum for nanoparticles analyzed during a new particle formation event in Lewes on 20 October 2007. Figure 8.1b shows the average (molar) elemental composition over the time period of the event. From the elemental composition, one can infer the molecular composition based upon knowledge of the major constituents that are typically found in ambient nanoparticles: sulfate, nitrate, ammonium, and carbonaceous matter. The assumptions underlying the apportionment algorithm are described in detail in Chapter 7.[3] Briefly, sulfur and a stoichiometric amount of oxygen are apportioned to sulfate (1 S:4 O). Nitrogen is then apportioned as ammonium to neutralize the sulfate (2 N:1 S). Any remaining nitrogen not required to neutralize sulfuric acid (i.e. Excess N = N-2S) is assigned as ammonium nitrate using a stoichiometric amount of oxygen (2 N:3 O). The major uncertainty in the apportionment algorithm is the apportionment of the nitrogen signal to ammonium and nitrate. The appropriateness of this assumption will be explored in detail in Chapters 9 and 10. However, the main focus of this chapter is the apportionment of the sulfur signal to sulfate and the appropriateness of this assumption. For the event on 20 October 2007, sulfate constitutes 36% of the particle mass, as shown in Figure 8.1c.

Because NAMS is quantitative in elemental composition,[5] it should also be quantitative in apportioned sulfate, especially during new particle formation, for

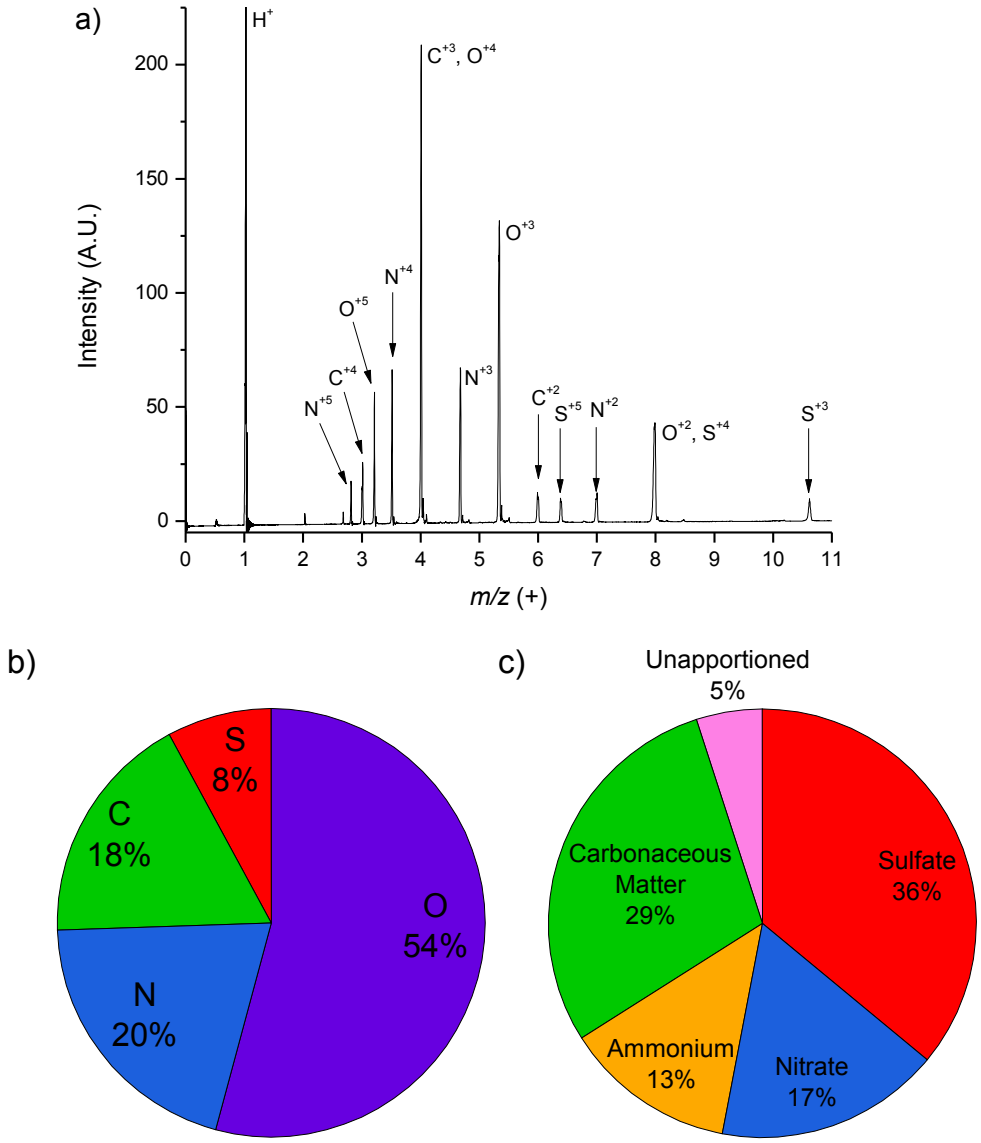

Figure 8.1: a) Average elemental mass spectrum of particles analyzed by NAMS for the new particle formation event on 20 October 2007 (10:40 a.m.-6:20 p.m. local time) in Lewes. b) Pie chart indicating elemental mole fractions during this event. c) Pie chart indicating relative mass fractions of molecular species during the event determined by apportionment of the elemental data.

several reasons. First, off-line molecular composition analysis of collected ultrafine particles in urban and rural environments indicates sulfate as a major constituent in these particles, with little to no contribution from other sulfur-containing species.[6-9] Second, on-line molecular analysis of ultrafine particles formed during new particle formation events indicate sulfate as a significant fraction of overall particle composition, again to the exclusion of other sulfur-containing species.[10-13] Third, new particle formation is thought to be driven by sulfuric acid,[14, 15] so particulate sulfate is a reasonable species to expect in particles arising from atmospheric new particle formation. Fourth, although organosulfates have been detected in 50-100 nm diameter particles in some environments,[16] quantitative measurements of the organosulfate contribution to ultrafine particle mass indicate that organosulfate content is very low.[17] Moreover, if organosulfates are present in an ultrafine nanoparticle, they are probably the result of aqueous-phase secondary processing of sulfate already contained in the particle and would be most significant during nighttime, rather than during daytime when new particle formation would occur.[18] Apportionment of sulfur from an organosulfate to inorganic sulfate (as would occur using the apportionment algorithm) will therefore still give a correct measure of the total sulfate in the particle from which the organosulfate was derived. Finally, S(IV) compounds such as SO_2, bisulfite, and sulfite, which may be significant in large particles such as cloud and fog droplets[19] or mineral dust,[20, 21] are unlikely to constitute a significant fraction of sulfur species in ultrafine aerosol.[22] Therefore, because of the very tight constraint on the variety of sulfur-containing species in ultrafine particles, apportioning all sulfur to sulfate is reasonable, especially for particles analyzed in the daytime during new particle

formation, and since NAMS is quantitative in sulfur, it should also be quantitative in apportioned sulfate.

Gas phase species contributing to nanoparticle growth during new particle formation are represented in the particle phase mass fraction according to each gas phase species's relative contribution to the growth of that particle. Figure 8.2 presents apportioned molecular mass fractions scaled to the growth rate during seven new particle formation events in Lewes. Sulfate constitutes a significant fraction of particle mass (29-36%) during these events. Nitrate (serving here as a proxy for addition nitrogen-containing species) also appears to be an important component of the particle mass (17-27%), as does ammonium (12-15%). Finally, carbonaceous matter constitutes 19-29% of the particle mass during these events. While there are minor chemical variations that contribute to small differences in the growth rates for individual chemical species in Lewes, chemical composition changes did not correlate with growth rate even though substantial changes to the magnitude of the growth rate were observed. This observed lack of correlation suggests 1) that a consistent source exists for all events (i.e. similar air masses, same season, same location[3]) and 2) that the driving forces affecting particle growth are physical (i.e. solar radiation, mixing, meteorology) rather than chemical and impact all chemical constituents of the particle in a roughly similar manner.

It is notable that although sulfate constitutes a significant fraction of the particle mass during these new particle formation events, it is clearly not the only species contributing to growth. The contribution of sulfuric acid to particle growth during new particle formation has been quantified through the parameter Γ_v, which

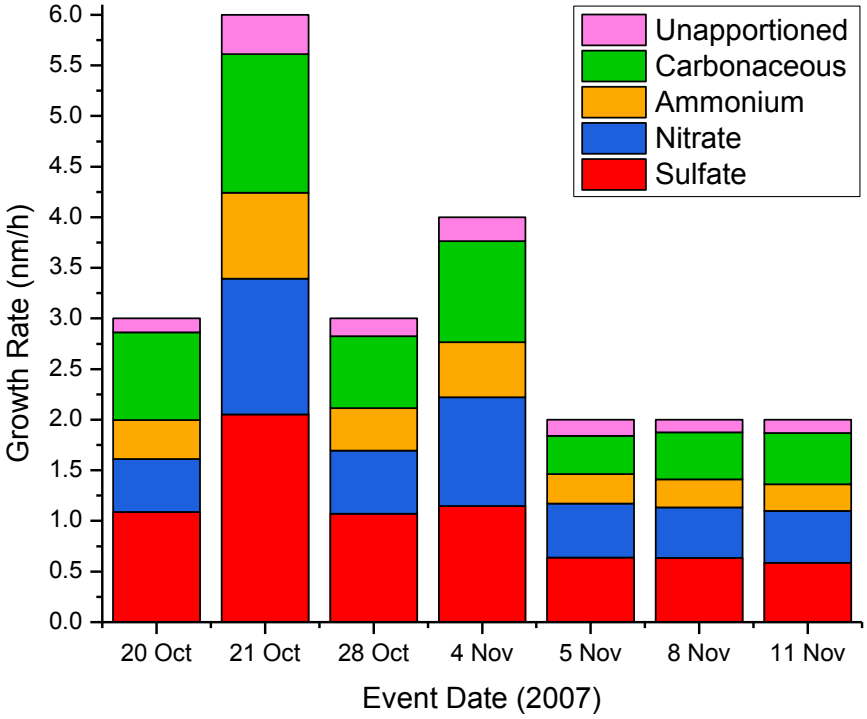

Figure 8.2: Apportioned mass fractions for particles analyzed during each individual event in Lewes scaled to the measured growth rate for that event.

represents the contribution of sulfuric acid condensation to nanoparticle growth.[23] Γ_v is calculated by dividing the measured growth rate by the growth rate for free-molecular condensation of sulfuric acid[24] and is given by:

$$\Gamma_v = \frac{2GR_{MEAS}}{\nu_1[H_2SO_4]\bar{c}_1} \quad (1)$$

where GR_{MEAS} is the measured growth rate ($nm \cdot h^{-1}$), $[H_2SO_4]$ is the number concentration of gas phase sulfuric acid ($molec \cdot cm^{-3}$), ν_1 is the volume occupied by a hydrated H_2SO_4 molecule (estimated at 1.7×10^{-22} cm^3), and $\bar{c}_1$ is the mean thermal speed of the condensing monomer ($nm \cdot h^{-1}$). This equation assumes knowledge of the gas phase concentration of sulfuric acid and gives a measure of the contribution of sulfate to the volume growth of the particles, hence the "v" subscript in Γ_v.

NAMS provides a quantitative measure of the contribution of sulfuric acid (i.e. sulfate) to the mass growth of the particles. The mass contribution of sulfuric acid to growth is given by:

$$\Gamma_m = \frac{m_{particle}}{m_{sulfate}} = \frac{1}{MF_{sulfate}} \quad (2)$$

where $m_{particle}$ is the total mass of the analyzed particles during the event, $m_{sulfate}$ is the total mass of sulfate in those analyzed particles, and $MF_{sulfate}$ is the average sulfate mass fraction for the event. Note that Γ_m is a mass-based description of the Γ parameter, whereas Γ_v is volume-based.

Table 8.1 gives Γ_m values for each studied event day in Lewes. Γ_m ranges from 2.8 to 3.5. If Γ_m were equal to one, this would indicate that all particle growth can be described by condensation of sulfuric acid (i.e. a sulfuric acid particle). However, for these events sulfuric acid accounts for only 29-36% of the measured particle growth, though sulfate is the most important individual species contributing to growth in this environment.

Table 8.1: Properties of new particle formation events in Lewes.

Date	Temperature (°C)	Growth Rate ($nm \cdot h^{-1}$)	Γ_m [a]	$[H_2SO_4]_{NAMS}$ ($molec \cdot cm^{-3}$) [b]
20 October	23	3	2.8	1.3×10^7
21 October	23	6	2.9	2.4×10^7
28 October	15	3	2.8	1.3×10^7
4 November	14	4	3.5	1.3×10^7
5 November	17	2	3.1	7.4×10^6
8 November	9	2	3.2	7.4×10^6
11 November	10	2	3.4	6.8×10^6

[a]An uncertainty of 10% is assigned to this value. [b]Assumes a particle density consistent with the apportioned molecular mass (ρ = 1.6 $g \cdot cm^{-3}$). As discussed in the text, an uncertainty of 30% is assigned to these values.

The relationship between Γ_m and Γ_v is given by:

$$\Gamma_v = \Gamma_m \times \frac{\rho_{sulfate}}{\rho_{particle}} \quad (3)$$

where $\rho_{sulfate}$ is the density of sulfuric acid or ammonium sulfate and $\rho_{particle}$ is the density of the particle. Table 8.2 shows how density affects the calculation of Γ_v from Γ_m. In the first case, the density of the particle was assumed to be equivalent to the density of ammonium sulfate (i.e. uniform density throughout the particle).[25] In this case, Γ_v is equivalent to Γ_m and can be considered a lower bound to Γ_v. In the second case, the particle density (ρ = 1.6 g·cm^{-3}) was calculated based on the relative abundance of the apportioned molecular species (ammonium sulfate, ammonium nitrate, and carbonaceous matter) assuming a density of 1.3 g·cm^{-3} for ambient organic matter.[26, 27] In this case, Γ_v is about 10% larger than Γ_m. This case can be considered a best estimate of the particle density, as it assumes that the apportionment accurately captures the relative contributions of the molecular species present in the particle. In the third and final case, the non-sulfate portion of the particle was assumed to be completely organic (ρ = 1.3 g·cm^{-3}), so the overall density of the particle was 1.4 g·cm^{-3}. This can be considered an upper limit to Γ_v, as the particle density differs significantly from the density of sulfuric acid. In this limiting scenario, Γ_v is about 30% larger than Γ_m.

Γ_m can be used to calculate the sulfuric acid concentration necessary to incorporate the measured amount of sulfate by rearranging Eq. (1) and adjusting for the particle density:

$$[H_2SO_4] = \frac{2GR_{MEAS}}{\nu_1 \bar{c}_1 \Gamma_m} \times \frac{\rho_{particle}}{\rho_{sulfate}} \quad (4)$$

Table 8.2: Sensitivity of Γ_v to particle density for the event on 20 October 2007. For this event, $\Gamma_m = 2.8$.

Density ($g \cdot cm^{-3}$)	Γ_v	$[H_2SO_4]_{NAMS}$ ($molec \cdot cm^{-3}$)
1.8[a]	2.8	1.4×10^7
1.6[b]	3.1	1.3×10^7
1.4[c]	3.6	1.1×10^7

[a]Particle density assumed to be equivalent to that of ammonium sulfate. [b]Non-ammonium sulfate particle mass split between ammonium nitrate ($\rho = 1.7\ g \cdot cm^{-3}$) and organics ($\rho = 1.3\ g \cdot cm^{-3}$) using the apportionment algorithm. [c]Non-sulfate particle mass assumed to be entirely organic ($\rho = 1.3\ g \cdot cm^{-3}$).

Table 8.1 provides calculated values of $[H_2SO_4]$ (listed as $[H_2SO_4]_{NAMS}$) from the NAMS nanoparticle composition measurements using Γ_m determined for each event and a particle density of 1.6 $g \cdot cm^{-3}$. $[H_2SO_4]_{NAMS}$ ranged from 6.8×10^6 to 2.4×10^7 $molec \cdot cm^{-3}$. Based on the uncertainty in the direct measurement of Γ_m by NAMS (10%) and the relatively low sensitivity of Γ_v to particle density (< 30%), an overall uncertainty of 30% is assigned to the calculated $[H_2SO_4]_{NAMS}$ values. Although no gas phase measurements were available at this location for comparison to $[H_2SO_4]_{NAMS}$, the calculated $[H_2SO_4]_{NAMS}$ values are within the range typically observed during new particle formation.[23]

NAMS was also deployed to an urban site in Wilmington, Delaware, where measurements of gas phase species were also taken for comparison to $[H_2SO_4]_{NAMS}$. New particle formation events were observed on four days during this campaign. Concurrent with NAMS measurements were some gas phase measurements that permit comparison to $[H_2SO_4]_{NAMS}$. For these events, growth rates were significantly higher than those observed in Lewes and ranged from 6 to 10 $nm \cdot h^{-1}$ (Table 8.3). As discussed in Chapter 7, during new particle formation in Wilmington, inorganic components (sulfur and nitrogen) increase in relative abundance whereas organic components (carbon) decrease in relative abundance. These observations are consistent with those in Lewes, as particles appear to have enhanced concentrations of the inorganic species during new particle formation. Apportionment of the elemental data to molecular species indicates that sulfate constituted 41-46% of the particle mass, whereas apportioned nitrate constituted only 7-8% of the mass. The low nitrate content is consistent with the observation that particles in Wilmington tended to be

Table 8.3: Properties of new particle formation events in Wilmington.

Date	Temperature (°C)	Growth Rate ($nm \cdot h^{-1}$)	Γ_m [a]	$[H_2SO_4]_{NAMS}$ ($molec \cdot cm^{-3}$) [b]	$[H_2SO_4]_{proxy}$ ($molec \cdot cm^{-3}$) [c]
1 July	29	9	2.3	4.5×10^7	4.6×10^7
8 July	25	6	2.4	3.0×10^7	2.8×10^7
10 July	26	10	2.2	5.2×10^7	N.A. [d]
14 July	28	6	2.3	3.2×10^7	4.5×10^7

[a]An uncertainty of 10% is assigned to this value. [b]Assumes a particle density consistent with the apportioned molecular mass ($\rho = 1.6\ g \cdot cm^{-3}$). As discussed in the text, an uncertainty of 30% is assigned to these values. [c]An uncertainty of 50% is assigned to this value as described in ref. 28. [d]SO_2 was not measured on this date.

more acidic than those in Lewes, as indicated by N/S elemental ratios less than 2 (Table 8.4). Ammonium accounted for 11-12% of the particle mass, and carbonaceous matter was 25-36% of the particle mass.

Figure 8.3 presents the scaled contributions of apportioned molecular species to particle growth for new particle formation events in Wilmington. As also seen in Lewes, no major shifts in the relative contributions of each molecular species are observed as a function of growth rate. This observation suggests that the main driving force(s) (i.e. photochemistry, mixing, meteorology) affecting particle growth impact all chemical constituents of the particle, and not just one individual species.

Γ_m and $[H_2SO_4]_{NAMS}$ values for Wilmington are presented in Table 8.3. Relative to Lewes, sulfate contributed more significantly to particle growth (larger mass fraction, smaller Γ_m), which is expected as Wilmington represents an urban environment highly influenced by local and regional industrial emissions. The lower Γ_m values, combined with higher particle growth rates, result in a higher range of calculated $[H_2SO_4]_{NAMS}$ (2.8-4.6 $\times$ 10^7 molec·cm^{-3}). Although gas phase measurements of sulfuric acid were not made during this campaign, SO_2 and solar radiation were measured. Recently, a statistical proxy for sulfuric acid ($[H_2SO_4]_{proxy}$) was developed whereby the gas phase concentration can be estimated from solar radiation, SO_2 concentration, and a temperature-dependent rate constant.[28] This proxy is an empirical equation capable of reproducing sulfuric acid concentrations in environments ranging from urban to remote throughout the world. The most general form of the proxy [given by Eq. (12) in ref. 28] is applied:

$$[H_2SO_4]_{proxy} = (1.86\times10^{-1})\cdot(k\times10^{12})\cdot\text{Radiation}\cdot[SO_2]^{0.5} \quad (5)$$

Table 8.4: Chemical composition data during new particle formation ("On") and before/after new particle formation ("Off") in Wilmington, Delaware.

Date		# Particles	Mole Fraction C	O	N	S	Si	Mole Ratio N/S	Average $[SO_2]$ (molec·cm^{-3})	Average Solar Radiation (W·m^{-2})
1 July	On	347	22%	51%	16%	12%	0.33%	1.4	8×10^{10}	730
	Off	225	43%	41%	9.9%	5.2%	1.7%	1.9		
8 July	On	428	27%	48%	15%	9.3%	0.12%	1.6	4.0×10^{10}	630
	Off	270	34%	42%	15%	8.9%	0.38%	1.6		
10 July	On	683	17%	53%	17%	12%	0.69%	1.5	not measured	not measured
	Off	304	42%	41%	10%	6.2%	1.3%	1.6		
14 July	On	173	24%	49%	16%	11%	0.15%	1.4	1.1×10^{11}	710
	Off	526	31%	45%	14%	8.9%	0.61%	1.6		

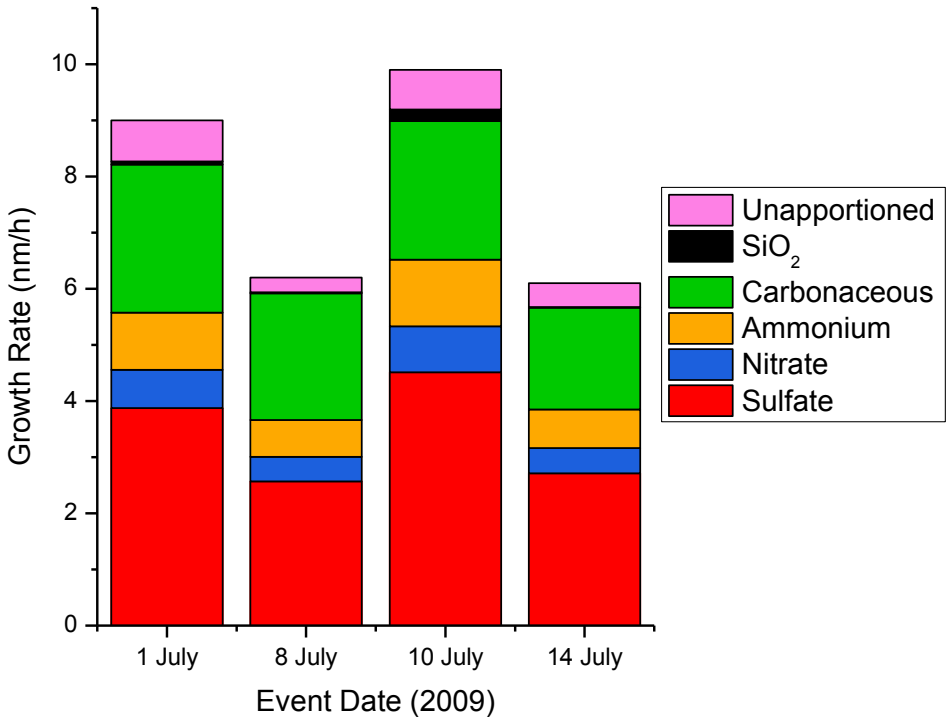

Figure 8.3: Apportioned mass fractions for particles analyzed during each individual event in Wilmington scaled to the measured growth rate for that event.

where k is the temperature-dependent rate constant ($cm^3 \cdot molec^{-1} \cdot s^{-1}$), Radiation is solar radiation ($W \cdot m^{-2}$), and $[SO_2]$ is the concentration of gas phase SO_2 ($molec \cdot cm^{-3}$). Hourly estimates for $[H_2SO_4]_{proxy}$ were calculated on event days. $[H_2SO_4]_{proxy}$ values during the time period of each event are given in Table 8.3. These values agree with $[H_2SO_4]_{NAMS}$ within the uncertainty in both measurements (30% for NAMS, 50% for the proxy). Such an agreement between the two methods corroborates the approach of apportioning sulfur to sulfate and using Γ_m to determine an average gas phase sulfuric acid concentration during an event.

The sulfuric acid concentration calculated by both methods is consistent with gas phase H_2SO_4 measurements by chemical ionization mass spectrometry in other urban environments, such as Atlanta, Georgia;[29] Boulder, Colorado;[30] and Tecamac, Mexico,[31] where the sulfuric acid concentration during new particle formation ranged from low 10^7 to mid 10^8 $molec \cdot cm^{-3}$. Note that $[H_2SO_4]_{NAMS}$ calculated during the Lewes campaign is lower than $[H_2SO_4]_{NAMS}$ calculated during the Wilmington campaign, which is consistent with particle composition measurements (less sulfate in Lewes) and SO_2 measurements from a previous campaign in Lewes[32] (lower $[SO_2]$ in Lewes than Wilmington). The results from both Lewes and Wilmington differ from observations in Tecamac, where sulfuric acid was hypothesized to account for only 10% of the growth of particles in a similar size range to those analyzed by NAMS.[11] Although the sulfuric acid concentration was very high in Tecamac, growth rates were also very high and ranged from 15-40 $nm \cdot h^{-1}$, resulting in Γ_v ranging from 4-25.[23, 31] On the other hand, sulfuric acid condensation was found to explain a significant portion of the aerosol growth in Atlanta, where Γ_v ranged from 1-4,[23, 33] and qualitative TDCIMS measurements for particles in a size range similar to NAMS

showed ammonium sulfate as the most abundant chemical species.[12] The Atlanta observations are similar to the observations in Wilmington. In Kent, Ohio, a rural environment impacted by nearby urban centers, sulfuric acid could only explain a small fraction of aerosol growth.[34] However, whereas the Kent growth rates were on the order of those observed in Lewes, the sulfuric acid concentration in Kent ($< 5.2 \times 10^6$ molec·cm^{-3}) was lower than the value calculated for Lewes ($0.68\text{-}2.4 \times 10^7$ molec·cm^{-3}).

8.4 Conclusions

NAMS measurements were performed in two separate environments, one rural/coastal and one urban, to determine quantitatively the elemental composition of ambient nanoparticles during new particle formation events. In both environments, the chemical composition shifted towards elements indicative of a higher inorganic content. Application of a molecular apportionment algorithm designed to place the elemental composition in a molecular context indicates the relative contributions of different molecular species to nanoparticle growth during new particle formation. Based on the apportioned data, sulfate can explain a considerable portion, but not all, of the observed particle growth. From the NAMS-measured sulfate mass fraction, the sulfuric acid contribution to the observed particle growth rate during new particle formation events was determined. Additionally, the average ambient sulfuric acid concentration required to produce the measured particle phase sulfate concentration during specific events was calculated and compared to values calculated using a sulfuric acid proxy. Both values agreed within experimental uncertainty. This agreement suggests the assumption of collision-limited growth by sulfuric acid (uptake coefficient close to 1)[23, 24, 35] is suitable for 10-20 nm diameter particles. If

sulfuric acid evaporation from the particles were significant, a disagreement between the indirectly determined gaseous and directly measured particulate sulfur would exist, and the magnitude of that disagreement would be related to the sulfuric acid uptake coefficient. This result also validates the assumption that the molecular form of particle phase sulfur is sulfate. Sulfate accounted for < 50% of total particle growth, meaning that other species (e.g. ammonium, nitrate, and carbonaceous matter) contributed to the remainder of the growth. Particle composition measurements at ~20 nm diameter inform as to the species contributing to growth from ~10-20 nm diameter, since most of the mass of a 20 nm particle was acquired during this period of growth. In future work, it should be possible to quantitatively relate size-resolved particle composition to measured gas phase concentrations of potential growth species. In this manner, the described method could permit size-resolved elucidation and quantification of which gas phase species contribute to particle growth.

8.5 References

1. Wang, S. Y.; Johnston, M. V., Airborne nanoparticle characterization with a digital ion trap-reflectron time of flight mass spectrometer. *Int. J. Mass Spectrom.* **2006,** *258* (1-3), 50-57.

2. Wang, S. Y.; Zordan, C. A.; Johnston, M. V., Chemical characterization of individual, airborne sub-10-nm particles and molecules. *Anal. Chem.* **2006,** *78* (6), 1750-1754.

3. Bzdek, B. R.; Zordan, C. A.; Luther, G. W.; Johnston, M. V., Nanoparticle chemical composition during new particle formation. *Aerosol Sci. Technol.* **2011,** *45* (8), 1041-1048.

4. Klems, J. P.; Pennington, M. R.; Zordan, C. A.; McFadden, L.; Johnston, M. V., Apportionment of motor vehicle emissions from fast changes in number concentration and chemical composition of ultrafine particles near a roadway intersection. *Environ. Sci. Technol.* **2011,** *45* (13), 5637-5643.

5. Zordan, C. A.; Pennington, M. R.; Johnston, M. V., Elemental composition of nanoparticles with the Nano Aerosol Mass Spectrometer. *Anal. Chem.* **2010,** *82* (19), 8034-8038.

6. Cass, G. R.; Hughes, L. A.; Bhave, P.; Kleeman, M. J.; Allen, J. O.; Salmon, L. G., The chemical composition of atmospheric ultrafine particles. *Philos. Trans. Royal Soc. A-Math. Phys. Eng. Sci.* **2000,** *358* (1775), 2581-2592.

7. Hughes, L. S.; Cass, G. R.; Gone, J.; Ames, M.; Olmez, I., Physical and chemical characterization of atmospheric ultrafine particles in the Los Angeles area. *Environ. Sci. Technol.* **1998,** *32* (9), 1153-1161.

8. Ning, Z.; Geller, M. D.; Moore, K. F.; Sheesley, R.; Schauer, J. J.; Sioutas, C., Daily variation in chemical characteristics of urban ultrafine aerosols and inference of their sources. *Environ. Sci. Technol.* **2007,** *41* (17), 6000-6006.

9. Pakkanen, T. A.; Kerminen, V. M.; Korhonen, C. H.; Hillamo, R. E.; Aarnio, P.; Koskentalo, T.; Maenhaut, W., Urban and rural ultrafine ($PM_{0.1}$) particles in the Helsinki area. *Atmos. Environ.* **2001,** *35* (27), 4593-4607.

10. Smith, J. N.; Barsanti, K. C.; Friedli, H. R.; Ehn, M.; Kulmala, M.; Collins, D. R.; Scheckman, J. H.; Williams, B. J.; McMurry, P. H., Observations of aminium salts in atmospheric nanoparticles and possible climatic implications. *Proc. Natl. Acad. Sci. U.S.A.* **2010,** *107* (15), 6634-6639.

11. Smith, J. N.; Dunn, M. J.; VanReken, T. M.; Iida, K.; Stolzenburg, M. R.; McMurry, P. H.; Huey, L. G., Chemical composition of atmospheric nanoparticles formed from nucleation in Tecamac, Mexico: Evidence for an important role for organic species in nanoparticle growth. *Geophys. Res. Lett.* **2008,** *35* (4), L04808, doi: 10.1029/2007gl032523.

12. Smith, J. N.; Moore, K. F.; Eisele, F. L.; Voisin, D.; Ghimire, A. K.; Sakurai, H.; McMurry, P. H., Chemical composition of atmospheric nanoparticles during nucleation events in Atlanta. *J. Geophys. Res.-Atmos.* **2005,** *110* (D22), D22s03, doi: 10.1029/2005jd005912.

13. Zhang, Q.; Stanier, C. O.; Canagaratna, M. R.; Jayne, J. T.; Worsnop, D. R.; Pandis, S. N.; Jimenez, J. L., Insights into the chemistry of new particle formation and growth events in Pittsburgh based on aerosol mass spectrometry. *Environ. Sci. Technol.* **2004,** *38* (18), 4797-4809.

14. Kulmala, M.; Kerminen, V. M., On the formation and growth of atmospheric nanoparticles. *Atmos. Res.* **2008,** *90* (2-4), 132-150.

15. Kulmala, M.; Vehkamaki, H.; Petaja, T.; Dal Maso, M.; Lauri, A.; Kerminen, V. M.; Birmili, W.; McMurry, P. H., Formation and growth rates of ultrafine atmospheric particles: A review of observations. *J. Aerosol Sci.* **2004,** *35* (2), 143-176.

16. Hatch, L. E.; Creamean, J. M.; Ault, A. P.; Surratt, J. D.; Chan, M. N.; Seinfeld, J. H.; Edgerton, E. S.; Su, Y. X.; Prather, K. A., Measurements of isoprene-derived organosulfates in ambient aerosols by Aerosol Time-of-Flight Mass Spectrometry—Part 1: Single particle atmospheric observations in Atlanta. *Environ. Sci. Technol.* **2011,** *45* (12), 5105-5111.

17. Lukacs, H.; Gelencser, A.; Hoffer, A.; Kiss, G.; Horvath, K.; Hartyani, Z., Quantitative assessment of organosulfates in size-segregated rural fine aerosol. *Atmos. Chem. Phys.* **2009,** *9* (1), 231-238.

18. Hatch, L. E.; Creamean, J. M.; Ault, A. P.; Surratt, J. D.; Chan, M. N.; Seinfeld, J. H.; Edgerton, E. S.; Su, Y.; Prather, K. A., Measurements of isoprene-derived organosulfates in ambient aerosols by Aerosol Time-of-Flight Mass Spectrometry—Part 2: Temporal variability and formation mechanisms. *Environ. Sci. Technol.* **2011,** *45* (20), 8648-8655.

19. Finlayson-Pitts, B. J.; Pitts, J. N., *Chemistry of the Upper and Lower Atmosphere*. Academic Press: New York, 2000.

20. Higashi, M.; Takahashi, Y., Detection of S(IV) species in aerosol particles using XANES spectroscopy. *Environ. Sci. Technol.* **2009,** *43* (19), 7357-7363.

21. Usher, C. R.; Michel, A. E.; Grassian, V. H., Reactions on mineral dust. *Chem. Rev.* **2003,** *103* (12), 4883-4939.

22. Kerminen, V. M.; Pirjola, L.; Boy, M.; Eskola, A.; Teinila, K.; Laakso, L.; Asmi, A.; Hienola, J.; Lauri, A.; Vainio, V.; Lehtinen, K.; Kulmala, M., Interaction between SO_2 and submicron atmospheric particles. *Atmos. Res.* **2000,** *54* (1), 41-57.

23. Kuang, C.; Riipinen, I.; Sihto, S. L.; Kulmala, M.; McCormick, A. V.; McMurry, P. H., An improved criterion for new particle formation in diverse atmospheric environments. *Atmos. Chem. Phys.* **2010,** *10* (17), 8469-8480.

24. Weber, R. J.; Marti, J. J.; McMurry, P. H.; Eisele, F. L.; Tanner, D. J.; Jefferson, A., Measured atmospheric new particle formation rates: Implications for nucleation mechanisms. *Chem. Eng. Commun.* **1996,** *151* (1), 53-64.

25. Lide, D. R., (ed.), *CRC Handbook of Chemistry and Physics, 90th Edition (Internet Version 2010)*. CRC Press/Taylor Francis: Boca Raton, FL, 2010.

26. Carlton, A. G.; Bhave, P. V.; Napelenok, S. L.; Edney, E. O.; Sarwar, G.; Pinder, R. W.; Pouliot, G. A.; Houyoux, M., Model representation of secondary organic aerosol in CMAQv4.7. *Environ. Sci. Technol.* **2010,** *44* (22), 8553-8560.

27. Kuwata, M.; Zorn, S. R.; Martin, S. T., Using elemental ratios to predict the density of organic material composed of carbon, hydrogen, and oxygen. *Environ. Sci. Technol.* **2011,** *46* (2), 787-794.

28. Mikkonen, S.; Romakkaniemi, S.; Smith, J. N.; Korhonen, H.; Petaja, T.; Plass-Duelmer, C.; Boy, M.; McMurry, P. H.; Lehtinen, K. E. J.; Joutsensaari, J.; Hamed, A.; Mauldin III, R. L.; Birmili, W.; Spindler, G.; Arnold, F.; Kulmala, M.; Laaksonen, A., A statistical proxy for sulphuric acid concentration. *Atmos. Chem. Phys.* **2011,** *11* (21), 11319-11334.

29. McMurry, P. H.; Fink, M.; Sakurai, H.; Stolzenburg, M. R.; Mauldin, R. L.; Smith, J.; Eisele, F.; Moore, K.; Sjostedt, S.; Tanner, D.; Huey, L. G.; Nowak, J. B.; Edgerton, E.; Voisin, D., A criterion for new particle formation in the sulfur-rich Atlanta atmosphere. *J. Geophys. Res.-Atmos.* **2005,** *110* (D22), D22s02, doi: 10.1029/2005jd005901.

30. Kuang, C.; McMurry, P. H.; McCormick, A. V.; Eisele, F. L., Dependence of nucleation rates on sulfuric acid vapor concentration in diverse atmospheric locations. *J. Geophys. Res.-Atmos.* **2008,** *113* (D10), D10209, doi: 10.1029/2007jd009253.

31. Iida, K.; Stolzenburg, M. R.; McMurry, P. H.; Smith, J. N., Estimating nanoparticle growth rates from size-dependent charged fractions: Analysis of new particle formation events in Mexico City. *J. Geophys. Res.-Atmos.* **2008,** *113* (D5), D05207, doi: 10.1029/2007jd009260.

32. Stecher, H. A.; Luther, G. W.; MacTaggart, D. L.; Farwell, S. O.; Crosley, D. R.; Dorko, W. D.; Goldan, P. D.; Beltz, N.; Krischke, U.; Luke, W. T.; Thornton, D. C.; Talbot, R. W.; Lefer, B. L.; Scheuer, E. M.; Benner, R. L.; Wu, J. G.; Saltzman, E. S.; Gallagher, M. S.; Ferek, R. J., Results of the gas-phase sulfur intercomparison experiment (GASIE): Overview of experimental setup, results and general conclusions. *J. Geophys. Res.-Atmos.* **1997,** *102* (D13), 16219-16236, doi: 10.1029/97JD01362.

33. Stolzenburg, M. R.; McMurry, P. H.; Sakurai, H.; Smith, J. N.; Mauldin, R. L.; Eisele, F. L.; Clement, C. F., Growth rates of freshly nucleated atmospheric particles in Atlanta. *J. Geophys. Res.-Atmos.* **2005,** *110* (D22), D22s05, doi: 10.1029/2005jd005935.

34. Erupe, M. E.; Benson, D. R.; Li, J. M.; Young, L. H.; Verheggen, B.; Al-Refai, M.; Tahboub, O.; Cunningham, V.; Frimpong, F.; Viggiano, A. A.; Lee, S. H., Correlation of aerosol nucleation rate with sulfuric acid and ammonia in Kent, Ohio: An atmospheric observation. *J. Geophys. Res.-Atmos.* **2010,** *115* (D23), D23216, doi: 10.1029/2010jd013942.

35. Bzdek, B. R.; DePalma, J. W.; Ridge, D. P.; Laskin, J.; Johnston, M. V., Fragmentation energetics of clusters relevant to atmospheric new particle formation. *J. Am. Chem. Soc.* **2013,** *135* (8), 3276-3285.

Chapter 9

QUANTITATIVE AND TIME-RESOLVED NANOPARTICLE COMPOSITION MEASUREMENTS DURING NEW PARTICLE FORMATION

9.1 Introduction

Chapter 7 addressed changes in nanoparticle elemental composition observed with the Nano Aerosol Mass Spectrometer (NAMS) during new particle formation. Chapter 8 addressed the connection between NAMS-measured particle phase composition to gas phase concentrations. A major limitation of Chapter 7 was the poor time resolution afforded by NAMS. A major limitation of Chapter 8 was the lack of directly measured gas phase sulfuric acid concentration to compare to the calculated value from NAMS measurements. In this chapter, both of these limitations are overcome: a sufficient number of particles were analyzed such that time resolution on the order of 5 min was achieved and gas phase measurements were made in tandem with NAMS measurements. The results provide substantial new insight into the mechanism of new particle formation. Particle phase composition is shown to change before the nucleated particles grow into the NAMS size range, illustrating how condensation of nucleation precursors can impact the composition of preexisting particles. Additionally, gas phase sulfuric acid is quantitatively linked to particle phase composition. Finally, a novel pathway for nanoparticle growth involving nitrogen-containing compounds is discussed. Taken together, these observations provide an important step forward in constraining the mechanism of new particle formation.

9.2 Experimental Section

The field campaign was conducted at the Hugh R. Sharp Campus of the University of Delaware in Lewes, Delaware (38°47'02" N, 75°09'39" W) from 23 July to 31 August 2012. The field site is located 800 m south of the Delaware Bay, which is at the outlet of the Delaware River to the Atlantic Ocean and 3 km west of the Atlantic Ocean. A large salt marsh sits adjacent to the site (< 50 m) on the west. This field site was used previously for a campaign to measure gas phase sulfur emissions[1, 2] as well as to study nanoparticle chemical composition during new particle formation in the autumn of 2007 (see Chapter 7).[3]

Nanoparticles were sampled through an inlet approximately 6 m above the ground. Nanoparticle chemical composition measurements were accomplished with NAMS, a single particle mass spectrometer that gives quantitative elemental composition measurements in the 10-30 nm size range.[4-6] Nanoparticles entering NAMS were charged with a unipolar charger[7] and then focused through two digital ion guides and size-selectively captured in an ion trap. Trapped particles were irradiated with a high-energy pulsed laser beam to reach the "complete ionization limit", thereby creating a laser-induced plasma and quantitatively disintegrating the nanoparticles into multiply charged positive atomic ions that were mass analyzed by time-of-flight. The integrated area underneath the ion signals gave the elemental composition. Relative to previous versions of NAMS, replacement of an aerodynamic lens with a second digital ion guide substantially improved focusing of 20 nm diameter nanoparticles into the ion trap, thereby improving the time resolution of composition measurements. (This upgrade to the instrument was accomplished by M. Ross Pennington.[8]) Deconvolution of overlapping signal intensities was accomplished by the method of Zordan et al. (2010).[9] The particle size range to be analyzed was

selected by the frequency applied to the ring electrode of the ion trap. During this campaign, NAMS was set to analyze the composition of 20 ± 3 nm mass normalized diameter particles, which corresponds approximately to 18 ± 3 nm mobility diameter particles.[10]

Nanoparticle chemical composition was averaged over one or multiple 5-min bins such that a minimum of 20 particles were included in the average. Averaging the measured compositions of 20 particles simultaneously maximizes time resolution while minimizing uncertainty from variations in the dynamics of the laser plume.[11] For the time periods discussed here, particle concentrations were such that at least 20 particles were analyzed in almost every 5-min bin during the daytime. Based on measurements with standard aerosols, elemental compositions measured by NAMS are generally within 10% of expected values after averaging a sufficient number of particles (e.g. 20).[9, 11]

Mass fractions for apportioned molecular species were determined from the elemental mole fractions by the method described in Chapter 7.[3] These results, together with diameter growth rates inferred from scanning mobility particle sizer (SMPS) measurements, were used to determine the sulfuric acid vapor ($[H_2SO_4]_{NAMS}$) required to explain particulate sulfur content (see Chapter 8):[12]

$$[H_2SO_4]_{NAMS} = \frac{2GR_{MEAS}}{\nu_1 \bar{c}_1 \Gamma_m} \times \frac{\rho_{particle}}{\rho_{sulfate}} \quad (1)$$

where GR_{MEAS} is the measured growth rate ($nm \cdot h^{-1}$), ν_1 is the volume occupied by a hydrated H_2SO_4 molecule (cm^3), $\bar{c}_1$ is the mean thermal speed of the condensing monomer ($nm \cdot h^{-1}$), $\rho_{particle}$ is the density of ambient particles during the time period of interest (estimated to be 1.5 $g \cdot cm^{-3}$), $\rho_{sulfate}$ is the density of condensed phase sulfuric acid (1.8 $g \cdot cm^{-3}$), and $\Gamma_m = \frac{1}{MF_{sulfate}}$, where $MF_{sulfate}$ is the average sulfate mass fraction

for the time period of interest. Equation (1) does not include the Fuchs-Sutugin correction for mass flux, which only affects the calculated sulfuric acid concentration by < 5%, much smaller than the uncertainties of GR and Γ_m measurements (approximately 10% to 30%). Equation (1) also assumes that the mass accommodation coefficient is close to 1.[13, 14] Note that the parameter Γ_m obtained from NAMS measurements is related to the more familiar Γ_v obtained from gas phase sulfuric acid measurements[14] by:

$$\Gamma_v = \Gamma_m \times \frac{\rho_{sulfate}}{\rho_{particle}} \quad (2)$$

Gas phase sulfuric acid concentrations were measured independently (by Jun Zhao, Coty Jen, and Peter McMurry from University of Minnesota) using the Cluster-Chemical Ionization Mass Spectrometer (Cluster CIMS), which has been described previously.[15, 16] Agreement between $[H_2SO_4]_{NAMS}$ and $[H_2SO_4]_{CIMS}$ would imply that Eqs. (1) and (2) are valid models for the uptake of S onto freshly nucleated particles.

Ambient gas phase ammonia and amine concentrations were measured using the Ambient pressure Proton transfer Mass Spectrometer (AmPMS). These measurements were conducted by David Hanson from Augsburg College.[17] Size-resolved cloud condensation nuclei (CCN) activation was measured at 5 different mobility diameters from 50 to 175 nm using a condensation particle counter (CPC; model 3760, TSI, Inc., St. Paul, Minnesota) and a cloud condensation nucleus counter (CCNc; Droplet Measurement Technologies, Boulder, Colorado) downstream of a differential mobility analyzer (DMA; model 3081, TSI, Inc., St. Paul, Minnesota) following the setup described by Levin et al.[18] Calibrations with ammonium sulfate particles were performed weekly during the campaign. After inverting the CPC and CCNc data following the procedures described in Levin et al., CCN activation curves

were constructed and the critical supersaturation (S_c) at each sampled diameter was found. CCNc measurements were performed by James Smith from the National Center for Atmospheric Research.

Particle size distributions were measured using an SMPS (electrostatic classifier model 3080, CPC model 3788, TSI, Inc., St. Paul, Minnesota). Growth rates from 10-25 nm diameter were determined by plotting the mode particle diameter against local time, fitting the result linearly and taking the derivative. During the year 2012 (with the exception of July-September 2012), nanoparticle number concentrations were monitored with 15-minute time resolution on a daily basis using an ultrafine particle monitor (model 3031, TSI, Inc., St. Paul, Minnesota) at an adjacent Delaware Department of Natural Resources and Environmental Control monitoring site. This instrument provided nanoparticle number concentrations for six size bins: 20-30 nm, 30-50 nm, 50-70 nm, 70-100 nm, 100-200 nm, and > 200 nm.

9.3 Results and Discussion

9.3.1 Nanoparticle Events in Lewes

The Lewes field site is frequently impacted by nanoparticle events where the concentration of sub-50 nm diameter particles increases quickly over a short period of time. During a previous one-month-long campaign to study new particle formation at this site in October-November 2007,[3] regional new particle formation was observed on nearly half of the measurement days (see Chapter 7). During 2012, nanoparticle number concentrations were monitored with an ultrafine particle monitor. Figure 9.1 shows that nanoparticle events were most frequent in the late winter/early springtime

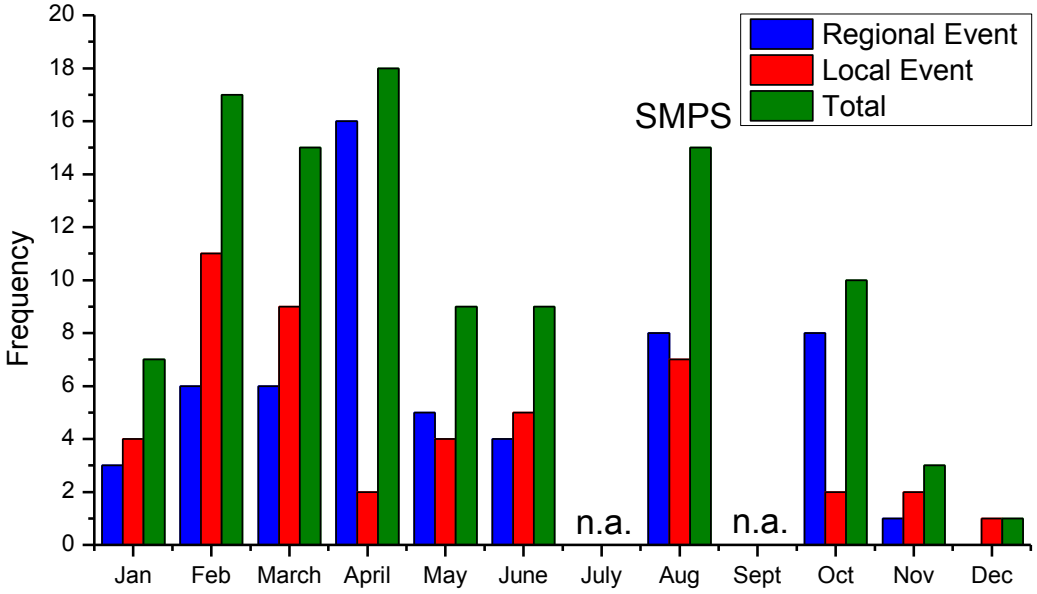

Figure 9.1: Nanoparticle event frequency, measured with an ultrafine particle monitor, during 2012. n.a. = data not available. In August, data are from a SMPS instead of the ultrafine particle monitor.

months (February-April; average of 17 nanoparticle events/month) and were least frequent in November-December (average of 2 nanoparticle events/month). These nanoparticle events could be divided into two groups. One group consisted of an increase in nanoparticle number concentration for a fixed duration with little to no growth to larger sizes. These events were classified as local events. The second group was described by an increase in nanoparticle number concentration in the 20-30 nm size bin followed by growth to larger sizes (30-50 nm and 50-70 nm size bins). These events were classified as regional events when the initial burst of nanoparticles was followed by growth to larger sizes. These two event classes had very different air mass histories, as determined by HYSPLIT.[19] Air masses during local events typically transported to the site from the south, having passed over areas with substantial development and a coal-fired power plant. On the other hand, air masses during regional events typically transported to the site from the northwest, having passed over largely rural areas, the Delaware Bay and salt marshes. As examples of these two classes of events, air mass back trajectories for 11-14 August 2012 are shown in Fig. 9.2. Both regional event days (12 and 13 August) have air masses coming from the northwest, whereas both non-event days (11 and 14 August) have air masses coming from the south.

9.3.2 Nanoparticle Chemical Composition on Regional New Particle Formation Days

Nanoparticle elemental composition data acquired by NAMS for two regional new particle formation days during the field campaign are presented in Fig. 9.3. Figure 9.3a shows the SMPS-measured aerosol size distribution for these two events. The

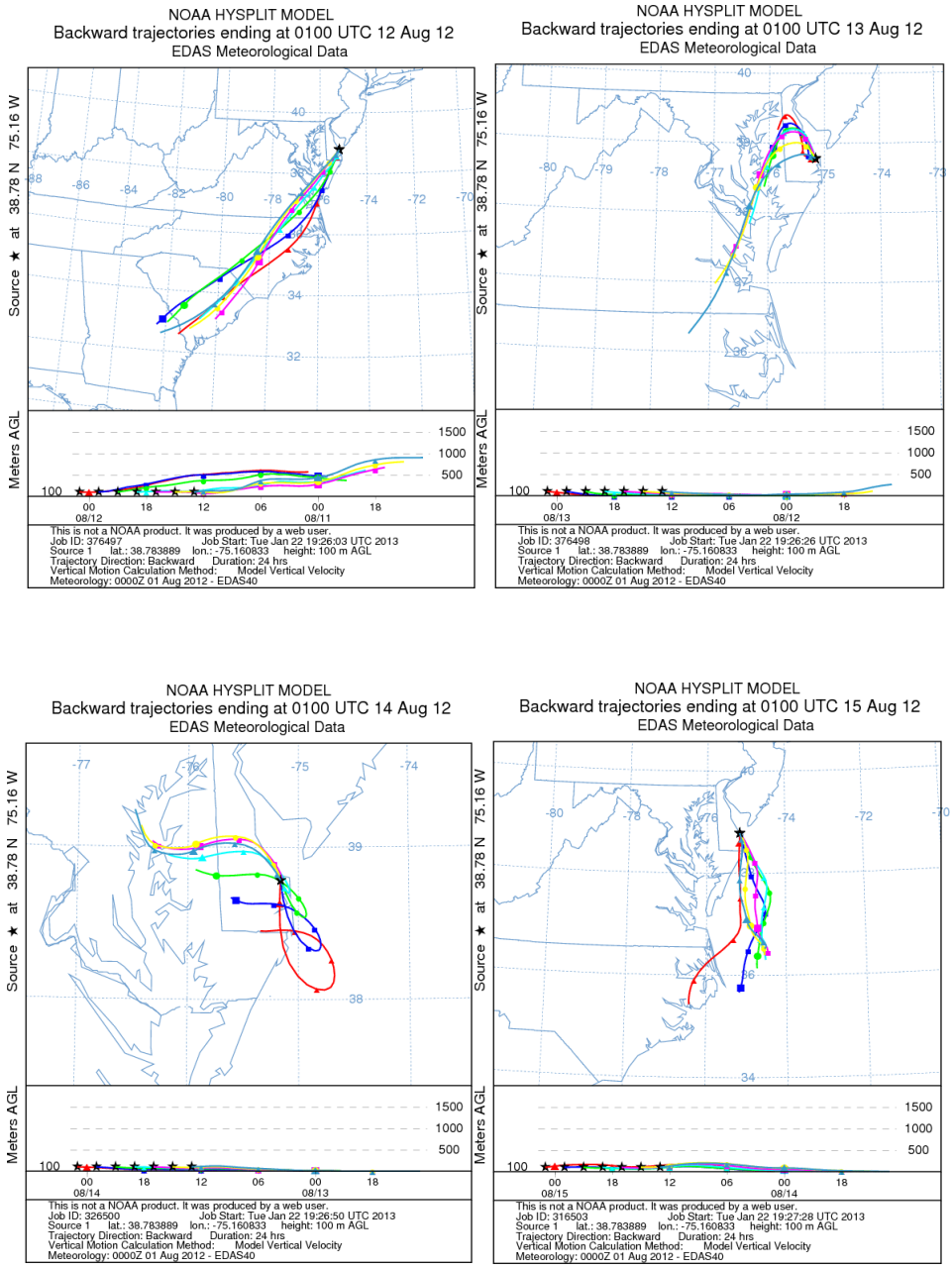

Figure 9.2: Air mass histories for a) 11 August, b) 12 August, c) 13 August, and d) 14 August 2012.

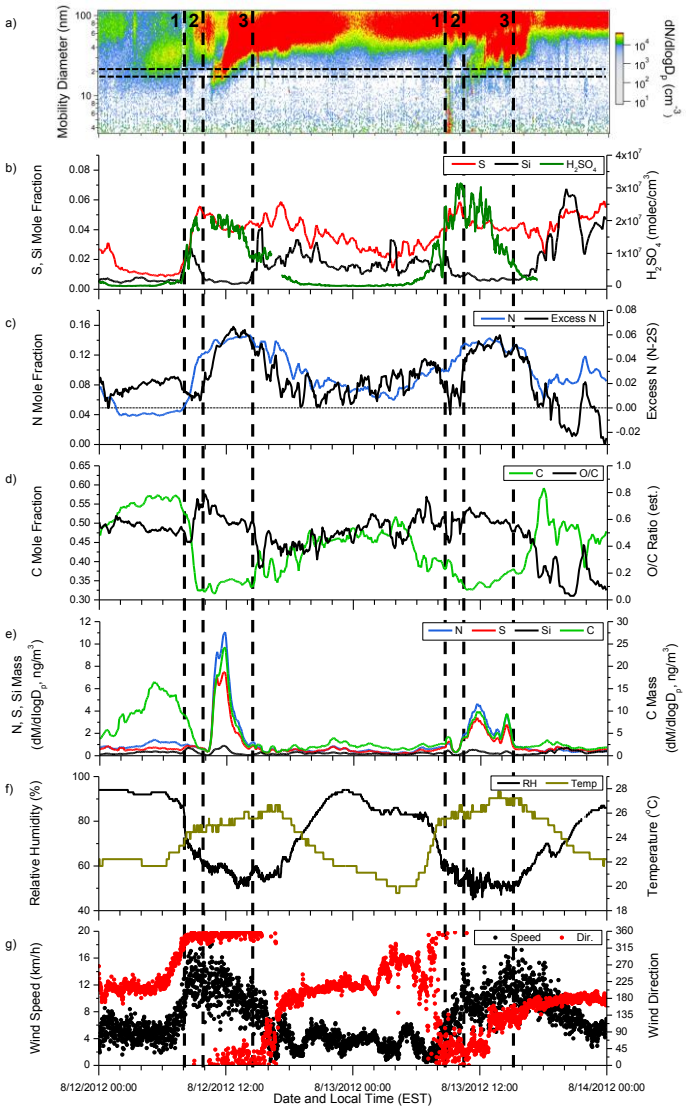

Figure 9.3: a) Aerosol size distributions, b) S and Si mole fraction as well as gas phase sulfuric acid concentration, c) N and Excess N mole fractions, d) C mole fraction and estimated O/C molar ratio, e) N, S, Si, and C elemental mass, f) relative humidity and temperature, and g) wind speed and wind direction for 12 and 13 August 2012. The horizontal dotted lines in a) indicate the NAMS-measured size range. The horizontal dotted line in c) indicates Excess N = 0. Vertical dotted lines indicate 1) when gas phase sulfuric acid increases, 2) when the mode diameter of the event passes into the NAMS-measured size range, and 3) when the mode diameter moves out of the NAMS-measured size range. Nanoparticle composition data were subject to 6-point smoothing; the sulfuric acid concentration was subjected to 10-point smoothing.

horizontal dotted lines indicate the size range of particles analyzed by NAMS during this study. The new particle formation event on 12 August 2012 is a strong event (i.e. high nanoparticle number concentration) with a low condensational sink and fast growth to larger sizes. The event on 13 August 2012 is a weak new particle formation event with a much larger condensational sink but a similar growth rate to larger sizes. For both events, air masses came from the northwest, although later in the day on 13 August there was some recirculation of the air mass around the site (Fig. 9.2).

Figure 9.3b shows NAMS-measured S and Si elemental mole fractions plotted together with Cluster CIMS-measured gas phase sulfuric acid concentration. Figure 9.3c shows NAMS-measured N mole fraction as well as "excess" nitrogen (Excess N), which is defined here as twice the S mole fraction subtracted from the N mole fraction (Excess Nitrogen = N-2S). If Excess N < 0, then not enough nitrogen is available to neutralize sulfuric acid, even if all of the N exists as cation forming species (ammonia, amines). Therefore, the particle necessarily is acidic. Implicit in this statement is the assignment of all elemental S as sulfate, the validity of which has been discussed in detail elsewhere (see Chapter 8).[12] If Excess N = 0 (dotted line in Fig. 9.3c) then exactly enough N exists to completely neutralize sulfuric acid. If Excess N > 0, then more nitrogen is present in the particle than required to neutralize sulfuric acid, meaning that a nitrogen-containing species other than ammonium or aminium sulfate must exist in the particle. Based on the uncertainty in the NAMS elemental composition measurement and the range of elemental mass fractions observed for S and N, an absolute uncertainty of 0.01 is assigned to the Excess N mole fraction.

Figure 9.3d shows C mole fraction and its estimated O/C molar ratio. The O/C ratio was estimated using a molecular apportionment algorithm described in Chapter

7.[3] Briefly, oxygen is first apportioned to the inorganic components of the aerosol (as SiO_2, SO_4^{-2}, NH_4^+, and NO_3^-) and the remaining oxygen mole fraction is divided by the carbon mole fraction (which is not apportioned to any other molecular species). The absolute uncertainty in the estimated O/C molar ratio ranges from 0.06-0.14 depending on the day and time. This range does not include systematic error arising from assumptions in the molecular apportionment algorithm. Figure 9.3e shows elemental mass for N, S, Si, and C. Elemental mass ($dM/dlogD_p$) was determined by multiplying elemental mass fractions by the SMPS-measured aerosol mass in the 17-21 nm size range. Figure 9.3f shows relative humidity (RH) and ambient temperature (^oC), and Fig. 9.3g shows wind speed ($km \cdot h^{-1}$) and wind direction. For each day, the three vertical dotted lines indicate 1) the time when gas phase sulfuric acid increases, 2) the time when the mode diameter of the particle size distribution associated with the event begins to move into the NAMS-measured size range, and 3) the time when the mode diameter grows past the NAMS-measured size range.

The event on 12 August is a strong regional event with fast growth (growth rate from 10-25 nm = 8.9 ± 0.8 $nm \cdot h^{-1}$). Figure 9.4 shows an expanded view of the key stages of the event. At the onset of new particle formation (vertical line 1), the increase in S mole fraction coincides with the rapid increase in gas phase sulfuric acid concentration (Fig. 9.3b; Fig. 9.4a). However, this increase does *not* correspond to an increase in aerosol mass in the NAMS-measured size range (Fig. 9.3e; Fig. 9.4d). While condensation of sulfuric acid over this (short) time period is sufficient to change the composition of pre-existing particles, it is not enough to significantly increase the aerosol mass concentration in the relevant size range. Nonetheless, the change in

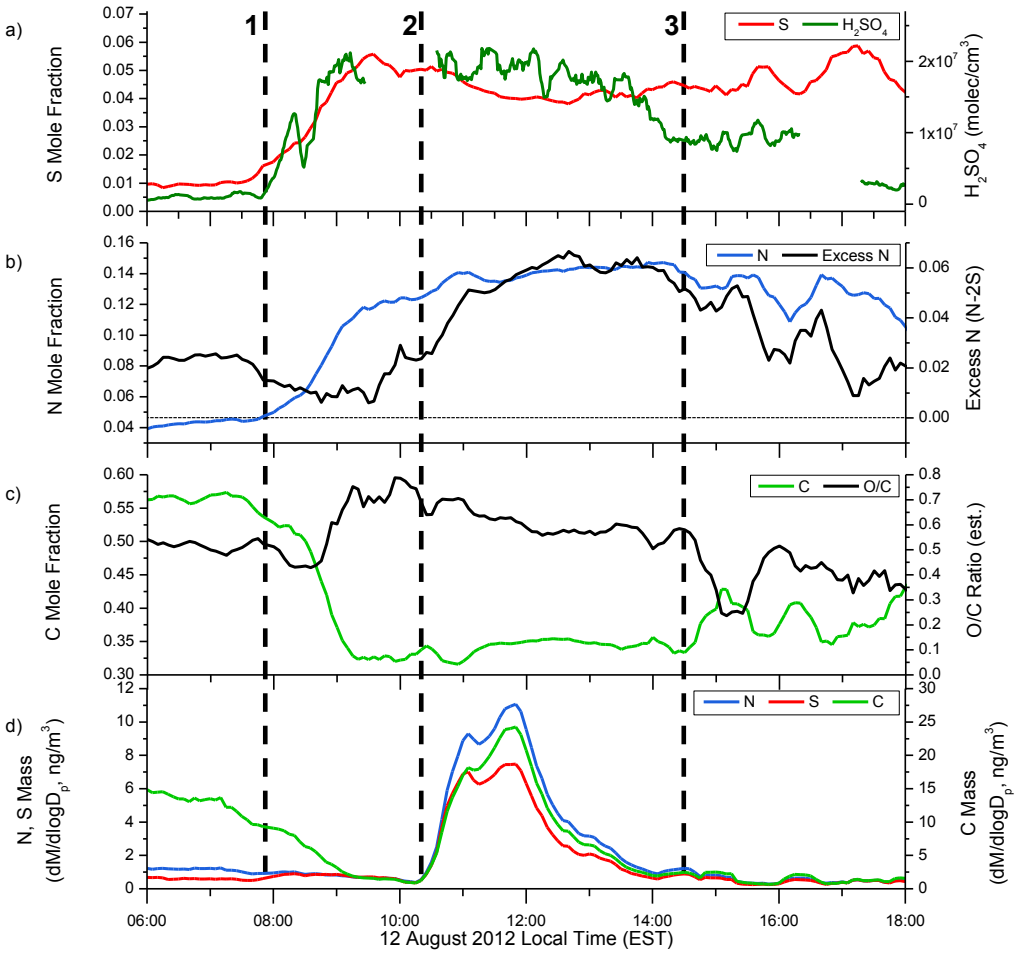

Figure 9.4: Expanded view of the event on 12 August 2012 showing a) S mole fraction and gas phase sulfuric acid concentration, b) N and Excess N mole fractions, c) C mole fraction and estimated O/C molar ratio, and d) N, S, and C elemental mass. The horizontal dotted line in b) indicates Excess N = 0. Vertical dotted lines indicate 1) when gas phase sulfuric acid increases, 2) when the mode diameter of the event passes into the NAMS-measured size range, and 3) when the mode diameter moves out of the NAMS-measured size range. Nanoparticle composition data were subject to 6-point smoothing; the sulfuric acid concentration was subjected to 10-point smoothing.

composition is important since it gives insight into the early steps of nanoparticle formation and growth, which must primarily involve sulfuric acid.

Later in the day, the gas phase sulfuric acid concentration decreases quickly, but the S mole fraction does not. This lack of correlation between the two is characteristic of a regional event. Initially, the sulfuric acid and S mole fraction are correlated because a local process (condensation of gas phase molecules) drives the composition change of pre-existing particles at the site. Near the end the day, the particles being analyzed have been transported to the site during the new particle formation event and their composition reflects growth processes along the way. Therefore in a regional event, the decrease in S mole fraction necessarily lags the decrease in gas phase sulfuric acid because the transported particles were previously exposed to a high gas phase sulfuric acid concentration.

A significant increase in the Si mole fraction is observed at the start of the event, coincident with the sulfuric acid and S mole fraction increases. However, the Si mole fraction quickly decreases as the mode diameter moves into the NAMS-measured size range. This dependence is consistent with a local, photochemical source of Si. This source is unknown but could involve siloxane emissions from plastic tubing and containers used at the site. A photochemical source of particle phase Si has been observed previously in a study of nanoparticles in Pasadena, California.[20] Later in the day, particles that have not been exposed to the local source of Si are transported to the site, and their composition reflects growth processes in the regional event.

Figures 9.3c and 9.4b show N mole fraction and Excess N. The N mole fraction increases simultaneously with the increase in gas phase sulfuric acid and S

mole fraction. The strong correlation between N and S suggests that cation forming species (ammonia or amines) are being incorporated into the particle to neutralize sulfate. During this time period, the N/S molar ratio approaches 2, indicating sulfate is neutralized. However, simply assigning N to sulfate neutralization is an oversimplification. Excess N, which is an indicator of species that cannot be associated with sulfate neutralization, does not increase until much later when the mode diameter moves into the NAMS-measured size range. The increase in Excess N correlates with the increase in aerosol mass (Fig. 9.3e; Fig. 9.4d), suggesting that it is associated with later (as opposed to earlier) stages of particle growth. Because NAMS only provides elemental composition, the molecular identity of these species was not directly measured. However, potential molecular species include ammonium or aminium nitrate, aminium-organic acid salts and organonitrates. The increase in Excess N occurs simultaneously with an increase in ambient temperature and a decrease in RH (Fig. 9.3f). If the identity of Excess N is ammonium nitrate, this dependence contradicts expected nitrate partitioning to aerosol, which is usually more abundant during periods of low temperature and high RH.[12, 21-25] Therefore, if ammonium nitrate is the identity of Excess N, that would mean a substantial gas phase nitric acid concentration (not measured in this campaign) must exist during the event. Gas phase ammonia concentrations, measured with AmPMS, were less than 200 pptv during this event. Based on the Aerosol Inorganics Model (AIM),[26, 27] particulate phase ammonium nitrate would require a gas phase nitric acid concentration on the order of 10-40 ppbv, which seems unlikely. Therefore, equilibrium partitioning of ammonium nitrate to the particle phase during this time period is also unlikely.

Figures 9.3d and 9.4c show C mole fraction and its estimated O/C molar ratio. During the new particle formation event, the C mole fraction decreases concurrently with the increase in S mole fraction and gas phase sulfuric acid. The C mole fraction does not increase again until after the aerosol mass has passed through the NAMS-measured size range. Although the C mole fraction does not increase during new particle formation, its aerosol mass does (Fig. 9.3e), indicating that carbonaceous matter contributes substantially to particle growth. The O/C ratio initially increases about the same time as the sulfuric acid and S mole fraction increase, suggesting highly oxidized organic molecules may be important in the early stage of nanoparticle growth.[28] As the aerosol mass passes into and through the NAMS-measured size range, the O/C ratio slowly decreases. Once the aerosol mass has passed through the NAMS-measured size range, the O/C ratio slowly increases again, suggesting that the carbonaceous matter is gradually aging.[29, 30] An average mass-weighted O/C ratio for the event is calculated by converting elemental mass (in $ng \cdot m^{-3}$) over the period of the event to elemental mole fraction and then apportioning to molecular components. This procedure gave an estimated O/C ratio of 0.63 over the event.

A weak regional event occurred on 13 August, which is shown in Fig. 9.3 and expanded in Fig. 9.5. On this day, growth was similar to that measured on 12 August (growth rate from 10-25 nm on 13 August = 7.1 ± 1.0 $nm \cdot h^{-1}$) but there was a substantial condensational sink. Many of the same trends are observed for this event as for the event on 12 August. When the gas phase sulfuric acid concentration increases, S mole fraction also increases. However, the change in particle phase S mole fraction is not as dramatic as for the event on 12 August because a substantially higher S mole

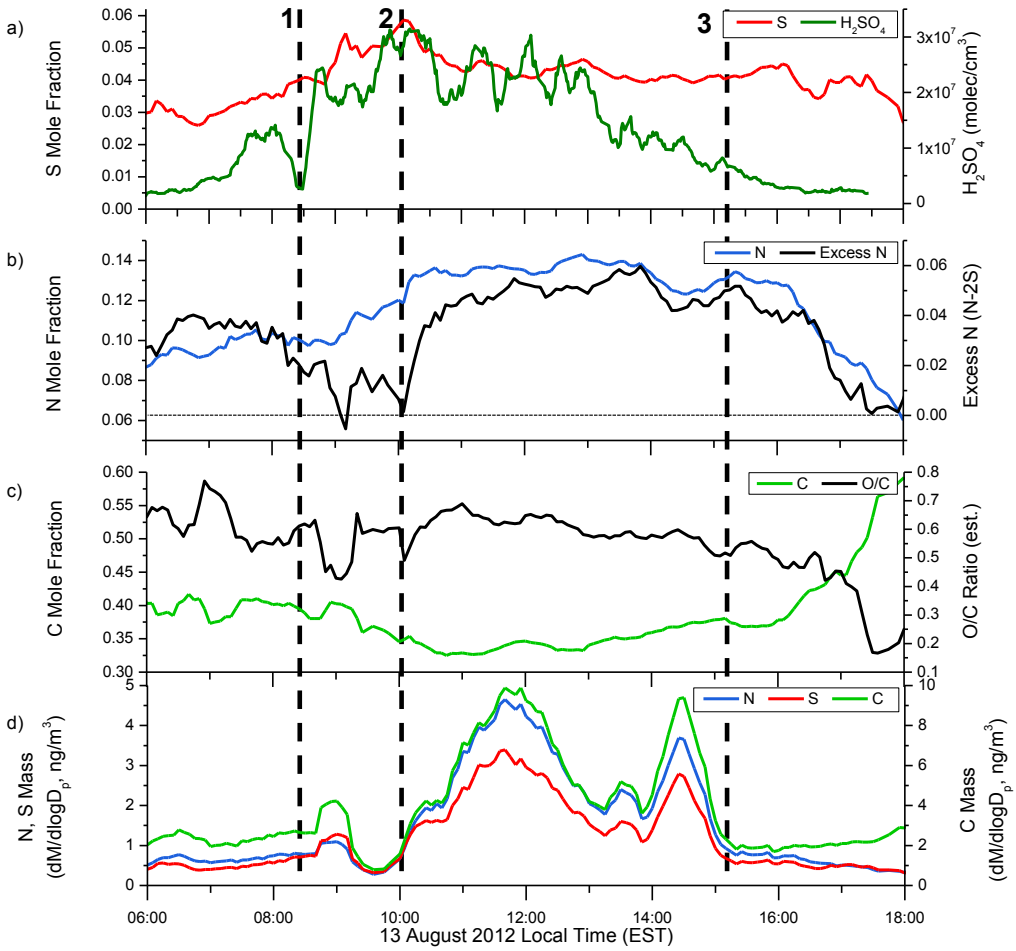

Figure 9.5: Expanded view of the event on 13 August 2012 showing a) S mole fraction and gas phase sulfuric acid concentration, b) N and Excess N mole fractions, c) C mole fraction and estimated O/C molar ratio, and d) N, S, and C elemental mass. The horizontal dotted line in b) indicates Excess N = 0. Vertical dotted lines indicate 1) when gas phase sulfuric acid increases, 2) when the mode diameter of the event passes into the NAMS-measured size range, and 3) when the mode diameter moves out of the NAMS-measured size range. Nanoparticle composition data were subject to 6-point smoothing; the sulfuric acid concentration was subjected to 10-point smoothing.

fraction in the background aerosol existed prior to the event on 13 August. Nonetheless, the same general trend is observed in that the S mole fraction increases simultaneously with the increase in gas phase sulfuric acid, whereas there is a substantial delay between the drop in gas phase sulfuric acid and S mole fraction at the end of the event. A local photochemical source of Si is indicated at the beginning of the event by the short-lived increase in Si mole fraction. A much higher increase in Si mole fraction in the evening of 13 August after the event has ended suggests the presence of a separate, non-photochemical source.

As on 12 August, the N mole fraction on 13 August increases simultaneously with the S mole fraction, suggesting that this nitrogen-containing species is associated with sulfate neutralization, and the N/S ratio of approximately 2 indicates full neutralization. Again as on 12 August, Excess N on 13 August increases later in time, simultaneous with the increase in aerosol mass. Furthermore, the increase in Excess N is coincident with an increase in temperature and a decrease in RH, opposite of what would be expected for ammonium nitrate partitioning. The C mole fraction also decreases relative to N and S, and the mass-weighted O/C ratio is 0.61, although the time-dependent trends of O/C ratio are not as pronounced as for 12 August.

Figure 9.6 presents mass-weighted average molecular mass fractions for both 12 and 13 August during the daytime. O/C ratios are given by the inset in the carbonaceous matter. The other two days presented in the figure will be discussed later. The average composition and O/C ratio are essentially the same during both events. An effective gas phase sulfuric acid concentration can be calculated from the average sulfate mass fraction and growth rate over each event as described in Eq.

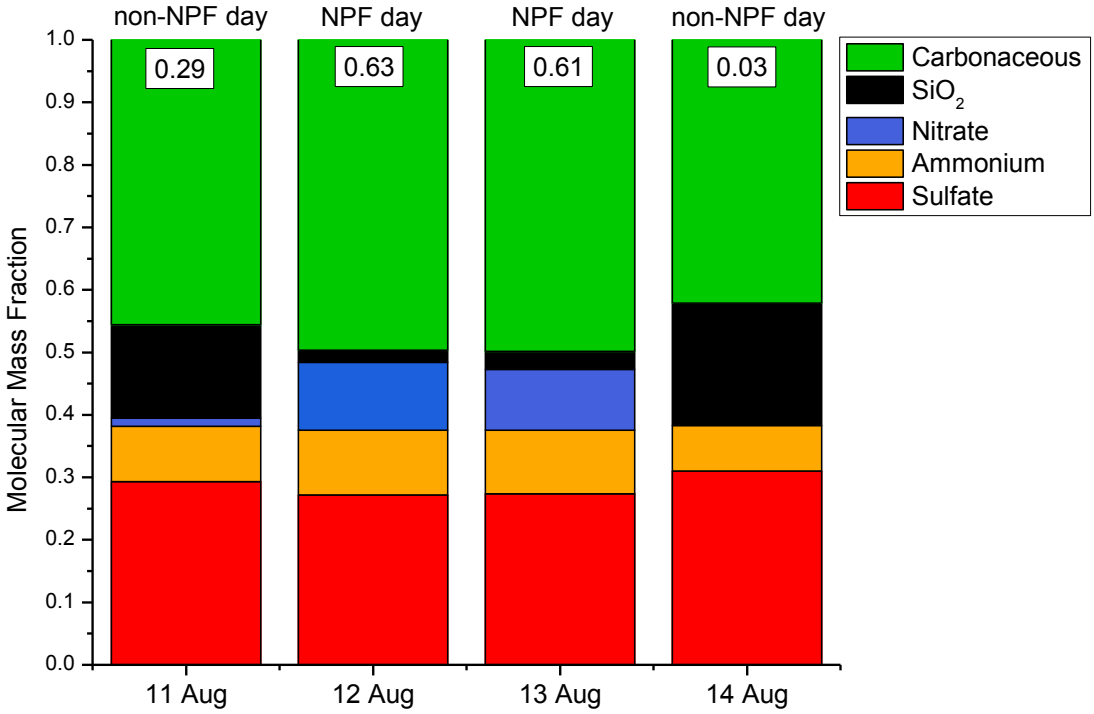

Figure 9.6: Average apportioned mass fractions during the daytime for all for days. Insets in the carbonaceous matter indicate estimated O/C molar ratios. Uncertainties for the O/C ratios range from 0.06 to 0.14 over these days and do not include systematic error arising from assumptions in the apportionment algorithm.

(1).[12, 14] The results of this calculation are shown in Table 9.1. For both events, the sulfuric acid concentration calculated from the sulfate mass fraction matches within experimental error the measured sulfuric acid concentration, showing that uptake of sulfuric acid is approximately collision limited. In other words, the sulfate mass fraction during new particle formation can be quantitatively explained by condensation of gas phase sulfuric acid molecules. This agreement is significant and has been studied only on two other occasions.[31, 32] The observed closure between gas and particle phase measurements validates existing models to describe S uptake.[14] Additionally, the Γ_v values (NAMS-measured Γ_m adjusted for particle density, as discussed in Eq. (2) in the experimental section) reported in Table 9.1 are consistent with those measured in Atlanta, Georgia, and Boulder, Colorado, as well as values for some new particle formation events in Mexico City, Mexico, and Hyytiälä, Finland,[14, 31] indicating that the contribution of S to particle growth is similar to that observed in those locations. Nanoparticles in Lewes are fully neutralized, consistent with a previous study in this location (Chapter 7),[3] but contrasting with a study in a remote boreal forest in the early spring (see dissertation of M. Ross Pennington[8]).[31] As a result, in Lewes the apportioned nitrate (proxy for Excess N) is substantial, whereas in the boreal forest no apportioned nitrate was present. With respect to carbonaceous matter, the O/C ratios in Lewes are higher than those measured in the boreal forest, indicating that the Lewes carbonaceous matter is more highly oxidized, though the O/C ratios measured at the end of the boreal forest campaign (mid spring) were close to those reported here.[31] Relative to the previous campaign to study new particle formation in Lewes (see Chapter 7),[3] O/C ratios are lower in this study, but the

Table 9.1: Particle growth rate from 10-25 nm diameter, NAMS-measured sulfate mass fraction and calculated [H_2SO_4] from the sulfate mass fraction for the events on 12 and 13 August 2012.

	12 August	13 August
Growth Rate ($nm \cdot h^{-1}$)[a]	8.9 ± 0.8	7.1 ± 1.0
Sulfate Mass Fraction[a]	0.27 ± 0.08	0.27 ± 0.08
Γ_v[b]	4.4 ± 1.3	4.4 ± 1.3
$[H_2SO_4]_{NAMS}$ ($molec \cdot cm^{-3}$)[c]	$2.6 \pm 0.8 \times 10^7$	$2.1 \pm 0.6 \times 10^7$
$[H_2SO_4]_{CIMS}$ ($molec \cdot cm^{-3}$)[a]	$1.9 \pm 1.0 \times 10^7$	$2.2 \pm 1.1 \times 10^7$

[a]Experimental measurement. [b]Assumes $\rho_{particle} = 1.5\ g \cdot cm^{-3}$. [c]Calculated from Eq. (1).

difference could be a result of the time of year (fall vs. summer) and the extent of anthropogenic contributions in the local environment (more vehicular emissions in the summer).

More generally, the Lewes data show four different chemical components important to particle growth during new particle formation: sulfate, cation forming nitrogen (ammonia or amine), carbonaceous matter, and nitrate (or, more precisely, Excess N). The relative contributions of these pathways to mass growth are quantitatively determined, as shown in Fig. 9.6. In contrast, only three of these components were important to mass growth in the boreal forest: sulfate, cation forming nitrogen, and carbonaceous matter. The general observation that nanoparticles are preferentially enhanced in inorganic components during new particle formation is consistent with several previous studies of nanoparticle chemical composition by NAMS (see Chapter 7 and the dissertation of M. Ross Pennington[8]).[3, 12, 31] However, it should be emphasized that over half of the mass growth arises from carbonaceous matter and Excess N, for which no models exist to suitably explain their contributions.

9.3.3 Nanoparticle Chemical Composition on Non-New Particle Formation Days

In this section, the two new particle formation days are compared to the days immediately preceding and succeeding them: 11 August and 14 August, both of which were non-new particle formation days. For both of these days, air masses arrived from the south (Fig. 9.2). Figure 9.7 presents data for 11 August, whereas Fig. 9.8 presents data for 14 August. The vertical dotted lines in each figure highlight periods where either chemical composition changes or aerosol mass changes.

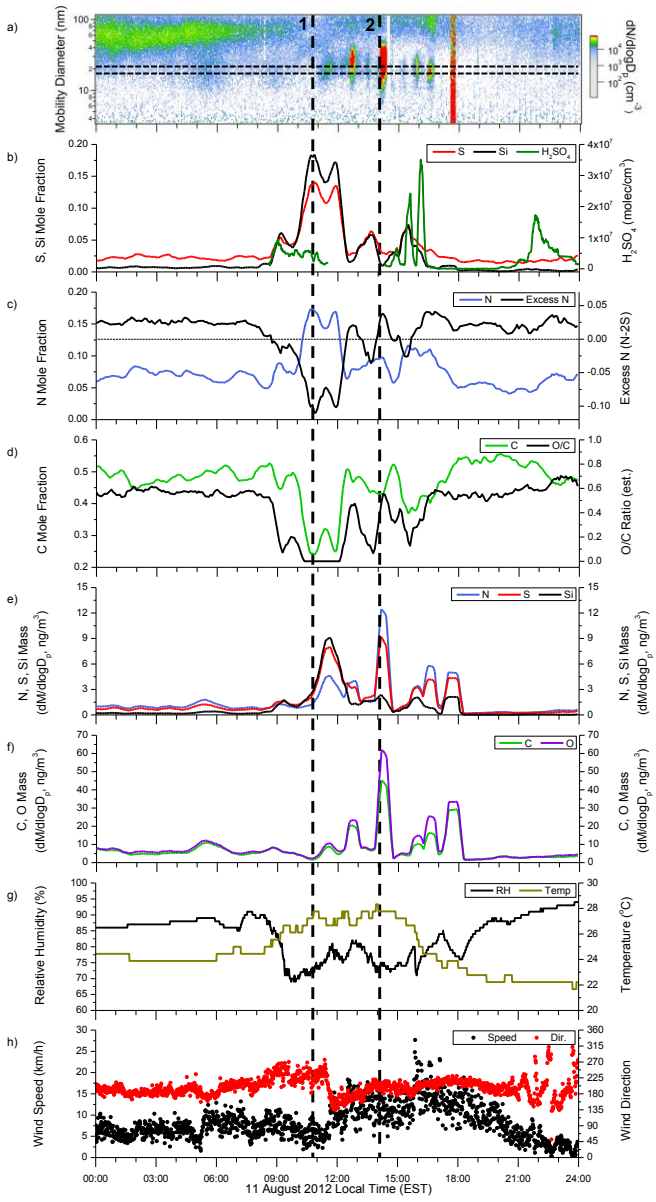

Figure 9.7: a) Aerosol size distributions, b) S and Si mole fraction as well as gas phase sulfuric acid concentration, c) N and Excess N mole fractions, d) C mole fraction and estimated O/C ratio, e) N, S, and Si elemental mass, f) C and O elemental mass, g) relative humidity and temperature, and h) wind speed and wind direction for 11 August 2012. The horizontal dotted lines in a) indicate the NAMS-measured size range. The horizontal dotted line in c) indicates Excess N = 0. Vertical dotted lines indicate periods of contrasting nanoparticle composition. Nanoparticle composition data were subject to 6-point smoothing; the sulfuric acid concentration was subjected to 10-point smoothing.

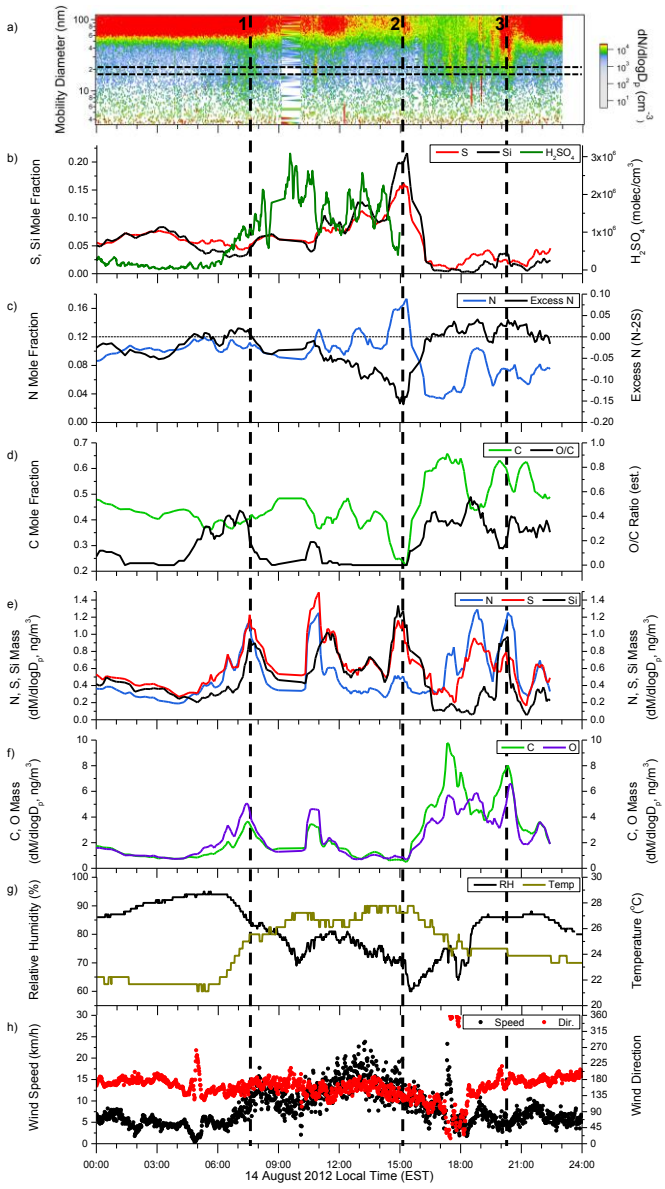

Figure 9.8: a) Aerosol size distributions, b) S and Si mole fraction as well as gas phase sulfuric acid concentration, c) N and Excess N mole fractions, d) C mole fraction and estimated O/C ratio, e) N, S and Si elemental mass, f) C and O elemental mass, g) relative humidity and temperature and h) wind speed and wind direction for 14 August 2012. The horizontal dotted lines in a) indicate the NAMS-measured size range. The horizontal dotted line in c) indicates Excess N = 0. Vertical dotted lines indicate periods of contrasting nanoparticle composition. Nanoparticle composition data were subject to 6-point smoothing; the sulfuric acid concentration was subjected to 10-point smoothing.

On both days, the nanoparticle chemical composition is dynamic. The dotted lines in Figs. 9.7 and 9.8 highlight specific time points to illustrate that these changes in nanoparticle chemical composition are not necessarily correlated with changes in aerosol mass or number concentration. For example, the first vertical dotted line on Fig. 9.6 shows a time period when chemical composition is static while aerosol mass changes substantially. On the other hand, the first dotted line on Fig. 9.7 shows particle composition changing before and during a change in aerosol mass.

Despite the dynamic nature of the aerosol on these days, some general trends are clear. Inorganic components are preferentially enhanced relative to carbonaceous matter during the daytime, which is evidenced by the substantial increases in S, Si, and N mole fractions. The Si mole fraction is particularly noteworthy because it is so high relative to new particle formation days. Si also has been reported previously in urban and suburban nanoparticle studies.[20, 33] On these days, Si and S are highly correlated ($r = 0.98$ and 0.89 for 11 August and 14 August, respectively), and the daytime enhancement of each suggests a photochemical source. By comparison, Si is a minor component of the aerosol on new particle formation days and it is not correlated with S (except at the very beginning of the event, after which the locally produced Si was presumably overwhelmed by other, regionally produced species). Changes in S mole fraction do not respond quickly to changes in gas phase sulfuric acid because the concentration of sulfuric acid is generally an order of magnitude lower than during event days, making the condensation rate slow.

Also interesting about the non-new particle formation days are the trends in N mole fraction and, more importantly, Excess N. Although the N mole fraction increases during the daytime of both non-new particle formation days, Excess N is < 0

during the daytime, whereas it is generally > 0 during the nighttime. This diurnal dependence is consistent with expected ammonium nitrate partitioning to the particle phase at night as well as organonitrate formation.[34]

Figure 9.6 presents apportioned mass fractions for the daytimes of 11 and 14 August in comparison to the new particle formation days of 12 and 13 August. Inorganics represent a similar fraction of the daytime aerosol mass on all four days. However, the identities of the species making up the inorganic fraction are different. On non-new particle formation days, Si (taken as SiO_2) is a substantial component of the nanoparticle mass, whereas on new particle formation days SiO_2 is replaced by ammonium nitrate (a proxy in the apportionment algorithm for Excess N). The aerosol is neutralized on new particle formation days, whereas it is acidic on non-new particle formation days. Notably, the average sulfate mass fraction is similar across all four days, despite substantial differences in gas phase sulfuric acid concentrations. The carbonaceous mass fraction is significantly more oxidized on new particle formation days relative to non-new particle formation days, most likely because local combustion sources dominate the aerosol on non-new particle formation days.

On new particle formation days, the critical supersaturation (S_c) of 50 nm diameter particles measured with the CCNc during the daytime have a hygroscopicity similar to that of pure ammonium sulfate (S_c = 0.4%), whereas those measured in the daytime on non-new particle formation days were less hygroscopic (S_c = 0.5-1.0%). The greater hygroscopicity on new particle formation days is consistent with more highly oxidized carbonaceous matter as measured by NAMS. The lower hygroscopicity on non-new particle formation days is consistent with less oxidized

carbonaceous matter, although the chemical form and effect of Si on particle hygroscopicity is unknown.

9.4 Conclusions

NAMS was used to obtain highly time-resolved nanoparticle chemical composition during days with and without new particle formation. Inorganic components are shown to be preferentially enhanced on both new particle formation and non-new particle formation days. Nanoparticle chemical composition is dynamic on both types of days, and these changes in chemical composition need not be correlated with changes in aerosol mass or number concentration. The composition measurements on new particle formation days substantially improve our understanding of the chemical processes underlying new particle formation. Because of its high time resolution and quantitative capabilities, NAMS is capable of distinguishing species likely to be associated with particle formation and early growth from those likely to be associated with later stages of growth.

At the onset of new particle formation, the particle phase S mole fraction increases simultaneously with the gas-phase sulfuric acid concentration, and both increase well before the mode diameter of the aerosol passes into the size range of the chemical composition measurement. Later in the event, the S mole fraction no longer correlates with the change (this time a decrease) in sulfuric acid concentration. These time dependent changes are likely to be general characteristics of new particle formation as they have been observed in a remote boreal forest as well. The measured S mole fraction during new particle formation is quantitatively explained by condensation of gas-phase sulfuric acid, indicating that existing models to describe S uptake into growing nanoparticles are appropriate.

Nitrogen is shown to be a key chemical component for new particle formation. Although some nitrogen is associated with neutralization of sulfuric acid at the onset of new particle formation, a substantial portion of the particle phase N mole fraction is associated with a (or several) separate chemical species. This observation is consistent with those from the previous study in Lewes discussed in Chapter 7. This so-called Excess N increases when the mode diameter of the aerosol passes through the size range of the chemical composition measurement, highlighting its role in particle growth but not particle formation. Carbonaceous matter contributes ~50% of the particle mass growth.

In this location, nanoparticles on non-new particle formation days are more acidic and have carbonaceous matter that is less oxidized than on new particle formation days. Inorganic components are enhanced during the daytime on both types of days, but the identities of these components are different. Non-new particle formation days are influenced mainly by local emissions, whereas new particle formation days are influenced by regional processes.

Future work should focus on elucidating the complex roles of nitrogen and carbon in new particle formation. Excess nitrogen on new particle formation days does not appear to follow the expected partitioning trend of ammonium nitrate. This observation suggests apportioning Excess N to ammonium nitrate is not reasonable in this environment. Additionally, carbonaceous matter was incompletely characterized, as O/C molar ratios could only be indirectly estimated. Uncertainties associated with nitrogen and carbon highlight the need for direct molecular composition measurements. Models exist that reasonably describe the incorporation of S into growing nanoparticles [e.g. Eqs. (1) and (2)]. To date, no models currently do the

same for N and C uptake. These observations strengthen confidence in models previously assumed to be correct and exemplify the need to accurately model uptake of the other species.

Bryan R. Bzdek, Andrew J. Horan, M. Ross Pennington, Joseph W. DePalma, Jun Zhao, Coty N. Jen, David R. Hanson, James N. Smith, Peter H. McMurry, and Murray V. Johnston, "Quantitative and time-resolved nanoparticle composition measurements during new particle formation," *Faraday Discussions*, **2013**, *165* (1), 25-43. Reproduced in part by permission of The Royal Society of Chemistry.

9.5 References

1. Luther, G. W.; Stecher, H. A., Preface: Historical background. *J. Geophys. Res.-Atmos.* **1997,** *102* (D13), 16215-16217, doi: 10.1029/96JD03986.

2. Stecher, H. A.; Luther, G. W.; MacTaggart, D. L.; Farwell, S. O.; Crosley, D. R.; Dorko, W. D.; Goldan, P. D.; Beltz, N.; Krischke, U.; Luke, W. T.; Thornton, D. C.; Talbot, R. W.; Lefer, B. L.; Scheuer, E. M.; Benner, R. L.; Wu, J. G.; Saltzman, E. S.; Gallagher, M. S.; Ferek, R. J., Results of the gas-phase sulfur intercomparison experiment (GASIE): Overview of experimental setup, results and general conclusions. *J. Geophys. Res.-Atmos.* **1997,** *102* (D13), 16219-16236, doi: 10.1029/97JD01362.

3. Bzdek, B. R.; Zordan, C. A.; Luther, G. W.; Johnston, M. V., Nanoparticle chemical composition during new particle formation. *Aerosol Sci. Technol.* **2011,** *45* (8), 1041-1048.

4. Wang, S. Y.; Johnston, M. V., Airborne nanoparticle characterization with a digital ion trap-reflectron time of flight mass spectrometer. *Int. J. Mass Spectrom.* **2006,** *258* (1-3), 50-57.

5. Wang, S. Y.; Zordan, C. A.; Johnston, M. V., Chemical characterization of individual, airborne sub-10-nm particles and molecules. *Anal. Chem.* **2006,** *78* (6), 1750-1754.

6. Pennington, M. R.; Johnston, M. V., Trapping charged nanoparticles in the nano aerosol mass spectrometer (NAMS). *Int. J. Mass Spectrom.* **2012,** *311* (1), 64-71.

7. McMurry, P. H.; Ghimire, A.; Ahn, H. K.; Sakurai, H.; Moore, K.; Stolzenburg, M.; Smith, J. N., Sampling nanoparticles for chemical analysis by low resolution electrical mobility classification. *Environ. Sci. Technol.* **2009,** *43* (13), 4653-4658.

8. Pennington, M. R. An Improved Nano Aerosol Mass Spectrometer for Ambient and Laboratory Measurements. University of Delaware, Newark, DE, 2012.

9. Zordan, C. A.; Pennington, M. R.; Johnston, M. V., Elemental composition of nanoparticles with the Nano Aerosol Mass Spectrometer. *Anal. Chem.* **2010,** *82* (19), 8034-8038.

10. Johnston, M. V.; Wang, S.; Reinard, M. S., Nanoparticle mass spectrometry: Pushing the limit of single particle analysis. *Appl. Spectrosc.* **2006,** *60* (10), 264A-272A.

11. Klems, J. P.; Johnston, M. V., Origin and impact of particle-to-particle variations in composition measurements with the Nano Aerosol Mass Spectrometer. *Anal. Bioanal. Chem.* **2013,** *405* (22), 6995-7003.

12. Bzdek, B. R.; Zordan, C. A.; Pennington, M. R.; Luther, G. W.; Johnston, M. V., Quantitative assessment of the sulfuric acid contribution to new particle growth. *Environ. Sci. Technol.* **2012,** *46* (8), 4365-4373.

13. Jefferson, A.; Eisele, F. L.; Ziemann, P. J.; Weber, R. J.; Marti, J. J.; McMurry, P. H., Measurements of the H_2SO_4 mass accommodation coefficient onto polydisperse aerosol. *J. Geophys. Res.-Atmos.* **1997,** *102* (D15), 19021-19028, doi: 10.1029/97jd01152.

14. Kuang, C.; Riipinen, I.; Sihto, S. L.; Kulmala, M.; McCormick, A. V.; McMurry, P. H., An improved criterion for new particle formation in diverse atmospheric environments. *Atmos. Chem. Phys.* **2010,** *10* (17), 8469-8480.

15. Zhao, J.; Eisele, F. L.; Titcombe, M.; Kuang, C.; McMurry, P. H., Chemical ionization mass spectrometric measurements of atmospheric neutral clusters using the cluster-CIMS. *J. Geophys. Res.-Atmos.* **2010,** *115* (D8), D08205, doi: 10.1029/2009JD012606.

16. Zhao, J.; Smith, J. N.; Eisele, F. L.; Chen, M.; Kuang, C.; McMurry, P. H., Observation of neutral sulfuric acid-amine containing clusters in laboratory and ambient measurements. *Atmos. Chem. Phys.* **2011,** *11* (21), 10823-10836.

17. Hanson, D. R.; McMurry, P. H.; Jiang, J.; Tanner, D.; Huey, L. G., Ambient pressure proton transfer mass spectrometry: Detection of amines and ammonia. *Environ. Sci. Technol.* **2011,** *45* (20), 8881-8888.

18. Levin, E. J. T.; Prenni, A. J.; Petters, M. D.; Kreidenweis, S. M.; Sullivan, R. C.; Atwood, S. A.; Ortega, J.; DeMott, P. J.; Smith, J. N., An annual cycle of size-resolved aerosol hygroscopicity at a forested site in Colorado. *J. Geophys. Res.-Atmos.* **2012,** *117* (D06201), doi: 10.1029/2011jd016854.

19. Draxler, R. R.; Rolph, G. D. *HYSPLIT (HYbrid Single-Particle Lagrangian Integrated Trajectory) Model access via NOAA ARL READY Website (http://ready.arl.noaa.gov/HYSPLIT.php)*, NOAA Air Resources Laboratory: Silver Spring, MD, 2013.

20. Pennington, M. R.; Klems, J. P.; Bzdek, B. R.; Johnston, M. V., Nanoparticle chemical composition and diurnal dependence at the CalNex Los Angeles

Ground Site. *J. Geophys. Res.-Atmos.* **2012,** *117* (D00), D00V10, doi: 10.1029/2011JD017061.

21. Drewnick, F.; Schwab, J. J.; Jayne, J. T.; Canagaratna, M.; Worsnop, D. R.; Demerjian, K. L., Measurement of ambient aerosol composition during the PMTACS-NY 2001 using an aerosol mass spectrometer. Part I: Mass concentrations. *Aerosol Sci. Technol.* **2004,** *38* (S1), 92-103.

22. Jimenez, J. L.; Jayne, J. T.; Shi, Q.; Kolb, C. E.; Worsnop, D. R.; Yourshaw, I.; Seinfeld, J. H.; Flagan, R. C.; Zhang, X. F.; Smith, K. A.; Morris, J. W.; Davidovits, P., Ambient aerosol sampling using the Aerodyne Aerosol Mass Spectrometer. *J. Geophys. Res.-Atmos.* **2003,** *108* (D7), 8425, doi: 10.1029/2001jd001213.

23. Lee, S. H.; Murphy, D. M.; Thomson, D. S.; Middlebrook, A. M., Nitrate and oxidized organic ions in single particle mass spectra during the 1999 Atlanta Supersite Project. *J. Geophys. Res.-Atmos.* **2003,** *108* (D7), 8417, doi: 10.1029/2001jd001455.

24. Tolocka, M. P.; Lake, D. A.; Johnston, M. V.; Wexler, A. S., Ultrafine nitrate particle events in Baltimore observed by real-time single particle mass spectrometry. *Atmos. Environ.* **2004,** *38* (20), 3215-3223.

25. Woo, K. S.; Chen, D. R.; Pui, D. Y. H.; McMurry, P. H., Measurement of Atlanta aerosol size distributions: Observations of ultrafine particle events. *Aerosol Sci. Technol.* **2001,** *34* (1), 75-87.

26. Clegg, S. L.; Brimblecombe, P.; Wexler, A. S., Thermodynamic model of the system H^+-NH_4^+-SO_4^{2-}-NO_3^--H_2O at tropospheric temperatures. *J. Phys. Chem. A* **1998,** *102* (12), 2137-2154.

27. Wexler, A. S.; Clegg, S. L., Atmospheric aerosol models for systems including the ions H^+, NH_4^+, Na^+, SO_4^{2-}, NO_3^-,Cl^-, Br^-, and H_2O. *J. Geophys. Res.-Atmos.* **2002,** *107* (D14), 4207, doi: 10.1029/2001jd000451.

28. Ehn, M.; Kleist, E.; Junninen, H.; Petaja, T.; Lonn, G.; Schobesberger, S.; Dal Maso, M.; Trimborn, A.; Kulmala, M.; Worsnop, D. R.; Wahner, A.; Wildt, J.; Mentel, T. F., Gas phase formation of extremely oxidized pinene reaction products in chamber and ambient air. *Atmos. Chem. Phys.* **2012,** *12* (11), 5113-5127.

29. Donahue, N. M.; Henry, K. M.; Mentel, T. F.; Kiendler-Scharr, A.; Spindler, C.; Bohn, B.; Brauers, T.; Dorn, H. P.; Fuchs, H.; Tillmann, R.; Wahner, A.;

Saathoff, H.; Naumann, K. H.; Mohler, O.; Leisner, T.; Muller, L.; Reinnig, M. C.; Hoffmann, T.; Salo, K.; Hallquist, M.; Frosch, M.; Bilde, M.; Tritscher, T.; Barmet, P.; Praplan, A. P.; DeCarlo, P. F.; Dommen, J.; Prevot, A. S. H.; Baltensperger, U., Aging of biogenic secondary organic aerosol via gas-phase OH radical reactions. *Proc. Natl. Acad. Sci. U.S.A.* **2012,** *109* (34), 13503-13508.

30. Hall, W. A.; Pennington, M. R.; Johnston, M. V., Molecular transformations accompanying the aging of laboratory secondary organic aerosol. *Environ. Sci. Technol.* **2013,** *47* (5), 2230-2237.

31. Pennington, M. R.; Bzdek, B. R.; DePalma, J. W.; Smith, J. N.; Kortelainen, A.-M.; Hildebrandt Ruiz, L.; Petaja, T.; Kulmala, M.; Worsnop, D. R.; Johnston, M. V., Identification and quantification of particle growth channels during new particle formation. *Atmos. Chem. Phys.* **2013,** *13* (20), 10215-10225.

32. Smith, J. N.; Dunn, M. J.; VanReken, T. M.; Iida, K.; Stolzenburg, M. R.; McMurry, P. H.; Huey, L. G., Chemical composition of atmospheric nanoparticles formed from nucleation in Tecamac, Mexico: Evidence for an important role for organic species in nanoparticle growth. *Geophys. Res. Lett.* **2008,** *35* (4), L04808, doi: 10.1029/2007gl032523.

33. Zordan, C. A.; Wang, S.; Johnston, M. V., Time-resolved chemical composition of individual nanoparticles in urban air. *Environ. Sci. Technol.* **2008,** *42* (17), 6631-6636.

34. Fry, J. L.; Draper, D. C.; Zarzana, K. J.; Campuzano-Jost, P.; Day, D. A.; Jimenez, J. L.; Brown, S. S.; Cohen, R. C.; Kaser, L.; Hansel, A.; Cappellin, L.; Karl, T.; Roux, A. H.; Turnipseed, A.; Cantrell, C.; Lefer, B. L.; Grossberg, N., Observations of gas- and aerosol-phase organic nitrates at BEACHON-RoMBAS 2011. *Atmos. Chem. Phys.* **2013,** *13* (17), 8585-8605.

Chapter 10

IDENTIFICATION AND QUANTIFICATION OF ADDITIONAL COMPONENTS TO NANOPARTICLE COMPOSITION AND GROWTH

10.1 Introduction

An important observation in Chapters 7-9 is that sulfuric acid (and any ammonia or amine apportioned to neutralize it) generally accounts for less than half of the total mass growth of nanoparticles during new particle formation. Other important components to nanoparticle growth include carbonaceous matter, other nitrogen containing compounds (Excess N), and silicon containing compounds. None of these components has a particularly well-defined molecular composition. Carbonaceous matter contains a host of different molecular species. As discussed in Chapter 9, Excess N could also be in a number of different forms. Silicon is assumed to be in the form of SiO_2, but this assignment is an assumption as the sources of particulate Si are not well known. This chapter examines all three of these species, with the aim of constraining their molecular identities, and/or improving quantification of their relative contribution to nanoparticle mass and growth during new particle formation. This is accomplished by measuring quantitatively nanoparticle elemental composition with the Nano Aerosol Mass Spectrometer (NAMS) and either apportioning the elemental composition to molecular species based upon collocated measurements of nanoparticle molecular composition or assessing trends in nanoparticle composition over several campaigns. Based on collocated elemental and molecular composition measurements, the identity of Excess N is determined to be carbonaceous. This is a

highly important advance, as it permits quantification of both the contribution and identity of the carbonaceous matter to new particle growth, which is important for modelers as the contribution of carbonaceous matter is the largest uncertainty in determining the climatic importance of new particle formation. Additionally, this observation for the first time indicates the importance of nitrogen to carbonaceous matter. Based on NAMS measurements over several campaigns, nanoparticulate Si is shown to arise as a result of photochemical processing of higher volatility Si-containing compounds. This Si comes from nearly ubiquitous diffuse sources and may be an important, previously overlooked anthropogenic component of aerosol mass that requires further investigation to resolve its atmospheric role. This chapter concludes with a discussion of how assumptions underlying molecular apportionment of elemental composition can impact quantification of the contribution and composition of various channels to nanoparticle growth.

10.2 Experimental Section

Measurements from seven field campaigns are considered in this chapter. These campaigns are: Lewes, Delaware, July-August 2012;[1] Pasadena, California, May-June 2010;[2] Wilmington, Delaware, May 2006;[3] Wilmington, Delaware, July 2009;[4] Wilmington, Delaware, December 2009;[4] Lewes, Delaware, October-November 2007;[5] and Hyytiälä, Finland, March-April 2011.[6] Two of these seven campaigns are discussed in detail. The first is a field measurement conducted at the Hugh R. Sharp Campus of the University of Delaware in Lewes, Delaware (38^{o}47'02" N, 75^{o}09'39" W) from 23 July to 31 August 2012 (see Chapter 9).[1] During this campaign, particles were sampled at a height of 6 m above the ground through a 0.5 in outer diameter copper tube. The second measurement is the CalNex campaign,[2, 7]

which took place at the California Institute of Technology in Pasadena, California (34°8'26.1594" N, 118°7'21" W) from 21 May to 10 June 2010. During this campaign, particles were sampled at a height of 4 m above the ground through a 0.5 in outer diameter copper tube.

Nanoparticle elemental composition was measured using NAMS, which gives quantitative elemental composition of individual nanoparticles in the 10-30 nm size range. NAMS has been described in detail in Chapters 1, 7, and 9.[1, 8-10] Briefly, particles are drawn in through an inlet, focused, size-selectively trapped in a digital ion trap, and irradiated with a high energy pulsed laser beam to quantitatively convert all molecular species to multiply charged, positive atomic ions. These ions are then mass analyzed by time-of-flight. Deconvolution of overlapping signal intensities was accomplished by the method of Zordan, et al. [11] Nanoparticle chemical composition was averaged such that a minimum of 20 particles was included in the average, as this number of particles simultaneously maximizes time resolution while minimizing uncertainty from variations in the dynamics of the laser plume.[12] For the Lewes campaign, NAMS was set to analyze the composition of 18 ± 3 nm mobility diameter particles. For the Pasadena campaign, NAMS was set to analyze 21 ± 3 nm mobility diameter particles. Measurements of particle composition around 20 nm diameter provide information on the species important to particle growth from 10-20 nm diameter, as most of the nanoparticle mass was added to the particle as it grew from 10 nm to 20 nm diameter.

During the Lewes campaign, nanoparticle chemical composition was measured by a second technique. This second method is the Thermal Decomposition Chemical Ionization Mass Spectrometer (TDCIMS).[13, 14] TDCIMS provides the molecular

composition of bulk nanoparticulate samples. This system uses a low resolution electrostatic classification technique[15] to collect nanoparticles on a metal filament and then resistively heats the filament and analyzes the desorbed gas using a chemical ionization time-of-flight mass spectrometer. Positive and negative ion mass spectra were measured sequentially in order to detect particulate bases and acids, respectively. For each run, nanoparticles with a peak mobility diameter of 30 nm and a half-width at half-maximum of 10 nm were collected for 30 minutes. TDCIMS measurements were performed by Michael Lawler and James Smith from the National Center for Atmospheric Research.

The discussion of particulate nitrogen (Section 10.3.1) focuses primarily on the new particle formation event on 21 August 2012, a day where both NAMS and TDCIMS were in full operation. Analysis of this particular day is instructive because the measured chemical composition exhibits key features that are typical of new particle formation in Lewes and other locations. After a detailed discussion of the event on 21 August, the results are generalized to the rest of the events studied in Lewes.

Importantly (with respect to Section 10.3.2), during all campaigns where ambient particles were sampled into NAMS, copper tubing was used in the inlet. No silicone tubing was used in the field setup. This tubing has been shown to emit contaminants that can impact particle composition.[16, 17] Additionally, Si was absent from the mass spectra of calibration aerosols at these sites, confirming that Si contamination did not arise from the measurement apparatus itself.

Aerosol size distribution and mass concentration measurements were accomplished with scanning mobility particle sizers (SMPS): Electrostatic Classifier

model 3080 and Condensation Particle Counter (CPC) model 3025a for Pasadena or CPC model 3788 for Lewes (TSI, Inc., St. Paul, Minnesota). In Lewes, gas phase sulfuric acid was measured using the Cluster Chemical Ionization Mass Spectrometer[18, 19] and gas phase ammonia and amine concentrations were measured using the Ambient pressure Proton transfer Mass Spectrometer (AmPMS).[20, 21] Nitric acid was not directly measured in Lewes. In its place, NO_2 measurements were taken using a chemiluminescence analyzer (model 42c, Thermo Environmental Instruments, Franklin, Massachusetts), and the underlying assumption was made that these measured NO_2 levels represent an upper limit for the nitric acid concentration because the measured NO_2 level includes HNO_3 that has been converted by the molybdenum NO_2 to NO converter. Aerosol thermodynamic calculations were performed with the Extended Aerosol Inorganics Model (E-AIM).[22-25]

10.3 Results and Discussion

10.3.1 Molecular Constraints on Particle Growth during New Particle Formation

Figure 10.1a presents the evolution of the SMPS-measured particle size distribution on 21 August 2012, a day when new particle formation was observed and both NAMS and TDCIMS were in full operation. Particles appear around 10 nm diameter at about 11:00 and grow over the course of the day to larger sizes. The dotted lines indicate the size ranges at which NAMS and TDCIMS measured nanoparticle chemical composition. Based on HYSPLIT back trajectories for this day (Fig. 10.2),[26] the air mass transporting the new particle formation event came from the northwest, although substantial air recirculation occurred around the field site. One characteristic

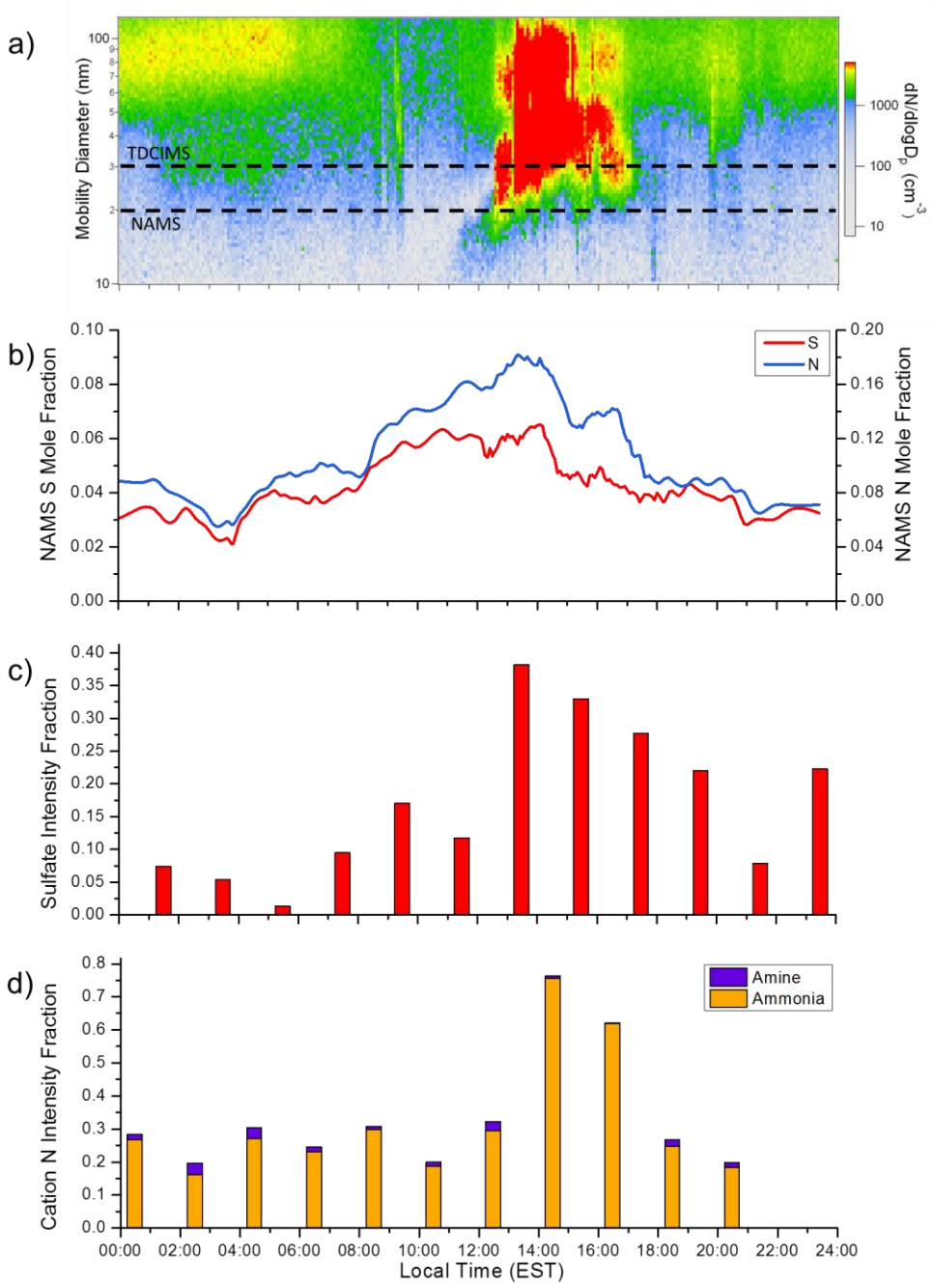

Figure 10.1: a) SMPS-measured aerosol size distribution, b) NAMS-measured S and N elemental mole fractions, c) TDCIMS-measured sulfate ion intensity fraction, and d) TDCIMS-measured cation-forming nitrogen ion intensity fraction for the new particle formation event on 21 August 2012. The horizontal lines in a) indicate the NAMS- and TDCIMS-measured sizes. NAMS data were subject to 6-point smoothing.

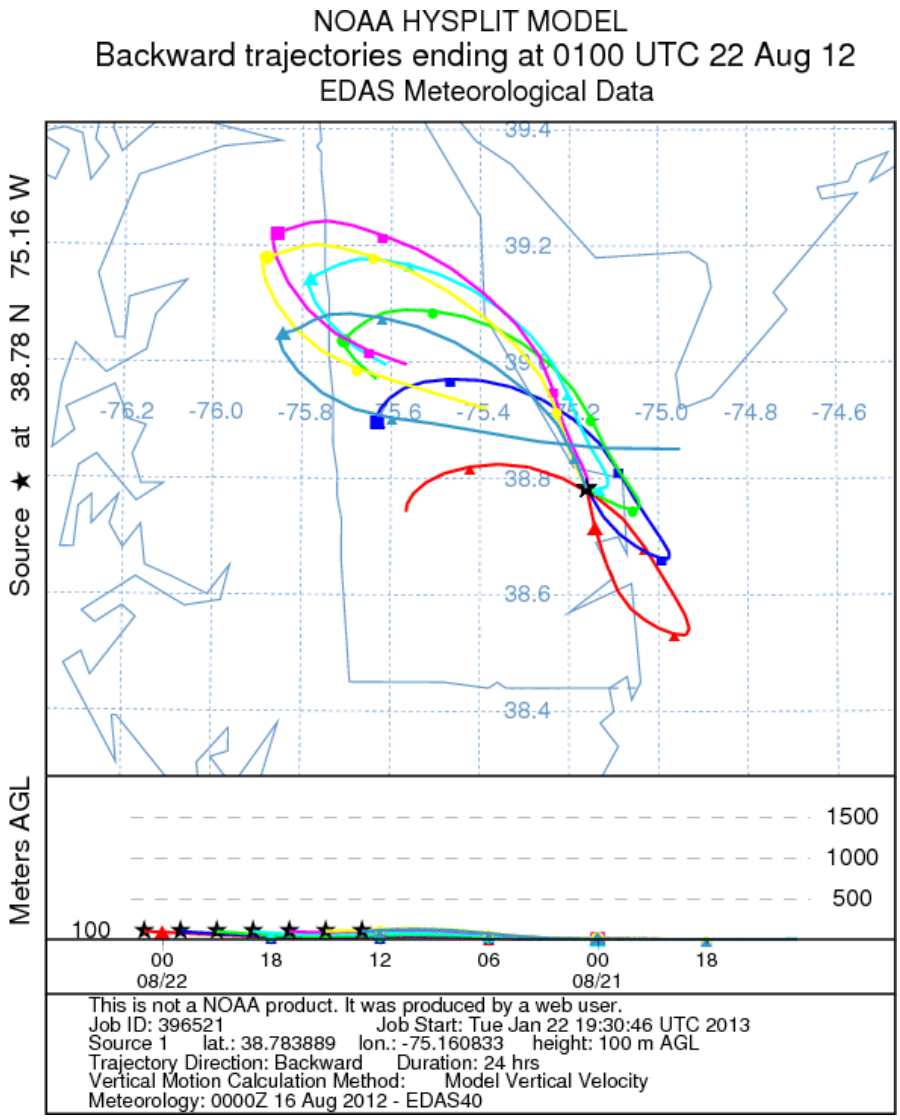

Figure 10.2: Air mass back trajectory for 21 August 2012, a new particle formation event day.

feature of new particle formation in Lewes is that on new particle formation days air masses generally arrive at the site from the northwest.[1, 5]

Figure 10.1b shows NAMS-measured sulfur and nitrogen elemental mole fractions as the event progresses and illustrates three key observations about new particle formation. First, particle phase S increases during the new particle formation event and this increase can be quantitatively ascribed to sulfuric acid condensation onto the growing particles. This increase in S mole fraction is a general observation and has been observed in every NAMS study of new particle formation (see Chapters 7 and 9 as well as the dissertation of M. Ross Pennington[27]).[1, 5, 6, 28] Second, particle phase N is correlated with the change in particle phase S. This, too, is a general observation of new particle formation and has been observed in every NAMS study. In Fig. 10.1b, N is scaled by a factor of 2 larger than S. If N and S overlap, they are exactly at a 2:1 ratio. At the beginning of the event, N/S = 2, suggesting sulfate is completely neutralized. Third, later on in the event, N increases more substantially than S, resulting in N/S >> 2. This ratio indicates that some nitrogen exists in excess of that required to neutralize sulfate (termed "Excess N"). The presence of Excess N appears to be a general characteristic of new particle formation in Lewes (see Chapters 7 and 9)[1, 5] but not of new particle formation in other locations studied by NAMS.[6, 27]

Figures 10.1c and 10.1d show the variation in TDCIMS-measured sulfate ion intensity (Fig. 10.1c, from negative mode mass spectra) and ammonia and amine ion intensity (Fig. 10.1d, from positive mode mass spectra) during the event day. The reported values are the intensity of a given ion relative to the total ion current at that polarity, and the width of the bar represents the time period of analysis. Both sulfate and ammonia ion intensity increase during the event period. These observations from

TDCIMS confirm the previous interpretation of the NAMS elemental signal changes. Specifically, the changes in NAMS-measured S can be attributed to sulfate and the concurrent NAMS-measured increase in N can be attributed to ammonium. Note that both ammonia and amines are detected with similar sensitivity by TDCIMS, so the relative signal intensities give an approximate measure of the mole ratio of the two species. The observed larger ammonium ion signal suggests that ammonia is the dominant cation-forming nitrogen compound in the aerosol. However, as will be discussed in more detail later, the observed ammonium signal is too large to be only associated with neutralization of sulfate.

Figure 10.3 explores in more detail the nitrogen-containing compounds measured by TDCIMS and how they relate to the NAMS-measured Excess N (= N-2S). In Fig. 10.3a, Excess N is plotted as a function of time of day. Excess N gives a quantitative description of the amount of N that cannot be associated with sulfate neutralization. If Excess N < 0, then all measured N could be apportioned to cation neutralization of sulfate (as either ammonia or amine). If Excess N = 0, then the aerosol is described as neutralized ammonium sulfate (N/S = 2). If Excess N > 0, then there exists additional N not associated with sulfate. A general feature of new particle formation in Lewes is that Excess N increases at the same time as the nanoparticle mode grows through the measured size range (see Chapter 9).[1]

Figure 10.3b shows how the TDCIMS-measured ammonia intensity fraction evolves over the course of the event day. When Excess N measured by NAMS reaches its peak values (corresponding to when the mode moves through the NAMS size range), the ammonia intensity fraction reaches its peak value (accounting for over 70%

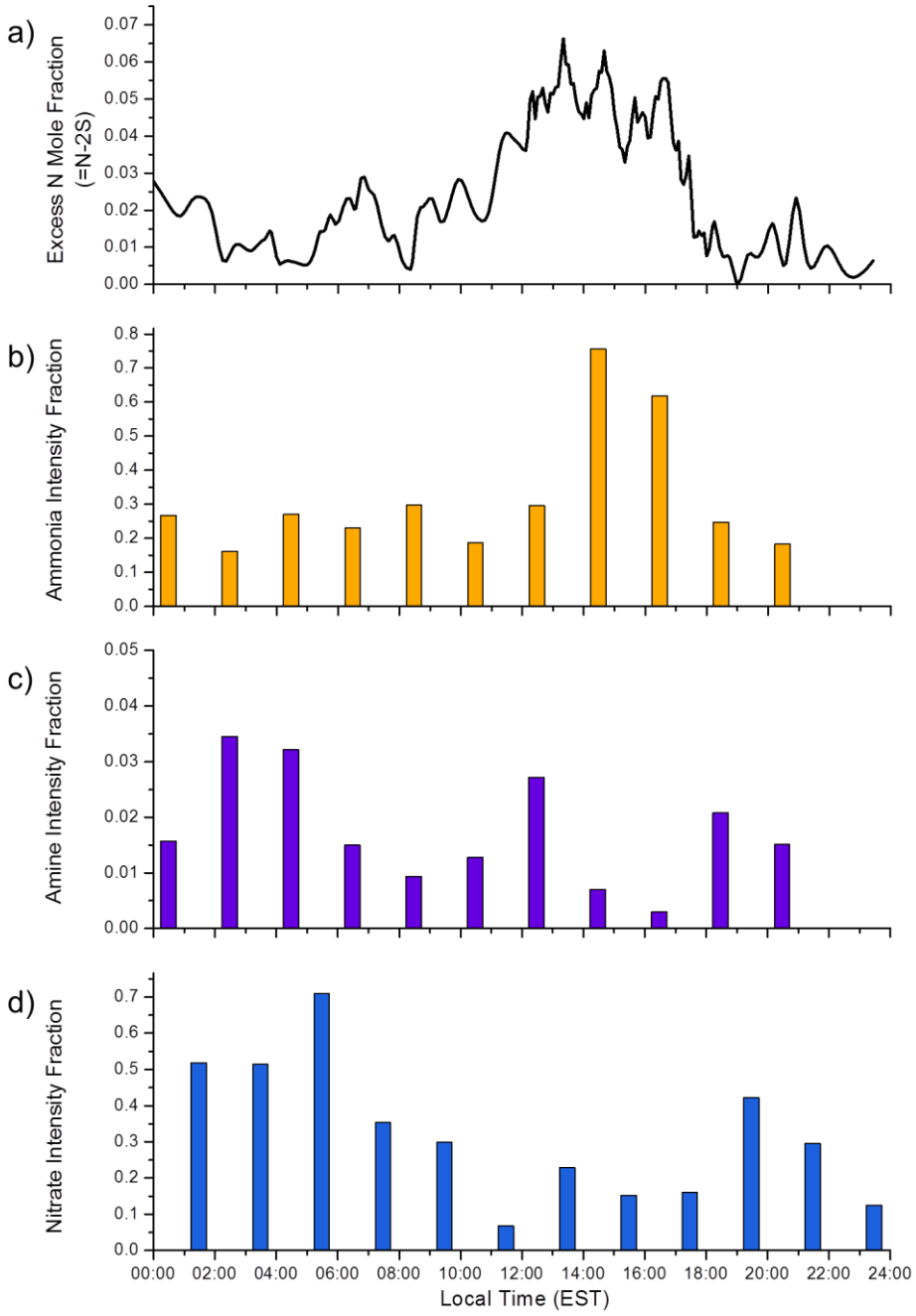

Figure 10.3: a) NAMS-measured Excess N mole fraction, b) TDCIMS-measured ammonia ion intensity fraction, c) TDCIMS-measured amine ion intensity fraction, and d) TDCIMS-measured inorganic nitrate ion intensity fraction for the new particle formation event on 21 August 2012. NAMS data were subject to 6-point smoothing.

of the total positive ion signal from TDCIMS). The slight time lag of the TDCIMS data relative to the NAMS data most likely arises from the slightly different particle sizes measured by each method. Figure 10.3c shows the evolution of the TDCIMS-measured amine intensity fraction on this day. Before the event begins (i.e. before 11:00), the amine accounts for several percent of the overall positive ion signal and represents 3-20% of the total cation-forming nitrogen signal (i.e. ammonia + amine). At the very start of the event but before the mode of new particles grows into the measured size range (i.e. at 12:30), both the ammonia and amine signals increase, but the amine signal increases more substantially relative to ammonia (going from 3% of the total cation-forming nitrogen signal – amines plus ammonia – at 8:30 to more than 8% of the signal at 12:30). This observation suggests amines might be important to the early stages of particle formation and growth. However, as the event moves through the analyzed size range and Excess N reaches its maximum value (from 14:00-16:00), the amine signal reaches its minimum value for the day. On the other hand (as mentioned above) the ammonia signal intensity reaches its maximum value during this same period. This observation suggests that amines are not responsible for the NAMS-measured increase in Excess N during new particle formation.

Figure 10.3d shows TDCIMS-measured inorganic nitrate intensity fraction. Nitrate appears to be a more significant component of the aerosol during the nighttime and early morning. Indeed, the nitrate intensity fraction is very low during the period where Excess N is very high. An important note is that TDCIMS is generally 100 times more sensitive to detection of ammonium nitrate than to detection of ammonium sulfate. Therefore, a large nitrate signal does not necessarily correlate to a large particulate nitrate fraction. In fact, during the period when Excess N is highest, the

nitrate/sulfate ratio is about 0.50, which (based on the relative sensitivities of the two species) would correspond to nitrate contributing < 1% of the total mole fraction during new particle formation. As a result, inorganic nitrate can be discounted as a substantial contributor to Excess N. Although these observations argue against inorganic nitrate as a substantial component of the nanoparticle composition, organonitrates cannot be completely excluded. TDCIMS measurements of hydroxynitrate and ammonium nitrate samples suggest that NO_2^- may correspond to inorganic nitrate, whereas NO_3^- may be associated with organonitrate. Although little signal attributable to organonitrates was measured, the sensitivity of TDCIMS to different organonitrates, including the role of particle-phase acidity, has not been extensively explored.

Experimental measurements of nanoparticle composition by NAMS and TDCIMS can be compared to predictions by E-AIM modeling of aerosol composition from measured gas phase concentrations of sulfuric acid, ammonia, dimethylamine, and NO_2 (measured by chemiluminescence analyzer and serves as an upper limit for HNO_3). Table 10.1 shows the modeled E-AIM results. Average gas phase concentrations used as model inputs are provided in Table 10.2. For the conditions during the event on August 21, E-AIM modeling predicts formation of solid ammonium sulfate without any amine or inorganic nitrate in the particle phase. If modeling is performed by disabling solid formation (i.e. requiring the aerosol to be exclusively in the liquid phase), the predicted N/S molar ratio is slightly larger than 2, amine is expected to account for 27% of the mole fraction of cations, and inorganic nitrate is expected to account for 3% of the mole fraction of anions. The TDCIMS measurements are broadly consistent with E-AIM modeling in that neither amine nor

Table 10.1: Results of E-AIM modeling for nanoparticle events in Lewes based on measured gas phase concentrations. AS = $(NH_4)_2SO_4$. Liquid phase results were obtained by disabling solid phase formation.

Date	Solid phase: Predicted N/S molar ratio	Liquid phase: Predicted N/S molar ratio	Liquid phase: Amine mole fraction of total cationic N	Liquid phase: Inorganic nitrate mole fraction of anions
10 August	No solid phase predicted	1.7	26%	0.6%
12 August	2 (solid AS)	No aerosol predicted	No aerosol predicted	No aerosol predicted
13 August	2 (solid AS)	1.5	27%	0.4%
21 August	2 (solid AS)	2.3	27%	3%

Table 10.2: Average gas phase concentrations used as model inputs for E-AIM.

Date	Average T (K)	Average RH (%)	$[NH_3]$ (molec·cm^{-3})	$[HNO_3]$ (molec·cm^{-3})	$[H_2SO_4]$ (molec·cm^{-3})	$[(CH_3)_2NH]$ (molec·cm^{-3})
10 August	298.3	84.4	5.65×10^9	1.19×10^{10}	1.95×10^7	2.28×10^8
12 August	298.2	58.4	4.18×10^9	1.28×10^{10}	1.95×10^7	7.13×10^7
13 August	299.4	52.8	4.08×10^9	4.29×10^{10}	2.39×10^7	9.27×10^7
21 August	296.8	67.3	7.51×10^9	9.46×10^{10}	1.28×10^7	2.02×10^7

inorganic nitrate accounts for a significant fraction of the particle composition. It is possible that the small amount of amine and inorganic nitrate detected by TDCIMS (measured amounts are much smaller than predicted amounts) arises from a liquid-like phase in addition to the solid.

Based on the above, only the ammonia signal from TDCIMS measurements correlates with the increase in Excess N measured by NAMS. This observation suggests two possibilities for the molecular identity of the Excess N. Both possibilities are consistent with the TDCIMS-measured ammonium to sulfate ratio during new particle formation, which (based on absolute ion abundances) is too large to arise from $(NH_4)_2SO_4$ alone: during new particle formation in Lewes, this ratio is ~5-15, whereas for ammonium sulfate standards the ammonium to sulfate ratio is 1.8. The first possibility is that Excess N is composed of ammonium salts of organic acids. This possibility seems unreasonable, since these salts are probably too volatile to remain in the aerosol phase and if there are ammonium salts, aminium salts would also be expected.[29, 30] A second possibility is that a portion of the ammonia signal arises from organic compounds that decompose to give ammonia upon thermal desorption and subsequent ionization. One candidate for such a process would be imines, which upon thermal desorption and ionization could undergo hydrolysis to release ammonia. Imines could arise from reaction of carbonyl-containing compounds with gas phase ammonia and have been measured frequently in aerosol.[31, 32] Although the specific molecular identity of this organic nitrogen is not fully determined, the broader conclusion is that the carbonaceous matter for this particular event contains a substantial amount of nitrogen.

Based on the above discussion, Fig. 10.4 maps the NAMS-measured elemental mole fractions onto molecular species for the event on 21 August as well as the other four event days during the Lewes campaign that were studied by NAMS. Molecular mass fractions are determined by apportioning the NAMS-measured elemental mole fractions to molecular species based on the measured TDCIMS molecular composition along with support from E-AIM modeling (see Table 10.1). First, sulfur and the accompanying oxygen (= 4S) are apportioned to sulfate. Then, Si and the accompanying oxygen (= 2Si) are apportioned as silicon dioxide. Note that Si accounts for only a small portion of the total elemental signal (< 1%) and virtually any reasonable assumption on the molecular identity of the silicon would have little impact on the apportioned mass fraction. Third, ammonium is apportioned to sulfate until the sulfate is fully neutralized. Based on the previously discussed TDCIMS and E-AIM results, neither amines nor inorganic nitrate contributes significantly to the nanoparticle mass. Therefore, the rest of the elemental signal is considered carbonaceous matter, with corresponding elemental ratios given in the boxes in Fig. 10.4. For the event on 21 August, the carbonaceous matter accounts for nearly 50% of the mass growth and has an average elemental composition of $CN_{0.2}O_{0.8}$.

If one generalizes the observations for the event on 21 August to all events studied by NAMS during the Lewes campaign, the results imply that carbonaceous matter is responsible for more than 50% of the nanoparticle growth on the other event days and that nitrogen is an important component of the carbonaceous matter. The NAMS-measured elemental ratios in Lewes show that N/C ranges between 0.1 and 0.2 and O/C between 0.6 and 0.9. If every organic molecule contains one nitrogen atom,

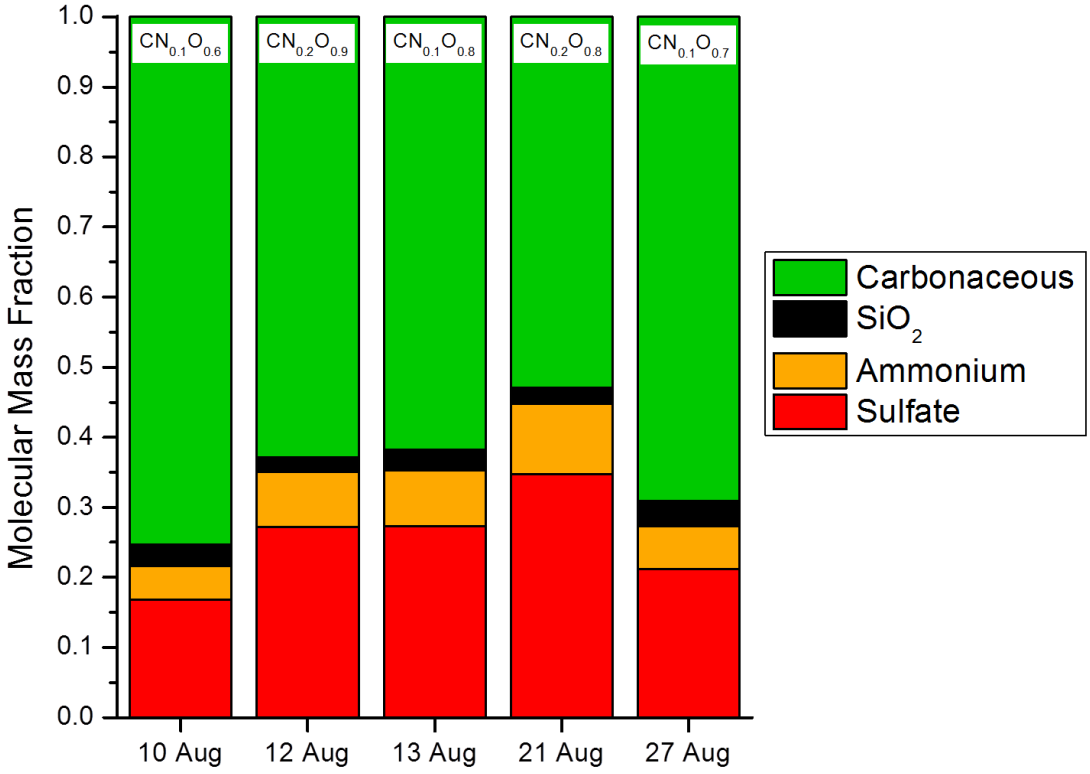

Figure 10.4: Quantitative molecular mass fractions for all five events measured by NAMS during the Lewes campaign. Molecular mass fractions were determined by apportioning the quantitative elemental composition (determined by NAMS) to molecular species based on TDCIMS-measured nanoparticle molecular composition.

these formulas imply only 5-10 C atoms per N atom. Note that the updated O/C ratios in Fig. 10.4 for 12 and 13 August differ from those reported previously (see Chapter 9).[1] In Chapter 9, ammonium nitrate was used as a surrogate for Excess N. The updated values reported here are based on a combination of elemental and molecular composition measurements, which permit more precise refinement of the elemental apportionment and ultimately allow for a better definition of the composition and contribution of carbonaceous matter to nanoparticle growth.

Table 10.1 provides E-AIM modeling results for all events where gas phase concentrations were measured. Even if liquid-like particles are assumed, including the small amount of inorganic nitrate and amine indicated in the table does not change the results presented in Fig. 10.4 beyond the precision of the NAMS measurements (~10%).

The measured elemental ratios for carbonaceous matter are consistent with the concept of extremely low volatility organic compounds (ELVOC) contributing to new particle formation,[33-35] as the O/C ratios measured here are generally between 0.6 and 1.0 depending on the particular event day and the assumptions underlying the molecular apportionment. However, previous reports of ELVOC do not explain the large amount of organic nitrogen in the Lewes nanoparticles. This observation of a substantial amount of organic nitrogen contributing to nanoparticle growth highlights the fact that the identities of the carbonaceous species contributing to nanoparticle growth during new particle formation are still not fully resolved.

10.3.2 Nearly Ubiquitous Measurements of Nanoparticulate Silicon

Silicon has been reported sporadically in ambient nanoparticles in the past,[36-38] but its quantitative contribution to nanoparticle mass has not been assessed. Here,

nanoparticle elemental composition measurements over several field measurement campaigns are combined to show that Si is a nearly ubiquitous component of atmospheric nanoparticles. This ubiquity suggests that an important anthropogenic contributor to nanoparticle mass has been overlooked.

Table 10.3 presents a summary of 7 field campaigns where nanoparticle composition was measured by NAMS. A surprising observation during many of these campaigns is that Si was found in a large fraction of ambient nanoparticles, which is indicated in Table 10.3 by the fraction of particles containing Si elemental mole fraction > 0.01. Several trends are evident from these measurements. First, Si is frequently observed in urban and suburban environments but rarely detected in remote environments. For example, in Pasadena, California (a suburban environment) 40% of all nanoparticles analyzed by NAMS contained a Si mole fraction > 0.01, whereas in Hyytiälä, Finland (a remote environment) only 1.5% of the analyzed nanoparticles contained a substantial mole fraction of Si. Second, the fraction of nanoparticles containing Si changes across different campaigns in the same location. The most obvious example is the two campaigns in Lewes, Delaware. In a campaign there in fall 2007 very few particles contained Si (see Chapter 7), whereas in summer 2012 nearly half of all analyzed particles contained Si (see Chapter 9). The local environment was very different during each campaign: due to its coastal location, the population in Lewes is very large during summer but very small during fall, winter, and spring. In urban Wilmington, Delaware, campaign-to-campaign differences are also evident, with more particles containing Si analyzed during campaigns in spring and summer, and fewer particles containing Si analyzed during winter. Most of the nanoparticulate

Table 10.3: Nanoparticle chemical composition campaigns using NAMS and frequency of nanoparticulate Si.

Location	Date	Environment	Fraction of Particles with Si Mole Fraction > 0.01	Reference
Lewes, Delaware	July-August 2012	rural/coastal[a]	48%	Bzdek et al. (2013)[1]
Pasadena, California	May-June 2010	suburban	40%	Pennington et al. (2012)[2]
Wilmington, Delaware	May 2006	urban	13%	Zordan et al. (2008)[3]
Wilmington, Delaware	July 2009	urban	7.0%	Klems et al. (2011)[4]
Wilmington, Delaware	December 2009	urban	4.8%	Klems et al. (2011)[4]
Lewes, Delaware	October-November 2007	rural/coastal[a]	2.5%	Bzdek et al. (2011)[5]
Hyytiälä, Finland	March-April 2011	remote boreal forest	1.5%	Pennington et al. (2013)[6]

[a]In the summertime only, Lewes is highly populated.

matter at the site in Wilmington arises from local traffic (primary emissions),[4, 39] so campaign-to-campaign variations may also reflect changes in local traffic patterns. These observations are consistent with nanoparticulate Si arising from human activity. Pasadena, summertime Lewes, and Wilmington are all heavily populated locations where Si was detected frequently. On the other hand, neither Lewes in the autumn nor Hyytiälä is heavily populated and Si was rarely detected. Campaign-to-campaign measurements in the same location (Lewes) also support the concept of human activity potentially serving as a source of Si.

The measurements in Pasadena are now discussed in more detail because 1) Si was observed frequently in ambient nanoparticles in this location, 2) this environment is of substantial interest with respect to air quality, and 3) mass concentrations in the nanoparticle size regime were much larger here than in other locations. Figure 10.5a presents a wind rose plot showing the 1 hour average Si mole fraction as a function of wind direction at the site. The numbers inside the plot indicate the number of one-hour time blocks during which the wind came from that direction and NAMS was fully operational. The average Si mole fractions range from 0.02 to 0.06 depending upon wind direction. However, there is no clear wind direction dependence. Note that the wind came from the northwest during only 8 of the 320 hour time-blocks, and the Si mole fraction varied substantially among these time-blocks. In fact, the standard deviation of each wind-direction average is of the same magnitude as the average itself. In other words, the Si mole fraction from each wind direction is highly variable, and there is no evidence for dominant stationary source(s). Together, these observations argue for a diffuse source of the Si around the site.

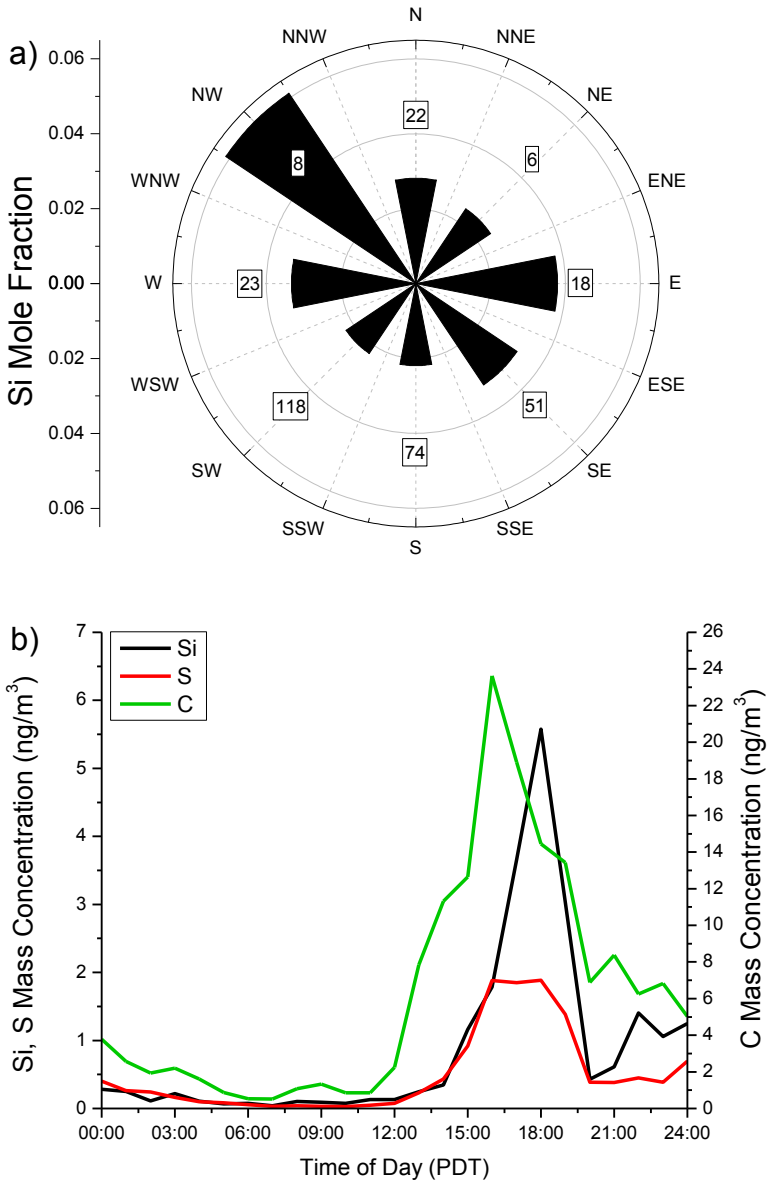

Figure 10.5: a) Wind rose plot showing average Si mole fraction for particles analyzed during the Pasadena, California, campaign. Concentric rings indicate Si mole fraction. Numbers in the plot indicate the number of one-hour time blocks when wind came from that direction and NAMS was fully operational. b) Si, S, and C elemental mass concentrations in particulate matter between 20-25 nm diameter on 01-02 June 2010 during the Pasadena campaign. Particle composition was averaged to one-hour time blocks.

Figure 10.5b presents time dependent elemental mass concentrations for 20-25 nm mass normalized diameter nanoparticles for two typical days during the campaign in Pasadena. These data are calculated by multiplying the NAMS-measured elemental mass fraction by the SMPS-measured aerosol mass concentration in the 19-26 nm mobility diameter size channels. On these days, plumes of nanoparticles resulting from photochemical processing of rush hour motor vehicle emissions advected to the site from downtown Los Angeles.[2] Such events were frequently observed during the campaign. The Si mass concentration is small during the morning (< 1 $ng \cdot m^{-3}$) but increases substantially during the afternoon after photochemical processing to nearly 6 $ng \cdot m^{-3}$ before decreasing again in the evening. The S mass concentration correlates well with changes in Si mass concentration, although during the plumes the Si mass concentration increases to a larger value than that of the S mass concentration. The observed increase in Si mass concentration during the daytime suggests that one component of nanoparticulate Si is photochemical, whereby volatile Si-containing precursors are oxidized to produce lower volatility products that partition to the particle phase. This conclusion is corroborated by the similar time dependencies of the Si and S elemental mass concentrations, as the most likely molecular form of S is photochemically-produced sulfuric acid.

Measurements made during the Lewes campaign in summer 2012 are consistent with those in Pasadena. In Lewes, nearly half of the analyzed nanoparticles contained a Si mole fraction > 0.01 with no discernable wind direction dependence (see Fig. 10.6). Similar to Pasadena, the Si mass concentration generally increases during the daytime, concurrent with S mass concentration, although the two elements

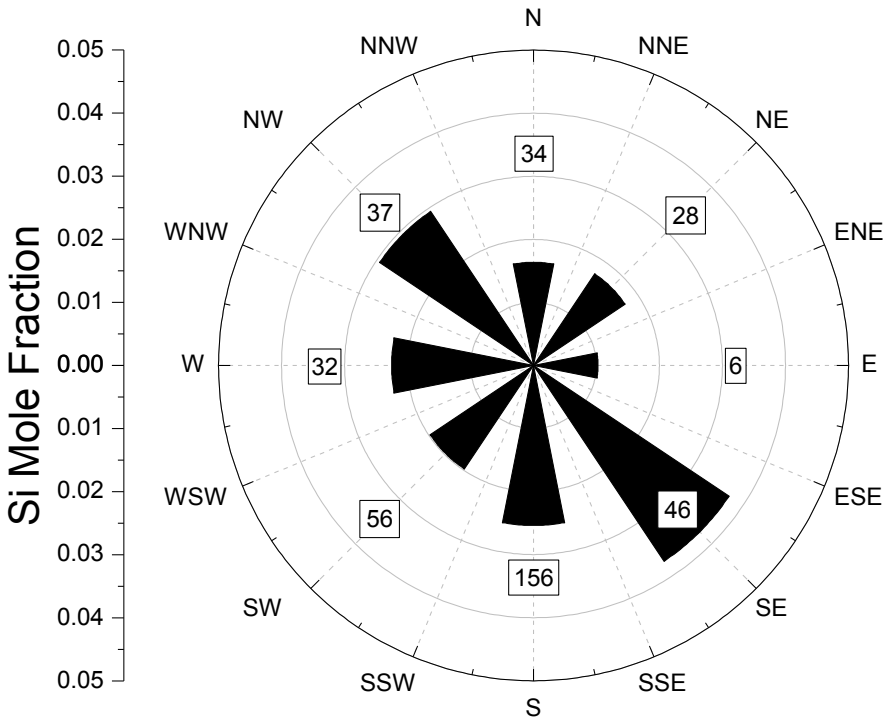

Figure 10.6: Wind rose plot showing average Si mole fraction for particles analyzed during the Lewes 2012 campaign.[1] Particle composition is averaged to 0.5-hour time blocks. Concentric rings indicate the Si mole fraction. Numbers in the plot indicate the number of time blocks when wind came from that direction and NAMS was fully operational.

do not always track each other exactly, suggesting the potential for different sources or production pathways for each.[1]

Because the method of nanoparticle analysis provides only elemental composition, it is not possible to determine the molecular forms of Si in the nanoparticles. However, several studies have addressed the atmospheric concentrations and lifetimes of organosilicon compounds such as cyclic siloxanes, which are widely used in personal care products and industrial applications and which have the potential for long range transport and bioaccumulation.[40-42] Atmospheric siloxane concentrations have been shown to vary widely depending upon location and time of day from < 1 $ng \cdot m^{-3}$ to > 1000 $ng \cdot m^{-3}$.[43-50] Organosilicon compounds may undergo atmospheric oxidation by the OH radical[51] and can be taken up onto aerosol.[52-56] During the Lewes campaign, nanoparticle chemical composition was measured during new particle formation events, where particles grow rapidly to larger sizes (see Chapter 9).[57] Based on knowledge of the nanoparticle composition and volume growth rate, it is possible to get a rough estimate of the concentration of condensable Si in the gas phase.

For this assessment, the molecular precursor is assumed to be decamethylcyclopentasiloxane (D_5), a cyclic siloxane whose gas phase concentration has been reported several times.[42-48, 50] The main pathway of D_5 oxidation is by OH[51] leading to formation of a condensable oxidized species referred to as o-D_5. For the purpose of estimating the gas phase concentration of o-D_5, its physical properties are assumed to be similar to the D_5 precursor except that the equilibrium vapor pressure has decreased substantially.

The gas phase concentration of condensable Si was calculated by modifying an equation used to calculate the gas phase sulfuric acid concentration from the particle size distribution (measured using a SMPS) and nanoparticle elemental composition (measured using NAMS).[28] The goal of this calculation was 1) to estimate the minimum concentration of a condensable Si compound required to explain the observed particle phase Si mole fraction during a growth event, and then 2) to compare this value to known concentrations of volatile organosilicon precursors, thereby determining whether or not it is feasible for organosiloxanes that have been previously detected in air to provide the requisite growth of nanoparticles during these events. Two assumptions are made in the application of this equation: 1) the condensing Si-containing compound (o-D_5) is an oxidation product of D_5 with all molecular properties of the condensing species (i.e. density, molar mass, molecular formula, number of Si atoms per molecule, and molecular volume) equivalent to that of D_5, and 2) the oxidation product has a volatility low enough that its uptake onto the aerosol is collision limited. Reasonable differences between molecular properties of D_5 and o-D_5 (density, molar mass, molecular volume) will affect the calculated concentration, but most certainly by less than ±50% of the reported value. More significantly, if the number of Si atoms per molecule is more/less than 5, the gas phase concentration would proportionally decrease/increase relative to the reported values. Furthermore, the calculated [o-D_5] provides only a lower limit of the gas phase condensable Si concentration due to the assumption that uptake onto the aerosol is collision limited.

Following the approach described in Chapter 8, the equation for estimating [o-D_5] is:

$$[\text{o-D}_5] = \frac{2\text{GR}_{\text{MEAS}}\text{MF}}{\upsilon_1 \bar{c}_1} \times \frac{\rho_{\text{particle}}}{\rho_{\text{o-D}_5}} \quad (1)$$

where $[\text{o-D}_5]$ is the calculated concentration of low volatility condensable Si vapor (molecules·cm^{-3}), GR_{MEAS} is the SMPS-measured growth rate from 10-20 nm diameter during the new particle formation event (nm·h^{-1}), MF is the apportioned o-D_5 molecular mass fraction (determined from the NAMS particle phase elemental Si measurement and the molar mass of o-D_5), υ_1 is the volume of an o-D_5 molecule (1.1×10^{-21} cm^3), $\bar{c}_1$ is the mean thermal speed of an o-D_5 molecule (4.6×10^{14} nm·h^{-1}), ρ_{particle} is the density of the analyzed particle (assumed to be 1.5 g·cm^{-3} for an ambient particle containing significant amounts of ammonium sulfate and secondary organic aerosol), and $\rho_{\text{o-D5}}$ is the density of o-D_5 (0.96 g·cm^{-3}).[58] The values for υ_1, $\bar{c}_1$ and $\rho_{\text{o-D5}}$ are assumed to be the same as those for D_5. The value used for υ_1 was calculated by construction of the D_5 molecule at the PW91/6-31++G level of theory[59, 60] using Gaussian.[61] The molecular volume was computed as the multidimensional definite integral of a molecule-shaped contour derived from the calculated electron density.

Measured particle-phase Si mole fractions and estimated gas-phase o-D_5 concentrations are given in Table 10.4 for three particle formation events. Also shown are corresponding particle-phase S mole fractions and gas-phase sulfuric acid concentrations for the same events. As discussed in Chapter 9,[1] the sulfuric acid concentrations calculated from the S mole fractions agree quantitatively with the measured sulfuric acid concentrations. It should be noted that the estimated o-D_5 concentrations represent lower limits since they assume diffusion limited condensation rather than equilibrium partitioning to the particle phase.

Table 10.4: Estimation of gas phase o-D_5 concentration during new particle formation events in Lewes.

Event Date	Volume Growth Rate ($nm \cdot h^{-1}$)	Si Mole Fraction	S Mole Fraction	[o-D_5][a] ($molec \cdot cm^{-3}$)	[H_2SO_4] ($molec \cdot cm^{-3}$)
12 August 2012	8.9 ± 0.8	0.005 ± 0.0005	0.04 ± 0.004	1.3×10^6	$1.9 \pm 1.0 \times 10^7$
13 August 2012	7.1 ± 1.0	0.007 ± 0.0007	0.04 ± 0.004	1.5×10^6	$2.2 \pm 1.1 \times 10^7$
21 August 2012	9.8 ± 0.3	0.006 ± 0.0006	0.06 ± 0.006	1.6×10^6	$1.3 \pm 0.7 \times 10^7$

[a]Estimated values depend in part on the chemical form of this species, which for the purpose of this calculation is assumed to include 5 Si atoms per molecule. The estimation also depends on the physical properties of o-D_5; the uncertainty associated with physical properties is expected to be on the order of ±50% of the tabulated concentration.

For these events, the o-D_5 concentrations required to grow the particles are on the order of 1×10^6 molec·cm^{-3} assuming 5 Si atoms per molecule. (The gas-phase concentration would increase proportionally for fewer Si atoms per molecule.) Except for remote sites,[46-48] gas-phase D_5 concentrations are generally on the order of several tens to hundreds of ng·m^{-3} or 10^7-10^8 molec·cm^{-3}.[43-45, 50] If gas-phase D_5 concentrations in Lewes were at a similar level during the particle formation events, then photooxidation of D_5 to o-D_5 could potentially explain the measured particle-phase Si mole fractions.

Particulate, non-crustal Si has not been reported in much detail before, with the exception of a large source of nanoparticulate Si observed in a study in Houston, Texas,[37] and much smaller amounts in Pittsburgh, Pennsylvania,[36] and Atlanta, Georgia.[38] If photochemical processes are the source of low volatility Si-containing products that condense onto particles, the impact will be more apparent in nanoparticles on a mole fraction basis than in larger (e.g. accumulation mode) particles because of the larger surface to volume ratio for nanoparticles, and also because the range of semivolatile compounds able to partition into nanoparticles is more restricted than for larger particles.

10.3.3 Effects of Assumptions Underlying Molecular Apportionment on Interpretation of Nanoparticle Composition

Chapter 7 introduced a molecular apportionment algorithm designed to put the elemental composition into a molecular context. The algorithm relied on several assumptions regarding the molecular forms of the various elements detected in ambient nanoparticles. The primary assumption is that all sulfur is in the form of sulfuric acid. As illustrated in Chapters 8 and 9, this is a reasonable assumption. The

earlier discussion in this chapter also corroborates the apportionment of sulfur to sulfuric acid.

Apportionment of the other elemental species is more problematic. The apportionment algorithm described in Chapter 7 and utilized to various extents in Chapters 8 and 9 first apportions N as ammonium to neutralize S (up to 2S). After apportionment of ammonia, this algorithm assumes that the molecular identity of all Excess N is ammonium nitrate. However, the discussion of Excess N in the first portion of this chapter effectively excludes ammonium nitrate as a possibility during new particle formation in Lewes based on combined NAMS and TDCIMS measurements along with support from E-AIM modeling. The conclusion that Excess N is necessarily carbonaceous (rather than inorganic ammonium nitrate) substantially impacts interpretation of the elemental composition. This impact is illustrated in Fig. 10.7, which shows the evolution of the apportioned nanoparticle molecular composition as the assumptions underlying the apportionment are refined. In this figure, nanoparticle chemical composition during the new particle formation event on 12 August 2012 in Lewes is shown for three different sets of assumptions on the molecular identity of the various elements. In all three cases, sulfur is apportioned to sulfuric acid.

Case A shows the original apportionment algorithm assuming Excess N in the form of ammonium nitrate and Si in the form of SiO_2. These assumptions were made based simply on the types of molecular species one might expect in ambient aerosol and were not grounded in any collocated measurement corroborating the molecular form of either species. Application of these assumptions results in inorganic

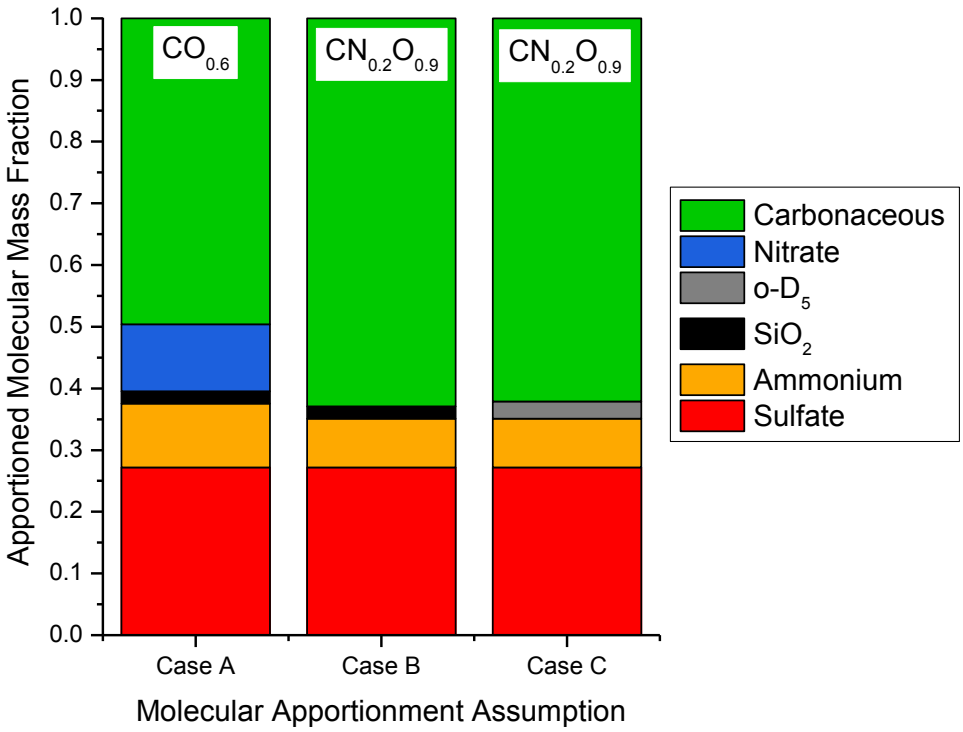

Figure 10.7: Apportioned molecular mass fractions for the new particle formation event on 12 August 2012 in Lewes, Delaware. Case A assumes Excess N in the molecular form of ammonium nitrate and Si in the form of SiO_2. Case B assumes Excess N as carbonaceous matter and Si as SiO_2. Case C assumes Excess N as carbonaceous matter and Si as $C_{10}O_{10}Si_5$.

ammonium nitrate accounting for ~13% of the average particle mass and gives an O/C ratio of 0.6.

Case B illustrates the refinement of the apportionment algorithm based upon a more precise partitioning of the inorganic components as a result of the collocated TDCIMS measurements discussed in the first portion of this chapter. Based upon the supporting molecular composition measurements, inorganic nitrate is ruled out as a substantial contributor to Excess N. Instead, the identity of Excess N is shown to be carbonaceous in nature. Therefore, Case B assumes Excess N as carbonaceous matter and Si (for lack of any supporting molecular information) as SiO_2. The refined apportionment results in a substantial change in molecular composition. First, the carbonaceous mass fraction increases from 50% (Case A) to 63% (Case B). Second, the elemental composition of the carbonaceous matter changes substantially from $CO_{0.6}$ (Case A) to $CN_{0.2}O_{0.9}$ (Case B). In other words, the carbonaceous matter is substantially more oxidized in Case B and necessarily contains more nitrogen (which was not allowed in Case A).

Case C also assumes that Excess N is carbonaceous (based on the discussion in the first portion of this chapter) but refines the assumption about the molecular form of Si based upon the discussion in the second portion of this chapter. Instead of assuming the molecular form of Si as SiO_2, Case C assumes an oxidized D_5 molecule ($C_{10}O_{10}Si_5$) as the molecular form of Si. Due to the overall small fraction of Si in the particle, the assumption of the molecular form does not have a large effect: it only increases the mass fraction from 2% (SiO_2) to 3% ($C_{10}O_{10}Si_5$). Additionally, the elemental composition of the carbonaceous matter is unchanged by this assumption. Note, however, that on non-new particle formation days in Lewes, the Si elemental

mole fraction was substantial (see Chapter 9).[1] For these days, the assumption about the molecular form of Si would have a larger impact.

From Fig. 10.7, it is clear that the assumptions underlying the molecular apportionment can substantially impact the conclusions drawn about the quantitative composition and contribution of carbonaceous matter to growth. During new particle formation events in Lewes, the assumption regarding the molecular identity of Excess N is most significant, and the figure illustrates how refinement of the molecular apportionment algorithm based upon collocated measurements can provide more precise information about the chemical species contributing to growth. However, for those assumptions to have a significant impact on the interpretation, the relevant elements must constitute a substantial component of the elemental mole fraction and/or the apportioned molecular species must have a large mass (on a per element basis). The apportionment of elemental silicon during new particle formation illustrates a case where the molecular form is not well-defined, but the specific assumption does not substantially impact the result because of its low abundance in growing nanoparticles.

10.4 Conclusions

This chapter addresses the role of three species important to nanoparticle composition and growth: carbonaceous matter, Excess N, and silicon. NAMS measurements permit a quantitative assessment of the composition and contribution of these components to nanoparticle composition. Results from both studies indicate that substantial work is still required to fully understand nanoparticle composition.

In the first portion of this chapter, quantitative elemental composition measurements by NAMS are combined with molecular composition measurements by

TDCIMS to better define the carbonaceous component contributing to the growth of 20 nm nanoparticles during new particle formation. This is accomplished by a more precise partitioning of the elemental composition to the inorganic components contributing to growth. Although ammonium (and some aminium) sulfate is important to the growth of new particles, the major fraction of particulate mass is carbonaceous. In Lewes, this carbonaceous matter is consistent with the O/C ratio of ELVOC. Unlike previously reported ELVOC, the carbonaceous matter in Lewes contains a substantial amount of organic nitrogen, which has not previously been observed during new particle formation. More work is required to confirm the molecular identities of these organic nitrogen compounds. The Lewes observations are in contrast to early springtime studies in a remote boreal forest (Hyytiälä, Finland), where nitrogen is not a substantial component of the carbonaceous matter.[6, 27] The combination of elemental and molecular measurements permits determination of the key molecular components contributing to nanoparticle growth, the quantitative contribution of each molecular component to growth, and more precise determination of the elemental ratios necessary to describe carbonaceous matter. These results are broadly relevant to aerosol modelers, as they better define the contribution of carbonaceous matter to nanoparticle growth, a key uncertainty in understanding the climatic impacts of new particle formation.[62]

Future work should focus on products and formation mechanisms of highly oxidized carbonaceous matter containing nitrogen. Models describing sulfuric acid incorporation into growing nanoparticles are robust. However, similarly robust models to describe the incorporation of organic nitrogen into growing nanoparticles are lacking.

The second portion of this work showed that the element Si has been observed in measurements of nanoparticle elemental composition in several locations. Si was more frequently detected in locations where anthropogenic impacts are expected to be greater, whereas Si was rarely observed in areas with little anthropogenic impact. Si was shown to have no obvious wind direction dependence, suggesting its sources are diffuse. The Si mass concentration tended to increase during the daytime, suggesting its presence in nanoparticles may arise from photochemical processing of Si-containing precursors. An initial estimate of the gas-phase concentration for the condensing species suggests that oxidation of cyclic siloxanes such as D_5 could explain the presence of nanoparticulate Si, but much more work is required to show this rigorously.

Future work should address the sources, oxidation pathways, partitioning behavior, and molecular forms of atmospheric particulate Si. Such knowledge would better constrain the lifetimes of Si-containing compounds in the atmosphere as well as the mechanism of human exposure (e.g. gas or aerosol phase). Additionally, if cyclic siloxanes are indeed an important source of atmospheric nanoparticulate Si, these observations suggest studies of nanoparticle composition in indoor environments are warranted, as indoor siloxane concentrations can be much larger than outdoor concentrations[44, 50] and indoor concentrations of oxidizing species can be of the same order of magnitude as outdoor concentrations.[63, 64] More generally, these observations indicate that nanoparticulate Si is ubiquitous, has been previously overlooked, and requires further study to elucidate its sources and atmospheric fate.

Lastly, these results illustrate how assumptions about the molecular forms of various elements important to nanoparticle growth may impact interpretation of the

results. Refinement of the assumptions underlying the apportionment based upon collocated measurements can aid in quantitative elucidation of the molecular species important to nanoparticle growth. These results essentially provide the framework for future goals in interpretation of ambient nanoparticle mass spectra. If it is possible to more precisely refine the molecular identity of the main elements observed in atmospheric nanoparticles (specifically, S, N, and Si), then substantial gains in quantitative interpretation of the molecular channels important to nanoparticle growth during new particle formation are enabled.

10.5 References

1. Bzdek, B. R.; Horan, A. J.; Pennington, M. R.; DePalma, J. W.; Zhao, J.; Jen, C. N.; Hanson, D.; Smith, J. N.; McMurry, P. H.; Johnston, M. V., Quantitative and time-resolved nanoparticle composition measurements during new particle formation. *Faraday Discuss.* **2013,** *165* (1), 25-43.

2. Pennington, M. R.; Klems, J. P.; Bzdek, B. R.; Johnston, M. V., Nanoparticle chemical composition and diurnal dependence at the CalNex Los Angeles Ground Site. *J. Geophys. Res.-Atmos.* **2012,** *117* (D00), D00V10, doi: 10.1029/2011JD017061.

3. Zordan, C. A.; Wang, S.; Johnston, M. V., Time-resolved chemical composition of individual nanoparticles in urban air. *Environ. Sci. Technol.* **2008,** *42* (17), 6631-6636.

4. Klems, J. P.; Pennington, M. R.; Zordan, C. A.; McFadden, L.; Johnston, M. V., Apportionment of motor vehicle emissions from fast changes in number concentration and chemical composition of ultrafine particles near a roadway intersection. *Environ. Sci. Technol.* **2011,** *45* (13), 5637-5643.

5. Bzdek, B. R.; Zordan, C. A.; Luther, G. W.; Johnston, M. V., Nanoparticle chemical composition during new particle formation. *Aerosol Sci. Technol.* **2011,** *45* (8), 1041-1048.

6. Pennington, M. R.; Bzdek, B. R.; DePalma, J. W.; Smith, J. N.; Kortelainen, A.-M.; Hildebrandt Ruiz, L.; Petaja, T.; Kulmala, M.; Worsnop, D. R.; Johnston, M. V., Identification and quantification of particle growth channels during new particle formation. *Atmos. Chem. Phys.* **2013,** *13* (20), 10215-10225.

7. Ryerson, T. B.; Andrews, A. E.; Angevine, W. M.; Bates, T. S.; Brock, C. A.; Cairns, B.; Cohen, R. C.; Cooper, O. R.; de Gouw, J. A.; Fehsenfeld, F. C.; Ferrare, R. A.; Fischer, M. L.; Flagan, R. C.; Goldstein, A. H.; Hair, J. W.; Hardesty, R. M.; Hostetler, C. A.; Jimenez, J. L.; Langford, A. O.; McCauley, E.; McKeen, S. A.; Molina, L. T.; Nenes, A.; Oltmans, S. J.; Parrish, D. D.; Pederson, J. R.; Pierce, R. B.; Prather, K.; Quinn, P. K.; Seinfeld, J. H.; Senff, C. J.; Sorooshian, A.; Stutz, J.; Surratt, J. D.; Trainer, M.; Volkamer, R.; Williams, E. J.; Wofsy, S. C., The 2010 California Research at the Nexus of Air Quality and Climate Change (CalNex) field study. *J. Geophys. Res.-Atmos.* **2013,** *118* (11), 5830-5866, doi: 10.1002/jgrd.50331.

8. Pennington, M. R.; Johnston, M. V., Trapping charged nanoparticles in the nano aerosol mass spectrometer (NAMS). *Int. J. Mass Spectrom.* **2012,** *311* (1), 64-71.

9. Wang, S. Y.; Johnston, M. V., Airborne nanoparticle characterization with a digital ion trap-reflectron time of flight mass spectrometer. *Int. J. Mass Spectrom.* **2006,** *258* (1-3), 50-57.

10. Wang, S. Y.; Zordan, C. A.; Johnston, M. V., Chemical characterization of individual, airborne sub-10-nm particles and molecules. *Anal. Chem.* **2006,** *78* (6), 1750-1754.

11. Zordan, C. A.; Pennington, M. R.; Johnston, M. V., Elemental composition of nanoparticles with the Nano Aerosol Mass Spectrometer. *Anal. Chem.* **2010,** *82* (19), 8034-8038.

12. Klems, J. P.; Johnston, M. V., Origin and impact of particle-to-particle variations in composition measurements with the Nano Aerosol Mass Spectrometer. *Anal. Bioanal. Chem.* **2013,** *405* (22), 6995-7003.

13. Smith, J. N.; Moore, K. F.; McMurry, P. H.; Eisele, F. L., Atmospheric measurements of sub-20 nm diameter particle chemical composition by thermal desorption chemical ionization mass spectrometry. *Aerosol Sci. Technol.* **2004,** *38* (2), 100-110.

14. Voisin, D.; Smith, J. N.; Sakurai, H.; McMurry, P. H.; Eisele, F. L., Thermal desorption chemical ionization mass spectrometer for ultrafine particle chemical composition. *Aerosol Sci. Technol.* **2003,** *37* (6), 471-475.

15. McMurry, P. H.; Ghimire, A.; Ahn, H. K.; Sakurai, H.; Moore, K.; Stolzenburg, M.; Smith, J. N., Sampling nanoparticles for chemical analysis by low resolution electrical mobility classification. *Environ. Sci. Technol.* **2009,** *43* (13), 4653-4658.

16. Timko, M. T.; Yu, Z. H.; Kroll, J. H.; Jayne, J. T.; Worsnop, D. R.; Miake-Lye, R. C.; Onasch, T. B.; Liscinsky, D.; Kirchstetter, T. W.; Destaillats, H.; Holder, A. L.; Smith, J. D.; Wilson, K. R., Sampling artifacts from conductive silicone tubing. *Aerosol Sci. Technol.* **2009,** *43* (9), 855-865.

17. Yu, Y.; Alexander, M. L.; Perraud, V.; Bruns, E. A.; Johnson, S. N.; Ezell, M. J.; Finlayson-Pitts, B. J., Contamination from electrically conductive silicone tubing during aerosol chemical analysis. *Atmos. Environ.* **2009,** *43* (17), 2836-2839.

18. Zhao, J.; Eisele, F. L.; Titcombe, M.; Kuang, C.; McMurry, P. H., Chemical ionization mass spectrometric measurements of atmospheric neutral clusters using the cluster-CIMS. *J. Geophys. Res.-Atmos.* **2010,** *115* (D8), D08205, doi: 10.1029/2009JD012606.

19. Zhao, J.; Smith, J. N.; Eisele, F. L.; Chen, M.; Kuang, C.; McMurry, P. H., Observation of neutral sulfuric acid-amine containing clusters in laboratory and ambient measurements. *Atmos. Chem. Phys.* **2011,** *11* (21), 10823-10836.

20. Hanson, D. R.; McMurry, P. H.; Jiang, J.; Tanner, D.; Huey, L. G., Ambient pressure proton transfer mass spectrometry: Detection of amines and ammonia. *Environ. Sci. Technol.* **2011,** *45* (20), 8881-8888.

21. Freshour, N. A.; Carlson, K. K.; Melka, Y. A.; Hinz, S.; Panta, B.; Hanson, D. R., Quantifying amine permeation sources with acid neutralization: calibrations and amines measured in coastal and continental atmospheres. *Atmos. Meas. Tech. Discuss.* **2014,** *7* (4), 3835-3861.

22. Clegg, S. L.; Brimblecombe, P.; Wexler, A. S., Thermodynamic model of the system H^+-NH_4^+-SO_4^{2-}-NO_3^--H_2O at tropospheric temperatures. *J. Phys. Chem. A* **1998,** *102* (12), 2137-2154.

23. Wexler, A. S.; Clegg, S. L., Atmospheric aerosol models for systems including the ions H^+, NH_4^+, Na^+, SO_4^{2-}, NO_3^-,Cl^-, Br^-, and H_2O. *J. Geophys. Res.-Atmos.* **2002,** *107* (D14), 4207, doi: 10.1029/2001jd000451.

24. Ge, X. L.; Wexler, A. S.; Clegg, S. L., Atmospheric amines - Part II. Thermodynamic properties and gas/particle partitioning. *Atmos. Environ.* **2011,** *45* (3), 561-577.

25. Clegg, S. L.; Qiu, C.; Zhang, R. Y., The deliquescence behaviour, solubilities, and densities of aqueous solutions of five methyl- and ethyl-aminium sulphate salts. *Atmos. Environ.* **2013,** *73* (1), 145-158.

26. Draxler, R. R.; Rolph, G. D. *HYSPLIT (HYbrid Single-Particle Lagrangian Integrated Trajectory) Model access via NOAA ARL READY Website (http://ready.arl.noaa.gov/HYSPLIT.php)*, NOAA Air Resources Laboratory: Silver Spring, MD, 2013.

27. Pennington, M. R. An Improved Nano Aerosol Mass Spectrometer for Ambient and Laboratory Measurements. University of Delaware, Newark, DE, 2012.

28. Bzdek, B. R.; Zordan, C. A.; Pennington, M. R.; Luther, G. W.; Johnston, M. V., Quantitative assessment of the sulfuric acid contribution to new particle growth. *Environ. Sci. Technol.* **2012,** *46* (8), 4365-4373.

29. Barsanti, K. C.; McMurry, P. H.; Smith, J. N., The potential contribution of organic salts to new particle growth. *Atmos. Chem. Phys.* **2009,** *9* (9), 2949-2957.

30. Yli-Juuti, T.; Barsanti, K.; Hildebrandt Ruiz, L.; Kieloaho, A. J.; Makkonen, U.; Petäjä, T.; Ruuskanen, T.; Kulmala, M.; Riipinen, I., Model for acid-base chemistry in nanoparticle growth (MABNAG). *Atmos. Chem. Phys.* **2013,** *13* (24), 12507-12524.

31. O'Brien, R. E.; Laskin, A.; Laskin, J.; Liu, S.; Weber, R.; Russell, L. M.; Goldstein, A. H., Molecular characterization of organic aerosol using nanospray desorption/electrospray ionization mass spectrometry: CalNex 2010 field study. *Atmos. Environ.* **2013,** *68* (1), 265-272.

32. O'Brien, R. E.; Nguyen, T. B.; Laskin, A.; Laskin, J.; Hayes, P. L.; Liu, S.; Jimenez, J. L.; Russell, L. M.; Nizkorodov, S. A.; Goldstein, A. H., Probing molecular associations of field-collected and laboratory-generated SOA with nano-DESI high-resolution mass spectrometry. *J. Geophys. Res.-Atmos.* **2013,** *118* (2), 1042-1051, doi: 10.1002/jgrd.50119.

33. Schobesberger, S.; Junninen, H.; Bianchi, F.; Lönn, G.; Ehn, M.; Lehtipalo, K.; Dommen, J.; Ehrhart, S.; Ortega, I. K.; Franchin, A.; Nieminen, T.; Riccobono, F.; Hutterli, M.; Duplissy, J.; Almeida, J.; Amorim, A.; Breitenlechner, M.; Downard, A. J.; Dunne, E. M.; Flagan, R. C.; Kajos, M.; Keskinen, H.; Kirkby, J.; Kupc, A.; Kürten, A.; Kurtén, T.; Laaksonen, A.; Mathot, S.; Onnela, A.; Praplan, A. P.; Rondo, L.; Santos, F. D.; Schallhart, S.; Schnitzhofer, R.; Sipilä, M.; Tomé, A.; Tsagkogeorgas, G.; Vehkamäki, H.; Wimmer, D.; Baltensperger, U.; Carslaw, K. S.; Curtius, J.; Hansel, A.; Petäjä, T.; Kulmala, M.; Donahue, N. M.; Worsnop, D. R., Molecular understanding of atmospheric particle formation from sulfuric acid and large oxidized organic molecules. *Proc. Natl. Acad. Sci. U.S.A.* **2013,** *110* (43), 17223-17228.

34. Ehn, M.; Thornton, J. A.; Kleist, E.; Sipila, M.; Junninen, H.; Pullinen, I.; Springer, M.; Rubach, F.; Tillmann, R.; Lee, B.; Lopez-Hilfiker, F.; Andres, S.; Acir, I.-H.; Rissanen, M.; Jokinen, T.; Schobesberger, S.; Kangasluoma, J.; Kontkanen, J.; Nieminen, T.; Kurten, T.; Nielsen, L. B.; Jorgensen, S.; Kjaergaard, H. G.; Canagaratna, M.; Maso, M. D.; Berndt, T.; Petaja, T.; Wahner, A.; Kerminen, V.-M.; Kulmala, M.; Worsnop, D. R.; Wildt, J.; Mentel, T. F., A large source of low-volatility secondary organic aerosol. *Nature* **2014,** *506* (7489), 476-479.

35. Zhao, J.; Ortega, J.; Chen, M.; McMurry, P. H.; Smith, J. N., Dependence of particle nucleation and growth on high-molecular-weight gas-phase products

during ozonolysis of alpha-pinene. *Atmos. Chem. Phys.* **2013,** *13* (15), 7631-7644.

36. Bein, K. J.; Zhao, Y. J.; Wexler, A. S.; Johnston, M. V., Speciation of size-resolved individual ultrafine particles in Pittsburgh, Pennsylvania. *J. Geophys. Res.-Atmos.* **2005,** *110* (D7), D07s05, doi: 10.1029/2004jd004708.

37. Phares, D. J.; Rhoads, K. P.; Johnston, M. V.; Wexler, A. S., Size-resolved ultrafine particle composition analysis - 2. Houston. *J. Geophys. Res.-Atmos.* **2003,** *108* (D7), 8420, doi: 10.1029/2001jd001212.

38. Rhoads, K. P.; Phares, D. J.; Wexler, A. S.; Johnston, M. V., Size-resolved ultrafine particle composition analysis, 1. Atlanta. *J. Geophys. Res.-Atmos.* **2003,** *108* (D7), 8418, doi: 10.1029/2001jd001211.

39. Klems, J. P.; Pennington, M. R.; Zordan, C. A.; Johnston, M. V., Ultrafine particles near a roadway intersection: Origin and apportionment of fast changes in concentration. *Environ. Sci. Technol.* **2010,** *44* (20), 7903-7907.

40. Balducci, C.; Perilli, M.; Romagnoli, P.; Cecinato, A., New developments on emerging organic pollutants in the atmosphere. *Environ. Sci. Pollut. Res.* **2012,** *19* (6), 1875-1884.

41. Graiver, D.; Farminer, K. W.; Narayan, R., A review of the fate and effects of silicones in the environment. *J. Polym. Environ.* **2003,** *11* (4), 129-136.

42. Wang, D. G.; Norwood, W.; Alaee, M.; Byer, J. D.; Brimble, S., Review of recent advances in research on the toxicity, detection, occurrence and fate of cyclic volatile methyl siloxanes in the environment. *Chemosphere* **2013,** *93* (5), 711-725.

43. Buser, A. M.; Kierkegaard, A.; Bogdal, C.; MacLeod, M.; Scheringer, M.; Hungerbuhler, K., Concentrations in ambient air and emissions of cyclic volatile methylsiloxanes in Zurich, Switzerland. *Environ. Sci. Technol.* **2013,** *47* (13), 7045-7051.

44. Companioni-Damas, E. Y.; Santos, F. J.; Galceran, M. T., Linear and cyclic methylsiloxanes in air by concurrent solvent recondensation-large volume injection-gas chromatography-mass spectrometry. *Talanta* **2014,** *118* (1), 245-252.

45. Genualdi, S.; Harner, T.; Cheng, Y.; MacLeod, M.; Hansen, K. M.; van Egmond, R.; Shoeib, M.; Lee, S. C., Global distribution of linear and cyclic volatile methyl siloxanes in air. *Environ. Sci. Technol.* **2011,** *45* (8), 3349-3354.

46. Kierkegaard, A.; McLachlan, M. S., Determination of linear and cyclic volatile methylsiloxanes in air at a regional background site in Sweden. *Atmos. Environ.* **2013,** *80* (1), 322-329.

47. Krogseth, I. S.; Kierkegaard, A.; McLachlan, M. S.; Breivik, K.; Hansen, K. M.; Schlabach, M., Occurrence and seasonality of cyclic volatile methyl siloxanes in Arctic air. *Environ. Sci. Technol.* **2013,** *47* (1), 502-509.

48. McLachlan, M. S.; Kierkegaard, A.; Hansen, K. M.; van Egmond, R.; Christensen, J. H.; Skjoth, C. A., Concentrations and fate of decamethylcyclopentasiloxane (D_5) in the atmosphere. *Environ. Sci. Technol.* **2010,** *44* (14), 5365-5370.

49. Wang, X. M.; Lee, S. C.; Sheng, G. Y.; Chan, L. Y.; Fu, J. M.; Li, X. D.; Min, Y. S.; Chan, C. Y., Cyclic organosilicon compounds in ambient air in Guangzhou, Macau and Nanhai, Pearl River Delta. *App. Geochem.* **2001,** *16* (11-12), 1447-1454.

50. Yucuis, R. A.; Stanier, C. O.; Hornbuckle, K. C., Cyclic siloxanes in air, including identification of high levels in Chicago and distinct diurnal variation. *Chemosphere* **2013,** *92* (8), 905-910.

51. Atkinson, R., Kinetics of the gas phase reactions of a series of organosilicon compounds with OH and NO_3 radicals and O_3 at 297 +/- 2 K. *Environ. Sci. Technol.* **1991,** *25* (5), 863-866.

52. Chandramouli, B.; Kamens, R. M., The photochemical formation and gas-particle partitioning of oxidation products of decamethyl cyclopentasiloxane and decamethyl tetrasiloxane in the atmosphere. *Atmos. Environ.* **2001,** *35* (1), 87-95.

53. Latimer, H. K.; Kamens, R. M.; Chandra, G., The atmospheric partitioning of decamethylcyclopentasiloxane (D_5) and 1-hydroxynonamethylcyclopentasiloxane (D_4TOH) on different types of atmospheric particles. *Chemosphere* **1998,** *36* (10), 2401-2414.

54. Navea, J. G.; Xu, S. H.; Stanier, C. O.; Young, M. A.; Grassian, V. H., Heterogeneous uptake of octamethylcyclotetrasiloxane (D_4) and decamethylcyclopentasiloxane (D_5) onto mineral dust aerosol under variable RH conditions. *Atmos. Environ.* **2009,** *43* (26), 4060-4069.

55. Navea, J. G.; Xu, S. H.; Stanier, C. O.; Young, M. A.; Grassian, V. H., Effect of ozone and relative humidity on the heterogeneous uptake of octamethylcyclotetrasiloxane and decamethylcyclopentasiloxane on model mineral dust aerosol components. *J. Phys. Chem. A* **2009,** *113* (25), 7030-7038.

56. Navea, J. G.; Young, M. A.; Xu, S. H.; Grassian, V. H.; Stanier, C. O., The atmospheric lifetimes and concentrations of cyclic methylsiloxanes octamethylcyclotetrasiloxane (D_4) and decamethylcyclopentasiloxane (D_5) and the influence of heterogeneous uptake. *Atmos. Environ.* **2011,** *45* (18), 3181-3191.

57. Zhang, R.; Khalizov, A.; Wang, L.; Hu, M.; Xu, W., Nucleation and growth of nanoparticles in the atmosphere. *Chem. Rev.* **2012,** *112* (3), 1957-2011.

58. Lide, D. R., *CRC Handbook of Chemistry and Physics*. 94th ed.; CRC Press: Boca Raton, FL, 2014; Vol. Section 3, No. 2747, p Section 3, No. 2747.

59. Perdew, J. P.; Burke, K.; Wang, Y., Generalized gradient approximation for the exchange-correlation hole of a many-electron system. *Phys. Rev. B* **1996,** *54* (23), 16533-16539.

60. Perdew, J. P.; Chevary, J. A.; Vosko, S. H.; Jackson, K. A.; Pederson, M. R.; Singh, D. J.; Fiolhais, C., Atoms, molecules, solids, and surfaces: Appplications of the generalized gradient approximation for exchange and correlation. *Phys. Rev. B* **1992,** *46* (11), 6671-6687.

61. Frisch, M. J.; Trucks, G. W.; Schlegel, H. B.; Scuseria, G. E.; Robb, M. A.; Cheeseman, J. R.; Scalmani, G.; Barone, V.; Mennucci, B.; Petersson, G. A.; Nakatsuji, H.; Caricato, M.; Li, X.; Hratchian, H. P.; Izmaylov, A. F.; Bloino, J.; Zheng, G.; Sonnenberg, J. L.; Hada, M.; Ehara, M.; Toyota, K.; Fukuda, R.; Hasegawa, J.; Ishida, M.; Nakajima, T.; Honda, Y.; Kitao, O.; Naka, H.; Vreven, T.; J. A. Montgomery, J.; Peralta, J. E.; Ogliaro, F.; Bearpark, M.; Heyd, J. J.; Brothers, E.; Kudin, K. N.; Staroverov, V. N.; Keith, T.; Kobayashi, R.; Normand, J.; Raghavachari, K.; Rendell, A.; Burant, J. C.; Iyengar, S. S.; Tomasi, J.; Cossi, M.; Rega, N.; Millam, J. M.; Klene, M.; Knox, J. E.; Cross, J. B.; Bakken, V.; Adamo, C.; Jaramillo, J.; Gomperts, R.; Stratmann, R. E.; Yazyev, O.; Austin, A. J.; Cammi, R.; Pomelli, C.; Ochterski, J. W.; Martin, R. L.; Morokuma, K.; Zakrzewski, V. G.; Voth, G. A.; Salvador, P.; Dannenberg, J. J.; Dapprich, S.; Daniels, A. D.; Farkas, O.; Foresman, J. B.; Ortiz, J. V.; Cioslowski, J.; Fox, D. J. *Gaussian 09, revision C.01*, Gaussian, Inc.: Wallingford, CT, 2010.

62. Carslaw, K. S.; Lee, L. A.; Reddington, C. L.; Mann, G. W.; Pringle, K. J., The magnitude and sources of uncertainty in global aerosol. *Faraday Discuss.* **2013,** *165* (1), 495-512.

63. Alvarez, E. G.; Amedro, D.; Afif, C.; Gligorovski, S.; Schoemacker, C.; Fittschen, C.; Doussin, J. F.; Wortham, H., Unexpectedly high indoor hydroxyl radical concentrations associated with nitrous acid. *Proc. Natl. Acad. Sci. U.S.A.* **2013,** *110* (33), 13294-13299.

64. Gligorovski, S.; Weschler, C. J., The oxidative capacity of indoor atmospheres. *Environ. Sci. Technol.* **2013,** *47* (24), 13905-13906.

Chapter 11

CONCLUSIONS AND FUTURE DIRECTIONS

11.1 Atmospheric Relevance of Dissertation Results

In this dissertation, laboratory and field measurements were conducted in order to elucidate the chemical mechanisms governing atmospheric new particle formation. These measurements were performed in two size regimes important to new particle formation: molecular clusters on the order of 1-3 nm diameter and nanoparticles on the order of 20 nm diameter. Studies of sub-3 nm diameter clusters give important information relevant to nucleation, whereas studies on 20 nm diameter nanoparticles give information about growth, which must be understood if the molecular clusters are to become atmospherically relevant. Measurements in each size regime were obtained using mass spectrometric approaches, but the specific approach depended on the size regime to be analyzed. Sub-3 nm clusters were studied using Fourier transform ion cyclotron resonance mass spectrometry (FTICR-MS), whereas 20 nm diameter nanoparticles were studied using the Nano Aerosol Mass Spectrometer (NAMS). A firm understanding of the contributors to nanoparticle growth in both size regimes enables a more precise and chemically rigorous description of how new particle formation proceeds. Such knowledge better enables modelers to determine the climatic relevance of new particle formation.

11.1.1 Chemical Processes Governing Sub-3 nm Diameter Cluster Composition and Dynamics

In the atmosphere, a sub-3 nm pool of clusters has been shown to exist.[1-5] The composition of these clusters is not well defined because only a couple of mass spectrometric techniques are able to directly measure their composition.[6-8] Unfortunately, these instruments operate predominantly in the negative mode and are most efficient below 500 *m/z*. As mentioned in Chapter 2, negatively charged salt clusters generally have no base incorporated at low *m/z*. For this reason, the ion-molecule reactions performed in a FTICR-MS are highly beneficial. The results of Chapters 2-6 provide significant insight into the expected composition and dynamics of these clusters in the atmosphere. Bases (e.g. ammonia and amines) were shown to incorporate into these small clusters via two mechanisms: 1) substitution of one base for another and 2) addition to neutralize acid. Chapters 3-5 showed that amines can efficiently displace ammonia in these clusters, even if the amine concentration is very low. This displacement depends on the difference in basicity between the incoming and outgoing base as well as the difference in binding between the base and sulfuric acid. These laboratory experiments have been validated by field measurements of molecular cluster composition, as amines have recently been detected in these clusters.[8]

Chapters 4 and 5 also examined size-dependent reactivity in ammonium salt clusters. The general conclusion is that as cluster size increases, cluster structure can impact exchange kinetics. Specifically, surface sites will exchange very quickly, whereas core sites exchange very slowly. This observation essentially implies that as the cluster becomes larger, the relative importance of amines versus ammonia decreases. In other words, one would expect amines to be a substantial component of

the cluster composition for very small clusters, but amines would not be as substantial a component of much larger clusters and particles. Instead, ammonia would be more important. Preliminary studies of amine exchange in larger ammonium sulfate aerosol appear to corroborate this hypothesis. Although there is still work to do to understand amine-ammonia chemistry in larger particles (see Section 4.3.4 and Section 11.2.1), these results are consistent with the field measurements described in Chapter 10, ammonia was shown to be the dominant cation-forming species in 20 nm diameter nanoparticles. Nonetheless, these observations suggest that the surface of larger particles is likely to consist of aminium rather than ammonium sulfates and bisulfates, which could have important implications in terms of heterogeneous atmospheric chemistry.

Additionally, as discussed in Chapters 4 and 5, bases can add to a cluster in order to neutralize acid and grow the cluster to larger size. The reaction probability for addition was always slower than the reaction probability for substitution. Additionally, amines added to the clusters more efficiently than ammonia added to the clusters. This observation suggests that amines are more efficient than ammonia for growing particles, although the relative importance of the two is not as clear because of the large difference in ambient concentrations. Chapter 6 expanded upon these observations by studying the energetics of ammonium bisulfate cluster fragmentation, with the assumption that cluster growth is simply the reverse of cluster fragmentation. The results indicate that cluster growth occurs by stepwise addition of sulfuric acid followed by the base. Additionally, the results gave evidence that there is an activation barrier to the addition of ammonia to these clusters. The concept of an activation

barrier is consistent with the slow kinetics of ammonia addition to these clusters, which was observed in Chapters 4 and 5.

The results presented in Chapters 2-6 fit in nicely with recent measurements of cluster nucleation and growth in the ultraclean Cosmics Leaving Outdoor Droplets (CLOUD) chamber at CERN.[9-11] A study of ammonia-sulfuric acid nucleation corroborated key conclusions from this dissertation.[10] First, amine-ammonia exchange chemistry was shown to be very important, albeit unintentionally, in this experiment. Although the chamber is "ultraclean", trace levels of amine contamination were present. This trace amine contamination presented itself by displacing ammonia in ammonium bisulfate clusters, resulting in a substantial ion signal arising from aminium bisulfate clusters. Because amine levels were necessarily very low in this experiment, this observed exchange highlights the favorability of amines over ammonia in these clusters, as first shown in Chapters 3-5. Second, clusters were shown to grow by stepwise addition of sulfuric acid followed by ammonia, which is consistent with the results presented in Chapter 6. Additionally, based on the measured ion abundances, acidic clusters contributed a substantial portion of the total ion current. As discussed in Chapter 6, such an observation is consistent with the concept of an activation barrier to ammonia addition. Finally, the amine-sulfuric acid experiment at CLOUD resulted in collision limited growth of clusters,[9] whereas the ammonia-sulfuric acid experiment resulted in cluster growth that did not proceed at the collision limited rate.[10] Such observations support the experimental results discussed in Chapters 4-6, which show that amine addition is much more efficient than ammonia addition and that ammonia addition involves an activation barrier. Indeed, an activation barrier could be invoked in order to rationalize recent computational

modeling of cluster thermodynamics with measured ion abundances in CLOUD ammonia-sulfuric acid experiments.[12]

A firm understanding of the role of amine-ammonia chemistry in the early steps of new particle formation enables the development of more accurate models of this process. The discovery of an activation barrier is also beneficial to modelers, as to date only thermodynamic endpoints have been included in models describing cluster growth during new particle formation. The work described in this dissertation shows that a trace component of the atmosphere can have a very large impact on cluster composition and that models of new particle formation should be reevaluated to more accurately represent the chemical mechanisms underlying the process.

11.1.2 Chemical Mechanisms of Nanoparticle Growth from 10 to 20 nm Diameter

The first portion of this dissertation addressed the composition and growth of clusters relevant to nucleation. For those clusters to become atmospherically relevant, they must grow larger by orders of magnitude. Critically, they must grow through the 10-20 nm diameter size range. Nanoparticle composition measurements on nanoparticles at 20 nm diameter provide information on growth processes operative as the particle grew from 10 nm to 20 nm, as most of the mass gained by the nanoparticle came during growth from 10 nm to 20 nm diameter. Nanoparticle chemical composition measurements are important in this size range because the range of chemical compounds able to condense onto these particles is more restricted than at larger sizes (e.g. diameters on the order of hundreds of nm). However, due to the small mass of 20 nm diameter nanoparticles (on the order of 4 attograms per particle), performing a measurement is very difficult, especially if one is to perform single

particle measurements.[13, 14] A benefit of NAMS is that such measurements are accessible. Indeed, a key aspect of the NAMS measurement is that particle composition is quantitative. The only negative aspect of the method is that elemental, rather than molecular, composition is obtained. However, as discussed in Chapters 7-10, this drawback can be overcome by apportioning the elemental composition to molecular components expected to exist in the nanoparticles. Therefore, NAMS measurements provide important information about the mechanisms of nanoparticle growth.

Chapter 7 showed that during new particle formation events, nanoparticle composition (on a relative basis) shifted towards inorganic components. Chapter 8 showed that it is possible to quantitatively link gas phase concentrations with particle phase composition. Chapter 9 presented results where nanoparticle composition measurements were highly time-resolved and a number of gas phase species were also measured. Highly time-resolved nanoparticle composition measurements permitted unprecedented insight into the progression of a new particle formation event. Particle phase sulfur and nitrogen mole fractions were shown to increase simultaneously with gas phase sulfuric acid. This simultaneous increase indicates the link between gas and particle phase species as well as the link between particle phase sulfate and cation-forming nitrogen. The gas phase sulfuric acid concentration and particle phase sulfur mole fraction can be quantitatively explained by diffusion limited sulfuric acid condensation onto the growing nanoparticles. The increase in particle phase sulfur and nitrogen mole fraction occurred before the newly formed nanoparticles grew into the NAMS size range, indicating that while new particles are nucleating on the order of a few nanometers in diameter and then growing to larger sizes, the gas phase nucleation

precursors are also condensing onto preexisting nanoparticles and changing their composition. When the mode diameter moves into the NAMS size range, the amount of particle phase nitrogen exceeds that required to neutralize sulfuric acid. As described in Chapter 10, a combination of elemental and molecular nanoparticle composition measurements indicated that this Excess N must be carbonaceous in nature. Moreover, the carbonaceous matter must be highly oxidized, which is consistent with very recent findings by other groups that extremely low volatility organic compounds (ELVOC) may be important to the formation and growth of nanoparticles.[11, 15, 16] This finding of highly oxidized, nitrogen-containing carbonaceous matter during the campaign in Lewes, Delaware, is important because it indicates that there is much left to learn about how nanoparticles grow, especially as it relates to the carbonaceous component of growth, which is still the major uncertainty in assessing the climatic impacts of new particle formation.[17]

More generally, NAMS measurements of new particle formation in several environments indicate that sulfuric acid/ammonium sulfate is always very important to growth. The fraction of sulfuric acid in the particle phase during new particle formation can be quantitatively explained using the model discussed in Chapter 8. However, ammonium sulfate generally accounts for less than half of the nanoparticle growth during new particle formation. Carbonaceous matter accounts for the rest of growth, but the identity of the carbonaceous matter can change substantially from campaign to campaign. For example, in Hyytiälä, Finland, the carbonaceous matter contained no nitrogen and had oxygen-to-carbon ratios that were lower than in Lewes.[18, 19] A better understanding of how the identity of the carbonaceous matter

changes in different locations would improve our understanding its contribution to nanoparticle growth.

In addition to the information gained from studies of new particle formation, as discussed in Chapter 10, NAMS measurements in a number of different environments provide strong evidence for a substantial component of particle phase silicon in locations with large anthropogenic impacts. This observation opens up a number of avenues for scientific exploration, as the molecular identity and sources of the silicon containing compounds are not well known. If nanoparticulate silicon is arising from gas-to-particle conversion of oxidized silicon containing precursors, then this represents an important anthropogenic source of aerosol mass. The importance of silicon to aerosol mass is exemplified by the measurements in Pasadena, California, where elemental silicon mass had an absolute abundance more than five times greater than elemental sulfur mass.

Measurements quantifying the contributions of different molecular channels to particle growth and linking those channels to specific gas phase compounds enable modelers to better describe new particle formation and evaluate its relevance to climate. Based on the results presented in Chapters 8 and 9, the contribution of sulfuric acid to nanoparticle growth is well understood, and this contribution can be accurately modeled. On the other hand, the contributions of carbonaceous matter and silicon to nanoparticle growth are not well understood. While it is possible to rather precisely define the composition and contribution of each to growth, no models yet exist to describe their incorporation into nanoparticles.

11.1.3 Trends in Nanoparticle Growth from Clusters to Nanoparticles

Although two very different size regimes important to nanoparticle growth were investigated in this dissertation, the results of both sets of measurements give some interesting trends across all sizes.

First, as discussed in Chapter 6 and in Chapters 8 and 9, sulfuric acid is shown to add to both small molecular clusters and 10-20 nm nanoparticles in a collision limited manner. In other words, with respect to sulfuric acid, the same mechanism of incorporation exists in small clusters and in larger nanoparticles.

Second, ammonia incorporation may involve an activation barrier. The presence of an activation barrier was suggested for the small molecular clusters discussed in Chapter 6. In measurements taken in Hyytiälä (see dissertation of M. Ross Pennington[18]), elemental nitrogen-to-sulfur ratios were much less than 2, indicating that the aerosol was acidic. In other words, the aerosol did not reach its final thermodynamic state (ammonium sulfate, N/S = 2) despite gas phase ammonia concentrations sufficient to neutralize the aerosol.[19] Whether an activation barrier is operative in both size regimes is not as clear, as one complicating factor in the measurements of 20 nm nanoparticles concerns aerosol phase, which is currently poorly understood.[20, 21] Measurements of ammonia uptake onto sulfuric acid droplets indicate that reaction probabilities are < 1.[22] However, these results are controversial.[23-25] A more recent study, though, showed that reaction probabilities for ammonia uptake onto sulfuric acid aerosol can be $<< 1$ due to competing uptake by organic gases.[26]

Third, forms of nitrogen other than ammonia are important to growth in both molecular clusters and in 20 nm diameter nanoparticles. In both cases, the form of this nitrogen is organic, rather than inorganic. For small molecular clusters, amines are

crucial to the very first steps of growth. On the other hand, for larger particles, organic nitrogen compounds whose molecular composition is not fully resolved (but is not amine) are important to nanoparticle growth in Lewes.

Taken together, what these observations across different size regimes emphasize is that in some cases (e.g. sulfuric acid) the pathway by which a molecular species contributes to growth is well-understood and uniform, but in other cases (e.g. nitrogen) the pathway by which it contributes to growth can change with size. It is important to better understand these size-dependent nanoparticle growth channels in order to ultimately solve the problem of atmospheric new particle formation.

11.2 Future Directions for Studying Clusters and Nanoparticles Relevant to New Particle Formation

This dissertation addressed the chemical mechanisms of new particle formation. Although substantial progress was made in elucidating the chemical species responsible for growth in different size regimes, there are still several key unknowns that require investigation. Some of these unknowns – and potential avenues to investigate them – are discussed below.

11.2.1 Amine-Ammonia Exchange in 10-500 nm Diameter Nanoparticles

Chapters 3-5 discussed measurements of amine-ammonia exchange in small molecular clusters, and Chapter 4 discussed in detail measurements of the size-dependent reactivity of ammonium bisulfate clusters with dimethylamine. Small clusters react to completion because all ammonium ions are on the surface of the cluster, whereas larger clusters do not react to completion because ammonium ions can become encapsulated in the core of the cluster, impeding exchange. This

observation could suggest that as the particle size becomes larger, the relative importance of amine chemistry decreases.

One method to investigate this is to perform flow tube experiments where ammonium sulfate nanoparticles are mixed with a gas phase amine flow and the resulting nanoparticle composition is measured in a time-dependent manner with aerosol mass spectrometry. The reactivity of ammonium sulfate aerosol can then be studied as a function of relative humidity (and, therefore, aerosol phase). Preliminary results from this experiment were discussed in Chapter 4 and seem to imply that amine-ammonia chemistry is not as relevant to larger nanoparticles as it is to small molecular clusters. However, more complete studies would be beneficial because amine-ammonia exchange is an important and relevant atmospheric process and also because size-dependent nano aerosol kinetics have not been reported in the literature. Therefore, such studies would 1) have substantial atmospheric relevance and 2) expand fundamental knowledge in the area of chemical kinetics.

11.2.2 Determination of Collisional Cross Sections for Atmospherically Relevant Clusters and Molecules

When performing measurements of atmospheric clusters, two fundamental properties are sought: 1) chemical composition of the cluster and 2) size of the cluster. Chemical composition measurements can be accomplished using mass spectrometry techniques,[6, 7] whereas cluster size measurements can be accomplished with instruments similar to scanning mobility particle sizer (SMPS) systems.[2, 27, 28] These are two separate instruments, and a major challenge is reconciling the two datasets. In other words, it is difficult to directly correlate changes in the evolution of the cluster size distribution with the appearance/disappearance of molecular clusters with a

specific chemical composition. A few recent high-profile studies have exemplified the need for such information, but to date few have pursued this goal with much success.[1, 11, 15]

One way to address this problem is to perform ion mobility spectrometry-mass spectrometry (IMS-MS) measurements, which provide mobility cross sections and chemical composition on individual ions.[29] This setup requires two components: an ion mobility spectrometer and a mass spectrometer. Some work is underway to extend this approach to better understand atmospheric clusters.[30]

An alternative, and perhaps more elegant, approach is to perform both measurements (collisional cross section and chemical composition) simultaneously. Such an approach is possible using ICR.[31-35] In short, during ICR measurements taken in absorption mode, if pressure is sufficiently high, a Lorentzian lineshape is obtained from collisional broadening of the ion packet. The collisional cross section is then proportional to the width of the Lorentzian lineshape.[34, 36-38] Note that this is only strictly true when absorption mode in used. In FTICR-MS, magnitude (rather than absorption) mode spectra are usually taken. When the time domain transient is recorded in FTICR-MS, the Fourier transform is used to convert to a frequency spectrum. Fourier transformation produces a complex output that can be expressed in either polar (magnitude and phase) or Cartesian (real and imaginary, or absorption and dispersion) terms. Magnitude mode plots frequency against the magnitude component of the output expressed in polar terms. Absorption mode plots frequency against the real component of the output expressed in Cartesian terms. The two can be linked by:

$$A^2 + D^2 = M^2 \quad (1)$$

or:

$$A = M\cos\theta \quad (2)$$

where A = absorption, D = dispersion, M = magnitude, and θ is the phase angle.

The problem with absorption mode is that excitation in the FTICR cell is accomplished by means of an excitation waveform which usually is in the form of a linear frequency sweep. As a result, ions of different *m/z* are excited at different times. After excitation, there is a time delay (order of milliseconds) before detection, where ions will continue to precess around the magnetic field. This manner of excitation results in a phase shift that would impact the apparent value of θ in Eq. (2), and it is difficult to correct for that phase shift on most commercial instrumentation. Therefore, magnitude mode is simply used.

Recent advances in data workflow have enabled more routine conversion of magnitude mode spectra to absorption mode spectra,[39, 40] which potentially could permit easier determination of collisional cross sections from the linewidths. Alternatively, Dearden has demonstrated a method for determining cross sections using the linewidth of the magnitude mode, which essentially relies on relative changes in the linewidth as the background damping pressure changes.[41] Obtained collisional cross sections using either absorption or magnitude mode may be larger than those measured by other IMS techniques, as larger energies are required to excite the ions and all processes contributing to removal of the ion from the packet (e.g. scattering, dissociation) are included in the measured value. Additionally, heavy gases (e.g. Xe) are preferred to lighter gases (e.g. He), as collision broadening is more efficient with heavier ions. This method could be useful up to ~1 kDa ions, so long as single collisions can dephase the ions.

If this technique were developed for atmospheric cluster analysis, precisely known cluster composition could be directly compared to collisional cross sections.

Such information would permit elucidation of the diameter at which specific, composition-resolved clusters would be expected to lie during studies of new particle formation. This information would be directly relevant to recent work where a key unknown was how changes in cluster size distributions might correlate with cluster chemical composition.[1, 15] An additional benefit of the conversion to absorption mode is an increase in resolving power by up to a factor of 2.[34, 37, 42] For more routine analysis of secondary organic aerosol samples, such an increase in resolving power could substantially aid in peak identification, especially as secondary organic aerosol experiments extend to more complicated systems (e.g. systems including N, S, and Si in addition to H, C, and O). If absorption mode were combined with recent advances in FTICR cell technology, such as the dynamically harmonized cell of Nikolaev, which has been shown recently to provide 12 million resolving power on a 4.7T instrument,[43] highly confident identification of the molecular species in secondary organic aerosol would be possible.[42]

11.2.3 Elucidation of the Role of Carbonaceous Matter in Cluster and Nanoparticle Growth

The contribution of carbonaceous matter to nanoparticle growth represents the greatest remaining uncertainty in our understanding of atmospheric new particle formation.[17, 44] Recent work has provided evidence that highly oxidized organic molecules can nucleate along with sulfuric acid to form small molecular clusters[11] and can also contribute substantially to the growth of nanoparticles.[15, 16] Both of these pathways are interesting and require further investigation.

With respect to molecular clusters, Schobesberger et al. posit that highly oxidized organic matter can cluster with sulfuric acid to form nonvolatile clusters.[11]

The evidence to support this hypothesis are cluster ion mass spectra. However, the resolving power of the instrument is on the order of 3000 and calibration of the instrument is somewhat challenging, so ion identification is not entirely certain.[6] Additionally, no tandem mass spectrometry was performed on these clusters to unequivocally show clusters containing sulfuric acid and organic molecules. This study would be improved by use of higher resolving power and tandem mass spectrometry approaches to more precisely define the composition and clustering behavior of carbonaceous matter with sulfuric acid. Both of these capabilities are available in the laboratory and could potentially clarify the composition and atmospheric relevance of organic-sulfuric acid clusters.

In addition to studying highly oxidized organic molecule clustering with sulfuric acid, the contribution of these molecules (also referred to as ELVOC) to nanoparticle growth is of substantial interest.[15] The underlying hypothesis is that these molecules contribute to growth by diffusion limited condensation onto nanoparticles. Methods to more quantitatively understand the composition and contribution of ELVOC to nanoparticle growth are available. For example, flow tube or chamber studies simulating nanoparticle growth could be coupled with a combination of online (NAMS) and offline (high resolution mass spectrometry) measurements of nanoparticle chemical composition. These types of studies would also enable elucidation of the importance and chemical form of organic nitrogen relevant to nanoparticle growth (Chapter 10).

11.2.4 Understanding the Sources, Composition, and Atmospheric Importance of Nanoparticulate Silicon

Chapter 10 discussed the surprising observation that nanoparticles contain a substantial amount of silicon which presumably adds to the particle from gas-to-particle conversion processes. Although the molecular precursors are not well understood, the sources must be anthropogenic, as there are very few sources of biogenic volatile organosilicon compounds. Therefore, the atmospheric fate of silicon could potentially be of high interest to regulatory agencies such as the Environmental Protection Agency, as particulate phase Si may represent a substantial anthropogenic contributor to aerosol mass. Organosilicon compounds can react with OH radical to produce lower volatility products, and those products may include oligomeric species. A study of secondary organic aerosol formation from organosilicon compounds may enhance our understanding of the oxidation pathways of other biogenic compounds, as the oxidation products may be more constrained than for biogenic compounds and determination of their molecular forms may be more straightforward (because of the presence of an additional element – silicon – in these products). Additionally, in the atmosphere, these organosilicon oxidation products will certainly encounter oxidation products from other secondary organic aerosol precursors, and an understanding of those interactions would be beneficial.

11.2.5 Provenance and Geographical Extent of New Particle Formation in Lewes

Chapters 7-10 focused substantially on measurements made during field campaigns in Lewes. As a result of these campaigns and especially due to the nanoparticle composition measurements, Lewes has become one of the best studied locations in the world with respect to new particle formation. As discussed in these chapters, during new particle formation air masses typically arrived from the north and

west of the site. One important remaining question is whether the Lewes site is representative of trends in new particle formation over a much larger geographical area (such as the eastern United States). One method to study the provenance and geographical extent of new particle formation in Lewes is to combine particle size distribution measurements, nanoparticle growth rates, and air mass back trajectories in order to determine the geographical area over which new particle formation occurred. As discussed in Chapter 9, an ultrafine particle monitor is located in Lewes and has been taking particle size distribution measurements for over two years. These data constitute a long term measurement of the frequency of new particle formation at the site. In order to combine these data with air mass back trajectories, one could use a recently developed program called NanoMap.[45] Preliminary results from NanoMap suggest that new particle formation occurs over a widespread area to the north and west of the site. Much of this land includes salt marshes, which may suggest that salt marshes provide a substantial amount of condensable organic material to promote new particle formation. The dynamics of new particle formation in Lewes appear to have a number of similarities to other measurements of new particle formation in eastern North America.[46] For example, nanoparticles appear to form initially at higher altitudes and then descend to ground level once particles have reached ~10 nm diameter.[5, 46] Additionally at other sites in eastern North America, new particle formation tends to occur when air masses are coming from the north and the west.[5, 46] An improved understanding the origin of new particles in Lewes will be beneficial, as Lewes is one of only a handful of sites in the world where nanoparticle chemical composition has been studied in substantial detail. Therefore, if Lewes can be considered a site representative of other locations, Lewes may become a key location

where other scientists come to perform measurements relevant to understanding the mechanisms of new particle formation.

11.3 Concluding Remarks

The goal of this dissertation was to better understand the chemical mechanisms of atmospheric new particle formation by studying molecular clusters and ambient nanoparticles with mass spectrometric techniques. As a result of the experiments described in this work, the role of sulfuric acid in new particle formation is clear. The role of cation-forming nitrogen compounds like ammonia and amines is relatively well understood, although there are some details that still require clarification. The largest remaining uncertainty in assessing the climatic impact of new particle formation relates to understanding the role of carbonaceous matter. Although some preliminary work on the elemental composition and quantitative contribution of carbonaceous matter to nanoparticle growth was addressed in this work, there is still substantial work to do to solve it, and several approaches to resolve the role of carbonaceous matter were discussed in this chapter. Lastly, although silicon may be of only minor importance during new particle formation, it appears to be a persistent, ubiquitous component of atmospheric nanoparticles. Because nanoparticulate silicon probably arises from gaseous organosilicon precursors, treatment of organosilicon in a manner similar to treatment of carbonaceous matter in general may provide substantial insight into the atmospheric role of silicon.

11.4 References

1. Kulmala, M.; Kontkanen, J.; Junninen, H.; Lehtipalo, K.; Manninen, H. E.; Nieminen, T.; Petäjä, T.; Sipilä, M.; Schobesberger, S.; Rantala, P.; Franchin, A.; Jokinen, T.; Järvinen, E.; Äijälä, M.; Kangasluoma, J.; Hakala, J.; Aalto, P. P.; Paasonen, P.; Mikkilä, J.; Vanhanen, J.; Aalto, J.; Hakola, H.; Makkonen, U.; Ruuskanen, T.; Mauldin, R. L.; Duplissy, J.; Vehkamäki, H.; Bäck, J.; Kortelainen, A.; Riipinen, I.; Kurtén, T.; Johnston, M. V.; Smith, J. N.; Ehn, M.; Mentel, T. F.; Lehtinen, K. E. J.; Laaksonen, A.; Kerminen, V.-M.; Worsnop, D. R., Direct observations of atmospheric aerosol nucleation. *Science* **2013,** *339* (6122), 943-946.

2. Kulmala, M.; Riipinen, I.; Sipila, M.; Manninen, H. E.; Petaja, T.; Junninen, H.; Dal Maso, M.; Mordas, G.; Mirme, A.; Vana, M.; Hirsikko, A.; Laakso, L.; Harrison, R. M.; Hanson, I.; Leung, C.; Lehtinen, K. E. J.; Kerminen, V. M., Toward direct measurement of atmospheric nucleation. *Science* **2007,** *318* (5847), 89-92.

3. Lehtipalo, K.; Kulmala, M.; Sipila, M.; Petaja, T.; Vana, M.; Ceburnis, R.; Dupuy, R.; O'Dowd, C., Nanoparticles in boreal forest and coastal environment: a comparison of observations and implications of the nucleation mechanism. *Atmos. Chem. Phys.* **2010,** *10* (15), 7009-7016.

4. Lehtipalo, K.; Sipilä, M.; Junninen, H.; Ehn, M.; Berndt, T.; Kajos, M. K.; Worsnop, D. R.; Petäjä, T.; Kulmala, M., Observations of nano-CN in the nocturnal boreal forest. *Aerosol Sci. Technol.* **2011,** *45* (4), 499-509.

5. Yu, H.; Gannet Hallar, A.; You, Y.; Sedlacek, A.; Springston, S.; Kanawade, V. P.; Lee, Y.-N.; Wang, J.; Kuang, C.; McGraw, R. L.; McCubbin, I.; Mikkila, J.; Lee, S.-H., Sub-3 nm particles observed at the coastal and continental sites in the United States. *J. Geophys. Res.-Atmos.* **2014,** *119* (2), 860-879, doi: 10.1002/2013jd020841.

6. Junninen, H.; Ehn, M.; Petaja, T.; Luosujarvi, L.; Kotiaho, T.; Kostiainen, R.; Rohner, U.; Gonin, M.; Fuhrer, K.; Kulmala, M.; Worsnop, D. R., A high-resolution mass spectrometer to measure atmospheric ion composition. *Atmos. Meas. Tech.* **2010,** *3* (4), 1039-1053.

7. Zhao, J.; Eisele, F. L.; Titcombe, M.; Kuang, C.; McMurry, P. H., Chemical ionization mass spectrometric measurements of atmospheric neutral clusters using the cluster-CIMS. *J. Geophys. Res.-Atmos.* **2010,** *115* (D8), D08205, doi: 10.1029/2009JD012606.

8. Zhao, J.; Smith, J. N.; Eisele, F. L.; Chen, M.; Kuang, C.; McMurry, P. H., Observation of neutral sulfuric acid-amine containing clusters in laboratory and ambient measurements. *Atmos. Chem. Phys.* **2011,** *11* (21), 10823-10836.

9. Almeida, J.; Schobesberger, S.; Kurten, A.; Ortega, I. K.; Kupiainen-Maatta, O.; Praplan, A. P.; Adamov, A.; Amorim, A.; Bianchi, F.; Breitenlechner, M.; David, A.; Dommen, J.; Donahue, N. M.; Downard, A.; Dunne, E.; Duplissy, J.; Ehrhart, S.; Flagan, R. C.; Franchin, A.; Guida, R.; Hakala, J.; Hansel, A.; Heinritzi, M.; Henschel, H.; Jokinen, T.; Junninen, H.; Kajos, M.; Kangasluoma, J.; Keskinen, H.; Kupc, A.; Kurten, T.; Kvashin, A. N.; Laaksonen, A.; Lehtipalo, K.; Leiminger, M.; Leppa, J.; Loukonen, V.; Makhmutov, V.; Mathot, S.; McGrath, M. J.; Nieminen, T.; Olenius, T.; Onnela, A.; Petaja, T.; Riccobono, F.; Riipinen, I.; Rissanen, M.; Rondo, L.; Ruuskanen, T.; Santos, F. D.; Sarnela, N.; Schallhart, S.; Schnitzhofer, R.; Seinfeld, J. H.; Simon, M.; Sipila, M.; Stozhkov, Y.; Stratmann, F.; Tome, A.; Trostl, J.; Tsagkogeorgas, G.; Vaattovaara, P.; Viisanen, Y.; Virtanen, A.; Vrtala, A.; Wagner, P. E.; Weingartner, E.; Wex, H.; Williamson, C.; Wimmer, D.; Ye, P.; Yli-Juuti, T.; Carslaw, K. S.; Kulmala, M.; Curtius, J.; Baltensperger, U.; Worsnop, D. R.; Vehkamaki, H.; Kirkby, J., Molecular understanding of sulphuric acid-amine particle nucleation in the atmosphere. *Nature* **2013,** *502* (7471), 359-363.

10. Kirkby, J.; Curtius, J.; Almeida, J.; Dunne, E.; Duplissy, J.; Ehrhart, S.; Franchin, A.; Gagne, S.; Ickes, L.; Kurten, A.; Kupc, A.; Metzger, A.; Riccobono, F.; Rondo, L.; Schobesberger, S.; Tsagkogeorgas, G.; Wimmer, D.; Amorim, A.; Bianchi, F.; Breitenlechner, M.; David, A.; Dommen, J.; Downard, A.; Ehn, M.; Flagan, R. C.; Haider, S.; Hansel, A.; Hauser, D.; Jud, W.; Junninen, H.; Kreissl, F.; Kvashin, A.; Laaksonen, A.; Lehtipalo, K.; Lima, J.; Lovejoy, E. R.; Makhmutov, V.; Mathot, S.; Mikkila, J.; Minginette, P.; Mogo, S.; Nieminen, T.; Onnela, A.; Pereira, P.; Petaja, T.; Schnitzhofer, R.; Seinfeld, J. H.; Sipila, M.; Stozhkov, Y.; Stratmann, F.; Tome, A.; Vanhanen, J.; Viisanen, Y.; Vrtala, A.; Wagner, P. E.; Walther, H.; Weingartner, E.; Wex, H.; Winkler, P. M.; Carslaw, K. S.; Worsnop, D. R.; Baltensperger, U.; Kulmala, M., Role of sulphuric acid, ammonia and galactic cosmic rays in atmospheric aerosol nucleation. *Nature* **2011,** *476* (7361), 429-433.

11. Schobesberger, S.; Junninen, H.; Bianchi, F.; Lönn, G.; Ehn, M.; Lehtipalo, K.; Dommen, J.; Ehrhart, S.; Ortega, I. K.; Franchin, A.; Nieminen, T.; Riccobono, F.; Hutterli, M.; Duplissy, J.; Almeida, J.; Amorim, A.; Breitenlechner, M.; Downard, A. J.; Dunne, E. M.; Flagan, R. C.; Kajos, M.; Keskinen, H.; Kirkby, J.; Kupc, A.; Kürten, A.; Kurtén, T.; Laaksonen, A.; Mathot, S.; Onnela, A.; Praplan, A. P.; Rondo, L.; Santos, F. D.; Schallhart, S.; Schnitzhofer, R.; Sipilä, M.; Tomé, A.; Tsagkogeorgas, G.; Vehkamäki, H.; Wimmer, D.; Baltensperger, U.; Carslaw, K. S.; Curtius, J.; Hansel, A.; Petäjä, T.; Kulmala, M.; Donahue, N.

M.; Worsnop, D. R., Molecular understanding of atmospheric particle formation from sulfuric acid and large oxidized organic molecules. *Proc. Natl. Acad. Sci. U.S.A.* **2013,** *110* (43), 17223-17228.

12. Olenius, T.; Schobesberger, S.; Kupiainen-Maatta, O.; Franchin, A.; Junninen, H.; Ortega, I. K.; Kurten, T.; Loukonen, V.; Worsnop, D. R.; Kulmala, M.; Vehkamaki, H., Comparing simulated and experimental molecular cluster distributions. *Faraday Discuss.* **2013,** *165* (1), 75-89.

13. Bzdek, B. R.; Johnston, M. V., New particle formation and growth in the troposphere. *Anal. Chem.* **2010,** *82* (19), 7871-7878.

14. Bzdek, B. R.; Pennington, M. R.; Johnston, M. V., Single particle chemical analysis of ambient ultrafine aerosol: A review. *J. Aerosol Sci.* **2012,** *52* (1), 109-120.

15. Ehn, M.; Thornton, J. A.; Kleist, E.; Sipila, M.; Junninen, H.; Pullinen, I.; Springer, M.; Rubach, F.; Tillmann, R.; Lee, B.; Lopez-Hilfiker, F.; Andres, S.; Acir, I.-H.; Rissanen, M.; Jokinen, T.; Schobesberger, S.; Kangasluoma, J.; Kontkanen, J.; Nieminen, T.; Kurten, T.; Nielsen, L. B.; Jorgensen, S.; Kjaergaard, H. G.; Canagaratna, M.; Maso, M. D.; Berndt, T.; Petaja, T.; Wahner, A.; Kerminen, V.-M.; Kulmala, M.; Worsnop, D. R.; Wildt, J.; Mentel, T. F., A large source of low-volatility secondary organic aerosol. *Nature* **2014,** *506* (7489), 476-479.

16. Zhao, J.; Ortega, J.; Chen, M.; McMurry, P. H.; Smith, J. N., Dependence of particle nucleation and growth on high-molecular-weight gas-phase products during ozonolysis of alpha-pinene. *Atmos. Chem. Phys.* **2013,** *13* (15), 7631-7644.

17. Carslaw, K. S.; Lee, L. A.; Reddington, C. L.; Mann, G. W.; Pringle, K. J., The magnitude and sources of uncertainty in global aerosol. *Faraday Discuss.* **2013,** *165* (1), 495-512.

18. Pennington, M. R. An Improved Nano Aerosol Mass Spectrometer for Ambient and Laboratory Measurements. University of Delaware, Newark, DE, 2012.

19. Pennington, M. R.; Bzdek, B. R.; DePalma, J. W.; Smith, J. N.; Kortelainen, A.-M.; Hildebrandt Ruiz, L.; Petaja, T.; Kulmala, M.; Worsnop, D. R.; Johnston, M. V., Identification and quantification of particle growth channels during new particle formation. *Atmos. Chem. Phys.* **2013,** *13* (20), 10215-10225.

20. Virtanen, A.; Joutsensaari, J.; Koop, T.; Kannosto, J.; Yli-Pirila, P.; Leskinen, J.; Makela, J. M.; Holopainen, J. K.; Poschl, U.; Kulmala, M.; Worsnop, D. R.; Laaksonen, A., An amorphous solid state of biogenic secondary organic aerosol particles. *Nature* **2010,** *467* (7317), 824-827.

21. Virtanen, A.; Kannosto, J.; Kuuluvainen, H.; Arffman, A.; Joutsensaari, J.; Saukko, E.; Hao, L.; Yli-Pirila, P.; Tiitta, P.; Holopainen, J. K.; Keskinen, J.; Worsnop, D. R.; Smith, J. N.; Laaksonen, A., Bounce behavior of freshly nucleated biogenic secondary organic aerosol particles. *Atmos. Chem. Phys.* **2011,** *11* (16), 8759-8766.

22. Swartz, E.; Shi, Q.; Davidovits, P.; Jayne, J. T.; Worsnop, D. R.; Kolb, C. E., Uptake of gas-phase ammonia. 2. Uptake by sulfuric acid surfaces. *J. Phys. Chem. A* **1999,** *103* (44), 8824-8833.

23. Hanson, D.; Kosciuch, E., The NH_3 mass accommodation coefficient for uptake onto sulfuric acid solutions. *J. Phys. Chem. A* **2003,** *107* (13), 2199-2208.

24. Hanson, D. R.; Kosciuch, E., Reply to "comment on 'The NH_3 mass accommodation coefficient for uptake onto sulfuric acid solutions'". *J. Phys. Chem. A* **2004,** *108* (40), 8549-8551.

25. Worsnop, D. R.; Williams, L. R.; Kolb, C. E.; Mozurkewich, M.; Gershenzon, M.; Davidovits, P., Comment on "The NH_3 mass accommodation coefficient for uptake onto sulfuric acid solution". *J. Phys. Chem. A* **2004,** *108* (40), 8546-8548.

26. Liggio, J.; Li, S. M.; Vlasenko, A.; Stroud, C.; Makar, P., Depression of ammonia uptake to sulfuric acid aerosols by competing uptake of ambient organic gases. *Environ. Sci. Technol.* **2011,** *45* (7), 2790-2796.

27. Kulmala, M.; Mordas, G.; Petaja, T.; Gronholm, T.; Aalto, P. P.; Vehkamaki, H.; Hienola, A. I.; Herrmann, E.; Sipila, M.; Riipinen, I.; Manninen, H. E.; Hameri, K.; Stratmann, F.; Bilde, M.; Winkler, P. M.; Birmili, W.; Wagner, P. E., The condensation particle counter battery (CPCB): A new tool to investigate the activation properties of nanoparticles. *J. Aerosol Sci.* **2007,** *38* (3), 289-304.

28. Vanhanen, J.; Mikkila, J.; Lehtipalo, K.; Sipila, M.; Manninen, H. E.; Siivola, E.; Petaja, T.; Kulmala, M., Particle size magnifier for nano-CN detection. *Aerosol Sci. Technol.* **2011,** *45* (4), 533-542.

29. Kanu, A. B.; Dwivedi, P.; Tam, M.; Matz, L.; Hill, H. H., Ion mobility–mass spectrometry. *J. Mass Spectrom.* **2008,** *43* (1), 1-22.

30. Steiner, G.; Jokinen, T.; Junninen, H.; Sipila, M.; Petaja, T.; Worsnop, D.; Reischl, G. P.; Kulmala, M., High-resolution mobility and mass spectrometry of negative ions produced in a Am-241 aerosol charger. *Aerosol Sci. Technol.* **2014,** *48* (3), 261-270.

31. Ridge, D. P.; Beauchamp, J. L., Interactions of ions with polar neutrals: The momentum transfer collision frequencies of Na^+ with the C_3H_6O isomers. *Chem. Phys. Lett.* **1976,** *41* (2), 301-304.

32. Ridge, D. P.; Beauchamp, J. L., Interactions of ions with nonpolar neutrals: Collision broadening of ion-cyclotron resonance lines of ion in hydrogen and methane. *J. Chem. Phys.* **1976,** *64* (7), 2735-2746.

33. Beauchamp, J. L., Theory of collision-broadened ion cyclotron resonance spectra. *J. Chem. Phys.* **1967,** *46* (4), 1231-1243.

34. Marshall, A. G., Theory for ion cyclotron resonance absorption line shapes. *J. Chem. Phys.* **1971,** *55* (3), 1343-1354.

35. Parisod, G.; Comisarow, M. B., Determination of ion-molecule collision frequencies by Fourier transform ion cyclotron resonance spectroscopy. *Chem. Phys. Lett.* **1979,** *62* (2), 303-305.

36. Comisarow, M. B.; Marshall, A. G., Theory of Fourier transform ion cyclotron resonance mass spectroscopy. I. Fundamental equations and low-pressure line shape. *J. Chem. Phys.* **1976,** *64* (1), 110-119.

37. Marshall, A. G.; Comisarow, M. B.; Parisod, G., Relaxation and spectral line shape in Fourier transform ion resonance spectroscopy. *J. Chem. Phys.* **1979,** *71* (11), 4434-4444.

38. Marshall, A. G.; Roe, D. C., Dispersion versus absorption: Spectral line shape analysis for radiofrequency and microwave spectrometry. *Anal. Chem.* **1978,** *50* (6), 756-763.

39. Kilgour, D. P. A.; Wills, R.; Qi, Y. L.; O'Connor, P. B., Autophaser: An algorithm for automated generation of absorption mode spectra for FT-ICR MS. *Anal. Chem.* **2013,** *85* (8), 3903-3911.

40. Qi, Y. L.; Barrow, M. P.; Li, H. L.; Meier, J. E.; Van Orden, S. L.; Thompson, C. J.; O'Connor, P. B., Absorption-Mode: The next generation of Fourier transform mass spectra. *Anal. Chem.* **2012,** *84* (6), 2923-2929.

41. Yang, F.; Voelkel, J. E.; Dearden, D. V., Collision cross sectional areas from analysis of Fourier transform ion cyclotron resonance line width: A new method for characterizing molecular structure. *Anal. Chem.* **2012,** *84* (11), 4851-4857.

42. Qi, Y. L.; Witt, M.; Jertz, R.; Baykut, G.; Barrow, M. P.; Nikolaev, E. N.; O'Connor, P. B., Absorption-mode spectra on the dynamically harmonized Fourier transform ion cyclotron resonance cell. *Rapid Commun. Mass Spectrom.* **2012,** *26* (17), 2021-2026.

43. Popov, I. A.; Nagornov, K.; Vladimirov, G. N.; Kostyukevich, Y. I.; Nikolaev, E. N., Twelve million resolving power on 4.7 T Fourier transform ion cyclotron resonance instrument with dynamically harmonized cell—Observation of fine structure in peptide mass spectra. *J. Am. Soc. Mass Spectrom.* **2014,** *25* (5), 790-799.

44. Lee, L. A.; Pringle, K. J.; Reddington, C. L.; Mann, G. W.; Stier, P.; Spracklen, D. V.; Pierce, J. R.; Carslaw, K. S., The magnitude and causes of uncertainty in global model simulations of cloud condensation nuclei. *Atmos. Chem. Phys.* **2013,** *13* (17), 8879-8914.

45. Kristensson, A.; Johansson, M.; Swietlicki, E.; Kivekäs, N.; Hussein, T.; Nieminen, T.; Kulmala, M.; Dal Maso, M., NanoMap: Geographical mapping of atmospheric new particle formation through analysis of 1 particle number size distribution and trajectory data. *Boreal Environ. Res.* **2014,** *Article in Press*.

46. Crippa, P.; Pryor, S. C., Spatial and temporal scales of new particle formation events in eastern North America. *Atmos. Environ.* **2013,** *75* (1), 257-264.